

KIBBLE-ZUREK MECHANISM IN A SPIN-1 BOSE-EINSTEIN CONDENSATE

A Thesis
Presented to
The Academic Faculty

by

Martin Anquez

In Partial Fulfillment
of the Requirements for the Degree
Doctor of Philosophy in the
School of Physics

Georgia Institute of Technology
December 2015

Copyright © 2015 by Martin Anquez

KIBBLE-ZUREK MECHANISM IN A SPIN-1 BOSE-EINSTEIN CONDENSATE

Approved by:

Professor Michael S. Chapman,
Advisor
School of Physics
Georgia Institute of Technology

Professor Pablo Laguna
School of Physics
Georgia Institute of Technology

Professor Brian Kennedy
School of Physics
Georgia Institute of Technology

Professor Phillip First
School of Physics
Georgia Institute of Technology

Dr. Jason M. Amini
Georgia Tech Research Institute
Georgia Institute of Technology

Date Approved: 17 September 2015

To my parents, Bernard and Béatrice Anquez

To my wife, Dr. Rachel Johnson Anquez

ACKNOWLEDGMENTS

How sweet to finally reach the point where I get to thank everyone who assisted me in this journey! I would first and foremost like to thank my advisor, Professor Michael Chapman. Even before I began my graduate studies, I was fortunate to meet with him and our encouraging conversation certainly helped me solidify my decision to pursue an advanced degree in physics. He welcomed me with open arms into his lab, where I had the opportunity to participate in cutting edge research using incredibly advanced equipment. I also was able to benefit from Mike's vast experience in our field and his deep insight into the big picture for physics research. I believe Mike has found the best balance with his interaction with his students: he gives us enough autonomy to grow and feel personally responsible about our role in the lab, but is present to provide guidance and support when we veer off-course. The atmosphere he cultivated in the lab was one where trust and autonomy led to motivation and confidence in a supportive, healthy, and friendly environment. I could not have asked for a better place to spend this challenging period of my life.

From my undergraduate years at Georgia State University, I would like to thank Dr. Brian Thoms, whose modern physics class set strong foundations for the rest of my studies, as did Dr. Stephen Manson's quantum mechanics class. I am also grateful to Dr. Gennady Cymbalyuk and Dr. Ramesh Mani, who gave me an experimental foundation in physics.

I received so much support from all the members of the Chapman group. I did not have the opportunity to work directly with Ming-Shien Chang and Eva Bookjans in the lab, but the advances they brought to the experimental setup and techniques are still very much used today. I did however have the pleasure to work directly with

many great graduate colleagues. The most senior was Chris Hamley, who was always generous with his knowledge and experience, despite his pretending to be annoyed by my many calls for assistance. Much of what I learned in the experimental side of the lab was shared with me by LTC Corey Gerving. He taught me how to run the experiment, and helped when the setup needed troubleshooting. Thai Hoang was the most recent student to graduate before me, so I worked most closely with him as my skills advanced. When he became the most senior member of the lab, he demonstrated tremendous leadership, and his intense work schedule and dedication were truly inspiring. I was very fortunate that he remained in the lab as a post-doc for some time, and when my turn came to take data, he was always willing to help, as were the current graduate students: Bryce Robbins, Matthew Boguslawski, and Bharath Hebbe Madhusudhana. Bryce always has a positive attitude, consistently eager to learn and to share his own knowledge. My coding in Mathematica became much more elegant and efficient after he joined the lab. Matt and Bharath are the newest additions to the lab, and after only a few months, these hard working juniors were able to join Thai and Bryce in assisting me to take data. In addition to quick thinking and great new ideas to improve the setup, Matt brought with him experimental skills he learned as an undergraduate. His competence allowed him to train Bharath, allowing me more time on data analysis and writing. Bharath has a broad and impressive source of knowledge, and I have learned much from our conversations, where he is able to give clear explanations about complex and abstract subjects. I would also like to thank Ben Land, an undergraduate student who significantly improved the code for the simulations used in this thesis. Chris and Ben also performed the initial simulations to test the KZM before we started the experimental study.

I have made many friends at Georgia Tech during the past five years, in which I am happy to include the former and current Chapman group members. There are two graduate students from my incoming class with whom I spent more time than

others: Jeff Tithof and Caitlin Baker. Jeff and I spent countless lunches discussing our similar taste in music, and I was lucky to have an optimistic friend to talk to when the experiment was not working well. Our trips to the campus gym left me fitter, happier, and more productive. I will also fondly remember the many afternoons spent at the rock climbing wall with Cait, which were the perfect breaks from a sometimes frustrating experiment.

I would also like to thank the faculty of the school of physics, and particularly the members of my defense committee. Among them are Dr. Brian Kennedy, who happened to have Dr. Kibble as a professor earlier in his career, and Dr. Pablo Laguna, who co-authored several publications with Dr. Zurek. Dr. Phillip First and Dr. Jason Amini brought their experimental expertise to the group. My compatriot Dr. Claire Berger is a good friend, and it is always a pleasure to hear her voice. A special thanks goes to Dr. Andrew Zangwill, our graduate supervisor, who had answers to any question I threw at him.

I would not have reached this moment if it weren't for my family. My parents Bernard and Béatrice always provided an environment where learning was fun, and particularly stimulated my curiosity in math and science. Along with my siblings Laure, Damien, and Julie, they were constantly by my side, sharing the good times and supporting me through the tougher parts of the journey. My grandmother "Grannie" also contributed to my early scientific uprising by getting me subscriptions to the magazine *Science & Vie Junior*.

Finally, I want to sincerely thank my wife, Dr. Rachel Johnson Anquez. Not only is she one of the smartest people I know, she is also the most caring person I have ever met. Her joy when I succeed is as intense as her compassion and love during hard times. She supported me from the moment I considered graduate school, and she has been my main source of comfort and motivation throughout the whole endeavor. She is my partner in crime and the love of my life, and I look forward to the next steps

in our life, as we continue this amazing journey together.

TABLE OF CONTENTS

DEDICATION	iii
ACKNOWLEDGMENTS	iv
LIST OF TABLES	xi
LIST OF FIGURES	xii
SUMMARY	xv
I INTRODUCTION	1
1.1 Kibble-Zurek Mechanism	1
1.2 Spinor Bose-Einstein Condensates	2
1.2.1 Previous Work in Our Group	3
1.3 Thesis Organization	6
II KIBBLE-ZUREK MECHANISM THEORY	7
2.1 Review of Phase Transitions	7
2.1.1 Classical Phase Transitions	7
2.1.2 Quantum Phase Transitions	9
2.2 Kibble-Zurek Mechanism	12
2.2.1 KZM in a Ferromagnetic Spin-1 BEC	14
III SPINOR BOSE-EINSTEIN CONDENSATE THEORY	20
3.1 Gross-Pitaevskii Equation	22
3.2 Single Mode Approximation	24
3.3 Quantum Approach	26
3.4 Mean Field Approach	29
3.5 Quantum Phase Transition	31
3.6 Phase Spaces	33
3.6.1 Spin-Nematic Phase Space	33
3.6.2 Polar Phase Space	35

3.6.3	Spinor Phase Space	37
3.7	Summary	37
IV	EXPERIMENTAL APPARATUS	39
4.1	Vacuum Chamber	39
4.2	Magneto-Optical Trap	42
4.2.1	Source of Atoms	42
4.2.2	Trapping Concept	42
4.2.3	MOT Lasers	47
4.2.4	Magnetic Field Coils	49
4.3	From Magneto-Optical Trap to Bose-Einstein Condensate	49
4.3.1	Optical Trap	50
4.3.2	Cross Trap	54
4.3.3	Magnetic Field Coils	55
4.3.4	Microwaves and RF	57
4.3.5	Control System	59
4.3.6	Data Acquisition	60
4.4	Imaging	61
4.4.1	Absorptive Imaging	61
4.4.2	Fluorescence Imaging	63
V	METHODS	67
5.1	Critical Magnetic Field Determination	67
5.2	Magnetic Field Ramps	72
5.2.1	Measurement of Spin Populations	75
5.3	Experimental Settings	76
VI	RESULTS	79
6.1	KZM Scaling	79
6.1.1	Determining the Beginning of Spin Dynamics	79
6.1.2	Loss Model	80

6.1.3	Error Analysis	86
6.1.4	Extraction of Scaling Exponents	93
6.2	Concluding Remarks	100
VII COMPARISON WITH SIMULATIONS		101
7.1	Simulations	101
7.1.1	Loss-Less Simulations	103
7.1.2	Simulations Including Atom Loss	112
7.1.3	Comparison of Semi-Classical and Quantum Simulations . . .	115
7.1.4	Pollution	118
7.2	Concluding Remarks	125
VIII CONCLUSION AND OUTLOOK		128
8.1	Future Work	129
8.1.1	High Precision Measurements	129
8.1.2	Spin Domains	129
8.1.3	Energy Gap	130
8.1.4	Improving Spin-Nematic Squeezing	130
8.1.5	Measurement of Entanglement	130
APPENDIX A — FUNDAMENTAL CONSTANTS AND EXPERIMENTAL PARAMETERS		132
APPENDIX B — SINGLE FOCUS TRAP		133
APPENDIX C — EXPERIMENTAL ISSUES AND IMPROVEMENTS		136
APPENDIX D — ADDITIONAL DATA		148
REFERENCES		169

LIST OF TABLES

3.1	Spin-1 dipole and quadrupole operators	27
6.1	Data sets	95
6.2	Summary of scaling exponents determined using ρ_0	98
6.3	Summary of scaling exponents determined using $\Delta\rho_0$	98
7.1	Effect of number of atoms with ramps starting at a high magnetic field (no loss)	106
7.2	Summary of exponents from loss-less simulations	112
7.3	Effect of number of atoms on scaling exponents (with loss)	115
7.4	Effect of atom loss on scaling exponents	116
7.5	Effect of pollution on scaling exponents	124
A.1	Fundamental constants and useful ^{87}Rb properties	132

LIST OF FIGURES

2.1	Adiabatic-impulse-adiabatic diagram with \hat{t}	17
2.2	Adiabatic-impulse-adiabatic diagram with \hat{q}	18
3.1	Energy gap between the ground state and first excited state	32
3.2	Spin-nematic phase space	34
3.3	Polar phase space	36
3.4	Spinor phase space	38
4.1	Diagram of the vacuum chamber	41
4.2	D2 line energy levels for ^{87}Rb	44
4.3	Energy levels of the $5^2\text{S}_{1/2}$ level in ^{87}Rb	46
4.4	Effect of the translation stage motion	53
4.5	Temperature and number of atoms during evaporation	54
4.6	Microwave and RF setup	58
5.1	Evolution close to the critical point (simulation)	68
5.2	Evolution compared with simulations best match	70
5.3	Evolution compared with range of simulations	71
5.4	Magnetic field control settings	73
5.5	Magnetic field response to the control settings (simulation)	74
5.6	Measurement of spin populations during a magnetic field ramp	75
5.7	Standard deviation of spin populations during a magnetic field ramp	76
5.8	Spin populations for several ramp times	77
6.1	Spinor dynamical rate $ c $ as a function of total number of atoms	83
6.2	Total number of atoms in the condensate during a magnetic field ramp	84
6.3	Effect of atom loss on q and \tilde{q}	85
6.4	Effect of atom loss on the critical time t_c and the rate of change of \tilde{q} at the critical point	86
6.5	Measurements of ρ_0 during a magnetic field ramp	88
6.6	Measurements of $\Delta\rho_0$ during a magnetic field ramp	89

6.7	Plots of \hat{t} and \hat{q} generated using ρ_0 (data set #2)	96
6.8	Plots of \hat{t} and \hat{q} generated using $\Delta\rho_0$ (data set #2)	97
6.9	Summary of \hat{t} exponents	99
6.10	Summary of \hat{q} exponents	99
7.1	Initial distributions of states in the polar phase space	102
7.2	Loss-less simulations starting from a high magnetic field	104
7.3	Effect of different numbers of atoms (no loss)	106
7.4	Loss-less simulations	108
7.5	Initial distributions of states and energy contours before and after the initial quench	109
7.6	Polar phase space right after the critical point	110
7.7	Effect of ramp initial magnetic field (no loss)	112
7.8	Simulations including atoms loss	113
7.9	Effect of different numbers of atoms (with loss)	114
7.10	Effect of atom loss	116
7.11	Comparison of semi-classical and quantum simulations	117
7.12	Measurements of ρ_0 and $\Delta\rho_0$ with pollution	120
7.13	Measurements of ρ_0 at constant high magnetic field showing pollution	121
7.14	Measurements of ρ_0 with pollution compensation	122
7.15	Quantum simulations with pollution	123
7.16	Summary of scaling exponents	126
B.1	Monitoring domain formation in the single focus trap	134
B.2	Measurements of ρ_0 during a magnetic field ramp in the single focus trap	135
C.1	Cross section of the CO ₂ laser before the AOM	137
C.2	Cross sections of the CO ₂ laser beam while changing the position of the lens mover	138
C.3	Double trap in the CO ₂ laser dipole force trap	139
C.4	Single trap in the CO ₂ laser dipole force trap	141
C.5	Drifting single focus trap	142

C.6	Single focus trap displacement	143
C.7	Effect of the 60 Hz magnetic field fluctuations	146
D.1	Measurements of ρ_0 during magnetic field ramps (data set #1)	148
D.2	Measurements of ρ_0 during magnetic field ramps (data set #2)	151
D.3	Measurements of ρ_0 during magnetic field ramps (data set #3)	154
D.4	Measurements of ρ_0 during magnetic field ramps (data set #4)	157
D.5	Data set #1, \hat{t} , ρ_0	161
D.6	Data set #1, \hat{q} , ρ_0	161
D.7	Data set #1, \hat{t} , $\Delta\rho_0$	162
D.8	Data set #1, \hat{q} , $\Delta\rho_0$	162
D.9	Data set #2, \hat{t} , ρ_0	163
D.10	Data set #2, \hat{q} , ρ_0	163
D.11	Data set #2, \hat{t} , $\Delta\rho_0$	164
D.12	Data set #2, \hat{q} , $\Delta\rho_0$	164
D.13	Data set #3, \hat{t} , ρ_0	165
D.14	Data set #3, \hat{q} , ρ_0	165
D.15	Data set #3, \hat{t} , $\Delta\rho_0$	166
D.16	Data set #3, \hat{q} , $\Delta\rho_0$	166
D.17	Data set #4, \hat{t} , ρ_0	167
D.18	Data set #4, \hat{q} , ρ_0	167
D.19	Data set #4, \hat{t} , $\Delta\rho_0$	168
D.20	Data set #4, \hat{q} , $\Delta\rho_0$	168

SUMMARY

The subject of this thesis is an experimental investigation of the Kibble-Zurek mechanism in an atomic spin-1 Bose-Einstein condensate. The Kibble-Zurek mechanism (KZM) primarily characterizes scaling in the formation of topological defects when a system crosses a continuous phase transition. The KZM was first used to study the evolution of the early universe, describing the topology of cosmic domains and strings as the symmetry breaking phase transitions acted on the vacuum fields during the initial cooling. A ferromagnetic spin-1 ^{87}Rb Bose-Einstein condensate (BEC) exhibits a second-order gapless quantum phase transition due to a competition between the magnetic and collisional spin interaction energies. Unlike the situation in extended systems where the KZM is illustrated by topological defects, we focus our study on the temporal evolution of the spin populations and observe how the scaling of the spin dynamics depend on how fast the system is driven through the critical point. In our case, the excitations are manifest in the temporal evolution of the spin populations illustrating a Kibble-Zurek type scaling, where the dynamics of slow quenches through the critical point are predicted to exhibit universal scaling as a function of quench speed. The KZM has been studied theoretically and experimentally in a large variety of systems. There has also been a tremendous interest in the KZM in the cold atoms community in recent years. It has been observed not only in ion chains and in atomic gases in optical lattices, but also in Bose gases through the formation of vortices or solitons. The KZM in the context of crossing the quantum phase transition in a ferromagnetic BEC has been theoretically studied, but this thesis is the first experimental investigation of this phenomenon.

CHAPTER I

INTRODUCTION

1.1 Kibble-Zurek Mechanism

The Kibble-Zurek mechanism (KZM) seeks to describe the dynamics of crossing continuous phase transitions at a finite rate. It was initially formulated in 1976 by Kibble [1] to determine the topology of defects created in the cooling of the early universe. Kibble argued that symmetry breaking phase transitions could have caused topological defects such as domain walls, cosmic strings, and monopoles. These defects may have influenced the structure of the universe we can observe today.

A few years later, Zurek suggested applying this concept of symmetry breaking to the scaling of domains in condensed matter systems [2]. His proposal was to test Kibble's idea in a superfluid helium experiment using pressure quenches to cross the critical point of a phase transition. The key prediction yields a scaling of defect size with respect to the quench speed. Close to the critical point in a continuous phase transition, the relaxation time diverges, usually as a power law involving critical exponents [3]. This relaxation time sets the time scale at which the system can react to an external change. Far from the critical point, the system can react quickly to change, and the evolution following the change is adiabatic. However, as the system is driven at a finite speed through the critical point, there comes a moment when the evolution can no longer be adiabatic, and the system enters an impulse stage, where the dynamics are "frozen." Once the critical point is passed, the system can recover its adiabatic evolution when the relaxation time is small enough. This argument is called the adiabatic-impulse approximation. The KZM predicts the scaling of the domain size and freeze-out time as a function of the quench speed using power

laws involving equilibrium critical exponents. Though initially applied to condensed matter systems, these predictions have since been extensively studied and tested in other systems. More recently, cold atoms have also been used as a test bed for the KZM. Initially formulated for classical continuous phase transitions, the KZM has also been tested in quantum phase transitions, which take place at absolute zero.

1.2 Spinor Bose-Einstein Condensates

Predicted in the 1920s, the concept of Bose-Einstein condensation relies on the wave-like properties of matter that become apparent at very low temperatures. When these quantum effects become comparable to the spacing between bosons, a phase transition takes place, as a macroscopic number of particles will simultaneously occupy the ground state [4]. Bose-Einstein condensation was initially attempted using atomic hydrogen in the 1970's and 1980's [5, 6]. Following the advent of laser cooling [7, 8], Bose-Einstein condensates (BECs) were first observed in dilute alkali gases [9–11]. BECs have started to be explored as a fertile testing ground for the wavelike properties of matter. A BEC can be described by a classical macroscopic matter wave with a coherent phase in the mean field limit [12, 13], not unlike a laser that can be described as a coherent optical field. The properties of coherence were among the first tested, including the interference of two expanding condensates [12] and atom lasers [14–16]. Tunneling BECs between adjacent potential wells [17, 18] was another demonstration of such properties. Most of these early experiments were performed in magnetic traps, which have the limitation of freezing the internal spin degrees of freedom since they can only trap one of the hyperfine levels of the ground state manifold. The use of optical traps, which can trap all the hyperfine states identically, opened the door for the study of spin exchanges between particles. The first so-called spinor BEC was achieved by transferring a BEC from a magnetic to an optical trap [19]. A few years later, our group successfully created a spinor BEC by all-optical means

[20].

The dynamics of such systems have yielded hundreds of theoretical and experimental studies. Some of the early studies involved the formation and evolution of spin domains in large condensates, as well as the miscibility of the spin components [21–23]. Spontaneous symmetry breaking was observed in large quasi-2D BECs [24, 25], resulting in transverse magnetization and helical spin textures. Other spatial features such as skyrmions [26] and spin waves [27] were also observed. An extensive overview of the work performed in spinor BECs can be found in Refs. [28, 29].

1.2.1 Previous Work in Our Group

Our group has been part of this endeavor for many years, and this thesis is built on strong foundations laid down by previous researchers in our lab. A brief summary of the work that led to the current project is presented here.

1.2.1.1 *Coherent Spin Mixing*

Following the creation of the first all optical BEC [20], our group studied the spin population dynamics of spin-1 ^{87}Rb BECs. It was determined by observing the spin populations evolve that such a BEC showed ferromagnetic ordering. This confirmed the prediction that the spinor dynamical rate would be negative, unlike anti-ferromagnetic condensates where it is positive.

The next study showed the validity of the mean field framework to describe our system. The coherent evolution due to spin mixing was measured and followed the dynamics predicted by the mean field at both high and low magnetic fields [27]. The system was also initialized in a metastable state at low field, where the system is not predicted to evolve in the mean field. However, quantum fluctuations drive it out of equilibrium, leading to spin mixing [30].

1.2.1.2 *Sub-Poissonian Fluctuations*

Our group observed sub-Poissonian fluctuations in the magnetization of a spinor ^{87}Rb BEC, or relative number squeezing [31]. The fluctuations in the magnetization showed a reduction of up to 10 dB below the classical shot noise limit. This achievement was made possible by significantly improving the imaging capabilities in our lab. Low-noise imaging techniques were developed, as well as a robust method for calibrating the counting of atoms [32].

1.2.1.3 *Spin-Nematic Squeezing*

Our system has also been shown to produce spin-nematic squeezing [33]. In simple terms, squeezing can take place when considering two quantities that initially share the same uncertainty when describing a system. When the uncertainty in one quantity is reduced at the expense of the other, the uncertainty is said to have been squeezed. Squeezing had previously been demonstrated in quadrature squeezing of the electromagnetic field [34]. In a BEC, pseudo spin-1/2 systems have shown squeezing [35, 36]. The interest in squeezing is motivated by increasing the measurement precision beyond the standard quantum limit (SQL), which has been achieved in atomic magnetometers [37, 38] and atomic clocks [39, 40].

In our system the squeezing takes place between quadratures of a spin moment and a quadrupole moment. When the system is initialized in a metastable state at a hyperbolic fixed point, the uncertainty due to the Heisenberg uncertainty limit is initially equally shared by both quadratures. Evolution causes the circular uncertainty in the phase space to squeeze into an ellipse, thus bringing the uncertainty below the SQL along one axis. The description of our spin-1 system using the underlying $\text{SU}(3)$ symmetry, initially developed for the spin-nematic squeezing work [41], will be used at times in this thesis. In addition to allowing the visualization of the states in a convenient phase space, it also provides the tools to create an initial distribution

in the mean field description that mimics the quantum fluctuations that drive the dynamics from metastable states. This bridge between the two frameworks is a very valuable resource.

1.2.1.4 Dynamics of a Quantum Inverted Pendulum

In the mean field picture, the equations of motion describing the evolution of our system are those of a non-rigid pendulum, a counter-intuitive model where a larger momentum reduces the length of the pendulum [42]. Nevertheless, when initialized in an inverted position, the dynamics of such a model correspond to the evolution of the spin populations in our system when all the atoms are initialized in the $m_F = 0$ state. This is the ground state at high magnetic fields, but becomes a metastable state at fields lower than the critical point. When the system is initialized in such a state, squeezing takes place, followed by spin mixing. The long term evolution of the system was studied, and the highly non-Gaussian distribution of the spin population predicted by theory and simulations were observed [43].

1.2.1.5 Dynamical Stabilization

The previous studies analyzed the evolution out of an unstable equilibrium. The subsequent work from our group demonstrated the dynamic stabilization of the aforementioned inverted pendulum [44]. The concept of applying an external periodic force to stabilize an inverted pendulum is over 100 years old, as shown by “Kapitza’s pendulum,” where stabilization is achieved by vertically vibrating the pivot point.

In our system, the driving was done by periodically applying microwave pulses, which shifts the spinor phase of the BEC. Each pulse rotates the state in the phase space such that it will “unsqueeze” and evolve towards its initial state. This stabilization of a quantum many-body system is a successful demonstration of a control technique that can be applied to other quantum systems.

1.3 Thesis Organization

Following in the footsteps of the graduate students whose work was presented above, a natural step forward was to replace the traditional fast quench through the critical point by a series of slower ramps to bring the system through the critical point at different rates. The measurements of the scaling of the freeze-out time with respect to quench speed is the main focus of this work.

This thesis is organized into eight chapters. This paragraph concludes the introductory chapter. Chapter 2 gives a review of phase transitions and introduces the Kibble-Zurek mechanism and its underlying theory, as well as an overview of the theoretical and experimental work in the field. After a short introduction to Bose-Einstein condensation, the theory of spinor BECs is covered in Chapter 3, where the Hamiltonian of the system is derived in the single mode approximation, starting with a quantum approach and followed by the mean field approach. The details of our system's quantum phase transition is presented, and phase spaces in which the system evolves are illustrated. Chapter 4 describes the experimental apparatus used to gather the data for this thesis. The data-taking methods are presented in Chapter 5, while the results are included in Chapter 6. Chapter 7 compares the results from the previous chapter with dynamical simulations, shows computations without atom loss, and investigates a broader range of parameters inaccessible with our experiment. Finally, we will offer some concluding remarks and present ideas for future work in Chapter 8.

CHAPTER II

KIBBLE-ZUREK MECHANISM THEORY

In this chapter we will survey the theory behind the Kibble-Zurek mechanism (KZM). We will first review the concept of a phase transition, focusing initially on classical transitions, and then on quantum phase transitions (QPTs). We will also discuss the QPT in our system, a ferromagnetic spin-1 BEC. After this introduction, the KZM will be presented, from its inception in the field of cosmology to ultracold atoms and other fields, reviewing both the theoretical and experimental work so far.

2.1 Review of Phase Transitions

Phase transitions range from first-order classical phase transitions to continuous quantum phase transitions. A brief review of the concepts and classifications of phase transitions is presented.

2.1.1 Classical Phase Transitions

The simplest example of phase transitions is the change in the state of matter, such as a substance melting from a solid to a liquid with heat transfer. In this case, one thermodynamic phase of the system changes to another when a thermodynamic variable, temperature in this case, reaches a certain value [45]. Other parameters can be changed to drive a phase transition, but for classical phase transitions, the transitions happen at a finite temperature, and the phase transition occurs at a critical temperature T_c . In a broader sense, phase transitions can be described as phenomena showing analytic discontinuities, or singularities, in the thermodynamics of the considered system [46].

There are several ways to classify phase transitions, with the original one being

the Ehrenfest classification, based on the free energy and its derivatives with respect to thermodynamical parameters [47]. The transitions are ranked by the lowest order of the discontinuous derivative of the free energy at the critical point. First-order transitions show a discontinuity in the first derivative of the free energy, and one of their characteristics is that they involve latent heat. The latent heat during a thermodynamic phase transition is the amount of energy that is exchanged as the system changes phase. This heat exchange takes place at constant temperature. A consequence is that during a first-order phase transition, the two phases coexist at the critical temperature. In fact, the latent heat is related to the change in entropy of the system, which can be expressed as a first derivative of the free energy with respect to temperature, and shows a discontinuity at the critical temperature. A typical example is water freezing. The density changes during the phase transition, and since volume is a first derivative of the free energy ($V = \left(\frac{\partial G}{\partial P}\right)_{T,N}$, where G is the Gibbs free energy [46]), there is a discontinuity in the free energy.

When the first derivatives of the free energy with respect to thermodynamical parameters are continuous, one must look at higher order derivatives. Logically, the phase transitions where the second derivative of the energy is discontinuous at the critical point are called second-order phase transitions. In this case, no latent heat is involved, and the entropy and volume are continuous. However, second derivatives of the free energy, such as the compressibility or heat capacity, can show a discontinuity.

An example is that of the order-disorder phase transition in β -brass, a binary alloy where copper and zinc atoms are in equal number, and whose ordering changes at the critical temperature T_c [48]. This concept of order and disorder is important and will be addressed in detail later. Another example is the ferromagnetic transition in metals. It involves a discontinuity in the metallic susceptibility, which is the second derivative of the free energy with respect to the magnetic field: $\left(\chi_T = \left(\frac{\partial M}{\partial H}\right)_T = -\left(\frac{\partial^2 F}{\partial H^2}\right)_T\right)$, where M , H , and F are the magnetization, magnetic field, and magnetic free energy,

respectively [46]. Transitions involving superfluidity and superconductivity fall in this category, and include Bose-Einstein condensation. Less intuitively perhaps, the early universe also saw phase transitions take place as it was cooling down after the big bang. For example, it is believed that a phase transition could have led to the breaking of the electroweak gauge symmetry, which resulted in the distinction of the weak and electromagnetic forces [49, 50].

The classification goes on for phase transitions where the third, fourth,... order is the lowest order of the derivative of the free energy that is discontinuous at the critical point. Although rarer, an example of a third order phase transition can be found in Chern insulators [51], which are realized in a 2D fermion lattice.

The Ehrenfest classification has been replaced by a simpler classification that solely deals with latent heat. The phase transitions are split into two categories. The first involve latent heat, and are still referred to as first-order transitions, and all of the other transitions are labeled as continuous phase transitions [47]. Continuous phase transitions can be seen as a cooperative phenomenon, with the propagation of a long-range order [46]. In fact, continuous phase transitions can exhibit features such as a divergent susceptibility, diverging correlation lengths, and power law decay of correlations near the critical point.

2.1.2 Quantum Phase Transitions

A defining feature of the classical phase transitions (CPTs) described above are that they take place at a finite, non-zero temperature, and the transition is driven by thermal fluctuations. Based on this definition, one may wonder if a phase transition can occur at absolute zero. In this case, there would be no critical temperature and no thermal fluctuations. A type of phase transition can in fact take place at absolute zero, and is driven by quantum fluctuations. This absolute zero condition is what defines quantum phase transitions (QPT), where a small variation in a parameter of

the Hamiltonian causes a fundamental change in the ground state [3].

A clarification must be made about the “quantum” part of the QPT denomination. Some phase transitions are classified as CPTs, despite the fact that they rely heavily on quantum-mechanical effects, such as superconductivity or superfluidity. Bose-Einstein condensation is a quantum phenomenon by its very nature, but these transitions take place at a finite (non-zero) temperature and feature a critical temperature, and are therefore considered classical phase transitions. Another way to differentiate QPTs from CPTs has to do with the fluctuations close to the critical point. While quantum fluctuations are important in the CPTs mentioned above, it is only at the microscopic scale that they play a role, unlike in QPTs where they dictate the critical behavior even at long scales. Quantum mechanics may be necessary, through an order parameter for example, but critical fluctuations can still be captured using classical statistical mechanics [45].

While first-order QPTs exist, [52–55], the large majority are second order (continuous), and we will only consider them from this point on. An example of a well-studied continuous QPT is the 1D quantum Ising chain [56]. A Mott insulator to superfluid transition driven in an optical lattice is an example of a QPT that can be studied experimentally [57–60]. In some condensed matter systems, the tuning of the carrier doping shift in an insulator to a d -wave superconductor can lead to a QPT [61]. Our system, a ferromagnetic spin-1 BEC, also exhibits a QPT, whose existence is the cornerstone of this thesis. In our case, the transition occurs between a symmetric polar phase and a disordered ferromagnetic phase [62–64]. More details about this QPT will be presented in the following chapter. Additional examples can be found in the references cited above, as well as in review articles [61, 65].

A feature of continuous phase transitions, both classical and quantum, is apparent in the vicinity of the critical point. When the system is close to the critical point, spatial fluctuations (density for example) are long-range. The length scale ξ of these

fluctuations, also known as the correlation length, behaves like

$$\xi \propto |\epsilon|^{-\nu}, \quad (2.1)$$

where ϵ represents a dimensionless “distance” from the critical point, and ν is a critical exponent [3]. Similarly, the time scale for the fluctuations τ , also called the relaxation or equilibration time, diverges as

$$\tau \propto |\epsilon|^{-\nu z}. \quad (2.2)$$

Since ν is associated with the length scale, it is simply called the correlation length critical exponent. z , another critical exponent, characterizes the reaction time of the system, so it is referred to as the dynamical critical exponent.

In the case of a QPT, one can also consider the energy gap Δ separating the ground state and the first available excited state. This energy gap vanishes at the critical point ($\epsilon = 0$) as

$$\Delta \propto |\epsilon|^{\nu z}, \quad (2.3)$$

which is not unexpected in light of Eq. (2.2). We will see that the inverse relationship between the time and energy scales play a central role in the KZM.

A key concept about critical exponents is that they can categorize systems that may be qualitatively different, with dynamics differing by several orders of magnitude, but their behavior near the critical point can be described simply by the same set of critical exponents. This is why these exponents are often called universal critical exponents, as they reveal similar behavior in the vicinity of the critical points, thus grouping systems into universality classes. This common behavior at the critical point is linked to the divergence of the correlation length described above. Indeed, the long range of the correlations and fluctuations reduces the role of the microscopic details of the Hamiltonian around the critical point. The behavior of the system can be reduced to a small number of parameters including the critical exponents.

A system undergoing a phase transition can usually be described by an order parameter. This quantity (which can be complex) is zero on one side of the transition and non-zero on the other. The phase where the order parameter is zero is termed the disordered phase, while the other is an ordered state. A typical example of an order parameter is the magnetization in a ferromagnet, which is non-zero under the critical temperature, but vanishes above it [46]. The concept of order and disorder in different phases is linked to the symmetries characterizing each phase. In fact, it is the symmetries of the order parameter, as well as the space dimensionality of the system, that determine the universality classes mentioned earlier. Phase transitions often involve the breaking of such a symmetry. A common example is the Curie transition in ferromagnets where the symmetry of the disordered state at high temperatures is broken as the spins align when the temperature is lowered under the Curie temperature. Spontaneous symmetry breaking in a continuous phase transition gives rise to massless Nambu-Goldstone modes [45].

2.2 Kibble-Zurek Mechanism

We now turn to the Kibble-Zurek mechanism, which deals with the dynamics of a system as it undergoes a phase transition. The Kibble-Zurek mechanism as originally formulated characterizes the formation of topological defects when a system undergoes a continuous phase transition at a finite rate. This concept was first introduced by Kibble in his study on topology of cosmic domains and strings in the early universe [1, 66]. In his seminal 1976 publication, “Topology of Cosmic Domains and Strings” [1], Kibble argues that right after the big bang, the universe started as a hot disordered state with symmetries that were broken as the universe cooled down and underwent phase transitions at several critical temperatures. He provides a framework suggesting that structures may have arisen during the initial cooling, such as monopoles, strings, and domain walls. The motivation of the study, rather than suggesting the remnants

of these defects should be observable, is more turned towards how the early topology may have influenced the early evolution and distribution of astrophysical objects studied today.

Kibble’s idea was extended by Zurek [2, 67, 68], who suggested applying Kibble’s symmetry breaking ideas to phase transitions in condensed matter systems, such as superfluids and superconductors. His initial publication on the subject, “Cosmological Experiments in Superfluid Helium?” [2], focused on the possibility of testing the concept in the laboratory. The example he chose for the analogy with the cosmic defects was ^4He . The framework seeks to predict the size of domains formed compared to the diameter of an annulus when the pressure is quenched. He also introduces the concept of a “freeze-out” time, which is one of the key concepts studied in this thesis. As will be developed in more detail later in the chapter, the intuitive argument is that the reaction time of a system to react to changes in the Hamiltonian increases close to the critical point of the phase transition. The resulting so-called “slowing down” therefore prevents adiabatic evolution through the critical point. As a result, the adiabatic evolution of the system is paused during the aforementioned freeze-out time. Zurek was particularly interested in the quenches through the critical point with a finite speed, and the scaling of the freeze-time and other quantities with that quench speed. One of the motivations behind Zurek’s approach is that this concept is testable in the laboratory. These key concepts from both authors led to what is now called the Kibble-Zurek mechanism (KZM).

This seminal work was followed by many theoretical studies applying the KZM to a variety of systems. There are hundreds of publications dealing with the subject, exploring through cosmology, condensed matter, cold atoms and more [56, 69–83], and there is no prospect of an end.

In parallel with these theoretical approaches, the KZM has been studied experimentally and verified in a large variety of systems, such as liquid crystals [84, 85], ^4He

[86] and ^3He [87, 88], optical Kerr media [89], annealed glass [90], Josephson junctions [91], and superconducting films [92]. There has also been a significant interest in the KZM within the cold atom community. In recent years, it has been studied and observed in ion chains [93–96], in atomic gases in optical lattices [59], and in Bose-Einstein condensates (BECs), through the formation of spatial domains during condensation [97–99], creation of solitons [100], vortices [101, 102] and supercurrents [103]. Only a handful of experiments have explored the subject using QPTs, namely the Mott insulator to superfluid transition [104]. A group has recently released a preprint [105], claiming that unlike previous experiments [93–96], they successfully managed to cool an ion chain to its ground state and observe the KZM in a QPT.

2.2.1 KZM in a Ferromagnetic Spin-1 BEC

We now turn to the system used in the work for this thesis. A ferromagnetic spin-1 BEC exhibits a QPT between a symmetric polar phase and a broken-symmetry ferromagnetic phase [106] due to the competition between magnetic and collisional spin interaction energies. There have been several theoretical studies predicting KZM power law scaling of the spin excitations for slow quenches through the critical point [62, 63, 107–110].

A distinguishing feature of our KZM investigation is that the excitations are not manifest as spatial defects. Our small spin condensates are in the single mode approximation where all the atoms share the same spatial wave function, so unlike in spatially extended systems where the KZM is manifested in topological defects, the excitations appear in the temporal evolution of the spin populations. In this thesis, we investigate slow quenches through the critical point, as opposed to sudden quenches which have been extensively examined [24, 33, 43, 44].

As mentioned in the previous section, the existence of a QPT universally results in a diverging correlation length. However, this is irrelevant for this experiment since

the system is in the single mode approximation, where condensates are smaller than the spin healing length. This length scale determines the smallest size of a spin domain. However, a relevant universal property of QPTs is a vanishing energy scale at the critical point, which in this case is the energy gap Δ between the ground state and first excited state. In general, the energy gap near the critical point is given by $\Delta \sim |g - g_c|^{z\nu}$, where g is the tuning parameter, g_c is its value at the critical point, and z, ν are critical exponents [3]. A consequence of this vanishing energy gap means that the system cannot cross the critical point adiabatically. As previously mentioned, the KZM is the framework that predicts how the system will behave as it crosses the critical point, as well as the scaling of the relevant parameters with regards to how fast the system is driven through the critical point.

2.2.1.1 Dynamics in the Vicinity of the Critical Point

In order to lead to the predictions of the KZM, we will first give some details about the behavior around the critical point as a system undergoes a second-order QPT. In addition to presenting the concept in the general case, we will also introduce the properties of the system for a derivation of the scaling exponents we will be measuring. As expected from a second-order QPT, our system is characterized by a vanishing energy scale, namely the energy gap between the ground state and the first accessible excited state, which approaches zero at the critical point. This vanishing energy scale results in critical slowing down, as observed in the divergence of the reaction time and correlation length of the system. The reaction time is also known as the relaxation time, and gives the time scale at which the system can adiabatically follow a changing ground state, or return to its ground state after an excitation. An intuitive way to consider this phenomenon is that the reflexes of the system deteriorate around the critical point. Similarly, the correlation length describes the scale on which the system can “heal” in space and collectively return to its ground state after an excitation.

We now briefly introduce some quantities from our system that will be presented in further detail in the following chapter. The parameter from the Hamiltonian that we change for the system to cross the critical point is the quadratic Zeeman energy $q \sim B^2$. The critical point takes place when $q = q_c = 2|c|$, where c is the spinor dynamical rate, which essentially characterizes the energy from the spin interactions [107]. In our experiment, we lower the magnetic field such that the QPT happens from the polar phase ($q > q_c$) to the ferromagnetic phase ($q < q_c$).

The expression for the energy gap in the ferromagnetic phase of our system is given by

$$\Delta = \sqrt{q_c^2 - q^2}. \quad (2.4)$$

Close to the critical point,

$$\Delta \approx \sqrt{2q_c(q_c - q)} \quad (2.5)$$

$$= \Delta_0 |q_c - q|^{1/2}, \quad (2.6)$$

with $\Delta_0 = \sqrt{2q_c}$. The energy gap approaching the critical point of a second-order phase transition is generically given by

$$\Delta \sim |g_c - g|^{z\nu}. \quad (2.7)$$

The product of the aforementioned critical exponents (z and ν) is $1/2$ for our system, corresponding to the mean field values of $z = 1$ and $\nu = 1/2$ [111]. The reaction time and characteristic length near to the critical point also have generic scalings, given by [106]

$$\tau \sim |g_c - g|^{-z\nu} \quad (2.8)$$

$$\xi \sim |g_c - g|^{-\nu}. \quad (2.9)$$

Therefore, the reaction time in our system is

$$\tau \sim |q_c - q|^{-1/2} \sim \Delta^{-1}. \quad (2.10)$$

The correlation length may be relevant in large spin-1 condensates where spin domains can form, but is not possible in our case since the size of the condensate is smaller than the healing length.

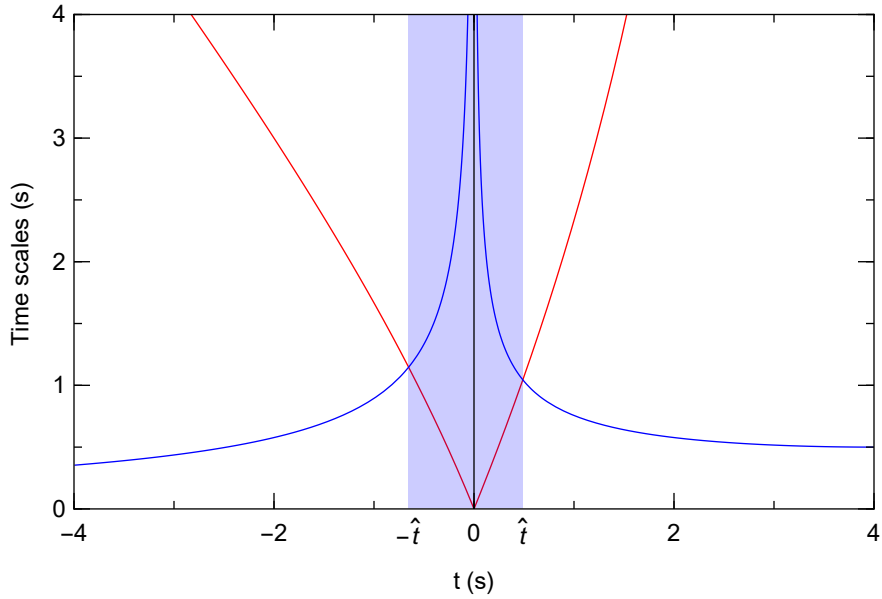


Figure 2.1: **Adiabatic-impulse-adiabatic diagram with \hat{t} .** The two timescales corresponding to the system’s reaction time (blue) and the rate of change of the energy gap (red) are compared. The “freeze-out,” or impulse, region where the reaction time of the system is too long to adiabatically follow the ground state is shown by the blue shaded region.

One of the key points behind the Kibble-Zurek mechanism is that the system cannot adiabatically follow the ground state when the ground state is changed too quickly compared to the reaction time. When the change occurs too fast, the evolution of the system switches from an adiabatic regime to an impulse regime where the system “freezes” with no evolution. This is followed by the system “unfreezing,” returning to an adiabatic regime. This freezing of the dynamics happens when the reaction time diverges, which is the case when the energy gap between the ground state and the first excited state vanishes, as seen in our system. A schematic illustrating the adiabatic-impulse-adiabatic approximation can be seen in Fig. 2.1. The transition from adiabatic to impulse and back to adiabatic regimes happens when the

time scales characterizing the system's reaction time and the rate of change of the energy gap are comparable. This can be described by

$$\tau(\hat{t}) = \frac{1}{\Delta(\hat{t})} = \left. \frac{\Delta}{d\Delta/dt} \right|_{t=\hat{t}} \quad (2.11)$$

where \hat{t} is the freeze-out time. In the experiment, we use a linear ramp of q such that $q(t) = q_0(1 - t/t_r)$, but this derivation is valid for any ramp that linearizes to $\dot{q} \propto 1/\tau_Q$ at the critical point. Solving Eq. (2.11) using the expression from Eq. (2.5) and $z\nu = 1/2$ gives

$$\hat{t} = (z\nu)^{\frac{1}{1+\nu z}} \left(\frac{\tau_Q}{2q_c} \right)^{\frac{\nu z}{1+\nu z}} = \left(\frac{\tau_Q}{8q_c} \right)^{1/3} \sim \tau_Q^{1/3}. \quad (2.12)$$

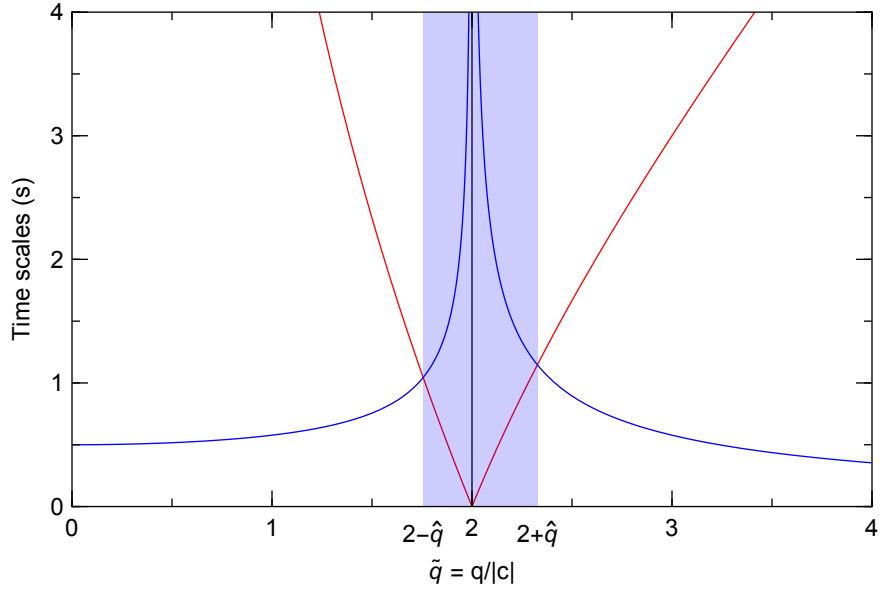


Figure 2.2: **Adiabatic-impulse-adiabatic diagram with \hat{q} .** Similarly as in Fig. 2.1, the timescales corresponding to the reaction of the system (blue) and the change of the energy gap (red) are shown. The impulse region is shaded in blue.

Introducing $\tilde{q}(t) = q(t)/|c(t)|$, where c is the spinor dynamical rate of the system, we can define \hat{q} as the change in \tilde{q} from the crossing of the critical point to the return to the adiabatic regime (see Fig. 2.2). After a similar derivation as the one for \hat{t} , we get

$$\hat{q} = 4^{\frac{-z\nu}{z\nu+1}} \left(\frac{\tilde{\tau}_Q}{z\nu} \right)^{\frac{-1}{1+\nu z}} = \frac{1}{4^{2/3}} \tilde{\tau}_Q^{-2/3} \sim \tilde{\tau}_Q^{-2/3}, \quad (2.13)$$

where $\tilde{\tau}_Q \equiv 1/|\dot{\tilde{q}}(t_c)|$ is a characteristic ramp time. A more detailed explanation of the variables introduced above will be presented in the following chapters.

These are the scaling exponents that we will compare with the results of our measurements. This introduction to the dynamics at the critical point in our system will be covered in more detail in the following chapters, as the theory of spinor condensates is presented and the data is analyzed.

CHAPTER III

SPINOR BOSE-EINSTEIN CONDENSATE THEORY

This chapter will give an overview of the theory behind spinor Bose-Einstein condensates. After discussing the basics of Bose-Einstein condensation, we will introduce the framework to deal with interacting BECs. The single mode approximation will be presented, and from there we will describe the system from a quantum and mean field perspective.

Nearly a century ago, an Indian physicist named Satyendra Nath Bose, worked on rederiving Planck's formula of quantized oscillators for the distribution of energy in blackbody radiation using the statistics of photons. In 1923, he tried to publish an article called "Planck's Law and the Hypothesis of Light Quanta," but was unsuccessful. Bose then contacted Einstein asking him to translate the article into German and submit it to the prestigious journal *Zeitschrift für Physik*. Einstein recognized the importance of Bose's work, and the paper was published in 1924. Einstein also saw that the approach could be applied to a quantum theory of the ideal gas, which eventually led to Bose-Einstein statistics. The particles called bosons (named after Bose) are defined by their integer spin, and do not obey the Pauli exclusion principle. Therefore, several bosons can simultaneously occupy the same energy state. Under the right conditions, many bosons can occupy the ground state of a given system, resulting in a Bose-Einstein condensate. An important condition for Bose-Einstein condensation is an extremely low temperature. Every particle has a thermal de Broglie wavelength given by $\lambda_{\text{dB}} = h/\sqrt{2\pi mk_B T}$, where h is the Planck constant, m is the mass of the particle, k_B is the Boltzmann constant, and T is the temperature. For a ^{87}Rb atom at room temperature (~ 300 K), this wavelength is smaller than the

size of the atom. Since the average distance between atoms is much larger than the wavelength, the atoms essentially behave like point particles. However, when the temperature becomes low enough, the de Broglie wavelength increases to the point where wavelike properties of particles can no longer be ignored. Starting with Bose-Einstein statistics, the critical temperature can be derived [4], and if a gas of identical bosons is cooled below this temperature, they will begin to gather in the ground state and form a BEC. Using the de Broglie wavelength, the critical point can be expressed by $n\lambda_{\text{dB}}^3 \geq 2.612$, where n is the atom density. This expression shows that Bose-Einstein condensation is only possible when the spacing between atoms is comparable to the de Broglie wavelength of the atoms. When all of the atoms condense in the ground state, a BEC essentially behaves like a macroscopic matter wave.

The first experimental attempts to produce a BEC were performed using hydrogen [6, 112–114], and the cooling techniques used heat exchange with liquid helium. However, increasing the density of atoms to reach condensation resulted in a rise of three-body loss, which prevented the formation of a BEC. When laser cooling techniques were developed for alkali atoms, a door opened to avoid the challenges faced with hydrogen. The optical molasses and magneto-optical trapping techniques were successful in bringing the temperature to the microkelvin regime. With the atoms confined in magnetic traps, evaporation cooling was used to further cool the gas to below the critical temperature. Three groups succeeded in creating BECs in their labs: NIST-JILA [9], MIT [10], and Rice [11, 115], all in 1995. These BECs were created in dilute alkali gases in ultra high vacuum, where low atom densities (10^{13} cm^{-3}) limited three-body recombination. To compensate for this low density requirement, temperatures in the nanokelvin regime were necessary to increase the de Broglie wavelength. These temperatures were successfully reached with laser cooling and evaporative cooling. It was only 70 years after Bose’s initial idea that a BEC was experimentally observed. The 2001 Nobel prize was awarded to Cornell, Ketterle,

and Wieman for their pioneering work leading to the first realization of BECs.

The first BECs were realized in a magnetic trap, which has the disadvantage of only trapping atoms in a certain spin state, thus preventing potential spin dynamics such as spin exchange between particles. In 1998, a magnetically trapped BEC was successfully transferred into an optical trap [19]. Optical traps have the benefit of treating all spin levels identically, and the spins are no longer frozen. These condensates with spin internal degrees of freedom are called spinor BECs.

3.1 *Gross-Pitaevskii Equation*

We will now derive the properties of the dynamics in our spin-1 condensate. In our derivation, we consider the total wave function to be the product of single particle states, which is known as the Hartree-Fock approximation. The interaction between particles is modeled as a pseudo-potential involving the s -wave scattering lengths [116–118]. Due to the low temperature of the condensate, the higher order scattering events are prohibited. The Hamiltonian for N identical bosons is called the Gross-Pitaevskii equation (or nonlinear Schrödinger equation), and is expressed by

$$H = \sum_{i=1}^N \left(-\frac{\nabla^2}{2m} + V_T(\mathbf{r}_i) \right) + U, \quad (3.1)$$

where the two terms in the sum are the kinetic energy and trapping potential energy, and U is the contact interaction pseudo-potential given by

$$U = \sum_{i<j} g\delta(\mathbf{r}_i - \mathbf{r}_j). \quad (3.2)$$

The coupling strength is given by $g = 4\pi\hbar^2 a/m$, where a is the s -wave scattering length and m is the mass of the atom.

Our experiment uses a spin-1 BEC, meaning there are actually two scattering channels, each with their own scattering length. One corresponds to the channel for the total spin $F = 0$, while the other one is for the total spin $F = 2$. We can therefore

rewrite the interaction term for two atoms as

$$U(\mathbf{r}_i, \mathbf{r}_j) = \delta(\mathbf{r}_i - \mathbf{r}_j) \sum_{F=0,2} g_F \sum_{m_F=-F}^F |F, m_F\rangle \langle F, m_F|. \quad (3.3)$$

Each channel also has its own coupling strength $g_F = 4\pi\hbar^2 a_F/m$.

A pair of colliding atoms can be expressed in the basis $|F_1, m_{F_1}; F_2, m_{F_2}\rangle$. In its hyperfine ground state, a spin-1 BEC has $F = 1$ and $m_F = -1, 0, 1$, so we can expand the two-body interaction term (3.3) into

$$\begin{aligned} & \sum_{F=0,2} g_F \sum_{m_F=-F}^F |F, m_F\rangle \langle F, m_F| \\ &= g_0 \left(\frac{4}{3} \hat{\Psi}_1^\dagger \hat{\Psi}_{-1}^\dagger \hat{\Psi}_1 \hat{\Psi}_{-1} + \frac{1}{3} \hat{\Psi}_0^\dagger \hat{\Psi}_0^\dagger \hat{\Psi}_0 \hat{\Psi}_0 - \frac{2}{3} \hat{\Psi}_1^\dagger \hat{\Psi}_{-1}^\dagger \hat{\Psi}_0 \hat{\Psi}_0 - \frac{2}{3} \hat{\Psi}_0^\dagger \hat{\Psi}_0^\dagger \hat{\Psi}_1 \hat{\Psi}_{-1} \right) \\ &+ g_2 \left(\hat{\Psi}_1^\dagger \hat{\Psi}_1^\dagger \hat{\Psi}_1 \hat{\Psi}_1 + 2\hat{\Psi}_1^\dagger \hat{\Psi}_0^\dagger \hat{\Psi}_1 \hat{\Psi}_0 + \frac{2}{3} \hat{\Psi}_1^\dagger \hat{\Psi}_{-1}^\dagger \hat{\Psi}_1 \hat{\Psi}_{-1} + \frac{2}{3} \hat{\Psi}_0^\dagger \hat{\Psi}_0^\dagger \hat{\Psi}_0 \hat{\Psi}_0 \right. \\ &\left. + \frac{2}{3} \hat{\Psi}_1^\dagger \hat{\Psi}_{-1}^\dagger \hat{\Psi}_1 \hat{\Psi}_{-1} + \frac{2}{3} \hat{\Psi}_0^\dagger \hat{\Psi}_0^\dagger \hat{\Psi}_1 \hat{\Psi}_{-1} + 2\hat{\Psi}_0^\dagger \hat{\Psi}_{-1}^\dagger \hat{\Psi}_0 \hat{\Psi}_{-1} + \hat{\Psi}_{-1}^\dagger \hat{\Psi}_{-1}^\dagger \hat{\Psi}_{-1} \hat{\Psi}_{-1} \right), \quad (3.4) \end{aligned}$$

where $\Psi_\alpha^\dagger \rightarrow |F = 1, m_F = \alpha\rangle$ has been used for compactness.

Instead of keeping the terms in the pseudo-potential grouped by their scattering strengths, it is more convenient for the rest of the derivation to arrange the terms into groups that are symmetric and asymmetric under exchange of indices. The symmetric terms describe spin-independent collisions, while the asymmetric terms are for collisions whose output is dependent on the spin of the atoms. The kinetic and trapping potential terms of the Hamiltonian are assumed to be symmetric and are included with the symmetric part. Along with a spatial integration over the condensate, the original Hamiltonian (3.1) is split into two parts:

$$\hat{H}_S = \sum_i \int d^3r \hat{\Psi}_i^\dagger \left(-\frac{\hbar^2 \nabla^2}{2m} + V_T \right) \hat{\Psi}_i + \frac{c_0}{2} \sum_{ij} \int d^3r \hat{\Psi}_i^\dagger \hat{\Psi}_j^\dagger \hat{\Psi}_i \hat{\Psi}_j \quad (3.5)$$

$$\begin{aligned} \hat{H}_A = & \frac{c_2}{2} \int d^3r \left(\hat{\Psi}_1^\dagger \hat{\Psi}_1^\dagger \hat{\Psi}_1 \hat{\Psi}_1 + \hat{\Psi}_{-1}^\dagger \hat{\Psi}_{-1}^\dagger \hat{\Psi}_{-1} \hat{\Psi}_{-1} - 2\hat{\Psi}_1^\dagger \hat{\Psi}_{-1}^\dagger \hat{\Psi}_1 \hat{\Psi}_{-1} \right. \\ & \left. + 2\hat{\Psi}_1^\dagger \hat{\Psi}_0^\dagger \hat{\Psi}_1 \hat{\Psi}_0 + 2\hat{\Psi}_{-1}^\dagger \hat{\Psi}_0^\dagger \hat{\Psi}_{-1} \hat{\Psi}_0 + 2\hat{\Psi}_0^\dagger \hat{\Psi}_0^\dagger \hat{\Psi}_1 \hat{\Psi}_{-1} + 2\hat{\Psi}_1^\dagger \hat{\Psi}_{-1}^\dagger \hat{\Psi}_0 \hat{\Psi}_0 \right), \quad (3.6) \end{aligned}$$

where $i = 0, \pm 1$. The terms in each part of the Hamiltonian share the same coupling strengths: $c_0 = (2g_2 + g_0)/3$ for the symmetric spin-independent part \hat{H}_S , and $c_2 = (g_2 - g_0)/3$ for the asymmetric spin-dependent part \hat{H}_A . \hat{H}_S is responsible for spatial and motional dynamics, while \hat{H}_A drives spin exchanges through collisions. The total spin is conserved during collisions, but the hyperfine state will be allowed to change. Despite only the spin-dependent part being responsible for the spin-mixing dynamics, the sum of \hat{H}_S and \hat{H}_A is referred to as the spin-mixing Hamiltonian.

3.2 Single Mode Approximation

Spin-1 BECs are a versatile testing ground for the study of quantum behavior, and spatial dynamics are a large part of research for many groups. Vortices [101, 102], skyrmions [26], spin waves [27] and more spatial features have been observed and studied in condensates. As fascinating as these phenomena are, one can also investigate cases where these dynamics are suppressed in order to focus on spin dynamics alone, as in our case. To reach this condition, we must compare the length scales involved in the symmetric and asymmetric part of the spin-mixing Hamiltonian. For the spin-dependent part, the length scale is the spin-healing length $\xi = 2\pi\hbar/\sqrt{2m|c_2|n}$. For a density $n \approx 3.8 \times 10^{14} \text{ cm}^{-3}$, and given that $|c_2| \approx h \times 0.036 \text{ Hz } \mu\text{m}^3$, the spin-healing length in our system is $\xi \approx 12.9 \mu\text{m}$. This length sets the distance over which the spin modes can change. Similarly, the same expression using c_0 instead of c_2 gives the length scale over which the spatial density can vary. Given the fact that the scattering lengths a_0 and a_2 differ by less than 2% in the case of ^{87}Rb , the coupling strengths $c_0 \propto (2a_2 + a_0)$ and $c_2 \propto (a_2 - a_0)$ are such that $c_0 \gg |c_2|$, which in turn yields a much larger length scale for the spin dependent part. In ferromagnetic spin-1 condensates such as ours, $a_0 > a_2$, so $c_2 < 0$. For antiferromagnetic condensates such as ^{23}Na , c_2 has the opposite sign. Essentially, this offset in length scales means that if a BEC is smaller than the spin-healing length, all the spin modes will be forced

to share the same spatial wave function. This condition is known as the single mode approximation (SMA), and the wave function of each spin component can be written as $\hat{\Psi}_i \approx \hat{a}_i \phi(\mathbf{r})$, where the annihilation operator \hat{a}_i follows the bosonic commutation relations such that $[\hat{a}_\kappa, \hat{a}_\iota^\dagger] = \delta_{\kappa\iota}$ and $[\hat{a}_\kappa, \hat{a}_\iota] = 0$. As long as the trap treats all spin projections equally, and that there is no magnetic field gradient applying a force on the spins, as is the case in our experiment, the SMA should be valid. Since $c_0 \gg |c_2|$ as shown earlier, the symmetric part of the Hamiltonian is the dominant term, and it determines the common spatial wave function $\phi(\mathbf{r})$. It is found using the mean field scalar Gross-Pitaevskii equation:

$$\hat{H}_S \phi = \left(-\frac{\nabla^2}{2m} + V_T + c_0 N |\phi|^2 \right) \phi = \mu \phi, \quad \int d^3r |\phi(\mathbf{r})|^2 = 1, \quad (3.7)$$

where μ is the chemical potential. By neglecting the kinetic energy in Eq. (3.7) and integrating over the condensate, the two parts of the Hamiltonian can be rewritten as

$$\hat{H}_S = \mu \hat{N} - \tilde{c}_0 \hat{N} (\hat{N} - 1) \quad (3.8)$$

$$\begin{aligned} \hat{H}_A = & \tilde{c}_2 \left(\hat{a}_1^\dagger \hat{a}_1^\dagger \hat{a}_1 \hat{a}_1 + \hat{a}_{-1}^\dagger \hat{a}_{-1}^\dagger \hat{a}_{-1} \hat{a}_{-1} - 2\hat{a}_1^\dagger \hat{a}_{-1}^\dagger \hat{a}_1 \hat{a}_{-1} \right. \\ & + 2\hat{a}_1^\dagger \hat{a}_0^\dagger \hat{a}_1 \hat{a}_0 + 2\hat{a}_{-1}^\dagger \hat{a}_0^\dagger \hat{a}_{-1} \hat{a}_0 \\ & \left. + 2\hat{a}_0^\dagger \hat{a}_0^\dagger \hat{a}_1 \hat{a}_{-1} + 2\hat{a}_1^\dagger \hat{a}_{-1}^\dagger \hat{a}_0 \hat{a}_0 \right), \end{aligned} \quad (3.9)$$

where $\hat{N} = \hat{a}_1^\dagger \hat{a}_1 + \hat{a}_0^\dagger \hat{a}_0 + \hat{a}_{-1}^\dagger \hat{a}_{-1}$ represents the total number of atoms, and $\tilde{c}_i = \frac{c_i}{2} \int |\phi(\mathbf{r})|^4 d^3r$ are the spatially integrated interaction strengths. Note that the symmetric part of the SMA Hamiltonian (3.8) is constant, as long as the number of atoms and the trapping potential do not change. This means that all of the dynamics occur because of the spin-dependent part.

Our system can be described using two approaches, quantum and mean field, and we will briefly explain both. A convenient way to analyze the system in either

description is to identify the operators used to characterize the states of our system in the context of the Lie algebra of a SU(3) group [33, 41]. The operators used in this framework have been derived many times before [41, 42, 119], so we will only make some simple remarks and list the operators. There are eight operators, three spin (or dipole) and five quadrupole. The spin operators are derived using angular momentum algebra, and the quadrupole operators can be expressed as combinations of spin operators [33, 41]. In the quantum description, the operators are second quantized operators, while in the mean field picture, they are represented by 3×3 matrices. The operators in both the matrix and the second quantized operator forms can be found in Table 3.1.

3.3 Quantum Approach

The asymmetric part \hat{H}_A of the spin-mixing Hamiltonian (3.9) can now be rewritten using the second quantized operators from Table 3.1:

$$\hat{H}_A = \tilde{c}_2 \left(\hat{S}^2 - 2\hat{N} \right), \quad (3.10)$$

where $\hat{S}^2 = \hat{S}_x^2 + \hat{S}_y^2 + \hat{S}_z^2$. So far, we have ignored the effect of the magnetic field. As will be discussed in detail in the next chapter, an external magnetic field will shift the energy of the $m_F = -1$ and $m_F = +1$ Zeeman sub-levels with respect to the $m_F = 0$ atoms that are not affected by the field. These energy shifts come from the linear and quadratic Zeeman effects at low fields. The shifts due to the linear and quadratic part are $p = \mu_B B_z g_F$ and $q = \mu_B^2 B_z^2 / (\hbar^2 \Delta E_{\text{hf}}) = q_z B_z^2$, respectively, where μ_B is the Bohr magneton, g_F is the Landé g -factor, and ΔE_{hf} is the ground state hyperfine energy splitting. For our system, the magnitude of the prefactor for the quadratic Zeeman energy is $q_z \approx 71.6 \text{ Hz/G}^2$. For an atom in the m_F state, its energy will be

$$E_F = E_0 + p m_F + q (m_F)^2, \quad (3.11)$$

Table 3.1: Spin-1 dipole and quadrupole operators [41].

$$\begin{aligned}
S_x &= \frac{1}{\sqrt{2}} \begin{pmatrix} 0 & 1 & 0 \\ 1 & 0 & 1 \\ 0 & 1 & 0 \end{pmatrix} & \hat{S}_x &= \frac{1}{\sqrt{2}} \left(\hat{a}_1^\dagger \hat{a}_0 + \hat{a}_0^\dagger \hat{a}_{-1} + \hat{a}_0^\dagger \hat{a}_1 + \hat{a}_{-1}^\dagger \hat{a}_0 \right) \\
S_y &= \frac{i}{\sqrt{2}} \begin{pmatrix} 0 & -1 & 0 \\ 1 & 0 & -1 \\ 0 & 1 & 0 \end{pmatrix} & \hat{S}_y &= \frac{i}{\sqrt{2}} \left(-\hat{a}_1^\dagger \hat{a}_0 - \hat{a}_0^\dagger \hat{a}_{-1} + \hat{a}_0^\dagger \hat{a}_1 + \hat{a}_{-1}^\dagger \hat{a}_0 \right) \\
S_z &= \begin{pmatrix} 1 & 0 & 0 \\ 0 & 0 & 0 \\ 0 & 0 & -1 \end{pmatrix} & \hat{S}_z &= \left(\hat{a}_1^\dagger \hat{a}_1 - \hat{a}_{-1}^\dagger \hat{a}_{-1} \right) \\
Q_{yz} &= \frac{i}{\sqrt{2}} \begin{pmatrix} 0 & -1 & 0 \\ 1 & 0 & 1 \\ 0 & -1 & 0 \end{pmatrix} & \hat{Q}_{yz} &= \frac{i}{\sqrt{2}} \left(-\hat{a}_1^\dagger \hat{a}_0 + \hat{a}_0^\dagger \hat{a}_{-1} + \hat{a}_0^\dagger \hat{a}_1 - \hat{a}_{-1}^\dagger \hat{a}_0 \right) \\
Q_{xz} &= \frac{1}{\sqrt{2}} \begin{pmatrix} 0 & 1 & 0 \\ 1 & 0 & -1 \\ 0 & -1 & 0 \end{pmatrix} & \hat{Q}_{xz} &= \frac{1}{\sqrt{2}} \left(\hat{a}_1^\dagger \hat{a}_0 - \hat{a}_0^\dagger \hat{a}_{-1} + \hat{a}_0^\dagger \hat{a}_1 - \hat{a}_{-1}^\dagger \hat{a}_0 \right) \\
Q_{xy} &= i \begin{pmatrix} 0 & 0 & -1 \\ 0 & 0 & 0 \\ 1 & 0 & 0 \end{pmatrix} & \hat{Q}_{xy} &= i \left(-\hat{a}_1^\dagger \hat{a}_{-1} + \hat{a}_{-1}^\dagger \hat{a}_1 \right) \\
Q_{xx} &= \begin{pmatrix} -\frac{1}{3} & 0 & 1 \\ 0 & \frac{2}{3} & 0 \\ 1 & 0 & -\frac{1}{3} \end{pmatrix} & \hat{Q}_{xx} &= -\frac{1}{3} \hat{a}_{+1}^\dagger \hat{a}_{+1} + \frac{2}{3} \hat{a}_0^\dagger \hat{a}_0 - \frac{1}{3} \hat{a}_{-1}^\dagger \hat{a}_{-1} + \hat{a}_{+1}^\dagger \hat{a}_{-1} \\
& & & & + \hat{a}_{-1}^\dagger \hat{a}_{+1} \\
Q_{yy} &= \begin{pmatrix} -\frac{1}{3} & 0 & -1 \\ 0 & \frac{2}{3} & 0 \\ -1 & 0 & -\frac{1}{3} \end{pmatrix} & \hat{Q}_{yy} &= -\frac{1}{3} \hat{a}_{+1}^\dagger \hat{a}_{+1} + \frac{2}{3} \hat{a}_0^\dagger \hat{a}_0 - \frac{1}{3} \hat{a}_{-1}^\dagger \hat{a}_{-1} - \hat{a}_{+1}^\dagger \hat{a}_{-1} \\
& & & & - \hat{a}_{-1}^\dagger \hat{a}_{+1} \\
Q_{zz} &= \begin{pmatrix} \frac{2}{3} & 0 & 0 \\ 0 & -\frac{4}{3} & 0 \\ 0 & 0 & \frac{2}{3} \end{pmatrix} & \hat{Q}_{zz} &= \frac{2}{3} \hat{a}_{+1}^\dagger \hat{a}_{+1} - \frac{4}{3} \hat{a}_0^\dagger \hat{a}_0 + \frac{2}{3} \hat{a}_{-1}^\dagger \hat{a}_{-1}
\end{aligned}$$

where E_0 is the degenerate ground state energy when no magnetic field is present.

Combining the energy for every atom of the condensate:

$$E = p(N_1 - N_{-1}) + q(N_1 + N_{-1}) + NE_0. \quad (3.12)$$

Therefore, when adding this energy to Eq. (3.10), we get the following Hamiltonian:

$$\hat{H}_A = \tilde{c}_2 \left(\hat{S}^2 - 2\hat{N} \right) + p \left(\hat{N}_1 - \hat{N}_{-1} \right) + q \left(\hat{N}_1 + \hat{N}_{-1} \right) + \hat{N}E_0. \quad (3.13)$$

The last term in Eq. (3.13) is constant, so it will not contribute to the dynamics. Taking advantage that the quadrupole moment \hat{Q}_{zz} can be written as [41]

$$\hat{Q}_{zz} = 2 \left(\hat{N}_1 + \hat{N}_{-1} \right) - \frac{4}{3} \hat{N}, \quad (3.14)$$

and noticing that $\hat{S}_z = \hat{N}_1 - \hat{N}_{-1}$, we can rewrite the Hamiltonian in a more compact form:

$$\hat{H}_A = \tilde{c}_2 \left(\hat{S}^2 - 2\hat{N} \right) + p\hat{S}_z + \frac{q}{2}\hat{Q}_{zz}, \quad (3.15)$$

where some constant terms have been omitted for the same reason as discussed earlier.

In order to find the eigenenergies of this Hamiltonian, we need to find a more convenient basis. Indeed, even though \hat{S}_z commutes with the whole Hamiltonian, \hat{S}^2 and \hat{Q}_{zz} do not commute. Note that the eigenstates of the asymmetric part \hat{H}_A of the Hamiltonian (3.9) can be expressed in the Fock basis $|N_{-1}, N_0, N_1\rangle$. Since Fock states are also eigenstates of \hat{Q}_{zz} , this is an appropriate basis to use. An even more convenient basis in the context of our experiment is the $|N, M, k\rangle$ basis, where N is the total number of atoms in the BEC, $M = N_1 - N_{-1}$ is the magnetization, and k is the number of pairs of atoms in the $m_f = \pm 1$ state. This basis is equivalent to the Fock basis, and it is ideal since the total number of atoms and the magnetization are conserved by the Hamiltonian. This essentially simplifies the problem to the single parameter k that can take $N/2 + 1$ values.

With this choice of basis in mind, the Hamiltonian (3.15) is expanded into number operators:

$$\begin{aligned} \hat{H}_A = & \tilde{c}_2 \left(\left(\hat{N}_1 - \hat{N}_{-1} \right)^2 + \left(2\hat{N}_0 - 1 \right) \left(\hat{N}_1 + \hat{N}_{-1} \right) + 2\hat{a}_1^\dagger \hat{a}_{-1}^\dagger \hat{a}_0 \hat{a}_0 + 2\hat{a}_0^\dagger \hat{a}_0^\dagger \hat{a}_1 \hat{a}_{-1} \right) \\ & + p \left(\hat{N}_1 - \hat{N}_{-1} \right) + q \left(\hat{N}_1 + \hat{N}_{-1} \right) + \hat{N} E_0. \end{aligned} \quad (3.16)$$

Since our experiment is consistently initialized with all the atoms in the $m_F = 0$ state, we can set $M = N_1 - N_{-1} = 0$, which produces a so-called ‘‘hopping’’ tridiagonal

Hamiltonian whose matrix elements are given by

$$\begin{aligned}
H_{k,k'} &= (2\tilde{c}_2k(2(N-2k)-1) + 2qk) \delta_{k,k'} \\
&+ 2\tilde{c}_2 \left((k'+1)\sqrt{(N-2k')(N-2k'-1)}\delta_{k,k'+1} \right. \\
&\left. + k'\sqrt{(N-2k'+1)(N-2k'+2)}\delta_{k,k'-1} \right)
\end{aligned} \tag{3.17}$$

This Hamiltonian can easily be diagonalized to find the eigenenergies, and it is also used in simulations by numerically integrating the time dependent Schrödinger equation.

In the context of this thesis, the form of the Hamiltonian can be further simplified. The total number of atoms \hat{N} and the longitudinal magnetization \hat{S}_z are conserved, so these terms do not contribute to the dynamics and can be discarded, which simplifies Eq. (3.15) to

$$\hat{H}_A = \tilde{c}_2\hat{S}^2 + \frac{q}{2}\hat{Q}_{zz}. \tag{3.18}$$

For a reason that will be made clear later in the chapter, the operator \hat{Q}_z is introduced. Despite the notation, \hat{Q}_z is not a quadrupole moment, but it is related to the \hat{Q}_{zz} moment by

$$\hat{Q}_z = -\frac{\hat{N}}{3} - \hat{Q}_{zz}. \tag{3.19}$$

As noted earlier, the factor proportional to \hat{N} will not contribute to the dynamics, and the simplified Hamiltonian reads:

$$\hat{H} = \tilde{c}_2\hat{S}^2 - \frac{q}{2}\hat{Q}_z. \tag{3.20}$$

3.4 Mean Field Approach

Another way to describe the system is to use a mean field approach. The steps are relatively simple, and we begin by assuming a large number of atoms and ignore the quantum fluctuations. The description of the system can then be simplified by replacing the field operators by complex numbers. All of the atoms share the same

spinor wave function $\sqrt{N}|\zeta_i|e^{i\theta_i}$, where $|\zeta_i|^2 = \rho_i = N_i/N$ are the fractional spin populations.

Combining the full spin-mixing Hamiltonian (3.5) and (3.6) with the single mode spatial Hamiltonian (3.7), along with the mean field notation, yields three coupled Gross-Pitaevskii equations:

$$i\hbar\dot{\zeta}_1 = c [(\rho_1 + \rho_0 - \rho_{-1})\zeta_1 + \zeta_0^2\zeta_{-1}^*] \quad (3.21a)$$

$$i\hbar\dot{\zeta}_0 = c [(\rho_1 + \rho_{-1})\zeta_0 + 2\zeta_1\zeta_{-1}\zeta_0^*] \quad (3.21b)$$

$$i\hbar\dot{\zeta}_{-1} = c [(\rho_{-1} + \rho_0 - \rho_1)\zeta_{-1} + \zeta_0^2\zeta_1^*] \quad (3.21c)$$

The common factor of \sqrt{N} has been removed, and $c = 2\tilde{c}_2N$. The BEC is now well described by a vector order parameter

$$\psi = (\zeta_1, \zeta_0, \zeta_{-1})^T, \quad (3.22)$$

which has six parameters. However, they are not all independent, since the normalization condition $\sum_{i=1}^3 \rho_i = \sum_{i=1}^3 |\zeta_i|^2 = 1$ and the conservation of magnetization $m = \rho_1 - \rho_{-1}$ reduce the number of independent parameters to four. The order parameter can therefore be written as

$$\psi = \left(\sqrt{\frac{1 - \rho_0 + m}{2}} e^{i\chi_+}, \sqrt{\rho_0}, \sqrt{\frac{1 - \rho_0 - m}{2}} e^{i\chi_-} \right)^T, \quad (3.23)$$

where $\chi_{\pm} = \theta_{\pm 1} - \theta_0$. By defining the spinor phase $\theta_s = \theta_{+1} + \theta_{-1} - 2\theta_0$ and magnetization phase $\theta_m = \theta_{+1} - \theta_{-1}$, the dynamical equations (3.21) can be reduced to a pair of equations:

$$\dot{\rho}_0 = \frac{2c}{\hbar} \rho_0 \sqrt{(1 - \rho_0)^2 - m^2} \sin \theta_s \quad (3.24)$$

$$\dot{\theta}_s = \frac{2c}{\hbar} \left[(1 - 2\rho_0) + \frac{(1 - \rho_0)(1 - 2\rho_0) - m^2}{\sqrt{(1 - \rho_0)^2 - m^2}} \cos \theta_s \right] - \frac{2q}{\hbar} \quad (3.25)$$

The pair of parameters (ρ_0, θ_s) span the spinor phase space, where the mean field dynamics of the system can be represented. The energy contours can be plotted by

finding the mean field spinor energy per particle [120]:

$$\mathcal{E} = \frac{c}{2}m^2 + c\rho_0 \left[(1 - \rho_0) + \sqrt{(1 - \rho_0)^2 - m^2} \cos \theta_s \right] + pm + q(1 - \rho_0). \quad (3.26)$$

While the energy functional above is very convenient when describing our system exclusively with the two variables ρ_0 and θ_s , we will introduce another phase space that works well with our study later in the chapter.

3.5 Quantum Phase Transition

One of the key concepts in this thesis is that of the continuous QPT of our system. This QPT takes place when the magnetic field crosses a critical value, corresponding to $q_c = 2|c|$. At high magnetic field ($q > q_c$), the system is in the polar phase, where the dynamics are dominated by the quadratic Zeeman energy q . Using the normalized vector order parameter $\psi = (\zeta_1, \zeta_0, \zeta_{-1})^\top$, the ground state is $\psi = (0, 1, 0)^\top$. At low magnetic fields ($q < q_c$), the spin interactions are strong enough to give rise to a non-zero transverse magnetization that breaks the SO(2) symmetry. In addition to the U(1) symmetry, which assigns an arbitrary global phase to the condensate, each spin component also acquires a relative phase χ_i [106] and the ground state is given by:

$$\zeta_{\pm 1} = \frac{1}{2} \sqrt{1 - q/q_c} e^{i\chi_{\pm}} \quad \text{and} \quad \zeta_0 = \sqrt{\frac{1}{2} (1 + q/q_c)} e^{i(\chi_+ + \chi_-)/2}. \quad (3.27)$$

As presented in the previous chapter, our system displays an energy gap between the ground state and first excited state, which vanishes at the critical point. Using the Bogoliubov theory, it can be shown that the ferromagnetic phase ground state has three excitation modes [106]. Two are gapless modes (in the long wavelength limit), which arise from the SO(2) symmetry breaking as predicted by the Goldstone theorem [121], but the third mode has a non-zero eigenvalue, namely the energy gap Δ between the ground state and the first excited state. In our case, the energy gap in the ferromagnetic phase ($q < q_c$) is given by $\Delta = \sqrt{q_c^2 - q^2}$. In the polar phase,

the energy gap is given by $\Delta = \sqrt{q(q - q_c)}$. A plot of the energy gap Δ can be seen in Fig. 3.1.

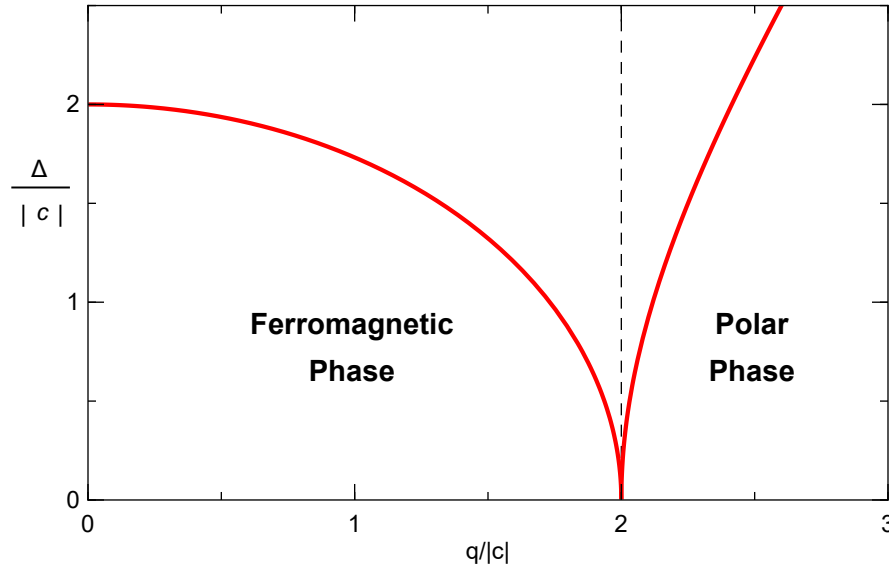


Figure 3.1: **Energy gap between the ground state and first excited state.** The energy gap Δ is plotted against the quadratic Zeeman energy q , both in units of the spinor dynamical rate c . The vertical dashed line indicates the boundary between the ferromagnetic and polar phase spaces.

3.6 Phase Spaces

In order to describe and visualize the evolution of the system, we will be using several phase spaces, which are the spin-nematic, polar, and spinor phase spaces.

3.6.1 Spin-Nematic Phase Space

The first of three phase spaces relies on our system's property that any state can be represented on the surface of a unit sphere with axes S_{\perp} , Q_{\perp} , and Q_z . The new variables S_{\perp} and Q_{\perp} are defined from dipole and quadrupole moments: $S_{\perp}^2 = S_x^2 + S_y^2$, and $Q_{\perp}^2 = Q_{xz}^2 + Q_{yz}^2$. S_{\perp} represents the transverse spin, and Q_{\perp} the off-diagonal quadrupole moment. While this phase space is not a proper representation of a SU(2) subspace from the SU(3) phase space describing spin-1 systems [33, 41], it does serve the same purpose of visualizing the states of the system on its surface. Additionally, despite the variables S_{\perp} , Q_{\perp} , and Q_z not being actual dipole and quadrupole moments, they are constructed from them. Therefore, by analogy with the SU(2) subspaces used to visualize the system in [33, 41], this phase space will be referred to as the spin-nematic phase space.

The third variable was introduced earlier as the operator \hat{Q}_z , and is given by $Q_z = \langle \hat{Q}_z \rangle / N$. The interest in the variable Q_z is that it can be expressed simply by $Q_z = 2\rho_0 - 1$, where ρ_0 is the fractional population of atoms in $m_F = 0$. Representations of the spin-nematic phase space for different values of $\tilde{q} = q/|c|$ are shown in Fig. 3.2. There are three types of energy contours. In the ferromagnetic phase ($\tilde{q} < 2$), the separatrix (green line) represents the boundary between the closed orbits (red lines), and the phase winding orbits (blue lines). The degenerate ground states on each side of the sphere are shown by a red dot. In the polar phase ($\tilde{q} > 2$), all the energy contours are phase winding, there is no separatrix, and the ground state sits on the top pole of the sphere. The energies of the energy contours were arbitrarily

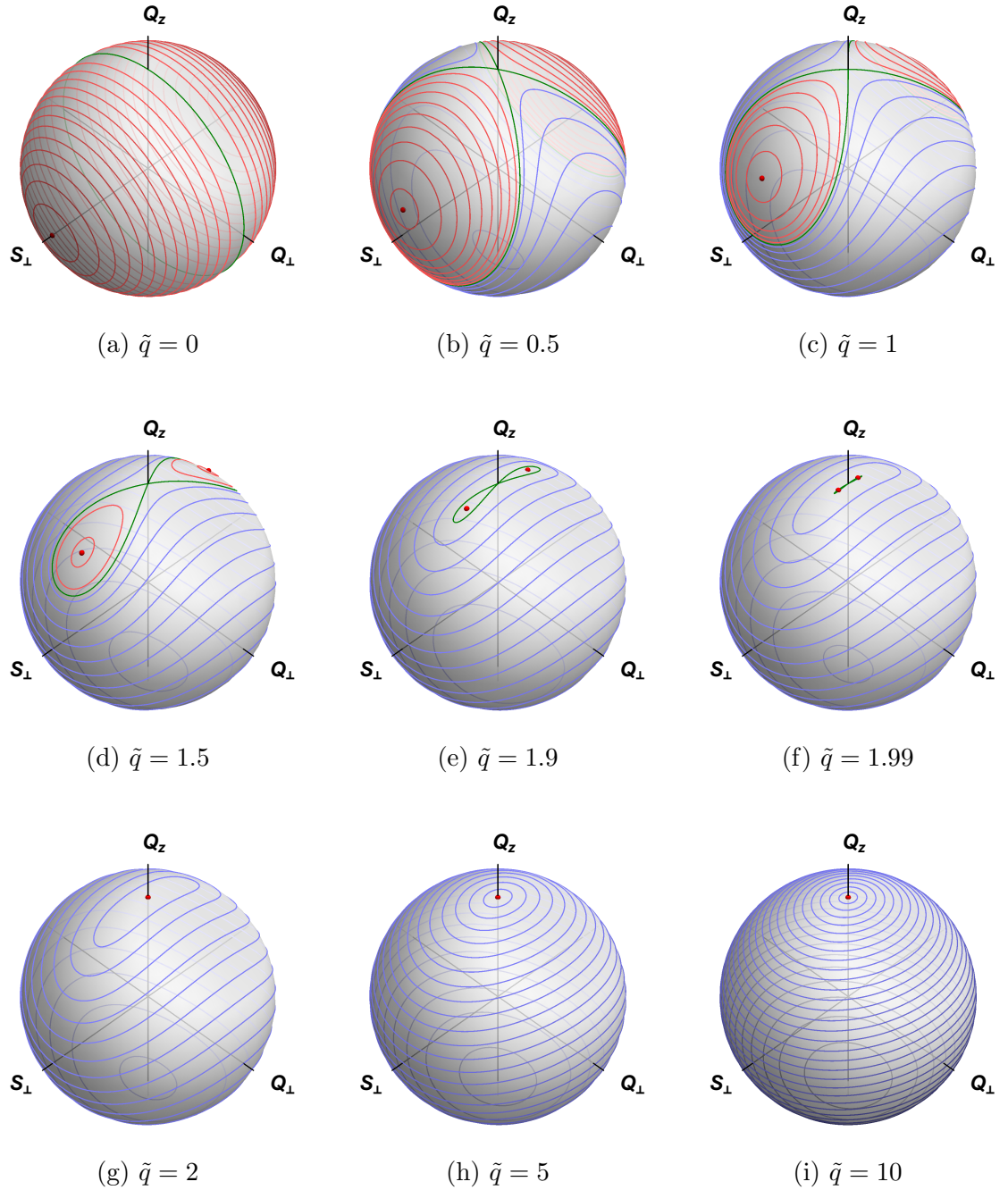


Figure 3.2: **Spin-nematic phase space.** Spin-nematic phase space for several values of \tilde{q} . The closed orbits (red) are separated from the phase-winding orbits (blue) by the separatrix (green), and the red dots represent the ground states. The energy contours are the same for every sphere.

chosen for illustration purposes, but they are the same for every value of \tilde{q} . In addition, the energy contours are the same for every representation of any phase space in the rest of the chapter.

3.6.2 Polar Phase Space

The second phase space is a polar projection of the top half of the spin-nematic phase space. This two-dimensional phase space with axes representing S_{\perp} and Q_{\perp} is centered on the pole of the spin-nematic sphere, which is the location of the polar ground state. For this reason, this phase space focuses on the critical dynamics in the vicinity of the critical point. Representations of the phase space for different values of $\tilde{q} = q/|c|$ can be seen in Fig. 3.3.

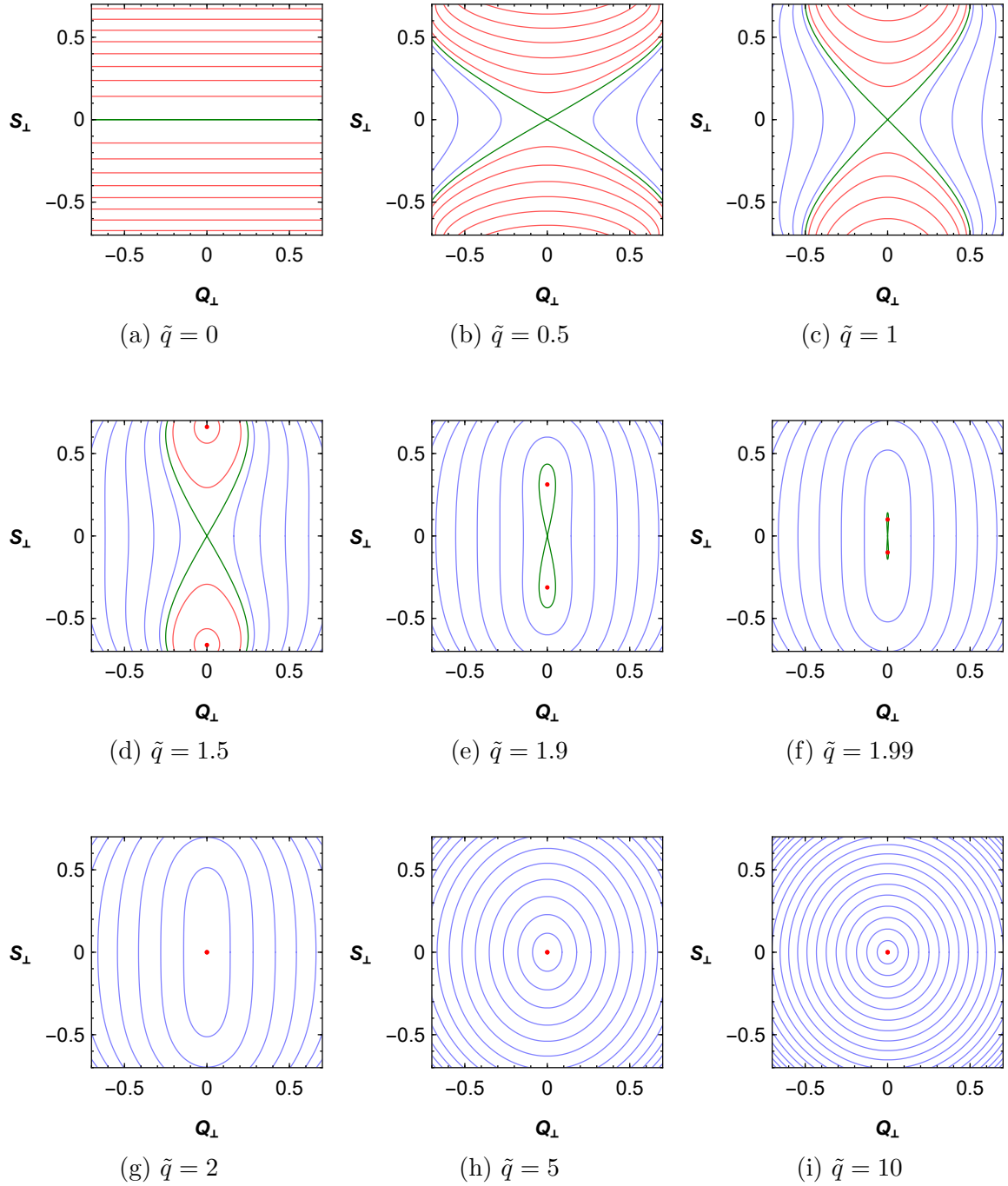


Figure 3.3: **Polar phase space.** Polar phase space for several values of \tilde{q} . The energy contours are the same for every plot, and are the same as in Fig. 3.2. These plots are a polar projection of the top half of the spheres in Fig. 3.2.

3.6.3 Spinor Phase Space

The third phase space is the spinor phase space with the variables ρ_0 and θ_s described earlier in the chapter. This phase space is a Mercator projection of one half of the spin-nematic phase space perpendicularly to the S_\perp axis. Representations of the spinor phase space for different values of $\tilde{q} = q/|c|$ are displayed in Fig. 3.4.

3.7 Summary

After a brief historical review of Bose-Einstein condensation, the Hamiltonian of our system in the single mode approximation has been derived using quantum and mean field methods. Focusing on the only relevant terms for our study and the rest of this thesis, the most convenient form of the Hamiltonian is the mean field using S and Q_z as observables, where $Q_z = 2\rho_0 - 1$, and c and q as parameters for the collisional and magnetic energies:

$$H = \frac{c}{2}S^2 - \frac{q}{2}Q_z \quad (3.28)$$

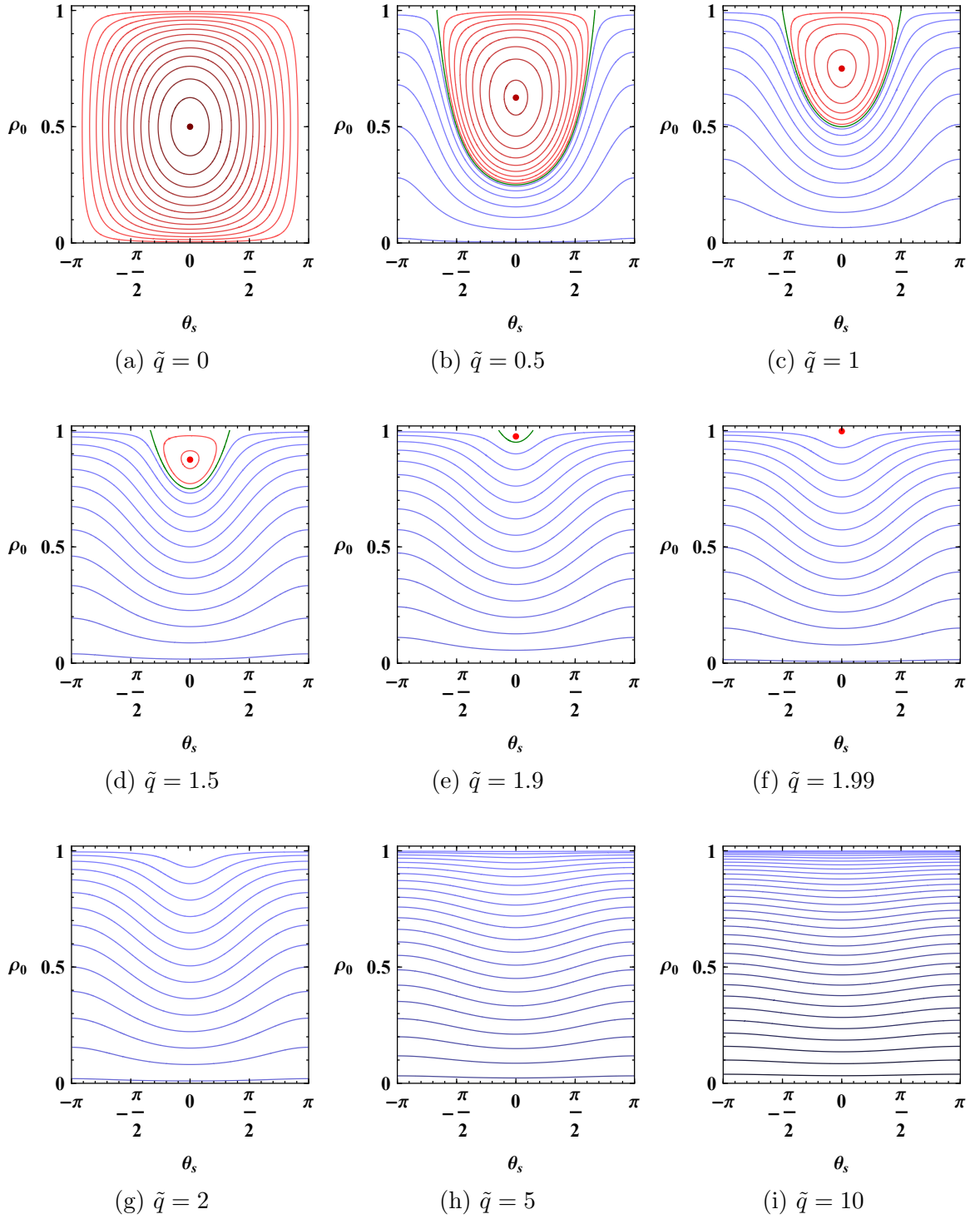


Figure 3.4: **Spinor phase space.** Spinor phase space for several values of \tilde{q} . The energy contours are the same for every plot, and are the same as in Fig. 3.2 and Fig. 3.3.

CHAPTER IV

EXPERIMENTAL APPARATUS

The experimental setup used to measure the data for this thesis has a long history behind it, parts of which date back to the thesis work of Murray Barrett [122]. His thesis work demonstrated the realization of the first all-optical BEC in 2001 [20]. Some of the electronics have survived all these years and are still being used in the current setup. Most of the experiment and its components, however, have changed over the years. Many graduate students have had the opportunity to work on the spinor BEC experiment, and each has contributed to building a more robust and versatile setup. The description of the experimental setup will be presented keeping the order of a typical experimental cycle in mind. We will first describe the vacuum chamber, followed by the setup needed to create a magneto optical trap (MOT). We will then explore how the cold atoms from the MOT are transferred to an optical dipole force trap, where evaporative cooling takes place, leading to Bose-Einstein condensation. The methods used to interact with the BEC will be presented, and we will end with the description of the control and imaging systems.

4.1 Vacuum Chamber

The heart of the experiment is the vacuum chamber, where the ultracold atom physics takes place. A schematic of the chamber can be seen in Fig. 4.1. Ultra high vacuum (UHV) is necessary to maintain the long lifetimes of the trapped dilute gas of atoms that will eventually become a BEC. Any experiment performed at a slightly higher pressure would also be impacted by collisions from particles in the background. The only desired atoms in the vacuum chamber are rubidium (Rb) atoms, some of which will be used in the experiment. The experiment takes place in a stainless steel octagon

(Kimball Physics), featuring two large glass windows on 6" flanges at the top and bottom, as well as eight 2.75" ports on the sides. Of the eight side ports, five are glass windows. All the glass windows, including the large ones on the top and bottom of the octagon, are broad-band anti-reflection (AR) coated. This coating optimizes the transmission of near-infrared light (~ 780 nm) used for the experiment. Two other ports are fitted with windows used for the entrance and exit of a CO₂ laser beam with a wavelength of ~ 10.6 μ m. Since glass is opaque to light at that wavelength, these two windows are made of zinc selenide (ZnSe), and are AR coated. The remaining port is used to connect the octagon to the rest of the vacuum apparatus, which includes two permanently mounted vacuum pumps, a valve to connect the chamber to an external pump, and a Rb getter source. There is another small glass window on the other side of the vacuum apparatus, which serves as the entrance for the absorptive imaging probe beam.

Inside the chamber, a pair of 1.5" (3.8 cm) focal length ZnSe lenses is mounted on the axis of propagation of the CO₂ laser beam. This pair of lenses forms a 1:1 telescope that tightly focuses the laser beam. This tight focus will serve as an optical dipole force trap. The second lens re-collimates the beam before it exits the chamber and has been used in the past to focus a counter-propagating beam in order to create an optical lattice. The pair of lenses is mounted such that their foci overlap at the geometric center of the octagon. On the horizontal axis perpendicular to the CO₂ laser beam, a high-aperture laser objective (HALO) is used to collect light for imaging purposes. Its role will be explained in detail later in the chapter.

The pressure in the chamber is lowered from atmospheric pressure to UHV and maintained by several vacuum pumps. When initially setting up the experiment, the pressure is first lowered by a roughing pump and a turbo pump. Once the pressure has been lowered by the turbo pump, the whole vacuum chamber is heated to remove impurities from the chamber's walls and windows. The temperature of the so-called

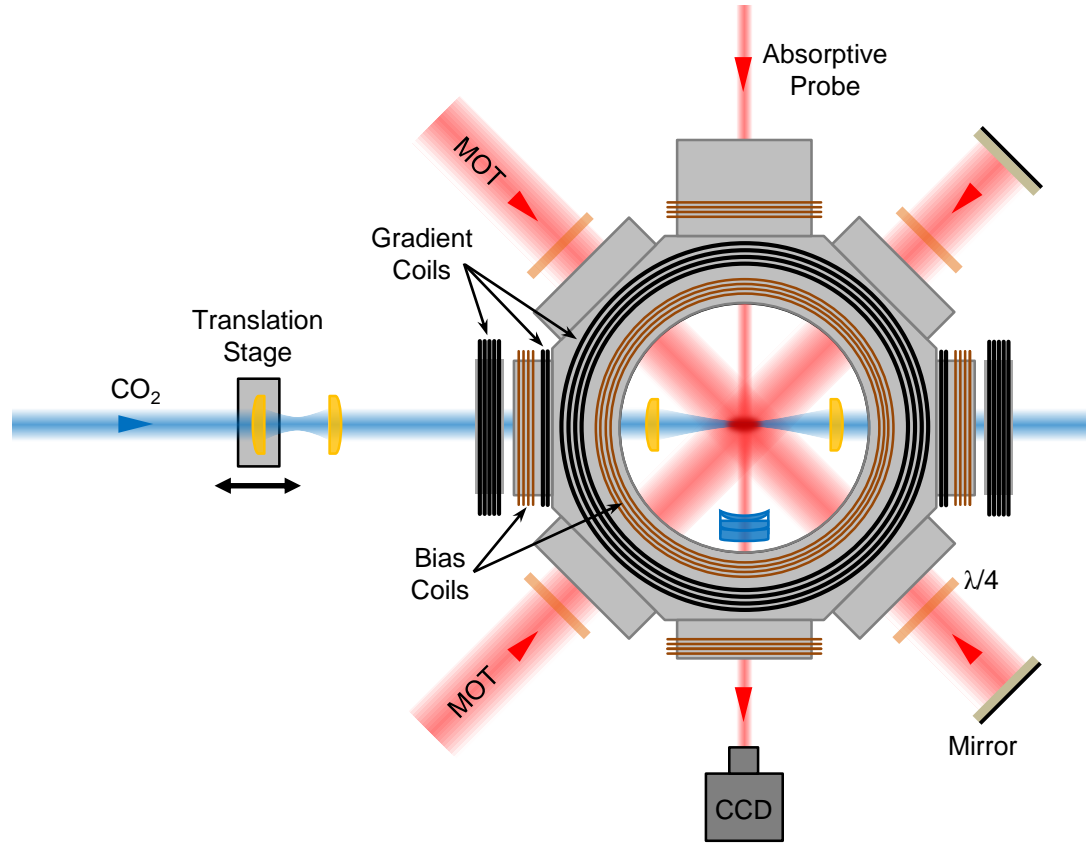


Figure 4.1: **Diagram of the vacuum chamber.** Top view of the vacuum chamber. The axis perpendicular to the page also contains a pair of MOT beams, as well as the repump beam.

“bake-out” can reach $\sim 400^\circ\text{C}$ when only metallic parts are heated, but when the octagon with its windows and lenses are present, the bake-out temperature must be lowered. The following step involves turning on an ion pump. As its name indicates, it ionizes particles and collects them using strong electric and magnetic fields, the latter supplied by powerful permanent magnets. The chamber is also equipped with a titanium (Ti) sublimation pump. When a high current ($\sim 50\text{ A}$) is applied to a Ti filament for a few minutes, Ti is emitted, and it will eventually deposit on the walls of the chamber. The Ti-coated surfaces will capture hydrogen atoms that are incident on it, thus lowering the pressure further. All these steps bring the pressure to a level too low to be read by vacuum gauges, in the 10^{-11} torr regime. The ion

pump is constantly on and the Ti layer remains active, which maintains the pressure to UHV level despite the continuous out-gassing of hydrogen from the steel chamber.

4.2 Magneto-Optical Trap

The first step on the cooling path to degeneracy is achieved by using a magneto-optical trap (MOT). This ingenious concept was first realized in 1987 [7], and contributed to awarding the 1997 physics Nobel prize for cooling and trapping atoms with laser light. The combination of laser beams and a magnetic field gradient in the optimal conditions can trap atoms with a depth in the millikelvin regime.

4.2.1 Source of Atoms

The Rb atoms that will be trapped in the MOT originate from a background Rb vapor. The atoms themselves are released from a getter, which is heated using a variable current source. The resistive heating causes the getter to release both stable Rb isotopes, ^{85}Rb and ^{87}Rb at their natural abundances of 72.2% and 27.8%, respectively.

Light at ~ 455 nm from LEDs is used in conjunction with the getter. This light promotes light intensity assisted de-adsorption (LIAD), which is non-negligible since Rb has a tendency to adhere to glass windows [123]. This light not only recycles some of the Rb in the chamber, it also keeps the Rb from permanently damaging the windows. Turning on the blue lights makes a noticeable difference in the size of the MOT, and consequently in the number of atoms in the BEC.

4.2.2 Trapping Concept

The bare necessities for a MOT are 3 orthogonal pairs of counter-propagating laser beams with opposing circular polarization, in addition to a magnetic field gradient. In order to understand the concept behind the MOT, one must start with the electronic energy structure of Rb.

Rb is an alkali, ordered in the first column of the periodic table because of its single

valence electron. This single valence electron gives a Rb atom a relatively simple energy structure, which will be taken advantage of for trapping. The simplicity arises from the fact that all the other electrons are in closed, stable shells. The electronic structure of Rb in the ground state is $[\text{Kr}]5s^1$. With its unpaired s electron, a Rb atom behaves to a first approximation similarly to a hydrogen atom in respect to electronic energy levels. The first excited level corresponds to the valence electron in a $5p$ orbital, with an orbital angular momentum of 1. This $5p$ energy level is split due to spin-orbit coupling: the non-zero orbital angular momentum \mathbf{L} and the spin angular momentum \mathbf{S} of the electron give rise to the so-called fine structure. The energy shift depends on the relative orientation of the orbital and spin angular momenta. Consider the total electronic angular momentum $\mathbf{J} = \mathbf{L} + \mathbf{S}$. Since $L = 1$ and $S = \frac{1}{2}$, the possible values are $J = \frac{1}{2}$ and $J = \frac{3}{2}$. Therefore, the ground state is $5^2S_{1/2}$, and two resulting fine-structure sub-levels are $5^2P_{1/2}$ and $5^2P_{3/2}$, where the Russel-Saunders notation $n^{2S+1}L_J$ has been used. This results in two transitions from $5s$ to $5p$, both of which are in the near-infrared. The spectral lines form a doublet, so the transitions are referred to by D_1 and D_2 lines, from $5^2S_{1/2}$ to $5^2P_{1/2}$ and $5^2P_{3/2}$, respectively. Our experiment uses the transitions on the D_2 line, at a wavelength of ~ 780.2 nm, which is conveniently accessible using simple diode lasers. The energy levels of the D_2 are shown in Fig. 4.2.

The Rb energy level structure is complicated further due to the interaction between of the total electronic angular momentum \mathbf{J} and that of the nucleus. This coupling between \mathbf{J} and the nuclear angular momentum \mathbf{I} gives rise to the hyperfine structure, which affects both the $5s$ and $5p$ levels. The coupling is characterized by the total atomic angular momentum $\mathbf{F} = \mathbf{I} + \mathbf{J}$. The isotope we use in the experiment (^{87}Rb) has a nuclear angular momentum of $I = \frac{3}{2}$. For the $5^2S_{1/2}$ level, $J = \frac{1}{2}$, which combined with $I = \frac{3}{2}$ gives $F = |I - J| = 1$ and $F = I + J = 2$. The energy separation between these two hyperfine levels lies in the microwave part of the electromagnetic

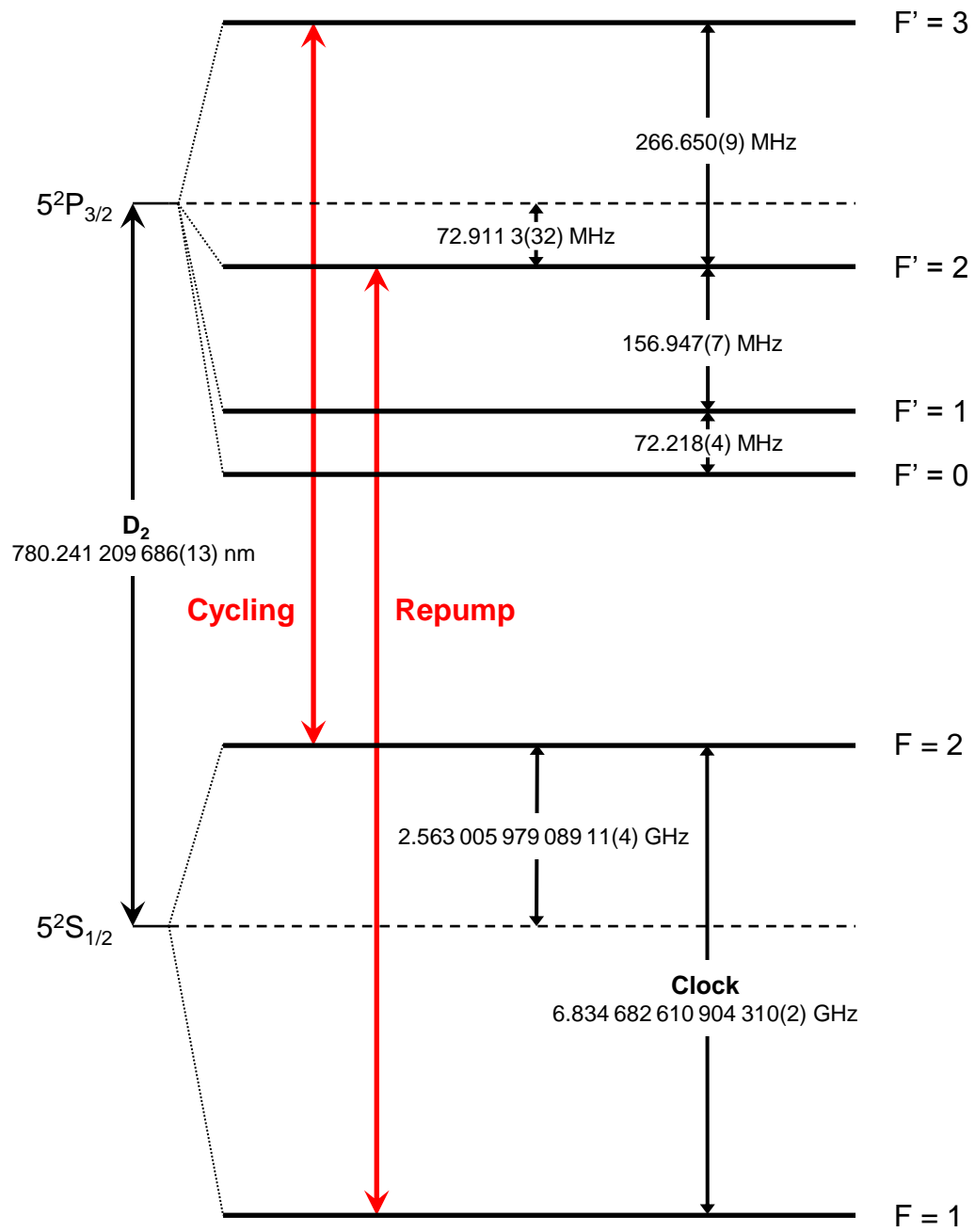


Figure 4.2: D2 line energy levels for ^{87}Rb .

spectrum at ~ 6.8 GHz. Similarly, $5^2\text{P}_{1/2}$ has $J = \frac{1}{2}$, which yields the same hyperfine structure. However, for $5^2\text{P}_{3/2}$ we have $J = \frac{3}{2}$, and since the values for F range from $|I - J|$ to $I + J$, this results in $F' = 0, 1, 2, 3$. Note that the hyperfine levels for excited electronic states will be labeled as F' .

There is one more level of complexity in the energy structure, and it relates to the projection of the total atomic angular momentum along the quantization axis defined by an external magnetic field. When no magnetic field is present, atoms with different projections m_F of the total atomic angular momentum F have the same energy, but a magnetic field lifts the degeneracy. There are $2F + 1$ Zeeman sub-levels, with m_F ranging from $-F$ to $+F$. The energy shift for each m_F sub-level in a magnetic field B can be calculated using the Breit-Rabi formula [124]:

$$E_{|F, m_F\rangle} = -\frac{\Delta E_{\text{hf}}}{8} - g_I \mu_I B m_F - \frac{1}{2} \Delta E_{\text{hf}} \sqrt{1 + x m_F + x^2} \quad (4.1)$$

where

$$x = \frac{(g_J \mu_B + g_I \mu_I) B}{\Delta E_{\text{hf}}}.$$

Here, ΔE_{hf} is the hyperfine splitting, g_J and g_I are the electron and nuclear g -factors, μ_B and μ_I are the Bohr magneton and nuclear magnetic moment. The numerical values are tabulated in Appendix A. At low fields, the linear Zeeman shift (second term on the RHS of Eq. (4.1)) differs slightly from 700 Hz/mG depending on the hyperfine level. The transitions between Zeeman sub-levels are experimentally accessible for the range of magnetic fields used in the experiment by using RF frequencies. The details of the $5^2\text{S}_{1/2}$ level are shown in Fig. 4.3.

A MOT is an extension of the optical molasses technique, where atoms are cooled by absorbing a photon and its momentum, and re-emitting a photon in a random direction. The recoils from the emitted photons average out over time, but the radiation pressure from the absorbed photons can be used to push an atom along a given direction. It is necessary for the photons to have the correct frequency to be absorbed.

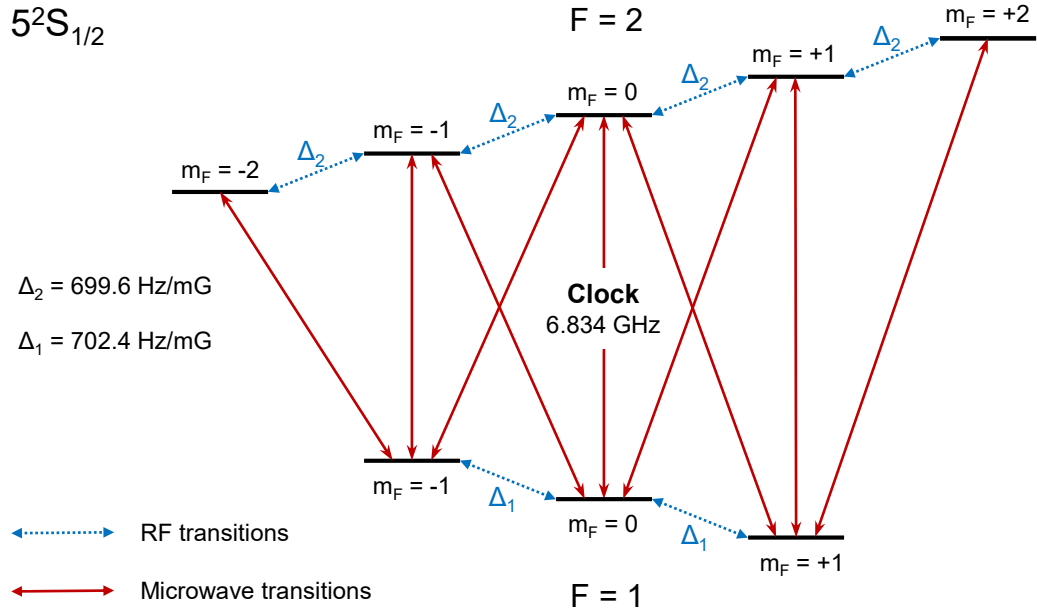


Figure 4.3: **Energy levels of the $5^2S_{1/2}$ level in ^{87}Rb .**

To slow down an atom, it would need to absorb photons traveling opposite to the atom's motion. This can be accomplished by slightly lowering the light's frequency, or detuning it to the red side of the spectrum. This compensates for the Doppler effect which effectively changes the resonance frequency in the frame of the moving atoms. That way, the light will only be resonant in the frame of an atom traveling against it.

For our experiment, we use a transition in the D_2 line ($5^2S_{1/2}$ to $5^2P_{3/2}$), from $F = 2$ to $F' = 3$. The benefits of this transition are two-fold. First, using polarized light with a right handedness optically pumps the atoms in the $|F = 2, m_F = 2\rangle$ to $|F' = 3, m_{F'} = 3\rangle$ transition, which is the strongest transition from $F = 2$ to $F' = 3$ [125]. In addition, the excited state $|F' = 3, m_{F'} = 3\rangle$ can only decay to $|F = 2, m_F = 2\rangle$, due to electric dipole transitions selection rules, which is why this transition is called the “cycling” transition. Despite these convenient features, there is a small probability of an off-resonant excitation to the $F' = 2$ level, which then has

a 50% probability of decaying to the $F = 1$ manifold. This level is “dark,” in the sense that the photons driving the cycling transition will no longer be absorbed. In order to continue cooling these atoms, a second source of light is needed. This light is resonant with the $F = 1$ to $F' = 2$ transition. This transition is called the repump transition as it returns the atoms on the cycling transition for efficient cooling. In fact, without the repump, the atoms are off-resonantly excited off the cycling transition, so using the cycling transition alone effectively “depumps” all the atoms to the $F=1$ level. These two frequencies are the only ones needed to cool, trap and image the atoms in the MOT. In practice, the trapping light driving the $F = 2$ to $F' = 3$ transition is detuned a few linewidths to the red of the transition.

4.2.3 MOT Lasers

The light we use for the MOT (cycling and repump) comes from homemade external cavity diode lasers (ECDL) [126, 127]. These relatively simple lasers use an inexpensive and commercially available laser diode and a grating. The distance from the diode to the grating acts as an optical cavity, the length of which is adjusted by a piezoelectric transducer. The current to the diode and its temperature are controlled and stabilized by simple electronic controllers, some of which are homemade. Both the cycling and repump light sent to the experiment comes from injection locked diode lasers (ILDs), or slaves, which are seeded by the master ECDLs. The frequencies are stabilized using saturated absorption spectroscopy, along with FM spectroscopy. Saturated absorption spectroscopy provides sharp Doppler-free peaks that are electronically transformed into slopes by modulating the light with a ~ 10 MHz signal. For the modulation to be applied, the current to the laser diode can be dithered, as we do for the cycling laser, while the repump light uses an acousto-optical modulator (AOM). This method provides an error signal and locking point that a PI circuit uses to stabilize the light’s frequency.

The cycling laser's light uses a complex detuning scheme to shift the frequency to the range needed for the various stages of the experimental cycle. The light is first shifted 160 MHz to reach its locking point, which is the $(F = 2 \rightarrow F' = 1) - (F = 2 \rightarrow F' = 3)$ crossover. A small portion of the light is sent to a double-pass AOM that shifts the frequency by 2×186 MHz right on resonance for the absorptive probe. The rest of the light is sent to another double pass AOM, which allows a variable frequency shift, from 2×140 MHz to 2×238 MHz. The frequency-shifted light then seeds the ILDL. The amplitude of the RF signal sent to the double-pass AOM is adjusted such that the power of the light seeing the ILDL is constant regardless of the frequency shift. The power of the beam is then amplified by a tapered amplifier (TA), outputting ~ 500 mW. The spatial mode out of a TA is notoriously poor, so a long path including cylindrical lenses is used to improve the quality of the mode. A final AOM is used to shift the frequency by 110 MHz to bring it to the slightly red-detuned frequency that will be sent to the atoms. This last AOM also controls the power sent to the chamber. The beam is finally split evenly in three using half-waveplates and polarizing beam cubes and sent to the experiment via optical fibers.

At the chamber, the light from each fiber is expanded and collimated into beams with a 15 mm waist and clipped to a top-hat profile of 25 mm diameter. Each beam is 30–35 mW, which is enough to saturate the cycling transition. The beams must be well balanced in order to give the MOT a spherical shape. The beams go through quarter-waveplates, which gives them a circular polarization. The light traverses the chamber and is then retroreflected. This essentially provides the atoms with six beams of light propagating both ways on three perpendicular axes.

The repump laser has a more simple setup than the cycling laser, since we only need one beam with a power of ~ 15 mW at the chamber. The master-slave configuration and the same locking mechanism are used. The light from the master is locked 80 MHz from the repump transition. After seeding the ILDL, the frequency is shifted

back to the repump transition by an AOM that also controls the power. The light is then fiber-coupled and sent to the chamber, where it is combined with the vertical cycling beam.

4.2.4 Magnetic Field Coils

The MOT needs a pair of coils mounted in an anti-Helmholtz configuration to provide a magnetic field gradient of ~ 7 G/cm. The purpose of this gradient is to create spatially dependent Zeeman energy shifts. When used in combination with circularly polarized light, this effect causes atoms to absorb photons only when they are located at a given position are moving at a certain velocity. The MOT is centered at the zero of the magnetic field gradient, with a larger Zeeman energy shift further away from the center. Recall that the cycling beams are detuned to the red of the transition. The sign of the energy shift changes at the center, so an atom moving towards the center of the trap will only absorb photons with the polarization driving the transition allowed by the energy shift. For example, an atom located to one side of the center of the trap will experience a Zeeman shift that favors the absorption of σ^+ photons, while a photon on the other side will preferentially absorb σ^- photons. This offset in radiation pressure pushes the atoms towards the center of the gradient field. The lowest temperature achievable in a MOT is limited to a few μK because of the randomness in the direction of the emitted photons, which heats the atoms and sets the temperature limit.

4.3 *From Magneto-Optical Trap to Bose-Einstein Condensate*

The Rb atoms initially in the chamber are at room temperature, and the trap depth of the MOT is ~ 1 mK, which means only the slowest atoms will be trapped. Because of the slow loading of the MOT, we must wait about 15 s for the size of the MOT to plateau. At that point, the MOT contains $\sim 10^8$ atoms, and the so called temporal

dark MOT sequence [128] can begin. This method can achieve sub-Doppler cooling, and has the effect of spatially “collapsing” the MOT, thus greatly increasing the spatial density of atoms. This is achieved by decreasing the power of the cycling laser by half, and detuning its frequency by ~ 200 MHz, which is as far to the red as the setup allows. This is where the terminology of dark MOT originates from. The MOT coil gradient is halved, and the power of the repump laser is lowered to a few tens of microwatts. The final number of atoms in the optical trap is strongly dependent on the repump power during this sequence. For this reason, we must find the optimal value on a daily basis every time the experiment is started. The combination of these changes leads to the collapsing of the MOT along the repump axis into a pancake shape, and the location is dependent on the final repump power. The other parameters used have been empirically determined to optimize atom loading. Both cycling and repump beams are shuttered after a few hundred milliseconds, but the repump is turned off shortly (~ 1 ms) before the cycling light. This delay optically pumps all the atoms down to the $F = 1$ hyperfine ground state. The position of the collapsed atoms is optimized to overlap with the focus of the CO₂ laser, where 10 to 15 million atoms at ~ 30 μ K are transferred.

4.3.1 Optical Trap

The rest of the experiment takes place in an optical dipole force trap. The trapping concept relies on the dispersive interaction between the intensity gradient of the light field and the electric dipole moment induced in the atoms by that same field [129]. For an electric field \vec{E} , the induced dipole moment is $\vec{p} = \alpha\vec{E}$, where α is the frequency-dependent complex polarizability. This leads to a spatially dependent potential $U = -\langle \int \vec{p} \cdot d\vec{E} \rangle = -\frac{1}{2}\langle \vec{p} \cdot \vec{E} \rangle$, where the brackets are the time average over a period of oscillation of the field. There are several regimes for optical traps, which have to do with the detuning $\Delta = |\omega - \omega_0|$ between the angular frequency ω of the

trapping light and the angular frequency ω_0 of the cycling transition.

Introducing the on-resonance damping rate $\Gamma = e^2\omega_0^2/6\pi\epsilon_0m_e c^3$, the trapping potential and scattering rate in a dipole force trap can be expressed by

$$U(\vec{r}) = -\frac{3\pi c^2}{2\omega_0^3} \left(\frac{\Gamma}{\omega_0 - \omega} + \frac{\Gamma}{\omega_0 + \omega} \right) I(\vec{r}), \quad (4.2)$$

$$\Gamma_{\text{sc}}(\vec{r}) = \frac{3\pi c^2}{2\hbar\omega_0^3} \left(\frac{\omega}{\omega_0} \right)^3 \left(\frac{\Gamma}{\omega_0 - \omega} + \frac{\Gamma}{\omega_0 + \omega} \right)^2 I(\vec{r}), \quad (4.3)$$

where I is the intensity of the trapping laser. In the case of a far off resonance trap (FORT), the condition $\Delta = |\omega - \omega_0| \ll \omega_0$ is met, so the expressions (4.2) and (4.3) can be approximated by

$$U(\vec{r}) = -\frac{3\pi c^2}{2\omega_0^3} \frac{\Gamma}{\Delta} I(\vec{r}), \quad (4.4)$$

$$\Gamma_{\text{sc}} = \frac{3\pi c^2}{2\hbar\omega_0^3} \left(\frac{\Gamma}{\Delta} \right)^2 I(\vec{r}) = \frac{\Gamma}{\hbar\Delta} U(\vec{r}). \quad (4.5)$$

In our case, we use a CO₂ laser, which has a wavelength of $\sim 10.6 \mu\text{m}$. This laser is so far off resonance that the approximation $\Delta \ll \omega_0$ made for the FORT is no longer valid. Instead, we have $\omega \ll \omega_0$. The expressions (4.2) and (4.3) can therefore be reduced to

$$U(\vec{r}) \simeq -\frac{3\pi c^2 \Gamma}{\omega_0^4} I(\vec{r}) = -\frac{\alpha_s}{2\epsilon_0 c} I(\vec{r}), \quad (4.6)$$

$$\Gamma_{\text{sc}} = \frac{2\Gamma}{\hbar\omega_0} \left(\frac{\omega}{\omega_0} \right)^3 U(\vec{r}). \quad (4.7)$$

Here, $\alpha_s = 6\pi\epsilon_0 c^3 \Gamma / \omega_0^4 = 5.3 \times 10^{-39} \text{ m}^2\text{C/V}$ is the static polarizability for the ground state of ⁸⁷Rb [129], which must be used because we are now in the quasi electrostatic trap (QUEST) [130] regime. Despite the high power of the laser, the scattering rate is so low (around one photon per hour [131]) that the trap is essentially conservative. Another benefit of using a CO₂ laser is that because of its long wavelength, it has a short Rayleigh length. We use this feature by focusing the beam inside the chamber with a 1.5" (38 mm) focal length lens, and the axial trapping confinement is strong enough to produce a BEC in the focus of the CO₂ laser alone. This trap is cigar shaped, and we refer to it as the single focus trap.

We use an industrial laser (Coherent-DEOS GEM-100L) capable of outputting over 100 W of power. The power transmitted to the vacuum chamber is controlled by a germanium AOM. The +1 order beam is sent to the experiment, and the undeflected part ends in a water-cooled beam dump. By changing the power of the RF signal to the AOM, we can effectively control the trap's potential with practically no delay.

Further down the beam path, we find a nearly 1:1 telescope, with the first of the two ZnSe lenses on a motorized translation stage. The spacing of the lenses is adjusted to change the size of the beam as it enters the vacuum chamber. The inside of the chamber contains another 1:1 telescope, and the first lens focuses the beam to create the optical trap. The adjustable telescope before the chamber changes the width of the beam at that focusing lens. For transferring atoms from the MOT to the optical trap, a wide focus is preferable, as it increases the trapping volume overlap. However, the focus must be tightened during evaporation to ensure efficient rethermalization of the atoms. Because only one of the lenses moves, the collimation of beam after the telescope changes, which in turn causes a small displacement (~ 1 mm) of the trap along the laser axis, but this does not affect the evaporation process. The second ZnSe lens inside the chamber recollimates the beam before it exits, and the beam ends in a thermal detector that also serves as a beam dump.

During the evaporative cooling phase, the power to the CO₂ laser at the chamber is adiabatically lowered from 40 W to 50 mW. As mentioned earlier, the trap is simultaneously compressed by changing the length of the 1:1 telescope along the beam path. This narrowing of the trap increases the spatial density of the cloud of atoms, thus enabling efficient rethermalization during evaporation. As the trapping potential is lowered, the hottest atoms gradually have enough energy to leave the trap, while elastic collisions between the remaining atoms allow them to rethermalize. The waist of the trap inside the chamber is brought down from 120 μm to 20 μm in 1 s. See Fig. 4.4 for an illustration of this setup.

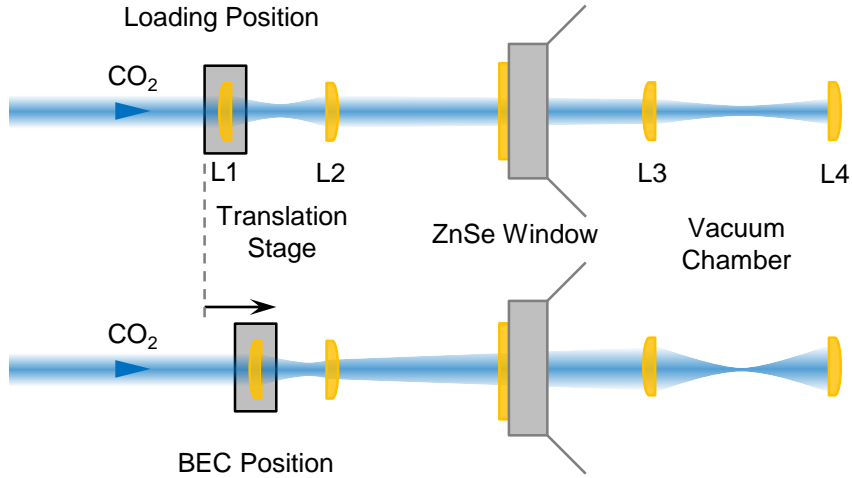


Figure 4.4: **Effect of the translation stage motion.**

This evaporation method produces a BEC with atoms in the $F = 1$ hyperfine ground state, but with a distribution of $m_F = -1, 0, +1$ Zeeman sub-levels. Our experiment requires an initial state with all the atoms in the $m_F = 0$ state, so in addition to a bias magnetic field along the laser axis to define the quantization axis, a strong magnetic field gradient (~ 20 G/cm) is turned on along the same axis. This axis has the weakest trapping potential, and the gradient causes preferential losses of the $m_F = -1$ and $+1$ atoms as they are pushed to the edges of the trap. The result is a pure $m_F = 0$ condensate with up to 2×10^5 atoms. The exact final temperature is difficult to determine, as there is no observable thermal component, but we estimate the temperature to be below 100 nK. The bias field mentioned above is ~ 2 G, which is high enough to guarantee that the system is the polar phase, where $m_F = 0$ is the lowest energy state, so the spin mixing dynamics are suppressed. A plot of the temperature and number of atoms during evaporation is shown in Fig. 4.5.

Aligning the CO₂ laser beam is a delicate task, due to its long wavelength making it invisible to the naked eye, as well as its high intensity. In order to guarantee a proper alignment through the center of the chamber, the CO₂ laser beam is initially

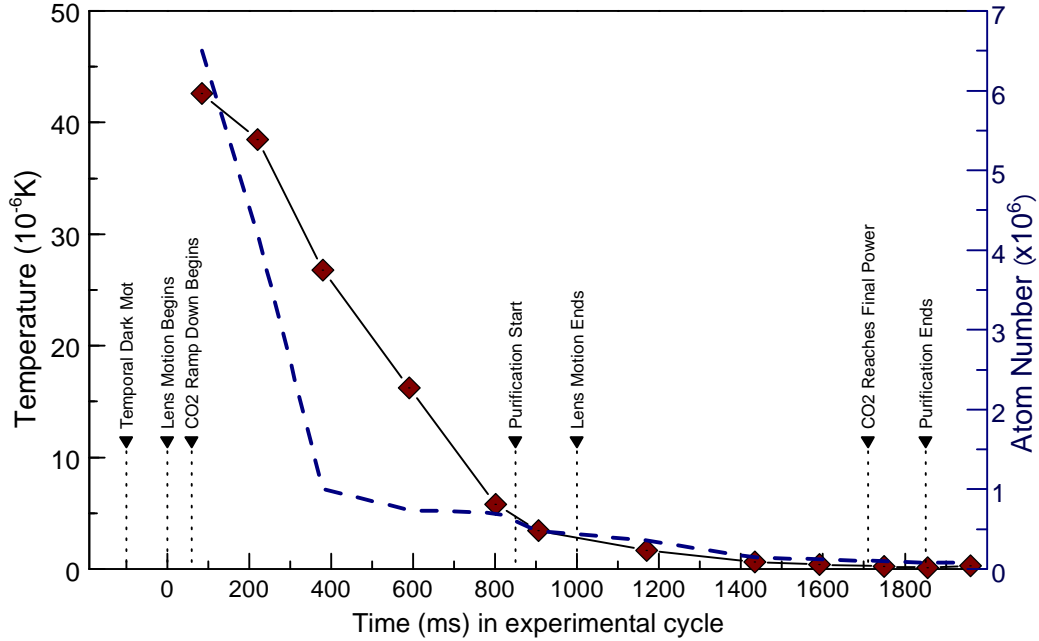


Figure 4.5: **Temperature and number of atoms during evaporation.** The red diamonds indicate the temperature measurements, and the blue dashed line corresponds to the number of atoms in the condensate.

overlapped using a beam combiner with a low power HeNe laser at 632 nm. This allows us to align the red visible beam at low risk. We also use thermal paper for lower powers, and at intermediate power, the beam is aligned using thermal image plates from Macken Instruments. These metal plates are coated with thermal-sensitive phosphors that fluoresce when exposed to UV light. However, if they are heated, which is what the CO_2 laser beam does, the incident beam will be visible as a dark dot.

4.3.2 Cross Trap

While interesting physics occur in the single focus trap, it is an anisotropic trap, and the weak axial confinement elongates the condensate enough so that its size becomes larger than the spin healing length. In other words, spin domains are energetically allowed to form. While the study of spatial spin structures in a BEC is an interesting topic in itself, we want the option to observe the spin dynamics in a trap smaller than the spin healing length, where no domains can form. We achieve this goal

by perpendicularly intersecting the CO₂ laser beam with an 852 nm beam at their respective foci. The two lasers' radial trapping potentials are comparable, so the result is a nearly spherical trap, which we refer to as the cross trap. This 852 nm beam also operates as an optical dipole force trap, but in the FORT regime described earlier. The power of the 852 nm laser is adiabatically ramped up (400 ms) towards the end of evaporation, once the lens mover has finished moving and the single focus trap is in its final position. An AOM controls the power, which is usually in the 20–30 mW range. At the chamber, the beam is focused into a 20 μm waist, which must precisely overlap with the 20 μm waist of the CO₂ laser beam. The alignment process is delicate and requires the use of a 2D translation stage with micrometers.

4.3.3 Magnetic Field Coils

In total, the experiment utilizes six pairs of coils. Three generate bias magnetic fields, while the other three create gradients. The bias coils are made of thin copper wire, and are mounted directly on the windows and flanges of the vacuum chamber for compactness. This means that they are not in the optimal Helmholtz configuration, but the size of the condensate is small enough that the effect is negligible. On the other hand, it guarantees that the coils are centered on the chamber. The three pairs are symmetric along three perpendicular axes, two of them being the CO₂ laser axis and the vertical axis. These bias coils cancel the Earth's magnetic field, which is ~ 0.5 G in Atlanta [132], as well as any constant bias magnetic fields generated nearby. Obviously, they also can provide a bias field in any direction. The pair centered around the CO₂ laser axis produces the field that defines the quantization axis. Another use of the bias coils is to change the direction of the gradient used for Stern-Gerlach separation of the atoms clouds.

Out of the three pairs of gradient coils, two are similar in construction. The first

pair consists of the MOT coils, which provide the gradient necessary for the space-dependent energy shifts described previously. They are mounted above and below the octagon, close but not in contact with the chamber, in a nearly anti-Helmholtz configuration. Since the zero of the gradient defines the location of the MOT, the coils can be displaced to move the MOT, which is sometimes necessary to optimize the overlap between the collapsed MOT and the optical trap. The top coil can be moved vertically and tilted, while the bottom one is free to move horizontally.

The second pair of gradient coils consists of the auxiliary gradient coils. As their name indicates, they provide an additional gradient, with a symmetry axis along the CO₂ laser beam. They are too far apart to be in an exact anti-Helmholtz configuration, but what is needed is a gradient, not necessarily a linear gradient. They have two main roles. The first has been previously mentioned: the purifying gradient used during evaporation, in order to begin the experiment with a pure $m_F = 0$ BEC. The second role is to generate a Stern-Gerlach type field to separate the atoms of different spin projections after they are released from the trap. That way, the three clouds do not overlap and the atoms in each cloud can be counted separately. For both of these actions, the current is raised to the maximum setting available by the current power supply, which is over 500 A. For this reason, the gradient coils are made of 1/4" copper pipe and are water cooled to prevent them from melting. Both of these pairs of gradient coils use the same power supply, and the current is switched between them using insulated-gate bipolar transistors (IGBTs). The IGBTs can handle the high current, but for no longer than a few seconds, which is typically the duration of the purification process.

Finally, a third pair of smaller gradient coils is wrapped on the CO₂ laser viewports. Their purpose is to cancel the magnetization that has gradually developed in the vacuum chamber over the years. The residual gradient is in the order of 100 mG/cm, which is small compared to the gradients delivered by the other coils,

but must be dealt with lest it has an effect on the spin dynamics.

4.3.4 Microwaves and RF

We have seen that we can use laser light in the near IR for trapping and cooling. In addition, we can access the transitions between the $F = 1$ and $F = 2$ hyperfine manifolds of the $5^2S_{1/2}$ energy level, as well as the transitions between the Zeeman sub-levels. These transitions can be driven using microwave and RF frequencies, as shown in Fig. 4.2. In this study, these transitions were principally used to measure and cancel the external magnetic fields, and to calibrate the number of atoms counted. In previous experiments, they have also been used to prepare the BEC in a particular state, or to measure the projection of a spin component on an axis other than the quantization axis. Examples of these additional capabilities can be found in earlier studies from our lab [32, 41, 42, 119, 131].

As mentioned above, the microwave and RF frequencies give us access to the transitions in the $5^2S_{1/2}$ level. The $|F = 1, m_F = 0\rangle \rightarrow |F = 2, m_F = 0\rangle$ ($|1, 0\rangle \rightarrow |2, 0\rangle$ for short) is called the clock transition, at ~ 6.8 GHz. It was named such because it shows no sensitivity to the linear Zeeman effect and is used in atomic clocks. However, it is sensitive to the magnetic field through the “clock shift” of 575 Hz/G^2 [124]. The other levels have non-zero values of m_F and show a linear energy offset for small fields due to the linear Zeeman shift, also called the anomalous Zeeman effect. This shift is close to $\Delta = 700 \text{ Hz/mG}$ for both $F = 1$ and $F = 2$, but they differ slightly (by $\sim 0.5\%$) because of the small nuclear part g_I of the Landé g -factor g_F that scales the energy shift between magnetic sub-levels. For more details, see [41, 124]. By using the clock frequency or by detuning the frequency by $\pm\Delta$, the atoms can be transferred from $|1, 0\rangle$ to $|2, -1\rangle$, $|2, 0\rangle$, and $|2, +1\rangle$.

The microwaves are sent to the atoms via a horn made of a copper cylinder of 1.5” diameter [41, 131], and are free-spaced coupled into the chamber through the

top window. The orientation is such that no polarization is favored, so all π , σ_+ , and σ_- transitions are accessible. The microwaves are generated by a HP E4422B frequency synthesizer that relies on the 10 MHz signal from a GPS receiver for its frequency reference. The output of the HP E4422B is capped at 4 GHz, and this limited range means we must use a frequency doubler to reach 6.8 GHz. The signal also goes through a fast RF switch and an isolator, followed by an amplifier before going to the horn. A diagram of the setup is shown in Fig. 4.6.

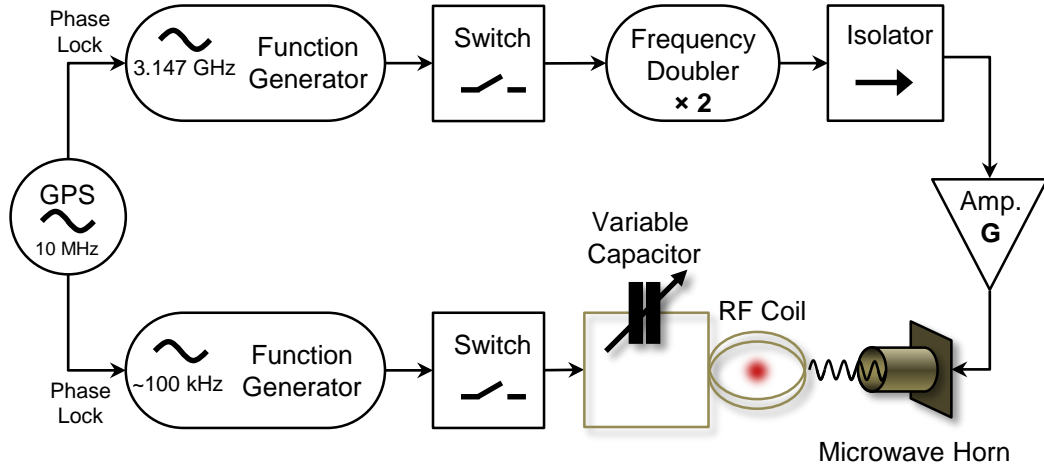


Figure 4.6: **Microwave and RF setup.**

The output of the frequency generator is always on, and the switch is activated through a pulse generator, which allows us to create pulses as short as a few μs . We control the power of the microwaves through the function generator. A lower power means that a longer pulse is necessary for the same number of atoms to change state, but the frequency resolution is higher, as expected from the Fourier transform from time to frequency domains.

For small magnetic fields, the quadratic Zeeman energy shift is negligible, so the energy spacing between $|1, -1\rangle$ and $|1, 0\rangle$ is the same as the one between $|1, 0\rangle$ and $|1, +1\rangle$. This means that applying an RF pulse resonant on that transition to a cloud of atoms in the $|1, 0\rangle$ will randomly transfer them to either the $|1, -1\rangle$ or the $|1, +1\rangle$

level. The RF radiation is sent to the atoms by a small two-turn coil sitting on the edge of the top window of the octagon. The coil is part of an LC circuit where a variable capacitor is tuned such that the circuit is resonant for the frequency used. The inductance of the coil currently used is $10.3 \mu\text{H}$.

4.3.5 Control System

Two computers are used to control the experiment. Basically, the control settings are entered in one computer, while the other acquires the data. The control computer runs Labview and sends controls to the experiment via National Instrument (NI) cards, GPIB and serial RS-232. The five NI cards in use send voltages to the equipment running the experiment. Three cards have analog outputs that generate voltages between 0 and 10 V, and the two other cards have digital TTL outputs. Each card has eight channels, so that gives us the possibility to control 40 parameters with a time resolution of $10 \mu\text{s}$. The cards are synchronized and triggered on the rising edge of a 60 Hz signal from an AC line. The analog outputs control the powers of the lasers and their detunings through AOMs, the magnetic field biases and gradients, and the current to the getter. The digital outputs operate RF switches, optical shutters, triggers for the cameras and pulse generators, IGBTs, blue lights and a piston, whose role will be described shortly. The microwaves and RF function generators, as well as the pulse generators, are controlled through GPIB. The GPIB control system is notoriously slow compared to the time scales of the experiment, so the settings are uploaded to the devices before the experimental sequence, and the sub-millisecond timing is handled by fast RF switches controlled by pulse generators, who are themselves triggered by the NI cards' outputs. The lens mover that controls the 1:1 telescope in the CO_2 laser beam path is operated through a RS-232 serial port, as is the SmartArb function generator, which we use to modulate the power of the CO_2 laser for trap frequency measurements. Just like for the GPIB controls, the

settings are uploaded as a short program before the experiment, and the machines execute the program when triggered during the experimental cycle.

A graphical interface is created by Labview. We usually control the experiment by constructing a timing sequence that will tell each channel what voltage to output, as that times to change it, and how to change it (step, linear ramp, or more complicated ramps). All the required information is entered in an Excel spreadsheet. A macro generates a csv file that is uploaded to Labview, which in turn interpolates between the control settings and provides each card with a voltage for every $10 \mu\text{s}$ of the experimental cycle. We also have the option to use Labview to get each channel to output a constant voltage, which is helpful for testing and troubleshooting.

4.3.6 Data Acquisition

All the raw data used in this thesis consists of images. We use two cameras: a simple black and white CCTV camera to observe the MOT, and a high quality Andor camera to image the BEC. The CCTV camera is a Cohu 2122-1000. Its main purposes are to provide us with a live feed of the MOT, and to grab a snapshot of the atoms from the collapsed MOT that have transferred to the dipole force trap. Having a live feed of the MOT tells us first of all if atoms are getting trapped in the MOT. If a MOT is present, we can see how large and stable it is, what shape it has, and by keeping track of its position, a change of its location can reveal an issue about the experiment. The live feed of the MOT is also used for the coarse alignment of the cross-trap. The resolution is 768×494 for a sensor of $6.4 \text{ mm} \times 4.8 \text{ mm}$, and we use the camera with a 1:1 imaging lens.

The Cohu camera is used in tandem with a PCI-1407 frame grabber. A trigger from a digital channel causes an asynchronous reset that starts the acquisition of a single image. The camera noise is too high to precisely image the BEC, but it is good enough to image the collapsed MOT following the temporal dark MOT sequence.

The collapsed MOT and the atoms that have started to transfer to the optical trap can be imaged simultaneously, which is one way to optimize their overlap. When the image is taken ~ 300 ms after turning off the MOT trapping beams, all the atoms have either made it in the CO₂ laser dipole force trap or have been lost. To measure the number of atoms loaded in the optical trap, the atoms are released from the trap and allowed to expand as they fall for 6 ms before probing them with resonant light for 100 μ s.

The second camera is an Andor iKon, a CCD (charge coupled device) camera with a high quantum efficiency ($> 90\%$ at a wavelength of 780 nm). This efficiency refers to the conversion rate of photons incident on the sensor to electrons. The sensor is cooled at -70°C , which reduces the camera noise. The sensor is 13.3×13.3 mm with a pixel resolution of 1024×1024 , which yields pixels of 13 μ m. Along with a magnification of $5\times$ (using another lens outside the chamber), a pixel in an image corresponds to 2.6 μ m. With a 16 bit depth for each pixel, this camera is well suited to image the BEC.

The light is collected in the chamber by a Linus HALO 0.3 8904 lens, a high aperture laser optics (HALO) with a 5 cm focal length and a high numerical aperture (NA) of 0.31.

4.4 Imaging

We use two imaging techniques to image the BEC: absorptive and fluorescent imaging. An excellent review of both techniques and how they are used in our setup is included in a previous thesis from Eva Bookjans [32], so we will give only a short overview and present the benefits and disadvantages of each imaging method.

4.4.1 Absorptive Imaging

Absorptive imaging consists of shining a weak collimated probe on resonance with the cycling transition for a short time, and imaging the shadow of the BEC. This signal

image is then compared with a reference image taken in the same conditions, but with no atoms present. The division of both images using imaging software outputs a clear image of the BEC. The main advantage is that because of the short pulse (0.1 ms) and the weakness of the probe (a few tens of microwatts), the atoms do not move much, which yields an excellent spatial resolution, where the shape and spatial features (such as spin domains) of the condensate can be studied.

However, because of the fluctuations of the absorptive beam between the absorption and reference frames, getting an accurate counting is not trivial. In this thesis, we only use absorptive imaging as a qualitative tool. Additionally, the use of coherent light through several optics can generate interference patterns. The reference image must be taken as soon as possible following the signal image. The time between the two images must be short in order to minimize the variation in the probe's intensity. We wait 10 ms, which is not enough time to measure two successive complete frames with the camera. Instead, we only use the top half on the sensor for imaging while the bottom half is masked off. Between the two images, the charges on the sensor are shifted to the bottom half of the sensor, and the top is available to image again. This so-called kinetic imaging is what allows us to take two images in such a short time.

This absorptive imaging method has many uses, and we have taken advantage of the benefits in the following ways: by observing the shape and expansion of the cloud after releasing it from the single focus trap over several times of flight (TOF), we can confirm that the trapped atoms are indeed a BEC, in which case the cloud expands anisotropically, unlike thermal clouds that expand isotropically. In this thesis, absorptive imaging was most commonly used to optimize the alignment the 852 nm beam for the cross trap, which is done with no TOF. It also allows the detection of spatial spin domains (or more importantly for this work, the lack thereof). Finally, we use it to determine the magnification by measuring the speed of the condensate in free fall, and to optimize the focus of the BEC by translating the camera along the imaging

axis.

4.4.2 Fluorescence Imaging

Fluorescence imaging uses the MOT beams as a source of light to scatter photons off the atoms. The beams are as close to resonance with the cycling transition as our system allows (6 MHz detuned to the red), but despite this slight detuning that slightly decreases the fluorescence signal, the high power (30 times the saturation intensity) mitigates the issue. The probe times used for this thesis range from 200 μs to 400 μs . These durations are long enough that the cycling beam will start depumping atoms to the $F = 1$ hyperfine level, so the repump must also be turned on. The light scatters off the atoms isotropically, and the photons are collected by the HALO lens described above. Despite its relatively large numerical aperture of 0.31, the lens covers a small solid angle and only captures 2.5% of the light, which explains the higher laser power and longer probe times than for absorptive imaging.

A drawback for this method is the potential heating of the atoms. The radiation pressure from the MOT beams distorts the cloud of atoms, thus washing out the spatial features. On the other hand, we can use superpixels made of 4×4 pixels to lower the readout noise of the CCD camera [32]. The benefits of fluorescence imaging include a linear response between the number of photons collected and the number of atoms, as long as the optical depth of the cloud is low enough to prevent scattered photons from being reabsorbed by another atom in the cloud. For this reason, we let the BEC expand for 22 ms after it is released from the dipole force trap. The free fall takes place in a Stern-Gerlach gradient magnetic field. This also separates the centers of the clouds of different spin components by $\sim 900 \mu\text{m}$, which is enough to count the atoms in each state without overlap of the clouds. The longer probe times also increase the signal to noise ratio, and since the light scattered from the atoms is not coherent, there is no risk of interference patterns. However, the scattered

light from the walls of the chamber is a disadvantage. To limit this scattering, we narrow the diameter of the MOT beams to 12 mm during imaging by pneumatically dropping masks in their path during imaging. However, a background must be taken and subtracted from every image. A background is thus taken daily, or any time the camera is moved, by averaging a minimum of 20 shots without atoms present.

The camera outputs images with the electron counts (after amplification of the signal from the CCD sensor) per pixel. The method to convert the counts to number of atoms uses RF pulses of various lengths that transfer atoms from $|1, 0\rangle$ to $|1, -1\rangle$ and $|1, +1\rangle$. The details of the technique are developed in detail in [32, 41], but the basic concept is the following: the average number of counts (from the amplified number of electrons) from atoms transferred to the $m_F = -1$ and $m_F = +1$ states is compared to the variance of the magnetization (difference in the number of atoms transferred to each state). There is an equal probability of an atom being transferred to each state, and because of Poissonian fluctuations [32], the variance of the magnetization scales with the number of transferred atoms. The number of atoms transferred is proportional to the counts of electrons measured per atoms (CPA), while the variance is proportional to the square of the CPA. Therefore, as the variance of the magnetization is plotted against the number of transferred atoms for several RF pulse lengths, the slope given by a linear fit yields the CPA.

With the CPA determined, the images can be analyzed and the number of atoms in each cloud counted. Andor cameras come with their own interface and software, where we can define counting regions, or regions of interest (ROIs), which gives us an estimate of the number of atoms in each cloud, once the background has been subtracted. A more precise image analysis is performed in Mathematica[®], where the atom counts per pixel are uploaded. Unlike in Andor where the ROIs are fixed, a program automatically finds the centers of the atom clouds and centers the ROIs

around them. This is relevant because the distortion of the clouds caused by fluorescent imaging changes the center of the area where atoms are present depending on the number of atoms in the cloud. In addition to the mean background subtracted in Andor, the program analyzes every image one by one and determines the amount of extra scatter image by image by averaging the counts in the regions outside the ROIs, which is then subtracted to the counts of atoms inside the ROIs. This became extremely useful when the Andor camera started having issues that caused the background to fluctuate from shot to shot. This essentially prolonged the usefulness of the camera before a need for repair. Once the number of atoms per cloud was accurately determined, the data analysis could begin. It was also done in Mathematica[®], which automatically determined whether the image was a “bad shot.” In rare occasions ($< 0.1\%$), the lens mover would stay still during the experimental cycle, thus preventing the efficient rethermalization of atoms during evaporation, resulting in a small atom cloud instead of a BEC. This image would yield a small number of atoms which would impact the analysis of the rest of the data run, so automatically detecting this kind of image was essential. The subsequent steps included calculating the means and standard deviations of the numbers of atoms, as well as other quantities that will be discussed in the following chapters.

To complete the description of the experimental apparatus, we will mention the cooling requirements. In fact, without cooling, several parts of the experiment would suffer from instability, affect other pieces of equipment, or even be permanently damaged. The elements depending on a stable temperature for stability include the CO₂ laser and the AOM that controls its power. For stability, we use a chiller with a large thermal bath. It relies on heat exchange with the cold ($\sim 10^\circ\text{C}$) facility water, and provides the experiment with a stable supply of coolant (a mix of water and ethylene glycol) at 17°C . The elements cooled by the chiller are the CO₂ laser head and power supply, the CO₂ laser AOM and its RF amplifier. For the elements that need to avoid

overheating but do not require stability, we use tap water. The elements cooled this way are the auxiliary and MOT gradient coils, the IGBTs, the microwave amplifiers, and the CO₂ laser beam dump that receives the beam that is not deflected towards the vacuum chamber. To prevent accidents, several parts of the experiment are now rigged with thermocouples, and an alarm rings as soon as a temperature threshold is reached.

CHAPTER V

METHODS

In order to measure KZM scaling and extract a scaling exponent, one must first precisely determine the value of the magnetic field corresponding to the critical point. The quantities \hat{t} and \hat{q} used to determine the scaling exponents express how far the system resumes evolution from the critical point. Since the location of the critical point is directly linked to the spinor dynamical rate, which itself depends on the trap parameters, as well as density and the total number of atoms, a robust method is needed to accurately and efficiently determine the critical magnetic field. In fact, it is measured before data is taken in order to characterize the system, but also at regular intervals during the data runs to make sure that the experiment has not become unstable, due to the misalignment of the CO₂ trapping laser and the 852 nm laser used for the cross trap, for example.

Once the location of the critical point is known, the ramps lowering the magnetic field through the critical point can begin. This is how all the raw data used in this thesis was gathered. As discussed earlier, the KZM predicts the scaling of the freeze-out time with respect to ramp speed, so the key is to determine where the system starts to evolve. The method used is to choose a threshold for the fractional population ρ_0 in the $m_F = 0$ state. ρ_0 is measured at regular intervals during the ramp, and when it drops under the threshold, the system is considered to have “unfrozen.”

5.1 Critical Magnetic Field Determination

Before every data-taking session, the external magnetic field must be zeroed, and the magnetic field along the quantization axis must be calibrated, such that the control setting exactly corresponds to the field at the BEC. Once that step is complete,

the determination of the magnetic field B_c corresponding to the critical point can commence.

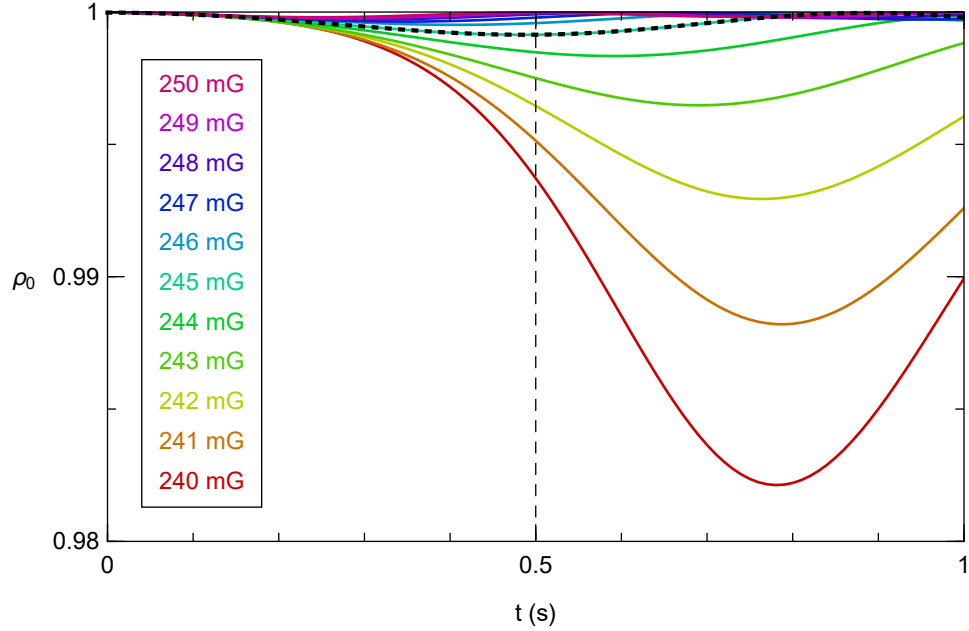


Figure 5.1: **Evolution close to the critical point (simulation).** When the field is suddenly lowered to a constant field near the critical point, the amplitude of the spin dynamics is related to how far the constant field is from the critical point. If the constant field is over the critical point, no measurable evolution takes place. However, when the field is under the critical point, the system will evolve out of its initial state of $\rho_0 = 1$. The traces shown go from 240 mG (red) to 250 mG (violet) with a step of 1 mG, for a critical field of 245 mG. The trace corresponding to the evolution at a field equal to the critical field is dashed. The slight dip in the dashed trace, which is too small to be experimentally measured, is due to the finite number of atoms (5.7×10^4) used in the simulation. For final fields larger than 245 mG, the traces are practically indistinguishable and remain at $\rho_0 = 1$. The vertical line shows the evolution time t_{evol} used to compare ρ_0 with the data in Fig. 5.2 and Fig. 5.3.

This procedure starts by initializing the system in the polar phase ground state at a high magnetic field, well above the critical point ($B_i \approx 2 \text{ G} \gg B_c$), where $\rho_0 = 1$ is the ground state. The magnetic field is then quickly (2 ms) lowered to a fixed value B_f near the expected critical field. If this final magnetic field value is above the critical point, the creation of $m_F = -1$ and $m_F = +1$ will be suppressed. However, if the system finds itself in the ferromagnetic phase, spin-mixing dynamics will occur.

These spin population dynamics are determined by how far the final magnetic field is from the critical point. A sample of simulated evolution dynamics for fields close to the critical point is shown in Fig. 5.1.

The system is allowed to evolve at the constant magnetic field B_f for a time t_{evol} (ranging from 150 ms in the cross trap to 500 ms in the single focus trap) prior to measurement, which is long enough to observe spin mixing when the field has been lowered below the critical point. This process is repeated for several final fields and the spin population transfer is measured. The mean of the fractional population ρ_0 and its standard deviation $\Delta\rho_0$ are then plotted against the final value of the field, as shown in Fig. 5.2. Determining the field for which the system has started to evolve after t_{evol} would be difficult to precisely determine looking at the data alone. In Fig. 5.2 for example, ρ_0 is still 1 when the final field is 246 mG, but no longer for 242 mG, and $\Delta\rho_0$ has also started to increase. This would suggest that the critical field is somewhere between 242 mG and 246 mG, but solely relying on these two data points is delicate, since intrinsic fluctuations and experimental noise could cause a slight offset, thus affecting the subsequent data analysis.

Determining the critical field with higher reliability and precision is necessary for a meaningful investigation of KZM scaling. One of the issues is the small amplitude of evolution close to the critical point. Previous studies from our group have examined the evolution of our system following a fast quench [43], which is essentially what is being performed here, but the final field used in the earlier work was much lower, corresponding to $q \approx |c| = 0.5 q_c$. In that case, the mean value of ρ_0 dipped as low as 0.3 during early evolution. In comparison, the value of q for a field 5 mG under B_c is $q \approx 0.96 q_c$ (when $B_c = 245$ mG), in which case ρ_0 remains above 0.98 (red trace in Fig. 5.1). This small amplitude of evolution motivated us to take measurements for a larger range of fields, allowing us to determine the critical field with much higher precision.

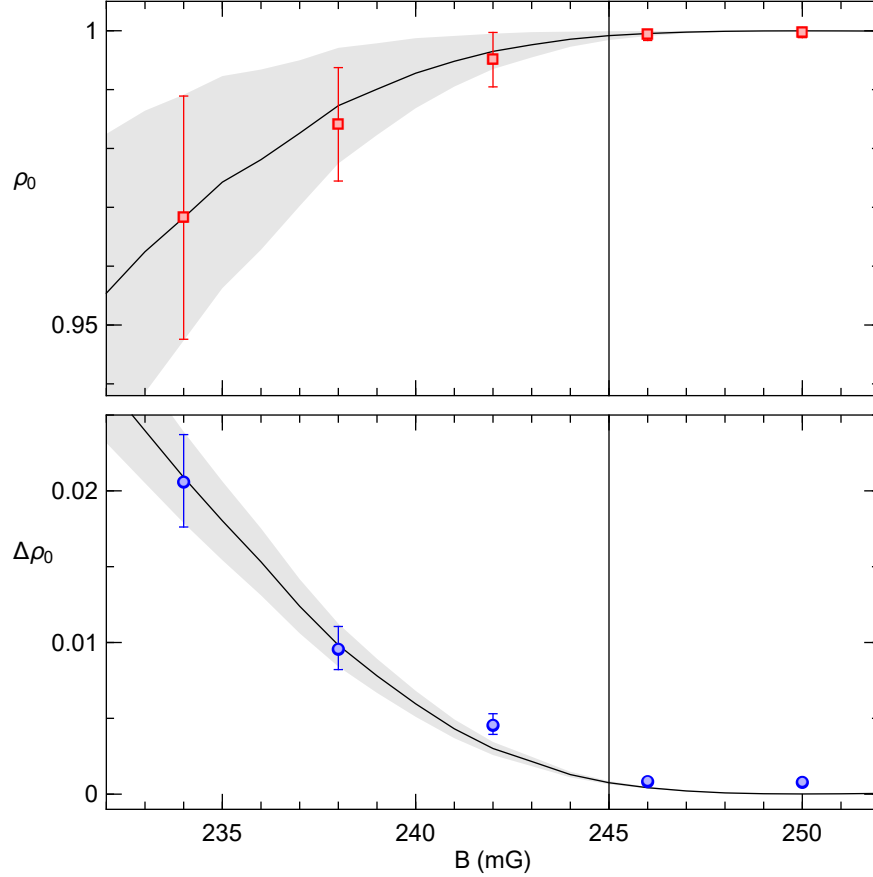


Figure 5.2: **Evolution compared with simulations best match.** Measurements of ρ_0 (red squares) and $\Delta\rho_0$ (blue circles) after 500 ms of evolution at constant magnetic field (shown on the horizontal axis) following a fast (2 ms) drop from 2 G ($q \gg 2|c|$). The data is compared with simulations, represented by solid lines. The simulations are performed using the same method as the experiment with a critical field setting of 245 mG (represented by a the vertical line). The shaded regions show \pm one standard deviation.

Once ρ_0 has been measured after the evolution time t_{evol} at different fields, its mean value is plotted and compared with simulations. An example of data and the simulation that is the best match is shown in Fig. 5.2, where not only ρ_0 but also its standard deviation $\Delta\rho_0$ show good agreement. This method is robust in the sense that it mitigates the effect of possible outliers due to the finite amount of data taken and experimental fluctuations.

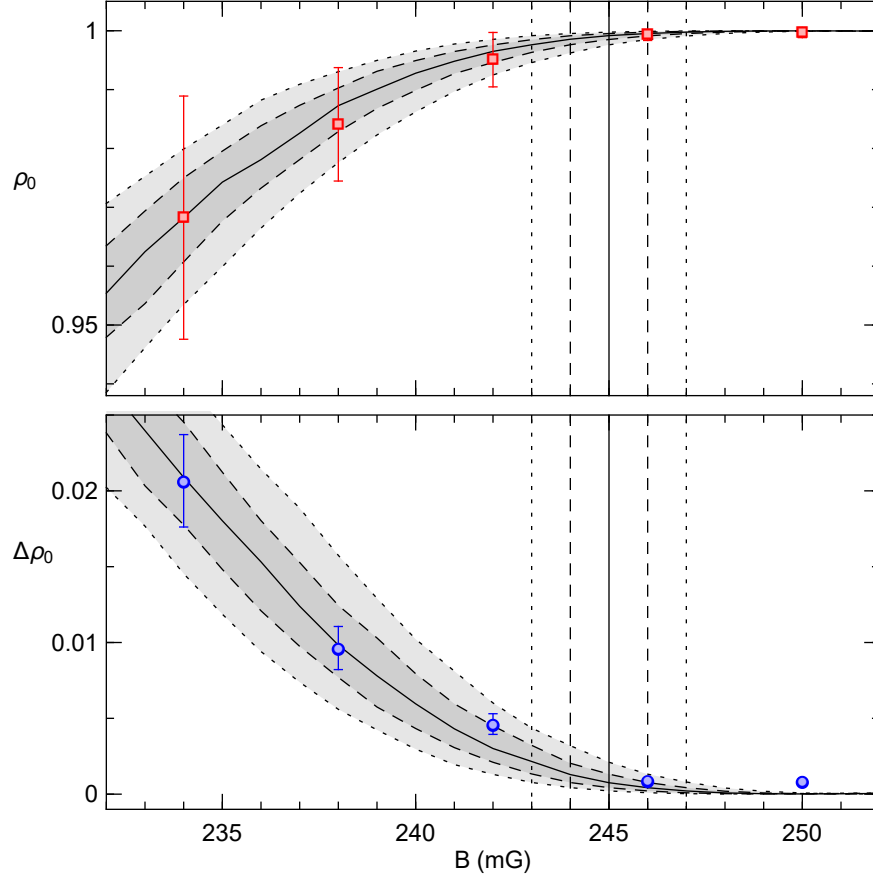


Figure 5.3: **Evolution compared with range of simulations.** Measurements of ρ_0 (red squares) and $\Delta\rho_0$ (blue circles) after 500 ms of evolution at constant magnetic field (shown on the horizontal axis) following a fast (2 ms) drop from 2 G ($q \gg 2|c|$), similarly as for Fig. 5.2. In this plot, the data is compared with five simulations, represented by solid, dashed, and dotted curved lines. The solid line shows the simulation performed using a critical field of 245 mG, whereas the dashed and dotted lines represent simulations with critical fields of ± 1 and ± 2 mG, respectively. The vertical lines indicate the different critical fields used in the simulations.

The precision of the determination of the critical point can be estimated by comparing the data with simulations performed using other critical fields, as illustrated in Fig. 5.3. The figure shows five simulations overlaid with the data, displaying the best match (solid) as well as ± 1 mG (dashed) and ± 2 mG (dotted). Note that the grey envelopes do not represent uncertainties, but instead guide the eye to differentiate the ranges of different critical fields. Even though all the data points do not fall right on one single trace, it is possible to pick the best match amongst the several simulations.

Depending on the quality of the match, the uncertainty in the determination of the critical field can be as low as 1 to 2 mG.

5.2 *Magnetic Field Ramps*

We now discuss the magnetic field ramps that will cause the system to cross the critical point at different speeds, which is how we will determine the KZM scaling. Once the critical point is precisely known, the next step is to monitor the spin populations as the magnetic field is ramped down through the critical point. The system is prepared in the polar ground state at high magnetic field ($B \approx 2 \text{ G} \gg B_c$), and all the atoms are in the $m_F = 0$ state. The system is first brought closer to the critical point by rapidly (2 ms) lowering the field such that $q = q_0 = 2.2|c| = 1.1q_c$. This value is still over the critical point, so the system is still very close to the polar ground state.

The system is then driven through the critical point by decreasing the magnetic field such that q varies linearly as $q(t) = q_0(1 - t/t_r)$, where t_r is the time it takes to ramp the field from $q = q_0$ to $q = 0$. Figure 5.4 shows the magnetic field for a 100 ms ramp.

The reason why the field is first quickly lowered close to the critical point is due to the limited lifetime of our condensates. In an ideal system, the slow ramps would start at higher fields to guarantee a slow evolution towards the critical point, but due to atom loss, that is unrealistic. In fact, for such ramps, too high a fraction of the atoms would be lost by the time the system reaches the critical point. More details about atom loss and the model we use to mitigate its effect during the data analysis will be covered in the next chapter.

The experiment is repeated for several values of t_r . The fastest ramp uses $t_r = 100$ ms, whereas the slowest ones last up to 4 s in the cross trap and 9 s in the single focus trap. The limited lifetime also affects our ability to test very long ramps, since a large number of atoms would be lost by the time the system reaches the critical

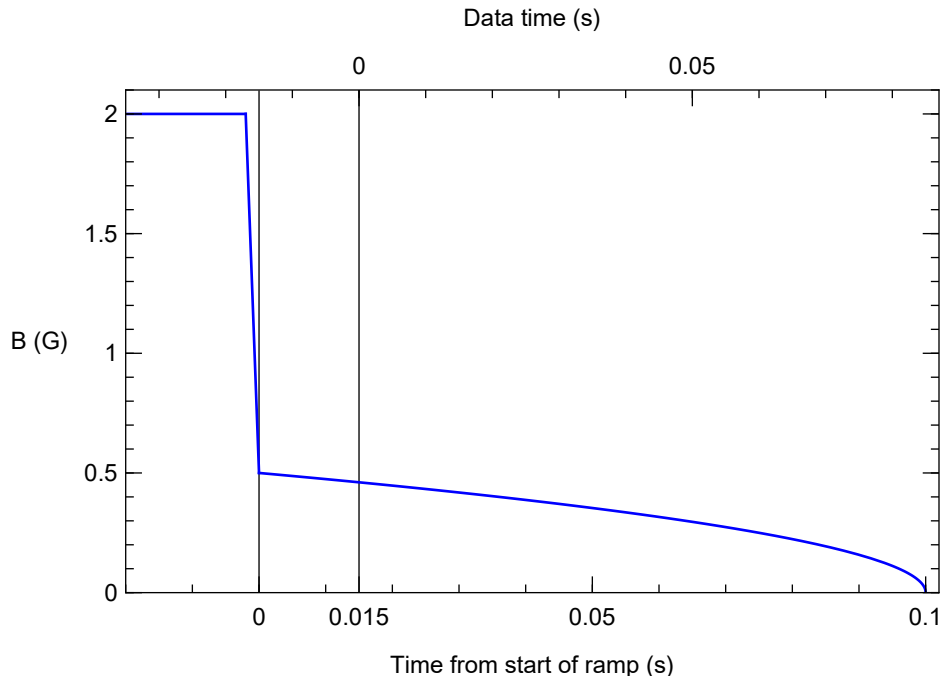


Figure 5.4: **Magnetic field control settings.** Magnetic field control settings for a 100 ms ramps from 500 mG to 0 mG. The initial magnetic field is 2 G, where the system is in the polar ground state. For this data set, the field is then quickly lowered to 500 mG ($q \approx 1.1q_c$), followed by the slower ramp, whose beginning is indicated by the left vertical line. This ramp is linear in q , but recall that $B \propto \sqrt{q}$. The data is measured 15 ms after the beginning of the slow ramp (right vertical line), and at regular times thereafter.

point. Immediately after entering the ferromagnetic phase, the system rests around what was the polar ground state, which is now an unstable equilibrium point, and eventually, quantum fluctuations cause the system to evolve out of this equilibrium. After a freeze-out time \hat{t} following the quantum phase transition, the system starts evolving along the separatrix. ρ_0 is measured multiple times at regular intervals during the ramp, and its mean and standard deviation $\Delta\rho_0$ are determined.

The real magnetic field at the condensate actually has a short delay compared to the control field. This is due to the inductive delay of the bias coils along the quantization axis that control the field responsible for the quadratic Zeeman energy q . By measuring the magnetic field during a fast rise and fast drop of the control value,

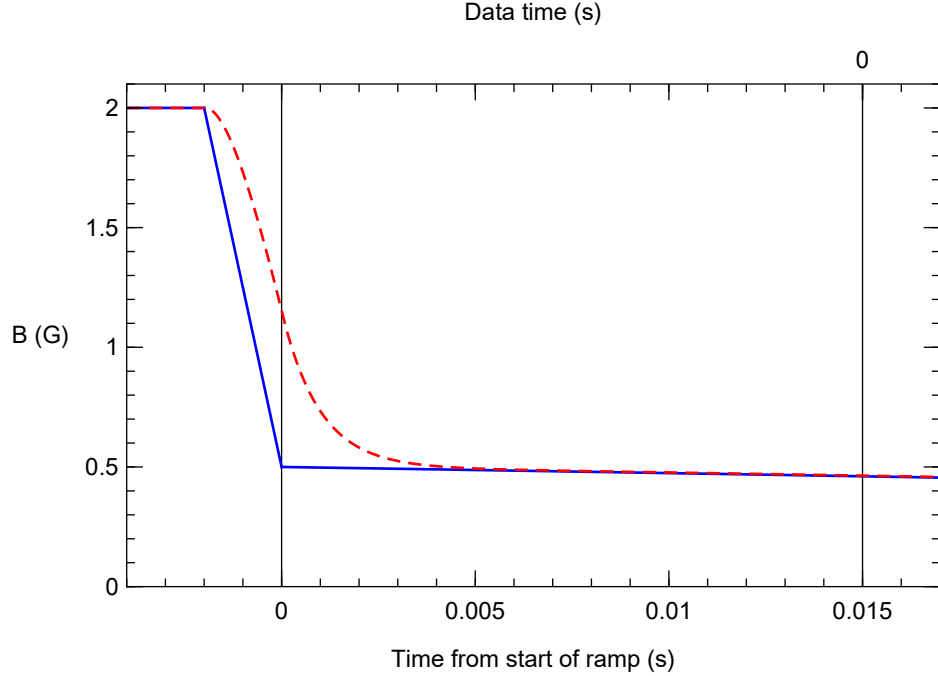


Figure 5.5: **Magnetic field response to the control settings (simulation)**. The actual magnetic field (red dotted line) at the condensate is delayed from the control values (blue solid line). The real field is calculated from the control field using an exponential decay time constant of 1 ms and numerically integrating the decay using steps of $10 \mu\text{s}$. This plot corresponds to a ramp time of 100 ms, but the focus is on the initial part, when there is a significant offset between the control and real magnetic fields. After 15 ms, which is when the measurements begin, the real field follows the control with a delay of 1 ms. In other words, the control field changes slower than how fast the real field can follow the control. This only breaks down during and following the fast drop from 2 G, as well as at the very end of the ramp when the field nears 0, as the field drops sharply due to the $B \propto \sqrt{q}$ relationship, but that has no effect on our current study.

we have determined that the real field reacts to the control with a 1 ms exponential decay time constant. The effect of this delay is analyzed with simulations to estimate the effect on the data. An example showing both the control value and a numerical simulation of the actual magnetic field is shown in Fig. 5.5. The spin populations are measured starting from 15 ms after the beginning of the ramp, when the gap between the control and the actual magnetic field is negligible.

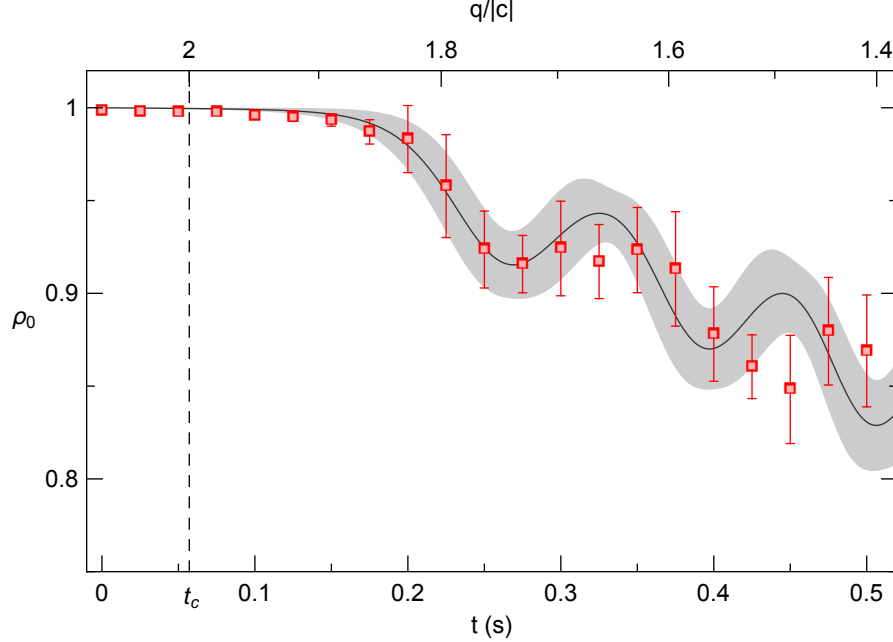


Figure 5.6: **Measurement of spin populations during a magnetic field ramp.** The mean of ρ_0 (red squares) during a typical experimental run where the magnetic field is slowly ramped down through the critical point such that q decreases linearly. The system shows good agreement with a simulation (black curve and envelope showing \pm one standard deviation) for long evolution times beyond the freeze-out period. The top axis shows q in units of $|c|$, and the vertical dashed line at $q = 2|c|$ marks the critical point, which is crossed after an evolution time t_c .

5.2.1 Measurement of Spin Populations

Figure 5.6 and Fig. 5.7 show data taken during a ramp where the field goes from 500 mG to 0 mG in 1.25 s. Since this study focuses on the scaling of the “freeze-out” time with ramp speed, data was only taken for the first 500 ms of the ramp. A given point in a plot such as Fig. 5.6 is the mean of the output of at least 10 measurements (usually more, depending on the data set). Since every measurement takes at least 20 s and there are up to 21 points per plot, it usually takes over one hour to generate a single plot like Fig. 5.6. As will be shown in the next chapter, one ramp ends up as a single point in a plot of \hat{t} or \hat{q} . That is why data was often only taken for the initial parts of the ramps, at least until the system has clearly started to evolve.

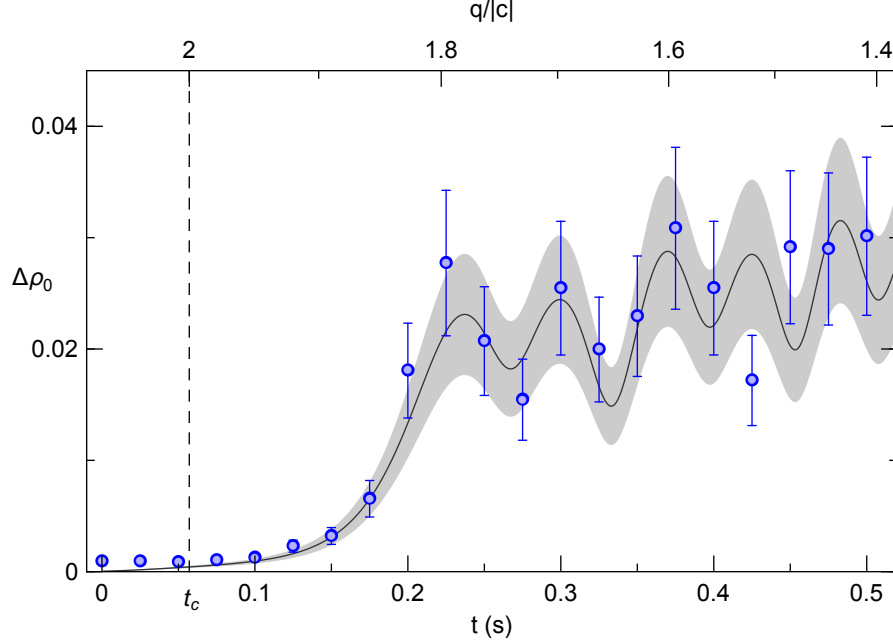


Figure 5.7: **Standard deviation of spin populations during a magnetic field ramp.** The standard deviation $\Delta\rho_0$ (blue circles) of ρ_0 in the same experimental conditions as in Fig. 5.6. $\Delta\rho_0$ agrees also agrees well with a simulation long after the critical point, marked by the vertical dashed line.

5.3 *Experimental Settings*

Measurements were performed using several settings. One of the parameters explored was the trap geometry. Most of the data used in this thesis was taken using a cross trap, but the single focus trap was also used. Even though the condensate in the single focus trap is no longer in the single mode approximation, this trap geometry provides a longer lifetime, as well as a different range of magnetic fields and dynamics. Spin domains were observed for long evolution times, but their formation took place long after the system had crossed the threshold indicating the resuming of dynamics. See Appendix B for details about the data set taken in the single focus trap.

Experimental conditions also changed somewhat between data sets. The ZnSe lens used to focus the beam from the CO₂ laser inside the chamber ended up being coated with rubidium after years of operating in rubidium vapor, to a point where

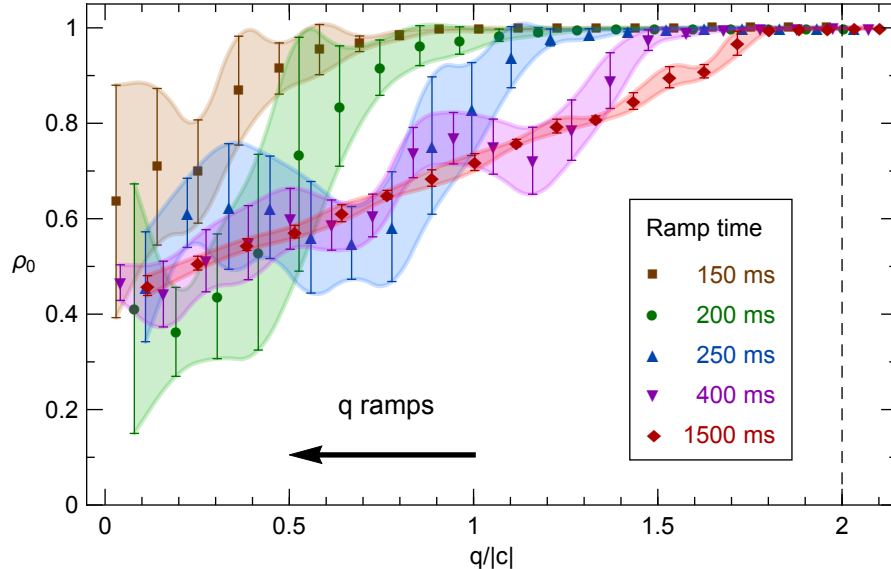


Figure 5.8: **Spin populations for several ramp times.** Measurements of ρ_0 for different ramp times t_r as a function of q . The legend shows the times t_r to ramp down the magnetic field from $q = 2.2|c|$ to $q = 0$. The longer ramps show evolution after a smaller change in q than the shorter ramps. For the latter, the system stays “frozen” in the polar ground state ($\rho_0 = 1$) until a larger change in q , as expected from the KZM. The vertical dashed line indicates the location of the critical point, and the envelopes are guides for the eye.

the intensity of the laser caused them to heat up and glow (see Appendix C). These thermal effects induced motion of the single focus trap, thus causing limitations as the overlap with the 852 nm laser beam used for the cross trap was compromised.

In parallel, the data-taking techniques were refined as our understanding of the KZM increased. While the first data sets took data for the whole ramp time, we later focused on the early part of the ramp, discarding the times beyond the beginning of evolution of the spin populations. Measuring the evolution of the system all the way through the ramp allowed us to get a good qualitative picture of the behavior of the system, but determining the KZM scaling was the main priority, so we turned our interest to shorter evolution times. This strategy motivated us to increase the time resolution of the measurements by taking data with shorter time steps, thus pinpointing the moment at which evolution started with more precision. Spending

less time taking data during the long-term evolution also allowed us to take more shots per data point in the early evolution. The spin populations at a given time have an intrinsic distribution [43] due to the quantum nature of our system, which is why taking a large number of shots for every measurement time is crucial to the validity of the study.

CHAPTER VI

RESULTS

The previous chapter described the methods used to gather the data necessary to study KZM scaling. This chapter presents the analysis of the raw data and the extraction of scaling exponents to characterize KZM scaling.

6.1 KZM Scaling

6.1.1 Determining the Beginning of Spin Dynamics

The measurements of ρ_0 during different ramp speeds through the critical point as described in the previous chapter provides the raw data we need to extract the scaling exponents. Once a precise measurement of the location of the critical point is obtained, the next step is to determine the moment when the system resumes its adiabatic evolution towards the ferromagnetic ground state after the freeze-out time [62]. The process consists of using thresholds for ρ_0 and $\Delta\rho_0$. In the case of ρ_0 , it is measured at regular intervals during the ramp, and the time when its mean drops below the threshold determines the beginning of evolution out of its initial state. The same threshold is used for every ramp. The choice of the threshold does not significantly impact the value of the scaling exponent, as long as it is not too far from the initial value of $\rho_0 = 1$ [62]. For this work, the ρ_0 threshold is $\rho_0 = 0.99$, unless indicated otherwise. The similar approach is taken with $\Delta\rho_0$, except the system is deemed to have resumed evolution once $\Delta\rho_0$ goes above the threshold. The choice of threshold is $\Delta\rho_0 = 0.005$. Comparisons of data analyzed using ρ_0 and $\Delta\rho_0$ thresholds shows no significant difference. Unless stated otherwise, the rest of this thesis will focus on the analysis of the evolution of ρ_0 .

The measurements of ρ_0 are performed at regular intervals of evolution time that

depend on the ramp length and the data set. For each ramp, the measurements are analyzed to determine the first measured time t_{under} at which the mean of ρ_0 falls below the threshold, $\rho_{0,\text{th}}$. Let t_{over} be the last measurement time before the threshold is crossed. This gives a first estimation of the time t_{th} when the system actually crosses the threshold: $t_{\text{over}} < t_{\text{th}} < t_{\text{under}}$. This estimation can be narrowed by simply performing a linear interpolation between the values of ρ_0 at t_{over} and t_{under} and finding the time corresponding to the value of ρ_0 that matches $\rho_{0,\text{th}}$. The precision with which t_{th} is determined incorporates the time step size between measurements.

In order to determine the freeze-out time \hat{t} , we also need to know the time t_c at which the system crosses the critical point. The magnetic field ramps are designed such that the quadratic Zeeman energy q changes linearly during the ramp such that

$$q(t) = q_0(1 - t/t_r). \quad (6.1)$$

Using the fact that $q(t_c) = q_c = q_z B_c^2$, where $q_z \approx 71.6 \text{ Hz/G}^2$, it is straightforward to find that

$$t_c = t_r \left(1 - \frac{q_z}{q_0} B_c^2 \right).$$

The freeze-out time $\hat{t} = t_{\text{th}} - t_c$ can now be calculated. However, this approach does not take atom loss into account. The effect of atom loss and how we model it by incorporating it into the analysis is detailed in the next section.

6.1.2 Loss Model

Since the condensates used in our experiment have limited lifetimes (2 s in the cross trap and 15 s in the single focus trap), it is essential to know how the loss of atoms affects the spin dynamics. The effect is significant for the intermediate and long ramps and must be characterized and incorporated in the data analysis for an accurate determination of the KZM scaling. Here we present a brief derivation of the expected scaling of the spinor dynamical rate $|c|$ with the total number of atoms in the BEC. This theoretical prediction is then compared with experimental data.

Within the Thomas-Fermi approximation [4], a relationship between the spinor dynamical rate c and the number of atoms can be calculated. When the kinetic energy is neglected, the density of atoms in the trap is given by

$$n_{\text{TF}}(\vec{r}) = \max \left[\left(\frac{\mu - U(\vec{r})}{c_0} \right), 0 \right], \quad (6.2)$$

where μ is the chemical potential, $U(\vec{r})$ is the trap potential, and $c_0 = 4\pi\hbar^2 a/m$ is the mean field density interaction strength. $a = (2a_2 + a_0)/3$ is an average scattering length which depends on the s-wave scattering lengths a_F for the collisions with total spin F , and m is the mass of the atom.

In a harmonic potential with frequencies ω_i ,

$$n_{\text{TF}}(\vec{r}) = \frac{15N}{8\pi\Pi_i R_i} \max \left[\left(1 - \sum_{i=1}^3 \frac{r_i^2}{R_i^2} \right), 0 \right], \quad (6.3)$$

where N is the total number of atoms and the Thomas-Fermi radii R_i are given by

$$R_i = \sqrt{\frac{2\mu}{m\omega_i^2}}. \quad (6.4)$$

Using the normalization condition $\int n(\vec{r})d^3r = N$, the chemical potential of the condensate can be calculated:

$$\mu = \left(\frac{15\hbar^2 m^{1/2}}{2^{5/2}} N \bar{\omega}^3 a \right)^{2/5}, \quad (6.5)$$

where $\bar{\omega}$ is the mean trap frequency. From Eq. (6.2), we get a peak density $n_0 = \mu/c_0$.

The value of c is determined using $c \equiv c_2 N \int |\phi(\vec{r})|^4 d^3r$, where $c_2 = \frac{4\pi\hbar^2}{3m}(a_2 - a_0)$.

Solving the integral gives

$$\int |\phi(\vec{r})|^4 d^3r = \frac{4}{7} \frac{\mu}{N c_0}. \quad (6.6)$$

The factors of N in front of and inside the integral in the expression for c cancel out, which yields

$$c = \frac{4}{7} \frac{c_2}{c_0} \mu. \quad (6.7)$$

Recall from Chapter 3 that the relative coupling strengths c_0 and c_2 only depend on the scattering lengths and the mass of the atom. In other words, the only dependence on the number of atoms N in c comes from the chemical potential μ from Eq. (6.5):

$$c = \frac{4}{7} \frac{c_2}{c_0} \left(\frac{15\hbar^2 m^{1/2}}{2^{5/2}} N \bar{\omega}^3 a \right)^{2/5}. \quad (6.8)$$

This expression yields the scaling we are interested in: $c \propto N^{2/5}$.

The next step is to test this derivation with experimental data. Using the technique described in the previous chapter, the magnetic field corresponding to the critical point is determined for different numbers of atoms in order to quantify the effect of atom loss on the spin dynamics. The spinor dynamical rate $|c|$ is calculated from the magnetic field B . Recall that the quadratic Zeeman energy q is given by $q = q_z B^2$, where $q_z \approx 71.6$ Hz/G², and that the critical point takes place at $q = q_c = 2|c|$. Figure 6.1 shows a measurement of $|c|$ vs. the number of atoms in the condensate. The inset shows the data in a log-log plot, showing a clear power law dependence. The exponent determined from a linear fit of the logarithm of the data gives 0.44(2), which is within 10% of the 0.4 exponent predicted by theory.

This relationship between the spinor dynamical rate and the number of atoms in the condensate allows us sensibly to incorporate atom loss in the data analysis. Instead of using the freeze-out time $\hat{t} = t_{\text{th}} - t_c$, which does not take atom loss into account, we use the dimensionless quantity $\tilde{q}(t) = q(t)/|c(t)|$. A measurement of the critical field at the beginning of the ramp $B_c(t = 0)$ is needed, as well as the total number of atoms $N(t)$ in the condensate throughout the ramp. The initial critical field is measured in order to know when the system crosses the critical point, and the total number of atoms is recorded every time a measurement is performed. To characterize the measurement of $N(t)$, we use a double exponential model to fit the measured total numbers of atoms:

$$N(t) = \frac{1}{2} N(0) (e^{-t/\tau_1} + e^{-t/\tau_2}). \quad (6.9)$$

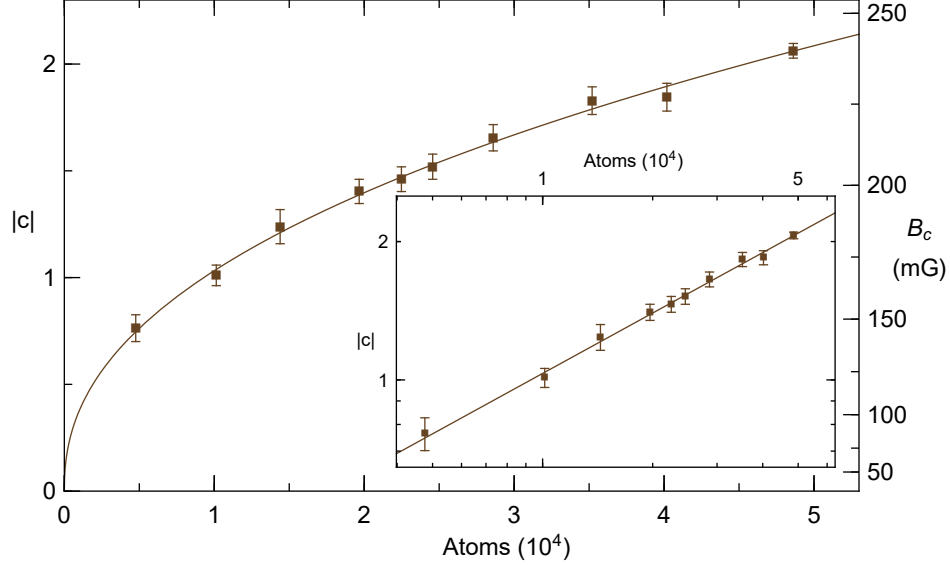


Figure 6.1: **Spinor dynamical rate $|c|$ as a function of total number of atoms.** The critical magnetic field was measured for different numbers of atoms in the condensate using the technique described in the previous chapter. The data shown was taken in the single focus trap. The right axis shows the critical magnetic field. The inset shows the data in a log-log plot, exhibiting a clear power law dependence. A linear fit of the logarithm of the data yields an exponent of $0.44(2)$, in close agreement with the $2/5$ predicted form theory.

This model fits our our data well, and an example is shown in Fig. 6.2.

Equation (6.9), with the experimentally determined values of τ_1 and τ_2 , is used to calculate the changing spinor dynamical $c(t)$ with

$$c(t) = c(0)e^{\frac{2}{5} \frac{N(t)}{N(0)}}, \quad (6.10)$$

where $c(0) = \frac{1}{2}q_z B_c^2(0)$.

The loss of atoms and the resulting shift in c has two direct consequences on the analysis. First, it changes the time at which the system crosses the critical point, since the critical field B_c is related to c by $B_c(t) = \sqrt{\frac{c(t)/2}{q_z}}$. In fact, this is the limiting factor that prevents us from using the data from the longest ramp times in the analysis. The losses shift the critical point so much that the slowest ramps are not able to reach the critical magnetic field until the very end of the ramps, at which point the evolution of the spin populations can no longer be measured.

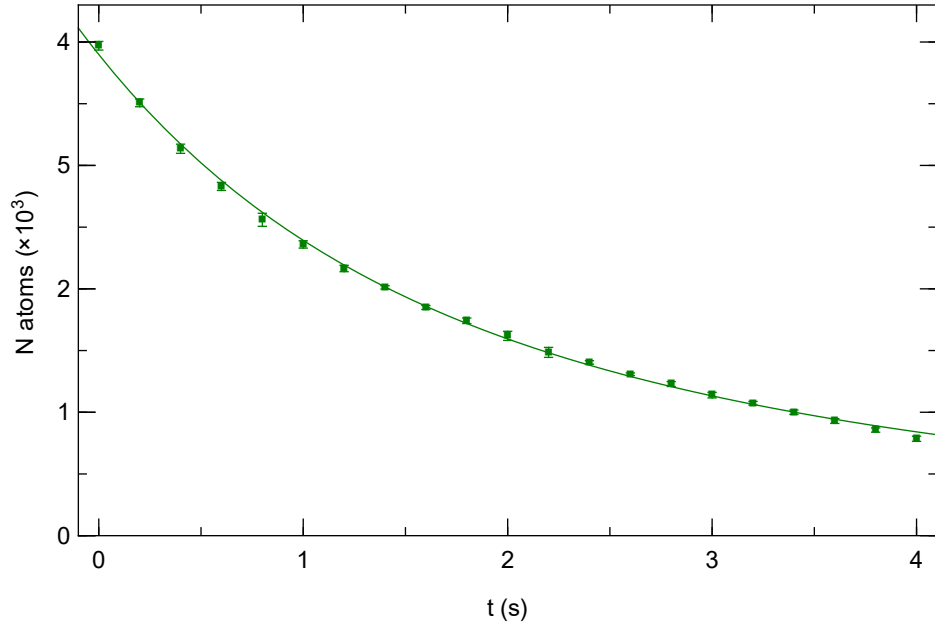


Figure 6.2: **Total number of atoms in the condensate during a magnetic field ramp.** The total number of atoms in the condensate is measured in the cross trap. The solid line shows a double exponential fit as in Eq. (6.9), yielding an initial number of atoms $N(0) = 38981(251)$, and lifetimes $\tau_1 = 1.20(3)$ and $\tau_2 = 4.32(7)$. These parameters are used to incorporate the effect of atom loss in the data analysis.

The other consequence resulting from the drift in c has to do with how fast the parameters in the Hamiltonian are evolving as the system crosses the critical point. Losses do not affect the rate of change of the magnetic field during the ramp, but since the critical field is changing due to losses, the rate of change of the ramped field relative to the drifting critical point is affected. These effects are illustrated in Fig. 6.3 and Fig. 6.4.

The KZM predicts scaling of the freeze-out period with respect to the time it takes to cross the critical point. Without atom loss, the quantity used as this time is simply the ramp time t_r from the applied ramp $q(t) = q_0(1 - t/t_r)$. We use this linear ramp in q in the experiment because it is easy to implement, but the predictions of the KZM would be equally valid in the case of a more complicated ramp shape. This holds true as long as the passage through the critical point can be linearized close to

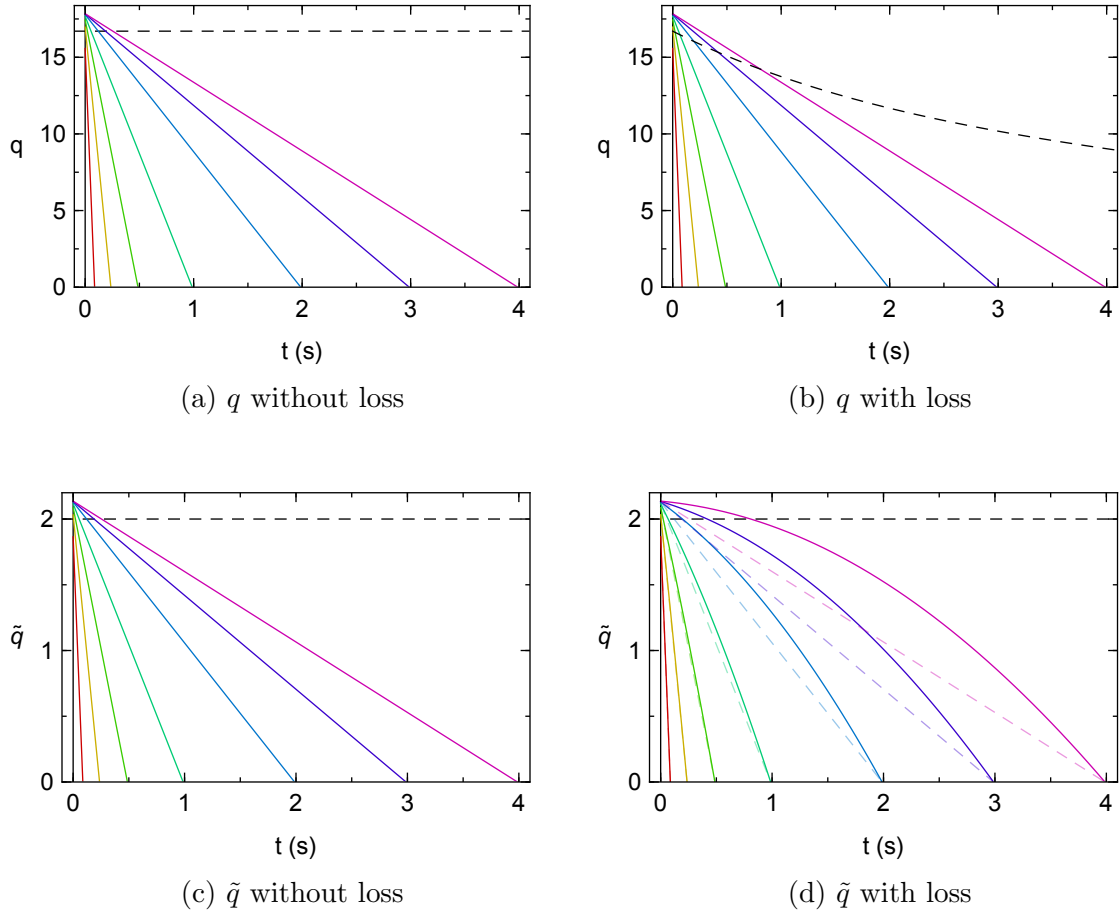


Figure 6.3: **Effect of atom loss on q and \tilde{q} .** The ramp times t_r shown are, from red (steepest) to violet: 100 ms, 250 ms, 500 ms, 1 s, 2 s, 3 s, and 4 s. Every ramp starts from 500 mG ($q \approx 17.9$ Hz and $\tilde{q} \approx 2.17$, given an initial critical magnetic field $B_c = 480$ mG). Plots (a) and (c) illustrate the loss-less case: q decreases linearly with time, as does $\tilde{q} = q/c$ since c remains constant. The horizontal dashed lines show the critical point ($q = 2|c| \approx 16.7$ Hz and $\tilde{q} = 2$). Plots (b) and (d) show q and \tilde{q} when atom loss is included in the analysis. The loss of atoms is modeled by a double exponential decay, as illustrated in Fig. 6.2. In plot (b), the q ramps remain linear, but the value of q_c corresponding to the critical point decreases with time (dashed trace), following the dropping value of $|c|$, as modeled by Eq. (6.10). In plot (d), the critical point remains at $\tilde{q} = 2$ (horizontal dashed line), regardless of the value of c , but the \tilde{q} ramps are distorted by the changing c . The faster c changes, as is the case during early evolution times, the slower the drop in \tilde{q} . Comparing the solid (with loss) and dashed (no loss) color lines in (d) clearly shows that atom loss not only delays the time at which the system crosses the critical point, but also lowers the rate of change of \tilde{q} at the critical point.

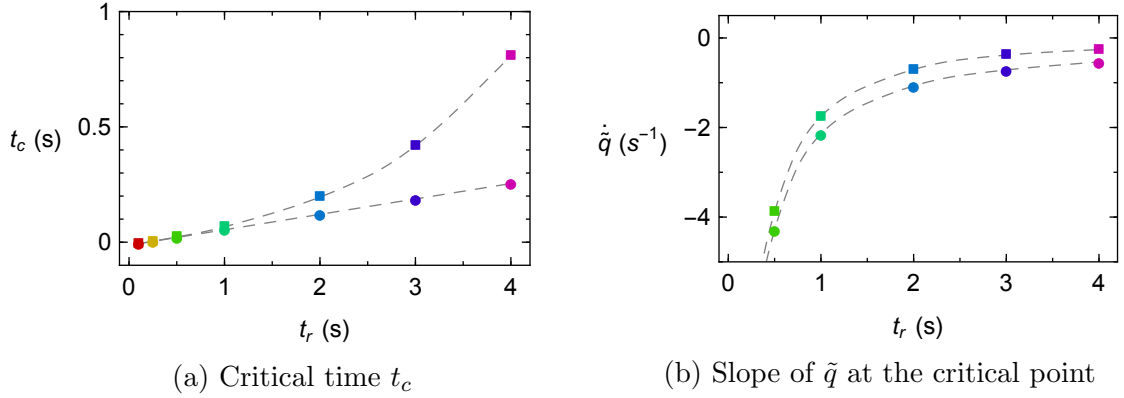


Figure 6.4: **Effect of atom loss on the critical time t_c and the rate of change of \tilde{q} at the critical point.** As in Fig. 6.3, the ramp times t_r shown are, from red to violet: 100 ms, 250 ms, 500 ms, 1 s, 2 s, 3 s, and 4 s. For both plots, the circles represent the loss-less case, and the squares show the atom loss case. The dashed lines are guides for the eye. Plot (a) illustrates the delay caused by atom loss to the time t_c at which the system crosses the critical point. Plot (b) shows how the rate of change of \tilde{q} at the critical point becomes less negative with the loss of atoms.

the transition, in which case a characteristic time τ_Q is used, such that $\tau_Q = 1/\dot{q}$ at the critical point. Due to atom loss, we cannot rely on t_r or τ_Q for the data analysis, so we need a time scale to describe how fast the system crosses the critical point. We use the rate of change of $\tilde{q} = q/|c|$ at the critical point. For each ramp, a characteristic ramp time $\tilde{\tau}_Q \equiv 1/|\dot{\tilde{q}}(t_c)|$ is calculated, where $\dot{\tilde{q}}(t) = \frac{d}{dt} \left(\frac{q(t)}{|c(t)|} \right)$.

Similarly than for \hat{t} , we can now derive an expression using \tilde{q} as a variable:

$$\hat{q} = \tilde{q}(t_c) - \tilde{q}(t_{\text{th}}) \quad (6.11)$$

where t_c and t_{th} are the times the system crosses the critical point and the assigned threshold, respectively.

6.1.3 Error Analysis

Once the effects of atom loss have been characterized and included in the data analysis, the next step is to calculate the uncertainties to use when determining the KZM scaling. The sources include the uncertainty in the determination of the time t_{th} at

which the system crosses the critical point and the uncertainty in the critical magnetic field B_c . The finite time steps taken while collecting data, as well as the finite number of measurements for a given evolution time, also contribute to the final error when determining the scaling exponents.

We will begin with the uncertainty when determining t_{th} . As described earlier in the chapter, t_{th} is found for a given ramp speed by finding between which two consecutive data points the mean of ρ_0 (or its standard deviation $\Delta\rho_0$) crosses the predetermined threshold. This first step is followed by taking a linear interpolation of the data between the two points, and finding the intersection with the threshold, which results in the value of t_{th} for the given ramp. However, measurements in our system are subject to an intrinsic uncertainty. In fact, both ρ_0 and $\Delta\rho_0$ show non-Gaussian distributions during the evolution, which were studied in [43], so accounting for this quantum noise in the analysis is essential. For every evolution time, between 10 and 20 measurements (depending on the data set) of the spin populations are performed, from which we extract the mean and standard deviations of ρ_0 . As described earlier, the mean of ρ_0 is used to find t_{th} . From the mean and standard deviation of ρ_0 we calculate $\rho_0^- = \rho_0 - \Delta\rho_0$ and $\rho_0^+ = \rho_0 + \Delta\rho_0$. The upper and lower bounds for the uncertainty in t_{th} are found by finding when ρ_0^- and ρ_0^+ cross the ρ_0 threshold. The same method as for finding t_{th} from ρ_0 is used. The error range used for the rest of the data analysis is $t_{\text{th}}^- < t_{\text{th}} < t_{\text{th}}^+$, where t_{th}^- and t_{th}^+ are the times when ρ_0^- and ρ_0^+ cross the threshold, respectively. This is illustrated graphically in Fig. 6.5. The lower bound t_{th}^- corresponds to the intersection between the red horizontal line showing the ρ_0 threshold of 0.99 and the dashed line connecting the lower ends of the error bars, which are the ρ_0^- values defined above. The same reasoning is applied to ρ_0^+ and the upper ends of the error bars in order to find t_{th}^+ .

The same method is used to find t_{th} with $\Delta\rho_0$. However, unlike for ρ_0 where the amplitude of the uncertainty was simply given by the standard deviation of the ρ_0

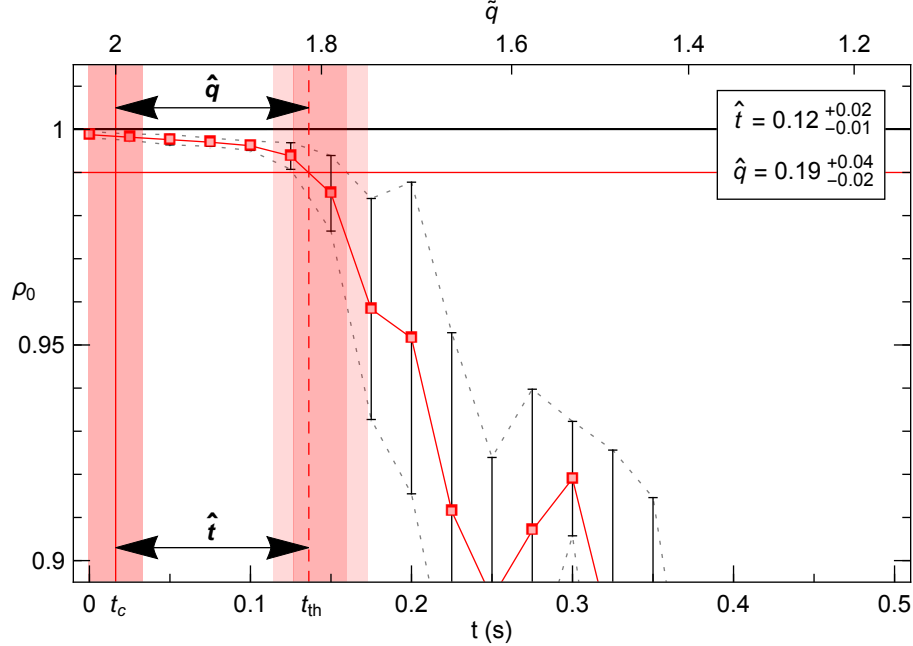


Figure 6.5: **Measurements of ρ_0 during a magnetic field ramp.** The data shown was taken during a ramp lowering the field from 500 mG to 0 mG in 1 s. Each point and its associated error bars correspond to the mean of and standard deviation of 10 measurements at a given time. The solid red line that connects the data points illustrates how the time t_{th} when ρ_0 crosses the threshold is determined. Graphically, t_{th} corresponds to the x -coordinate of the intersection between the line connecting the points and the horizontal red line, which shows the threshold of $\rho_0 = 0.99$. The time t_{th} is represented by the vertical dashed line. Similarly, the upper and lower ends of the error bars are connected by gray dashed lines. The edges of the darker shaded region around the vertical dashed line, which show the uncertainty in t_{th} , are determined by the intersection between the horizontal red line and the gray dashed lines. The lighter shaded regions show the uncertainty added by the finite time step between the measured evolution times. The vertical red line shows the time t_c of the critical point, and the shaded area is the uncertainty in its position. For this ramp, $t_c = 0.016_{-0.017}^{+0.017}$ s, $t_{\text{th}} = 0.136_{-0.022}^{+0.036}$ s, and the time step is 25 ms. This results in the values and errors of \hat{t} and \hat{q} shown in the inset.

measurements, we need a way to estimate the error in $\Delta\rho_0$ so that we can assign an uncertainty to the value of t_{th} determined using $\Delta\rho_0$. When measuring a quantity f , the fractional uncertainty for the standard deviation Δf from a sample of N measurements is given by [133]

$$\frac{\Delta(\Delta f)}{\Delta f} = \frac{1}{\sqrt{2(N-1)}}. \quad (6.12)$$

This result is applied to $\Delta\rho_0$, which gives the uncertainties shown by the error bars in Fig. 6.6. Using this method, values of t_{th} with an uncertainty can be extracted from both the mean of ρ_0 and $\Delta\rho_0$.

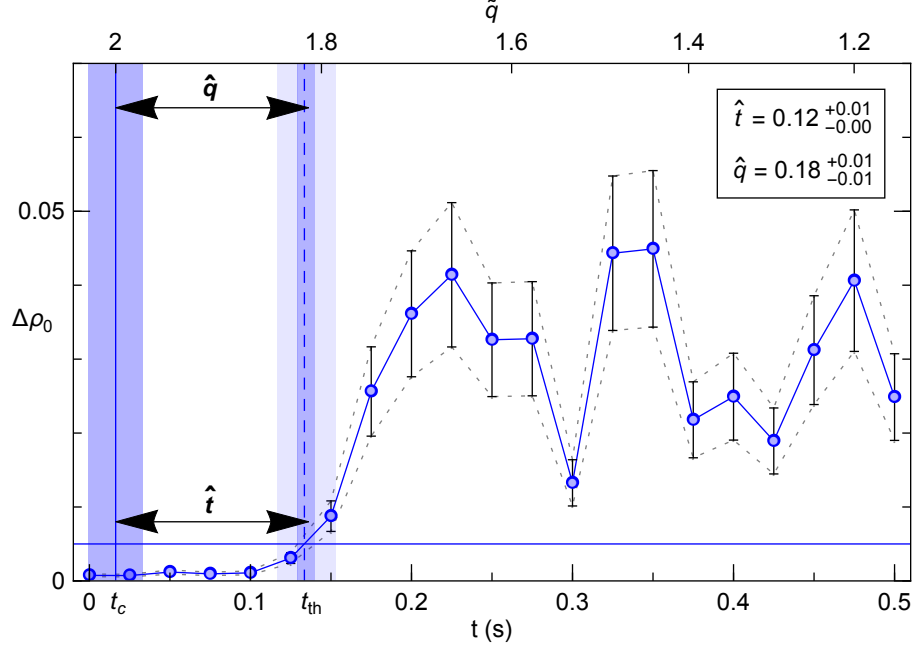


Figure 6.6: **Measurements of $\Delta\rho_0$ during a magnetic field ramp.** Similarly as in Fig. 6.5, values for \hat{t} and \hat{q} can be determined using $\Delta\rho_0$. t_c and its uncertainty are the same as when using ρ_0 , but t_{th} and its uncertainty may differ slightly. The threshold is $\Delta\rho_0 = 0.005$. The magnitude of the error bars is determined using Eq. (6.12).

Another source of uncertainty lies in the determination of the critical magnetic field B_c . As described in the previous chapter, we have a robust method for determining B_c by taking measurements after a short evolution time at constant fields around the critical field. The error on the estimation of B_c is determined by looking at the agreement between the data and simulations, using plots of both ρ_0 and $\Delta\rho_0$. Due to the finite number of measurements and experimental noise, every data point may not agree with simulations, which are performed by averaging the output of hundreds of runs. Since the simulations are performed by numerical integration, there is no analytical function to fit the data to and get an error from a fitting algorithm. Therefore, the uncertainties for B_c are estimated by visual comparison of the data with

simulations. The typical uncertainties range from 1 mG to 3 mG. Data sets where the comparison with simulations is not satisfactory to estimate B_c with a low enough error are deemed inconclusive and retaken. This uncertainty in B_c is significant; it affects how precisely the critical time t_c is known, and to a lesser extent, the rate of change of $\tilde{q} = q/|c|$ at the critical point because the initial value of $|c|$ (and its subsequent drift due to atom loss) follows directly from the initial value of B_c .

As mentioned earlier, the time step size between measurements is also taken into account when calculating the error in \hat{t} and \hat{q} . We can unequivocally determine a range for t_{th} by finding the times before and after ρ_0 crosses the threshold. However, we assign t_{th} a value by taking a linear interpolation between the data points at these two times. The real value of ρ_0 likely evolves more smoothly than the jagged solid red line in Fig. 6.5. Therefore, an uncertainty must be assigned to ρ_0 to account for this interpolation method. The time step between two consecutive measurements is used as an extra error, which will be combined with the other sources of uncertainty. The effect of adding this uncertainty is reflected in the lighter shaded regions in Fig. 6.5. The figures displaying the ρ_0 raw data as well as the extracted values of \hat{t} and \hat{q} and their respective uncertainties for every ramp of the data sets used in this thesis are shown in Appendix D.

6.1.3.1 Combining Uncertainties

The sources of uncertainty are combined to yield a total uncertainty for \hat{t} and \hat{q} . Every ramp time generates a single point that will be used to determine the scaling exponent. The fitting algorithm will be given weights to assign to each point, which depend on the associated error. This allows the outputs of the fit to reflect not only the quality of the fit itself, but also the reliability based on the error of each point.

The first step is to combine the error from t_{th} and the error due to the finite time step t_{step} . The range $t_{\text{th}}^- < t_{\text{th}} < t_{\text{th}}^+$, where t_{th}^- and t_{th}^+ are the times when ρ_0^- and ρ_0^+

cross the threshold, respectively, is widened by an amount equal to the time step for the considered ramp. This is accomplished by subtracting and adding $t_{\text{step}}/2$ to the bounds of the original error range. The combined error from the spread in ρ_0 and the finite time step results in: $t_{\text{th}}^- - t_{\text{step}}/2 < t_{\text{th}} < t_{\text{th}}^+ + t_{\text{step}}/2$. The original error range $t_{\text{th}}^- < t_{\text{th}} < t_{\text{th}}^+$ is represented by the darker shaded region around the vertical dashed line in Fig. 6.5. The lighter shaded area corresponds to the widening caused by the finite time step uncertainty. Note that the errors $\Delta t_{\text{th}}^- = t_{\text{th}} - (t_{\text{th}}^- - t_{\text{step}}/2)$ and $\Delta t_{\text{th}}^+ = (t_{\text{th}}^+ + t_{\text{step}}/2) - t_{\text{th}}$ are not necessarily equal, since t_{th}^- and t_{th}^+ are determined from the errors in ρ_0 , which can vary significantly throughout a ramp. In Fig. 6.5, for example, the shaded area to the left of the vertical dashed line (indicating t_{th}) is narrower than the one to the right. This is due to the changing magnitude of the error bars from point to point. In the case of Fig. 6.5, the error bars grow larger as ρ_0 drops under the threshold, which results in a larger uncertainty to the right of t_{th} .

The uncertainty ΔB_c found when determining the critical magnetic field B_c is incorporated in the error for t_c , which is the time at which the system crosses the critical point. This error is calculated by determining the times t_c^- and t_c^+ at which the system would cross the critical point if the critical magnetic field were $B_c^+ = B_c + \Delta B_c$ or $B_c^- = B_c - \Delta B_c$, respectively. Note that a higher critical magnetic field will make the system cross the critical point sooner in the ramp, which is why t_c^- corresponds to B_c^+ and vice versa, with $t_c^- < t_c^+$. These times t_c^- and t_c^+ form the bounds of the uncertainty range for t_c . Note that, as in the determination of t_c , atom loss is incorporated, since it delays the crossing of the critical point, as illustrated in Fig. 6.4a. In addition, due to the exponential nature of the decay of the total number of atoms in the condensate, the number of atoms lost between t_c^- and t_c and the number of atoms lost between t_c and t_c^+ will not be the same, thus creating a small imbalance between $\Delta t_c^- = t_c - t_c^-$ and $\Delta t_c^+ = t_c^+ - t_c$. This uncertainty in t_c is represented by the shaded area around the solid vertical line in Fig. 6.5. The difference

in the width of the shading to the left and right of the line is subtle and not noticeable in Fig. 6.5, but it is non-negligible in longer ramps and always taken into account when calculating the total uncertainty in \hat{t} and \hat{q} . The same method is used for the analysis with $\Delta\rho_0$, and the uncertainty ranges are displayed by the blue shaded areas in Fig. 6.6.

The errors Δt_{th} and Δt_c are then added in quadrature to get the total error in \hat{t} :

$$\Delta\hat{t}^+ = \sqrt{(\Delta t_{\text{th}}^+)^2 + (\Delta t_c^+)^2} \quad (6.13)$$

and

$$\Delta\hat{t}^- = \sqrt{(\Delta t_{\text{th}}^-)^2 + (\Delta t_c^-)^2}. \quad (6.14)$$

These errors will become vertical error bars when \hat{t} is plotted against the characteristic ramp time $\tilde{\tau}_Q$. We must now turn our attention to $\tilde{\tau}_Q$ and determine how to incorporate uncertainties if needed. Recall that $\tilde{\tau}_Q$ is the inverse of the rate of change of \tilde{q} evaluated at the time then the system crosses the critical point: $\tilde{\tau}_Q = 1/|\dot{\tilde{q}}(t_c)|$, where $\tilde{q}(t) = q(t)/|c(t)|$. This means that $\tilde{\tau}_Q$ will be impacted by the uncertainties in t_c , which follow from the uncertainties in B_c . The error in $\tilde{\tau}_Q$ is extracted from the values $\tilde{\tau}_Q^-$ and $\tilde{\tau}_Q^+$ that come from calculations using B_c^- and B_c^+ as the critical magnetic field. The errors in $\tilde{\tau}_Q$ are thus $\Delta\tilde{\tau}_Q^- = \tilde{\tau}_Q - \tilde{\tau}_Q^-$ and $\Delta\tilde{\tau}_Q^+ = \tilde{\tau}_Q^+ - \tilde{\tau}_Q$. Once again, $\Delta\tilde{\tau}_Q^-$ and $\Delta\tilde{\tau}_Q^+$ are slightly different. These errors will result in horizontal error bars when plotting \hat{t} against $\tilde{\tau}_Q$.

The methods described above give error estimations for \hat{t} , but we are also interested in \hat{q} , since it incorporates atom loss by including the changing spinor dynamical rate c . Recall that $\hat{q} = \tilde{q}_c - \tilde{q}_{\text{th}}$, where $\tilde{q}_c = q(t_c)/|c(t_c)|$ and $\tilde{q}_{\text{th}} = q(t_{\text{th}})/|c(t_{\text{th}})|$. The errors in t_{th} and t_c calculated earlier will be reflected in the error for \hat{q} , but one can not get the error in \hat{q} simply by converting the total \hat{t} error. Instead, the uncertainty in \tilde{q} is calculated step by step from the bounds of the error ranges for the relevant times. For example, to find the uncertainty in the value of \tilde{q} as ρ_0 crosses the threshold, we

consider $\tilde{q}_{\text{th}}^+ = \tilde{q}(t_{\text{th}}^-)$ and $\tilde{q}_{\text{th}}^- = \tilde{q}(t_{\text{th}}^+)$. Note the changing sign in the upper index, which is due to the decreasing nature of \tilde{q} with time. Switching the plus and minus signs ensures that $\tilde{q}_{\text{th}}^- < \tilde{q}_{\text{th}} < \tilde{q}_{\text{th}}^+$. Consequently, the errors for \tilde{q}_{th} are $\Delta\tilde{q}_{\text{th}}^- = \tilde{q}_{\text{th}} - \tilde{q}_{\text{th}}^-$ and $\Delta\tilde{q}_{\text{th}}^+ = \tilde{q}_{\text{th}}^+ - \tilde{q}_{\text{th}}$.

Similarly, an uncertainty can be assigned to \tilde{q}_c , which is the value of \tilde{q} at the critical point. By definition, $\tilde{q}_c = q(t_c)/|c(t_c)| = 2$. However, the uncertainty in t_c , which follows from the error in determining B_c , propagates an uncertainty in \tilde{q}_c . This uncertainty is determined by calculating $\tilde{q}_c^- = \tilde{q}(t_c^+)$ and $\tilde{q}_c^+ = \tilde{q}(t_c^-)$, where t_c^- and t_c^+ have been defined earlier. Once again, the plus and minus signs are exchanged in the upper indices. It follows that the errors for \tilde{q}_c are $\Delta\tilde{q}_c^- = \tilde{q}_c - \tilde{q}_c^-$ and $\Delta\tilde{q}_c^+ = \tilde{q}_c^+ - \tilde{q}_c$. Similarly as for \hat{t} , the errors for \tilde{q}_{th} and \tilde{q}_c are added in quadrature, resulting in a global uncertainties for \hat{q} :

$$\Delta\hat{q}^+ = \sqrt{(\Delta\tilde{q}_{\text{th}}^+)^2 + (\Delta\tilde{q}_c^+)^2} \quad (6.15)$$

and

$$\Delta\hat{q}^- = \sqrt{(\Delta\tilde{q}_{\text{th}}^-)^2 + (\Delta\tilde{q}_c^-)^2}. \quad (6.16)$$

With the values and uncertainties in \hat{t} , \hat{q} , and $\tilde{\tau}_Q$ now well defined, the determination of the scaling exponent characterizing the KZM scaling is now possible.

6.1.4 Extraction of Scaling Exponents

In order to determine the scaling exponents characterizing the KZM scaling, \hat{t} and \hat{q} are plotted against $\tilde{\tau}_Q$, and the scaling exponents are extracted from fits to the data. The data was originally fitted to a power law function:

$$\hat{t} = A \times (\tilde{\tau}_Q)^B \quad (6.17)$$

where A and B are fitting parameters. This method is biased to the large values of \hat{t} and \hat{q} , however, which becomes evident when plotting the data and the line

corresponding to the power law fit and visually examining the quality of the fit. To remove this bias, the scaling exponents are determined by fitting the logarithm of the data to a linear function:

$$\log_{10} \hat{t} = A' + B' \log_{10}(\tilde{\tau}_Q) \quad (6.18)$$

where A' and B' are the fitting parameters. Note that A' corresponds to $\log_{10} A$, and B' should be equal to B , but due to the discrepancy in the fitting methods, that is not necessarily the case. Linear fitting the logarithm of the data treats all points in the plot more evenly than when fitting the data to a power law. Calculating the logarithm of the data is trivial, but converting the uncertainties is a slightly more involved process, as one cannot simply take the logarithm of the magnitude of the error bars. This approach is particularly vulnerable to small errors, as it yields negative uncertainties when the error is less than 1. Therefore, another method was used, which is summarized as follows: for a data point (x_0, y_0) , where the uncertainties in x_0 are Δx_0^- and Δx_0^+ and the uncertainties in y_0 are Δy_0^- and Δy_0^+ , the errors in $\log_{10}(x_0)$ will be

$$\Delta(\log_{10}(x_0))^- = \log_{10}(x_0) - \log_{10}(x_0 - \Delta x_0^-) \quad (6.19)$$

and

$$\Delta(\log_{10}(x_0))^+ = \log_{10}(x_0 + \Delta x_0^+) - \log_{10}(x_0). \quad (6.20)$$

The same process is applied to y_0 . These calculations are necessary to display the uncertainties as error bars in the log-log plot and to determine the weights assigned to each point for the linear fits of the logarithm of the data. The fits are performed in Mathematica[®], and a weight given by $1/\Delta f_i^2$ is applied to each point, where each measurement f_i has an uncertainty Δf_i . The best fit is found using the Broyden-Fletcher-Goldfarb-Shanno (BFGS) algorithm [134].

6.1.4.1 Data Sets

The data used in this thesis was gathered in four separate data-taking sessions ranging from January 2014 to December 2014, resulting in four distinct data sets. Each data set uses the same concept of magnetic field ramps that decrease q linearly through the critical point, as described in Chapter 5. While all data sets give the same qualitative results, some changes in the details of how the data was taken yield some differences, which are analyzed and compared with simulations in the following chapter. The experimental settings of each data set are listed in Table 6.1.

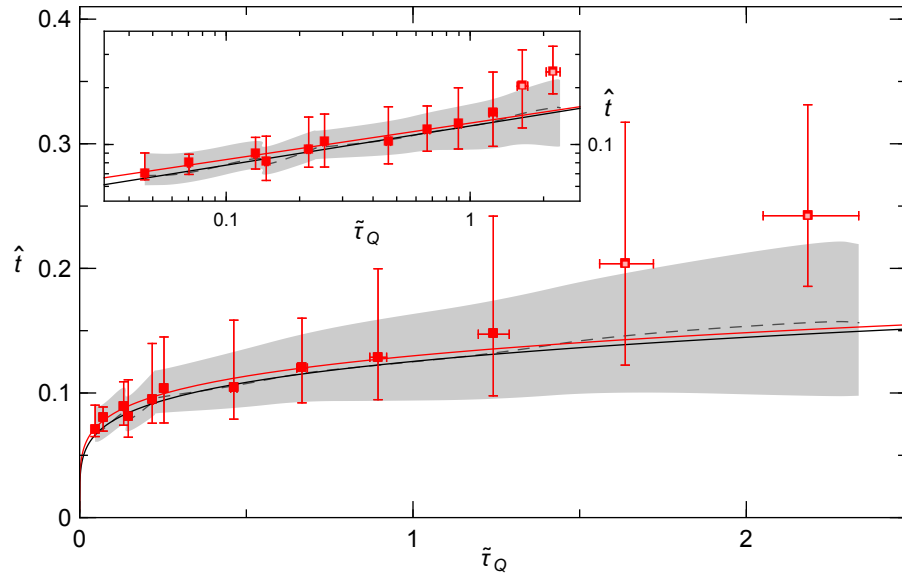
Table 6.1: **Data sets.** This table describes the conditions in which the data used in this thesis was acquired.

	Date	Trap Geometry	Comments
1	January 2014	Cross trap	Data taken for whole ramps
2	March 2014	Cross trap	Data focusing on initial part of ramps
3	November 2014	Cross trap	Longer lifetime and higher resolution than data sets #1 and #2
4	December 2014	Single focus trap	Very long lifetime with slower dynamics

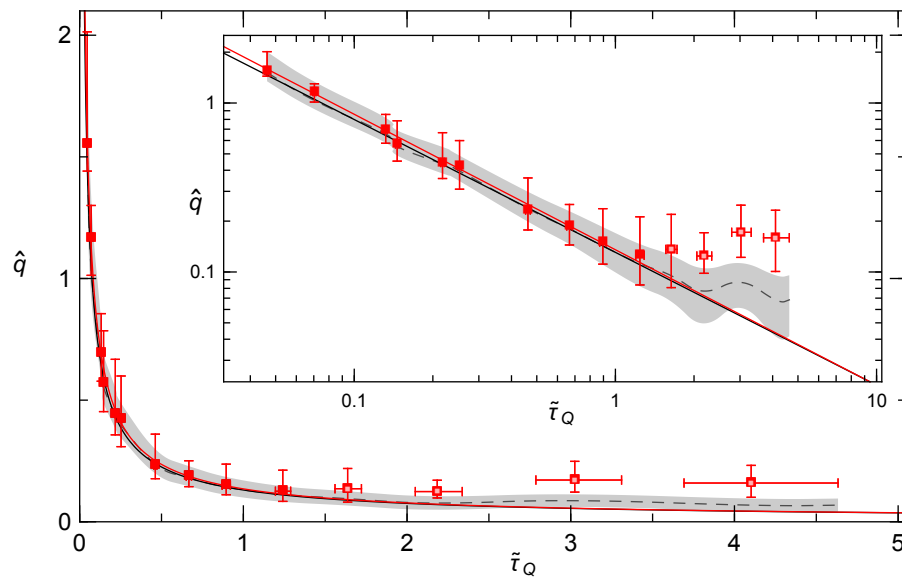
The first three data sets used a cross trap geometry, for which the size of the condensate is smaller than the spin healing length, therefore preventing spin domains. However, the data set #4 was taken in a single focus trap. Unlike in the cross trap, a condensate in this cigar-shaped trap is no longer in the single mode approximation, and the formation of spin domains is energetically allowed. A detailed description and analysis of the methods and results from data set #4 is presented in Appendix B.

The results for data set #2, as well as the fits and comparison with simulations, are shown in Fig. 6.7 and Fig. 6.8. For every data point, a simulation is performed with the same experimental parameters (ramp time, number of atoms, and initial value of c) and their corresponding errors, calculated in an identical way as the data.

The simulations generate values of \hat{t} and \hat{q} , as well as their errors. The points

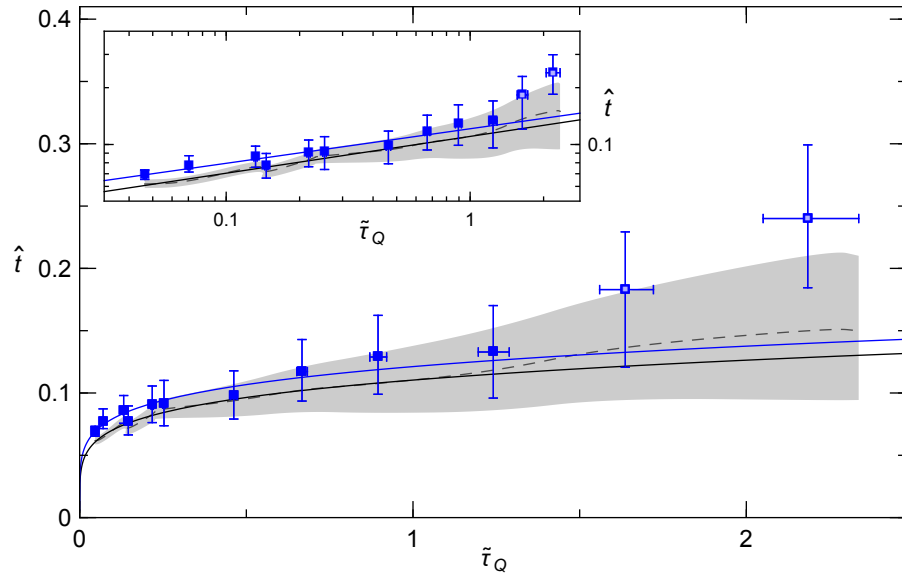


(a) Scaling exponents: data: 0.18(7), simulations: 0.20(7).

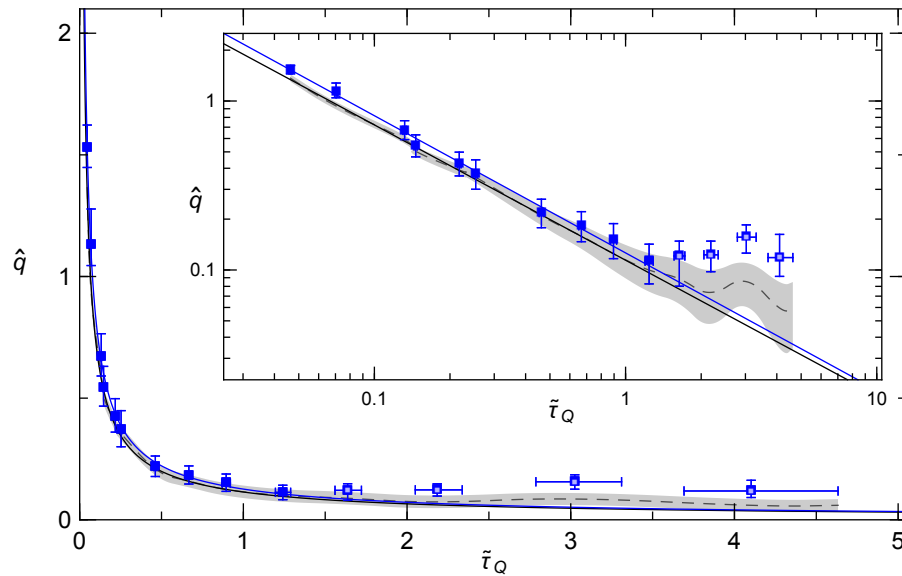


(b) Scaling exponents: data: $-0.80(8)$, simulations: $-0.79(7)$.

Figure 6.7: **Plots of \hat{t} and \hat{q} generated using ρ_0 (data set #2).** Fit range: $0.048 < \tilde{\tau}_Q < 1.24$.



(a) Scaling exponents: data: 0.17(4), simulations: 0.19(4).



(b) Scaling exponents: data: $-0.81(4)$, simulations: $-0.80(3)$.

Figure 6.8: Plots of \hat{t} and \hat{q} generated using $\Delta\rho_0$ (data set #2). Fit range: $0.048 < \tilde{\tau}_Q < 1.24$.

corresponding to the outputs of each simulation are not shown — instead, the simulations are plotted by interpolating between points as a gray dashed line, with a grey envelope displaying the uncertainty. The insets show the data and simulations plotted in a log-log plot. The power law fits are represented by the color and black solid lines for the data and simulations, respectively.

Table 6.2: **Summary of scaling exponents determined using ρ_0 .**

(a) Summary of \hat{t} scaling exponents			(b) Summary of \hat{q} scaling exponents		
Data set	Data	Simulation	Data set	Data	Simulation
1	0.29(9)	0.32(7)	1	-0.70(9)	-0.66(7)
2	0.19(8)	0.21(7)	2	-0.80(8)	-0.79(7)
3	0.25(11)	0.32(8)	3	-0.75(11)	-0.67(8)
4	0.19(10)	0.27(6)	4	-0.80(10)	-0.72(6)

Table 6.3: **Summary of scaling exponents determined using $\Delta\rho_0$.**

(a) Summary of \hat{t} scaling exponents			(b) Summary of \hat{q} scaling exponents		
Data set	Data	Simulation	Data set	Data	Simulation
1	0.29(6)	0.25(3)	1	-0.70(6)	-0.73(3)
2	0.18(4)	0.20(3)	2	-0.81(4)	-0.80(3)
3	0.22(6)	0.28(3)	3	-0.77(6)	-0.71(3)
4	0.20(5)	0.27(3)	4	-0.80(5)	-0.73(2)

The data clearly deviate from a power law fit at large $\tilde{\tau}_Q$. The causes of this discrepancy are likely due to the large number of atoms lost from the trap by the time the system reaches the critical point during the longest ramps. The limits of the loss model used in the data analysis is explored in the following chapter by using loss-less simulations. The fit is performed using only the linear region of the data, indicated by solid markers, where the effect of losses is limited; the points represented by empty markers are excluded from the fit. The results from the fits for all of the four data sets studied for this thesis are summarized in Table 6.2 and Table 6.3. For better comparison of the different data sets, the exponents are also combined and displayed in Fig. 6.9 and Fig. 6.10. The \hat{t} and \hat{q} plots for all the data sets can be

found in Appendix D.

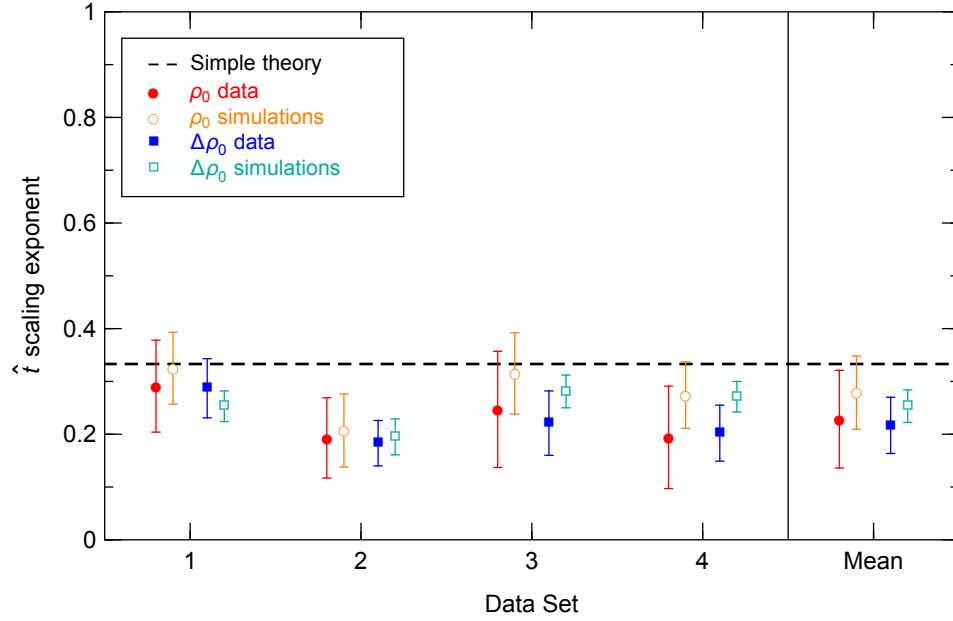


Figure 6.9: **Summary of \hat{t} exponents.** The dotted horizontal line represents the scaling exponent of $1/3$ predicted by the KZM.

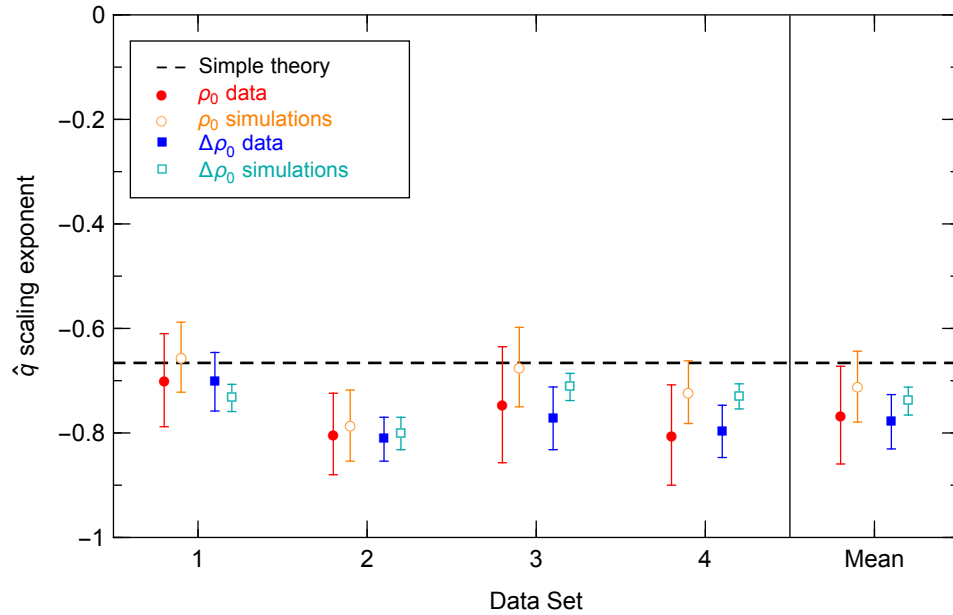


Figure 6.10: **Summary of \hat{q} exponents.** The dotted horizontal line represents the scaling exponent of $-2/3$ predicted by the KZM.

The results show the anticipated power law scaling, except for the slowest ramps which tend to deviate from the power law behavior. The scaling exponents differ slightly from the predictions of the KZM, but they agree well with simulations performed using the experimental parameters.

6.2 Concluding Remarks

In this chapter we presented the analysis of our data and the determination of scaling exponents for \hat{t} and \hat{q} . The loss model used to incorporate the effect of limited trap lifetimes was presented, and the steps of the error analysis were described. In the following chapter, we will use simulations to explain the discrepancy between the results and the KZM prediction, and also explore a wider range of parameters that are inaccessible experimentally.

CHAPTER VII

COMPARISON WITH SIMULATIONS

In the previous chapter, we determined scaling exponents from our experimental data. Recall from Chapter 2 that the KZM predicts the following scaling for our system:

$$\hat{t} \sim \tilde{\tau}_Q^{\frac{\nu z}{1+\nu z}} \sim \tilde{\tau}_Q^{1/3} \quad \text{and} \quad \hat{q} \sim \tilde{\tau}_Q^{\frac{-1}{1+\nu z}} \sim \tilde{\tau}_Q^{-2/3}, \quad (7.1)$$

where $\tilde{\tau}_Q$ is the inverse of the rate of change of \tilde{q} at the critical point, and the critical exponents $\nu = 1/2$ and $z = 1$ have been used.

The scaling exponents for \hat{t} listed in Tables 6.2 and 6.3 are slightly smaller than the value of $1/3$ that the simple theory predicts, both for the data and the simulations performed in same conditions as the experiment. Similarly, the scaling exponents for \hat{q} are slightly more negative than the predicted exponent of $-2/3$. In this chapter, we use simulations to explore the causes for the discrepancies between our data and theory, which are mostly due to the finite lifetime of the condensate. This finite lifetime limits the ability to investigate asymptotically long ramps and also prevents starting the ramps at a very high magnetic field; both of these limitations give rise to the observed discrepancy of the measured (and simulated) scaling exponents as compared to the KZM model. The presence of impurities in the form of unwanted pairs of $m_F = \pm 1$ atoms in the initial state is also explored.

7.1 *Simulations*

The data is compared with mean field and quantum dynamical simulations. The mean field simulations are performed by numerically integrating the equations of motion of the order parameter $\psi = (\zeta_1, \zeta_0, \zeta_{-1})^T$. These three coupled differential equations were derived in Chapter 3 and are shown in Eq. (3.21). However, our initial state is

the polar ground state, where all the atoms are in the $m_F = 0$ energy level. This state does not evolve according to these equations, even in the ferromagnetic phase where the state is a hyperbolic fixed point. The evolution seen experimentally is due to quantum fluctuations.

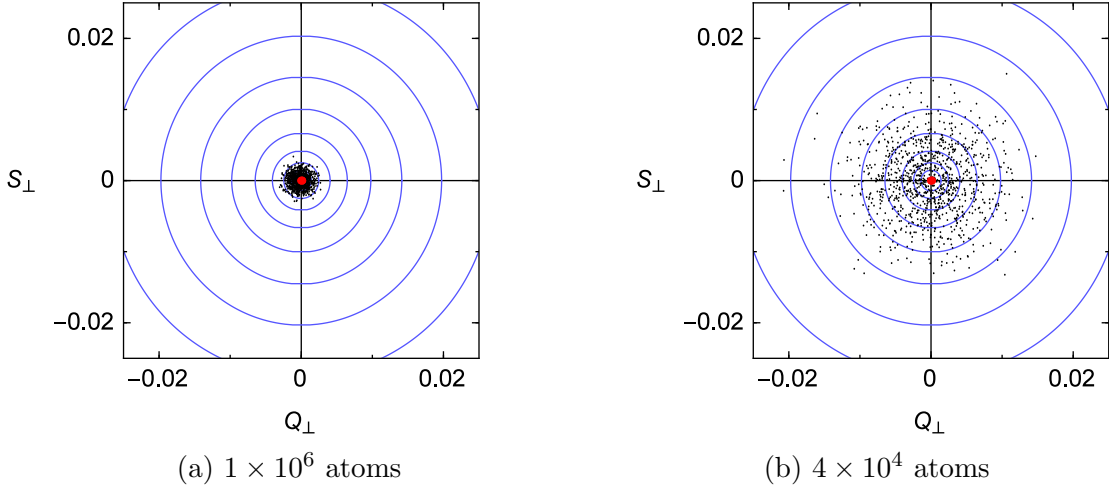


Figure 7.1: **Initial distributions of states in the polar phase space.** The semi-classical simulations are initialized with 1000 samples, randomly chosen with the constraint that S_x and Q_{yz} have Gaussian probability distributions. In general, the initial distributions of S_\perp and Q_\perp are not Gaussian, but for this simulation, S_y and Q_{xz} are initially set to zero, therefore resulting in Gaussian distributions in S_\perp and Q_\perp . The standard deviation of the Gaussian distributions is set by the standard quantum limit (SQL), calculated from the initial number of atoms N by $\text{SQL} = 1/\sqrt{N}$. The distributions shown are for (a) 1×10^6 atoms, and (b) 4×10^4 atoms (as in the experiment), which explains the different spreads. The system is initialized in the polar phase at $B = 2G \gg B_c$, so all the energy contours (blue lines) are phase winding. The energies of the contours are arbitrarily chosen, but are the same for both figures. The red dot shows the location of the ground state.

In order to account for these quantum fluctuations in the mean field picture, a quasi-probability distribution is generated from the quantum noise of the initial Fock state $|0, N, 0\rangle$ [33]. This type of simulation using mean field dynamical equations along with an initial distribution mimicking quantum fluctuations is referred to as semi-classical. The effect of the initial number of atoms on the initial distribution of states is illustrated in Fig. 7.1.

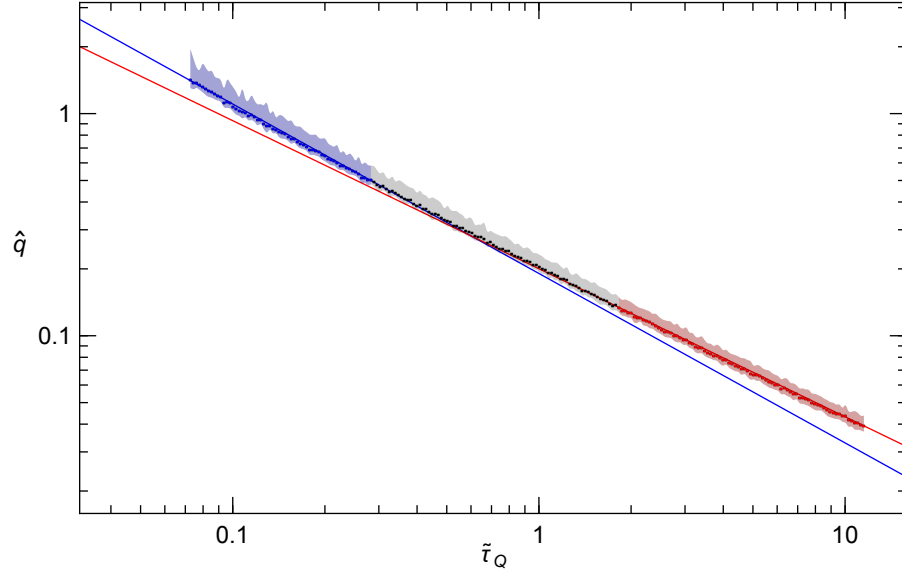
In the context of this study, this initial distribution essentially corresponds to a set of states slightly perturbed from the polar ground state. The quadratic Zeeman energy q is a parameter in the mean field equations of motion, so implementing a linear ramp in q , as in the experiment, is trivial. In order to account for atom loss, the spinor dynamical rate c is updated with the number of atoms in the condensate such that $c \propto N^{2/5}$, as derived in Chapter 6. The model can also be simulated by using the quantum Hamiltonian in the Fock basis, resulting in the same dynamics. More details about the simulations and the generation of the quasi-probability distribution can be found in Refs. [33, 41].

7.1.1 Loss-Less Simulations

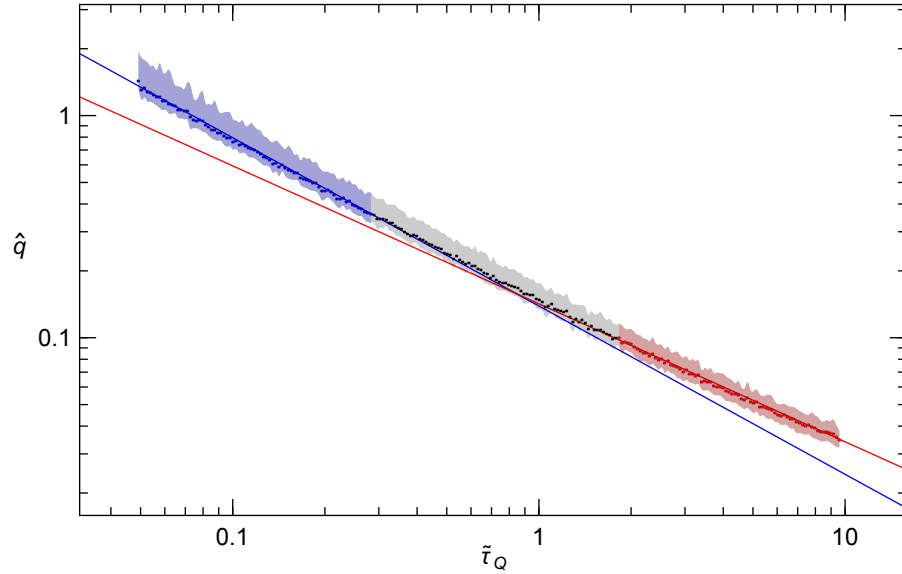
7.1.1.1 Simulations in Ideal Conditions

We begin by presenting simulations performed in ideal conditions: infinite condensate lifetime, allowing asymptotically long ramps, and ramps starting at a magnetic field much higher than the critical magnetic field. These ideal conditions provide a benchmark from which we will attempt to recover the scaling exponents predicted by the KZM.

We simulate ramps starting at a higher magnetic field (1 G) than in the experiment (500 mG), with a range of ramp times reaching well beyond the longest ramps used in the experiment. The dynamics of a condensate initialized with 1×10^6 atoms are compared with a condensate with 4×10^4 atoms (as in the experiment) in Fig. 7.2. The trace in Fig. 7.2a shows \hat{q} for the larger number of atoms, and Fig. 7.2b illustrates the effect of the lower number. Even though the plots show a slight curvature, good quality power law fits can be performed in different ranges of ramp speeds. The range of slow ramps shown in red in Fig. 7.2a satisfies the asymptotic settings used to derive the KZM scaling: slow ramps starting from a high magnetic field with a large number of atoms. In these ideal conditions, the scaling exponent extracted from simulations matches the value of $-2/3$ predicted by the KZM, which was also found



(a) 1×10^6 atoms



(b) 4×10^4 atoms

Figure 7.2: **Loss-less simulations starting from a high magnetic field.** The ramps start from $8.7|c|$ (1 G), which is much higher than the critical point, as compared to the experiment. A fit of the faster ramps (blue) with $0.05 < \tilde{\tau}_Q < 0.28$ gives a scaling exponents of $-0.76(5)$ for (a) and $-0.76(4)$ for (b). The slowest ramps (red) with $\tilde{\tau}_Q > 1.83$ yield scaling exponents of $-0.67(2)$ for (a) and $-0.62(3)$ for (b).

using numerics by Damski and Zurek in Ref. [62].

The reason the faster ramps deviate slightly from the KZM is the following: the derivation of scaling exponents described earlier assumes that the system is close to the critical point, which is where the universal critical exponents in the expressions for the energy gap appear. In our case, we approximate the energy gap Δ in the ferromagnetic phase ($q < q_c$) by

$$\Delta = \sqrt{q_c^2 - q^2} \approx \sqrt{2q_c(q_c - q)}, \quad (7.2)$$

and in the polar phase ($q > q_c$) by

$$\Delta = 2\sqrt{q(q - q_c)} \approx 2\sqrt{q_c(q - q_c)}. \quad (7.3)$$

These approximations are only valid when $q \approx q_c$. This means that for the derivation of the scaling exponents to be valid, the system must be driven slow enough such that the dynamics cease and resume their adiabatic evolution where the energy gap approximation is appropriate. As mentioned earlier, the limited trap lifetimes in our system prevent us from performing asymptotically long ramps.

A comparison of simulations with numbers of atoms ranging over three orders of magnitude is also shown in Fig. 7.3. There is no appreciable difference in the slopes of the four traces in the plot. In fact, the scaling exponents in Table 7.1 reveal that there is no significant difference within fitting errors.

From Fig. 7.2 and Fig. 7.3, we conclude that the scaling exponent is insensitive to atom numbers ranging from 10^4 to 10^7 , but the exact $\hat{q} \sim \tilde{\tau}_Q^{-\frac{1}{1+\nu z}} \sim \tilde{\tau}_Q^{-2/3}$ predicted from the KZM is only obtained with very slow ramps.

7.1.1.2 *Similar Ramps as in the Experiment*

The experiment begins with a condensate prepared at 2 G ($q = 17.3q_c$), which guarantees that all the atoms are in the polar ground state. Ideally, the magnetic field would be slowly ramped down from this high value through the critical point.

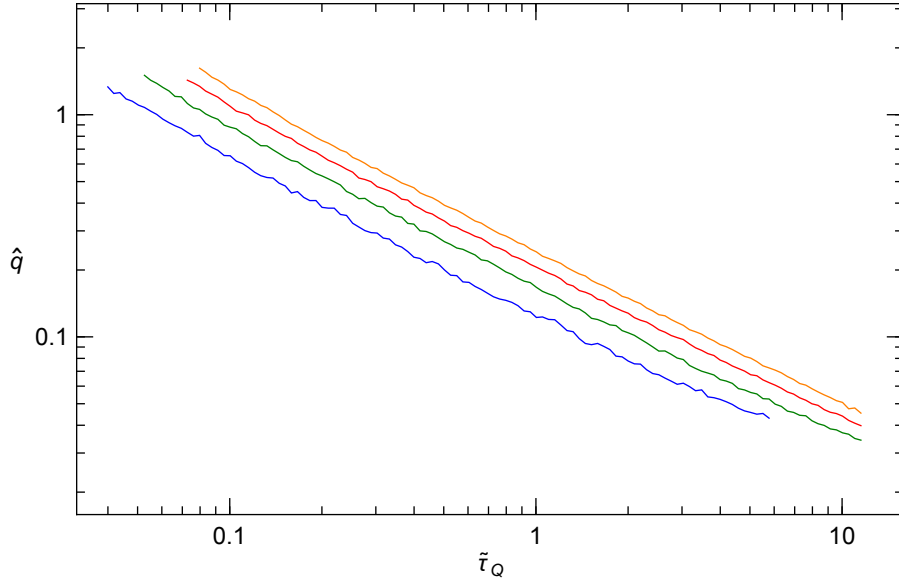


Figure 7.3: **Effect of different numbers of atoms (no loss)**. Loss-less semi-classical simulation where the ramps begin at 1 G for a critical magnetic field $B_c = 480$ mG for different numbers of atoms. The numbers of atoms shown are 10^4 (blue, bottom), 10^5 (green), 10^6 (red), and 10^7 (orange, top). For a given $\tilde{\tau}_Q$, \hat{q} will be smaller for a smaller number of atoms. This is consistent with the larger SQL for smaller numbers of atoms, resulting in a wider initial distribution (see Fig. 7.1). This will shorten the freeze-out time, thus decreasing the change in \tilde{q} before ρ_0 reaches its threshold of 0.99.

Table 7.1: **Effect of number of atoms with ramps starting at a high magnetic field (no loss)**. This table summarizes the scaling exponents for \hat{q} extracted from fits of the traces in Fig. 7.3. The range of the fit is $0.08 < \tilde{\tau}_Q < 0.40$. The ramps start at 1 G, and the ρ_0 threshold is 0.99.

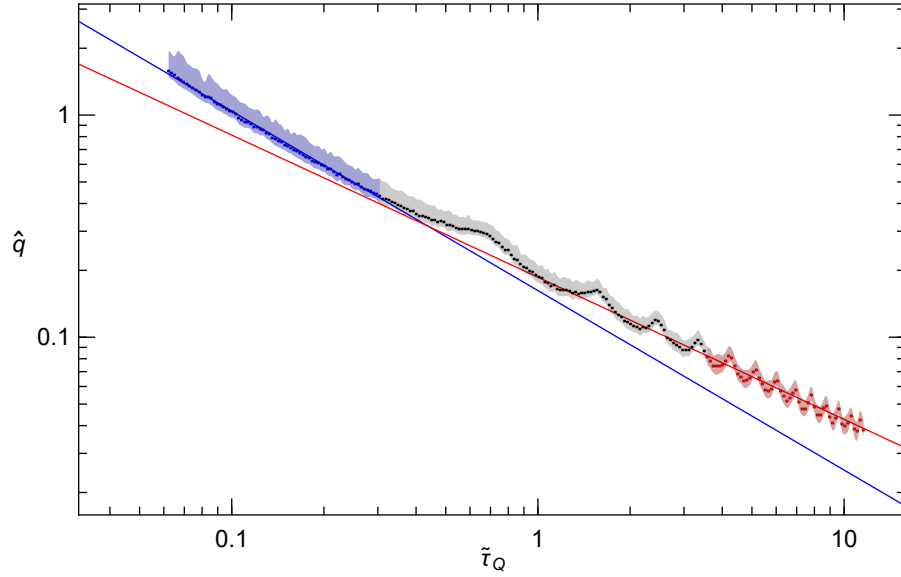
Number of atoms	Scaling exponent for \hat{q}
10^7	-0.76(3)
10^6	-0.75(4)
10^5	-0.74(5)
10^4	-0.73(7)

However, the limited trap lifetimes also set a limit regarding how high we can start the magnetic field ramps. Ideally, one would want to start a ramp at a field where the spin interactions are completely dominated by the quadratic Zeeman energy term from the Hamiltonian, and slowly ramp the magnetic field down towards the critical

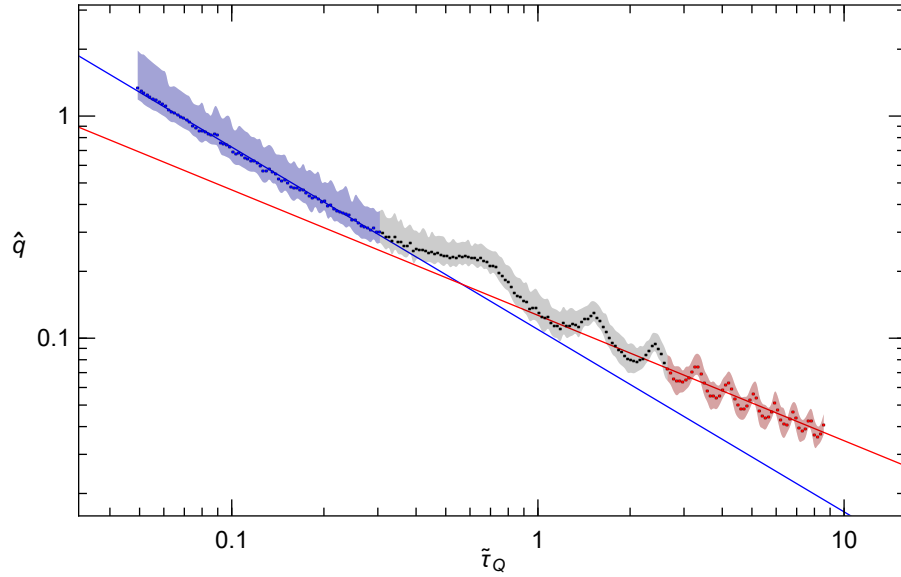
point. The magnetic field where we prepare the system in the polar ground state essentially suppresses any spin dynamics. However, if we were to lower the field using linear ramps in q starting from that value, we would be constrained to using ramps that reach the critical point without significant losses, which would result in a fast rate of change of the field at the critical point. In the lab, a compromise is reached by starting with a fast drop from 2 G to a value close to the critical field (see Fig. 5.4), but still sufficiently above it so as to prevent any spin-mixing dynamics.

Figure 7.4a shows a loss-less simulation using a large number of atoms (1×10^6) and a similar initial quench as in the experiment. The faster ramps show a clear power law dependence in \hat{q} , followed by an oscillatory behavior as the ramp times increase. When the number of atoms is reduced to 4×10^4 , as in the experiment, the oscillations are still present, and their amplitude is somewhat increased, as shown in Fig. 7.4b. For the faster ramps, corresponding to the regions plotted in blue in Fig. 7.4, the scaling exponents are $-0.81(3)$ for 1×10^6 atoms and $-0.82(4)$ for 4×10^4 atoms, confirming that the number of atoms has no effect in the range studied in the experiment.

The oscillations in Fig. 7.4 are caused by the 2 ms fast quench that lowers the magnetic field from 2 G to 500 mG. Even though 500 mG is higher than the critical field of 480 mG and the system is still in the polar phase, the energy contours in the spin-nematic phase space around the polar ground state suddenly change from circles to ellipses, as illustrated in Fig. 7.5. Before the quench, the initial distribution that corresponds to a slightly perturbed polar ground state is circularly symmetric and precesses around the ground state on the high field circular energy contours, as seen in Fig. 7.5a. Following the initial fast quench, the energy contours become ellipses, shown in Fig. 7.5b. As the initially circular distribution precesses around the ground state, its shape morphs back and forth from circular to elliptical until crossing the critical point and reaching the transition to the ferromagnetic phase. The ground



(a) 1×10^6 atoms



(b) 4×10^4 atoms

Figure 7.4: **Loss-less simulations.** The ramps start from 500 mG after a fast 2 ms drop from 2 G, as in the experiment. (a) is run with a large number of atoms (10^6), while the atom number is set at the same value as the experiment (4×10^4) in (b). The fits of the linear region (blue) with $0.06 < \tilde{\tau}_Q < 0.31$ gives a scaling exponent of $-0.81(3)$ for (a) and $-0.82(4)$ for (b). A fit for the slower ramps (red) for (a) gives an exponent of $-0.64(3)$ for $\tilde{\tau}_Q > 3.58$. For (b), the fit yields an exponent of $-0.56(5)$ with $\tilde{\tau}_Q > 2.65$.

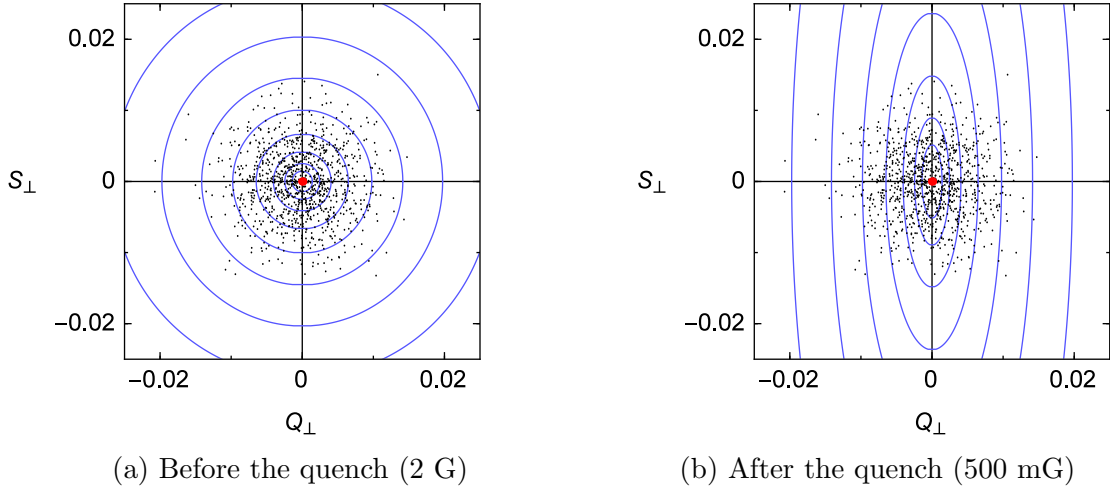


Figure 7.5: **Initial distributions of states and energy contours before and after the initial quench.** These figures illustrate the effect of the 2 ms quench on the energy contours in the polar phase space. The distribution is identical to the one shown in Fig. 7.1. The figures shows energy contours at magnetic fields of 2 G (a) and 500 mG (b). The critical magnetic field is 480 mG.

state, which lay on the pole of the spin-nematic sphere in the polar phase, drifts down the (degenerate) sides of the sphere along the S_{\perp} axis, which happens to be the major axis of the elliptical energy contours around the polar ground state. The reaction time of the system depends on the shape and orientation of the distribution as the system enters the ferromagnetic phase.

At that time, the top pole of the spin-nematic sphere is a hyperbolic fixed point. As illustrated in Fig. 7.6, a separatrix (green) marks the boundary between the closed orbits (red) and the phase-winding orbits (blue). A state situated in the vicinity of the separatrix will evolve parallel to it, clockwise around the ground state. This means that states in the neighborhood of the pole will tend to evolve towards or away from it, depending in which quadrant of the polar phase they are located. The quadrants where S_{\perp} and Q_{\perp} have the same sign contain the converging branch of the separatrix, while the other two quadrants contain the diverging branch.

If the distribution is in a stretched elliptical shape aligned along the diverging branch of the separatrix, as in Fig. 7.6a, most states in the distribution will be able

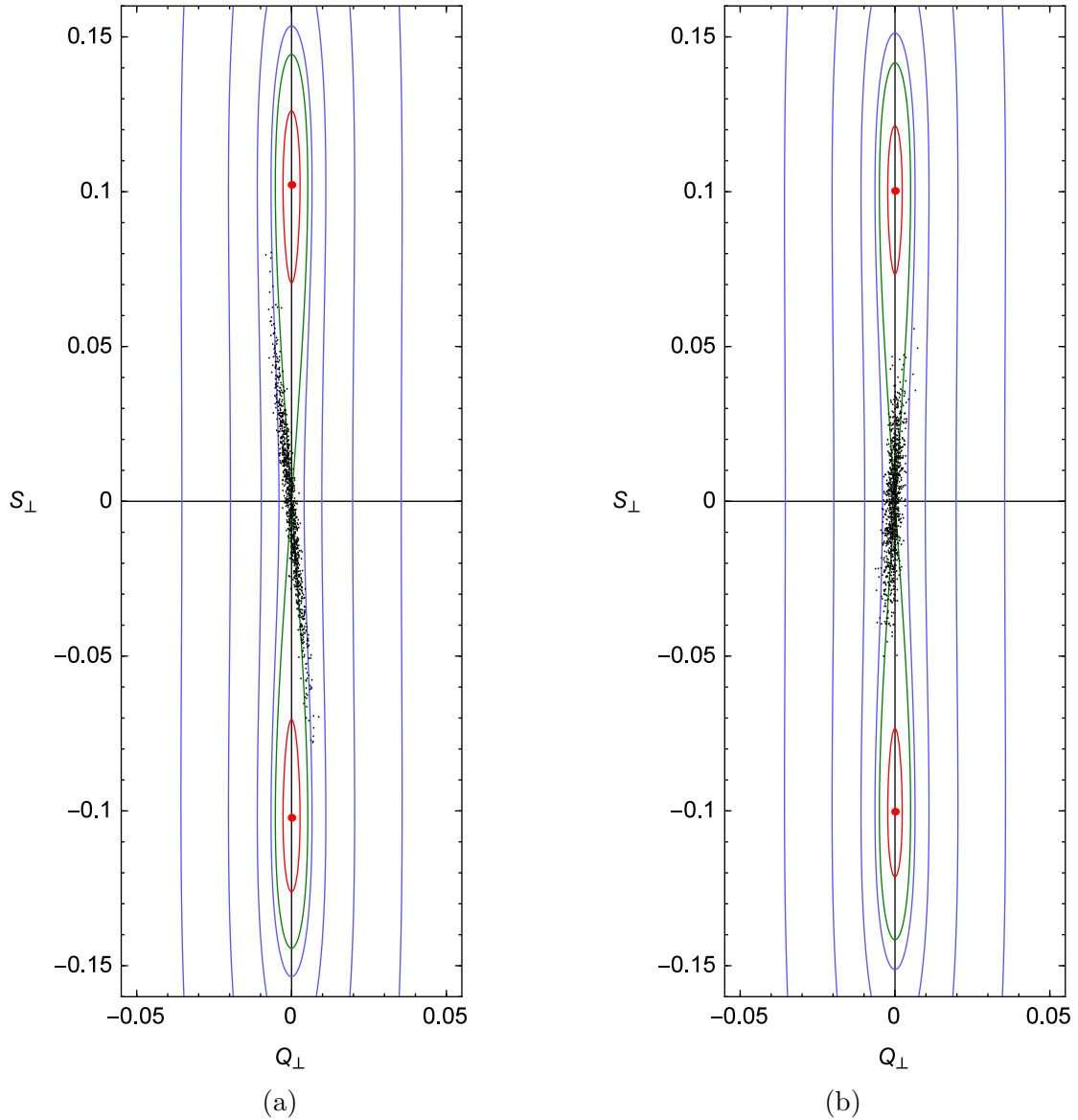


Figure 7.6: **Polar phase space right after the critical point ($\tilde{q} = 1.99$).** The polar phase space shows the separatrix in green, the phase winding contours in blue, and a red closed orbit, centered around the ground state represented by a red dot. The black dots represent 1000 samples initialized with a Gaussian distribution (for 4×10^4 atoms) around the pole, as in Fig. 7.1b. (a) shows the distribution during a 1.66 s ramp from 500 mG to 0 mG, and (b) during a 2 s ramp. Due to the precession of the distribution on the elliptical phase winding energy contours above the critical point, the distribution will be aligned along the diverging arm of the separatrix in (a), and the converging arm in (b) as the system crosses the critical point. This results in oscillations in the \hat{q} plots for ramps beginning at $\tilde{q} = 2.2$, as in Fig. 7.4.

to follow energy contours leading away from the pole, shortening the mean reaction time of the system. However, if the distribution is in a circular shape, or as an ellipse aligned with the converging branch of the separatrix at the critical time, as illustrated in Fig. 7.6b, most states will be evolving around energy contours bringing them back to the pole and away from the ferromagnetic ground state, thus delaying the evolution and increasing the freeze-out time.

The peaks of the oscillations in the \hat{q} plots indicate a larger delay between the time the system crosses the critical point and the time it reaches the ρ_0 threshold. They correspond to the ramps where the distribution was aligned with the converging branch of the separatrix. Conversely, the dips correspond to the ramps where the distribution was stretched and aligned along the diverging branch of the separatrix right after the critical point. These oscillations are present in both Fig. 7.4a and Fig. 7.4b, with a slightly smaller amplitude for the larger numbers of atoms.

As shown earlier, starting the ramps at a higher magnetic field eliminates the oscillations in the \hat{q} plots, which are only observed when the ramps start at the same field as the experiment. The comparison of both cases in a single plot is shown in Fig. 7.7, which reveals that despite the lack of oscillations for the ramps starting at 1 G, the traces seem to observe a similar asymptotic behavior for the longest ramps shown. Nevertheless, the left side of the plot, which is linear for both simulations, shows that the scaling exponent is less negative for the ramps starting at higher fields. The fits from Fig. 7.2b and Fig. 7.4b for the faster ramps were $-0.76(4)$ and $-0.82(4)$, respectively, and while the ramps starting at a higher field give a less negative scaling exponent than when starting at a lower field, it is still more negative than the $-2/3$ exponent from theory. The exponents extracted for different initial magnetic fields are included in Table 7.2.

Table 7.2: **Summary of exponents from loss-less simulations.** This table summarizes the scaling exponents for \hat{q} extracted from fits of loss-less simulations.

Initial ramp field	Number of atoms	Fast ramps	Slow ramps
1 G	1×10^6	-0.76(4)	-0.67(2)
1 G	4×10^4	-0.76(4)	-0.62(4)
0.5 G	1×10^6	-0.81(3)	-0.64(3)
0.5 G	4×10^4	-0.82(4)	-0.56(5)

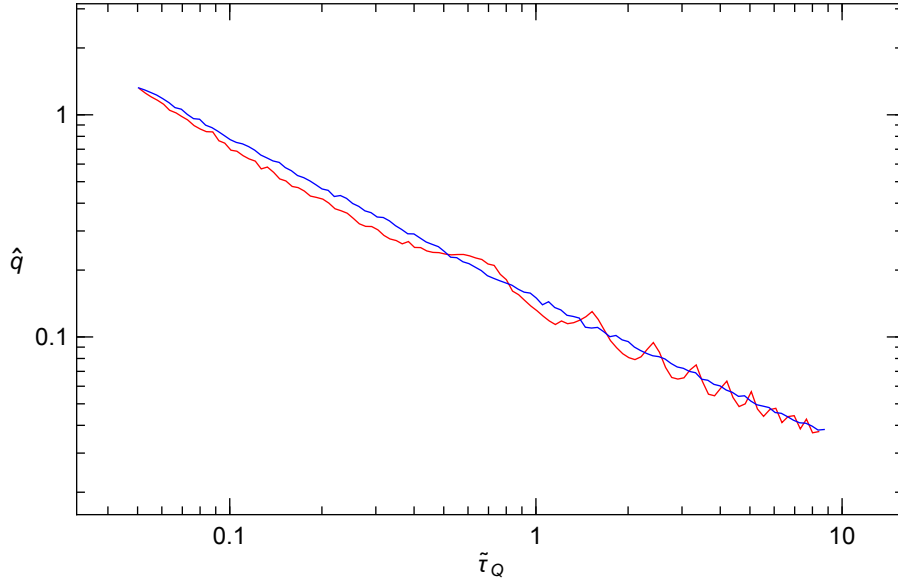
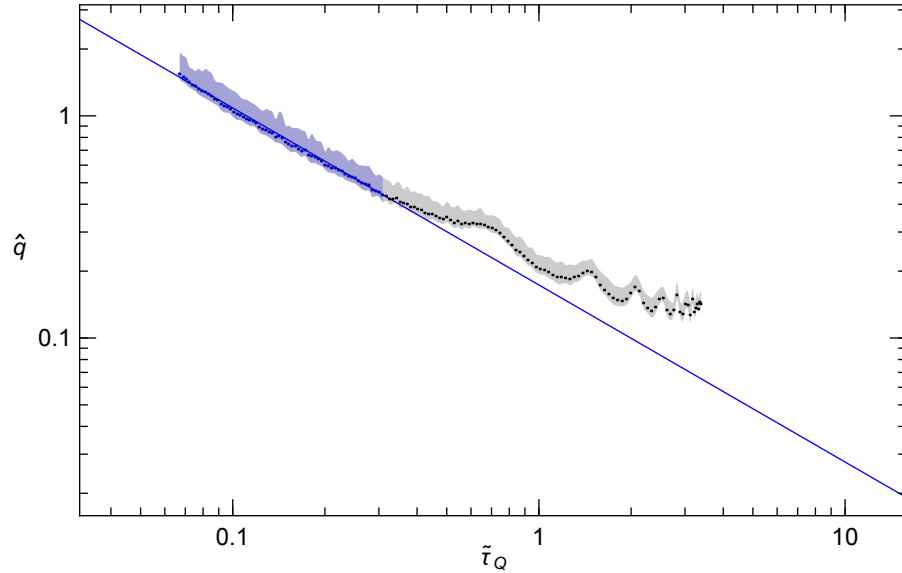


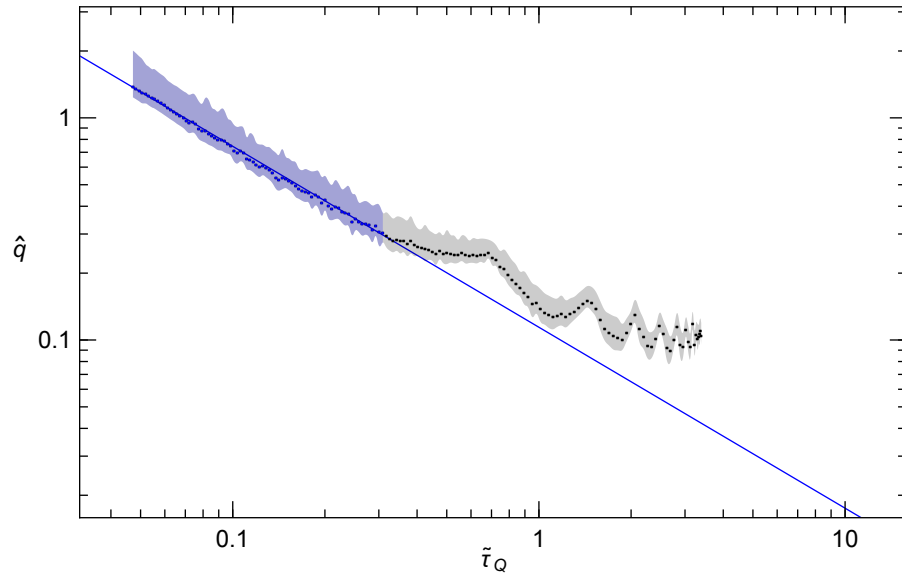
Figure 7.7: **Effect of ramp initial magnetic field (no loss).** In this loss-less semi-classical simulation with 4×10^4 atoms, the ramps that begin at 500 mG as in the experiment result in the red trace, while the ramps that start at 1 G are shown by the blue trace. In both cases, the critical magnetic field $B_c = 480$ mG, and the threshold for ρ_0 is 0.99. This plot shows the overlap of the simulations plotted in Fig. 7.2b and Fig. 7.4b.

7.1.2 Simulations Including Atom Loss

The loss model we use, which was detailed in the previous chapter, shows good agreement with measurements of the critical magnetic field for a large range of numbers of atoms, as shown in Fig. 6.1. However, despite clear power law fits shown by the data for the short ramps, the values of both \hat{t} and \hat{q} depart from the power law for the slowest ramps.



(a) 1×10^6 atoms



(b) 4×10^4 atoms

Figure 7.8: **Simulations including atoms loss.** (a) Simulation with 1×10^6 atoms. (b) Similarly as in the experiment, the initial number of atoms is 4×10^4 atoms. Fits of the linear region (blue) with $0.05 < \tilde{\tau}_Q < 0.31$ give scaling exponents of $-0.80(3)$ and $-0.81(4)$ for (a) and (b), respectively.

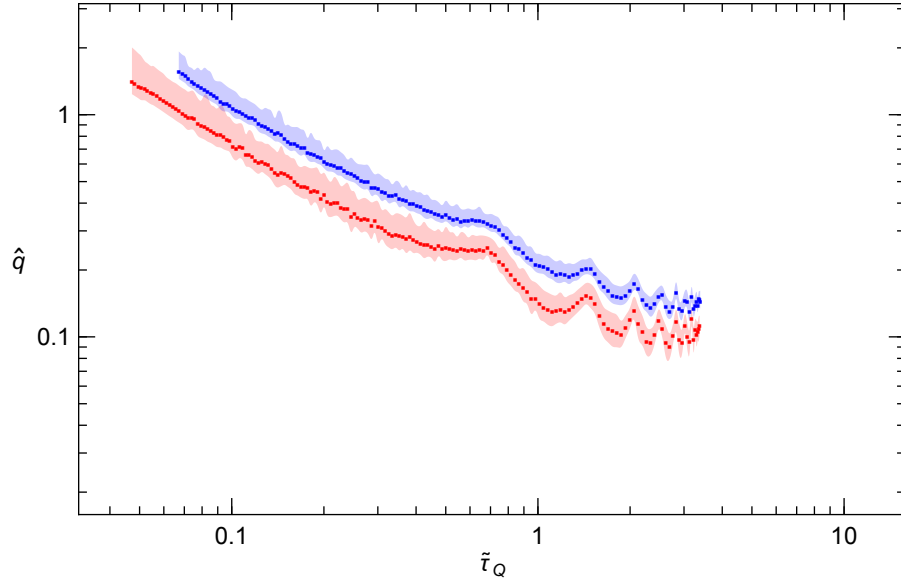


Figure 7.9: **Effect of different numbers of atoms (with loss)**. In this semiclassical simulation with atom loss where the ramps begin at 500 mG for a critical magnetic field $B_c = 480$ mG, \hat{q} is plotted against $\tilde{\tau}_Q$ for different numbers of atoms. The numbers of atoms shown are 4×10^4 (red, bottom) and 10^6 (blue, top). The shaded regions show \pm one standard deviation. The threshold for ρ_0 is 0.99. This figure combines the two plots from Fig. 7.8.

When atom loss is included for simulations, the number of atoms is modeled using a double exponential $N(t) = \frac{N(0)}{2}(e^{-t/\tau_1} + e^{-t/\tau_2})$, with lifetimes determined from the typical behavior of our experiment. When simulating the conditions in the cross trap, the lifetimes are $\tau_1 = 1$ s and $\tau_2 = 4.5$ s. In the single focus trap, which has a much longer lifetime, we use $\tau_1 = 15$ s and $\tau_2 = 30$ s. The effect of atom loss is included in the analysis by changing the spinor dynamical rate c , in the same fashion as for the data analysis. Unless specified otherwise, the threshold used to determine the return to the adiabatic regime is $\rho_0 = 0.99$, and the ramp times t_r range from 100 ms to 5 s. For ramps longer than 5 s, the number of atoms lost by the time the system crosses the critical point is too large to draw meaningful conclusions.

In order to emulate the behavior of our experiment, the simulations use the same magnetic field ramps as for the data. The linear q ramps start from 500 mG given a

critical magnetic field $B_c = 480$ mG, following a fast drop from 2 G. Unlike the lossless simulations presented earlier in this chapter, we are constrained by limited trap lifetimes, which means we cannot initialize the ramps at higher magnetic fields than the experiment or test very slow ramps, but one parameter that can be investigated despite atom loss is the initial number of atoms in the condensate. Simulations with atom loss for 1×10^6 and 4×10^4 atoms are shown in Fig. 7.8. The plot combining the data from Fig. 7.8a and Fig. 7.8b can be seen in Fig. 7.9. The key point from the simulations that include atom loss is that despite the offset between the two traces shown in Fig. 7.9, the higher number of atoms does not change the scaling exponents for \hat{q} beyond the fit errors when fitting the same range of parameters used in the analysis of the data.

Table 7.3: **Effect of number of atoms on scaling exponents (with loss).** This table summarizes the scaling exponents for \hat{q} extracted from fits of the traces in Fig. 7.8. The range of the fit is $0.05 < \tilde{\tau}_Q < 0.31$. The ramps start at 500 mG, and the ρ_0 threshold is 0.99.

Number of atoms	Scaling exponent for \hat{q}
1×10^6	-0.80(3)
4×10^4	-0.81(4)

A comparison of simulations with and without atom loss is illustrated in Fig. 7.10. The loss of atoms results in an upper limit for $\tilde{\tau}_Q$. Despite this limitation, the linear parts of the traces in Fig. 7.10 show good overlap in the range of faster ramps, thus confirming the validity of the loss model up to an intermediate number of lost atoms. The scaling exponents from the fits of the linear regions are shown in Table 7.4.

7.1.3 Comparison of Semi-Classical and Quantum Simulations

The simulations presented so far were semi-classical, using the mean field dynamical equations along with an initial distribution of states that mimics the quantum fluctuations due to the finite number of atoms. Semi-classical simulations are used instead

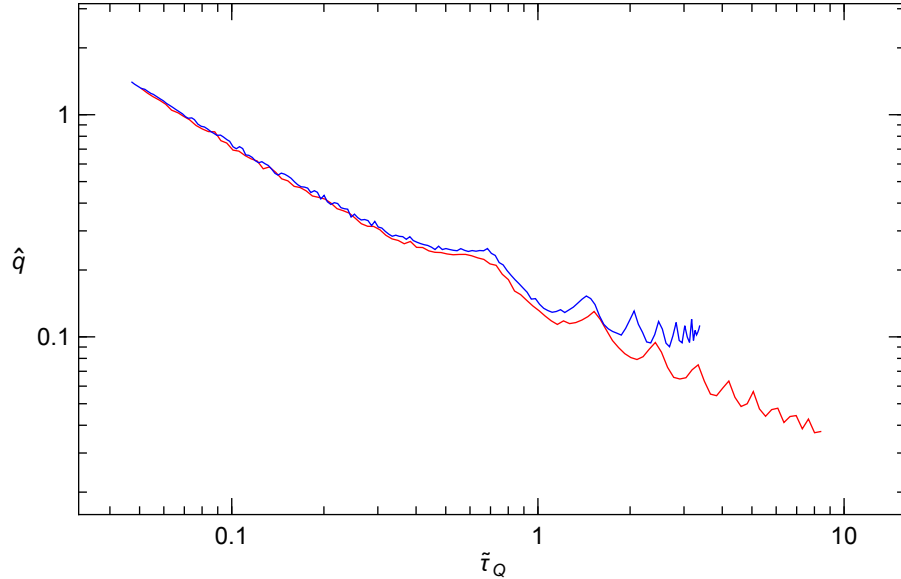


Figure 7.10: **Effect of atom loss.** The effect of atom loss is tested using semi-classical simulations with 4×10^4 atoms and ramps starting at 500 mG, with a critical magnetic field set at $B_c = 480$ mG. The red line shows the loss-less case, and the blue line represents the simulation with loss. This plot combines the simulations from Fig. 7.4b and Fig. 7.8b, and the resulting scaling exponents are in Table 7.4..

Table 7.4: **Effect of atom loss on scaling exponents.** This table summarizes the scaling exponents for \hat{q} extracted from fits of the traces in Fig. 7.4b and Fig. 7.8b. The range of the fit is $0.06 < \tilde{\tau}_Q < 0.31$. The number of atoms is 4×10^4 , and the initial ramp magnetic field is 500 mG, given a critical magnetic field of 480 mG. The overlap of the traces yielding these scaling exponents are shown in Fig. 7.10.

	Without loss	With loss
\hat{q} scaling exponent	-0.82(4)	-0.81(4)

of quantum simulations simply because the former are orders of magnitude faster to run, even though the use of graphics processing units (GPUs), recently implemented by fellow lab member Matthew Boguslawski, is helping to narrow the speed difference between the two methods.

One may question the validity of using semi-classical simulations over quantum simulations for the following reason. The KZM theory insists on the fact that the energy gap between the ground state and the first excited state vanishes at the critical

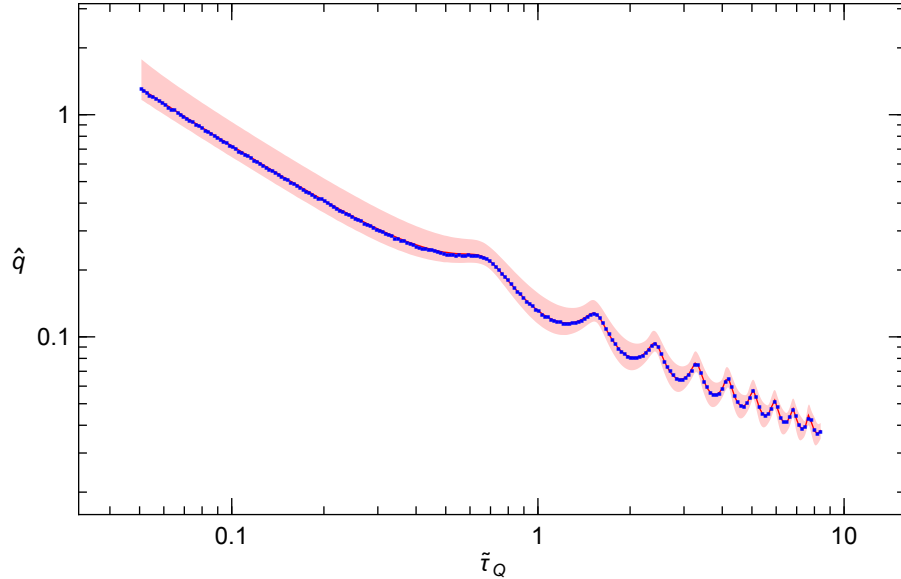


Figure 7.11: **Comparison of semi-classical and quantum simulations.** The outputs from loss-less semi-classical and quantum simulations for 4×10^4 atoms are compared. The ramps start at 500 mG, with a critical magnetic field set at $B_c = 480$ mG, which explains the oscillations for longer ramps. The solid red line is the output of the quantum simulation, and the shaded region represents one standard deviation. The blue dots show the output of the semi-classical simulation, performed with 1000 samples.

point, thus preventing the crossing of the critical point from occurring adiabatically. However, this claim is only strictly valid in the thermodynamic limit, for an asymptotically large numbers of atoms. With $\sim 4 \times 10^4$ atoms, the energy gap is actually non-zero because of the finite size of the condensate. In theory, it is possible to cross the energy gap without any excitations, provided the ramping is slow enough. However, given the limitations in the ramp times that were pointed out above, it is unlikely to cross the critical point slow enough for the limited number of atoms to have an effect on the dynamics. Even though the finite number of atoms is reflected in the width of the initial distribution through the standard quantum limit, testing the effect of this non-vanishing energy gap requires the quantum version of our simulations. A comparison of semi-classical and quantum simulations using 4×10^4 atoms

is shown in Fig. 7.11. The overlap of the two outputs is excellent, thus justifying the interchangeable use of semi-classical or quantum simulations.

7.1.4 Pollution

One issue we faced is the presence of unwanted atoms in the $m_F = \pm 1$ sub-levels in the initial state, which we refer to as pollution or impurities. The reason this pollution is an issue is that we expect our experiment to begin in the polar ground state, where all the atoms are in the $m_F = 0$ energy level. During evaporation, a strong magnetic field gradient is applied along the quantization axis, which induces preferential losses of $m_F = \pm 1$ atoms by pushing them along the weak axial confinement of the CO₂ laser dipole force trap. This creates a BEC which is uniquely composed of $m_F = 0$ atoms at the end of evaporation. However, data sets #1 and #3 have revealed that this purification is not consistently reliable, particularly when the cross trap is used. When pollution was detected, the fractional population of the impurities was typically lower than 0.2% in each undesirable state, but for a condensate of 4×10^4 atoms, this corresponds to 80 atoms.

The reason why this must be taken into account is that the KZM assumes that the system is initialized in the ground state. Having these impurities corresponds to a slightly excited state, more akin to thermal fluctuation than the inherent quantum fluctuations which are expected to drive our system out of an unstable equilibrium as it enters the broken-symmetry ferromagnetic phase. Due to the difficulties of bringing certain systems to the ground state, such as ion chains [93–96], the case of crossing QPTs in nonequilibrium steady-states has also been studied [135]. Nevertheless, if the system is not in the ground state, the unwanted atoms can be considered “seeds” for the unfreezing of the system out of the impulse period. Intuitively, the polluting atoms could precipitate the evolution of the system, thus influencing the freeze-out time \hat{t} and the related \hat{q} . The presence of impurities is not a new problem in our

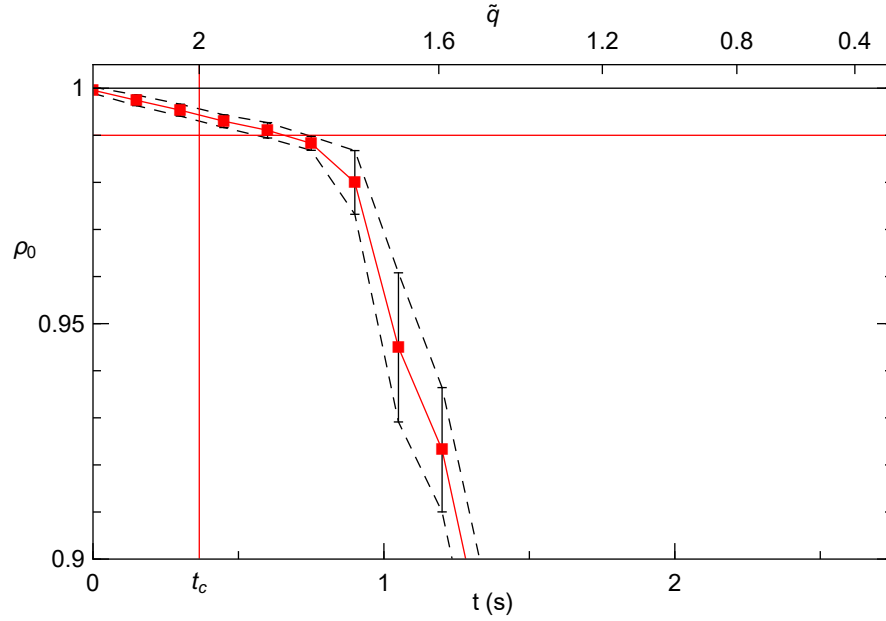
experiment. It has been discussed, and the potential effect has been quantified in previous studies, namely in the experiment presented in Ref. [43], which dealt with the evolution of the spin populations out of the polar ground state after an instant quench through the critical point.

In addition to the unwanted atoms in the initial state, the creation of additional $m_F = \pm 1$ atoms has also been detected in data sets #1 and #3 before the system crosses the critical point. During that time, the system is still in the polar phase since the magnetic field is higher than the critical field B_c , and all the atoms should remain in $m_F = 0$, which is the polar ground state. This means some mechanism other than spin mixing is taking place. We have determined the cause to be linked to the 852 nm light used for the cross trap. In the events when impurities were being created above the critical point, turning the cross trap off rids the system of pollution. In addition, increasing the power of the 852 nm laser increased the rate of creation of impurities. We believe the $m_F = \pm 1$ atoms could be created by off-resonant excitations by the 852 nm laser. The D_1 ^{87}Rb line has transitions around 795 nm [124]. An off-resonant excitation to one of the $5^2P_{1/2}$ energy levels followed by a decay to the $5^2S_{1/2}$ could explain the creation of impurities. The straightforward way to permanently avoid this problem would be to replace the 852 nm light by the output of a fiber laser at 1064 nm. The much larger detuning from the optical transitions of the D_1 and D_2 lines should remove the risk of off-resonant excitations.

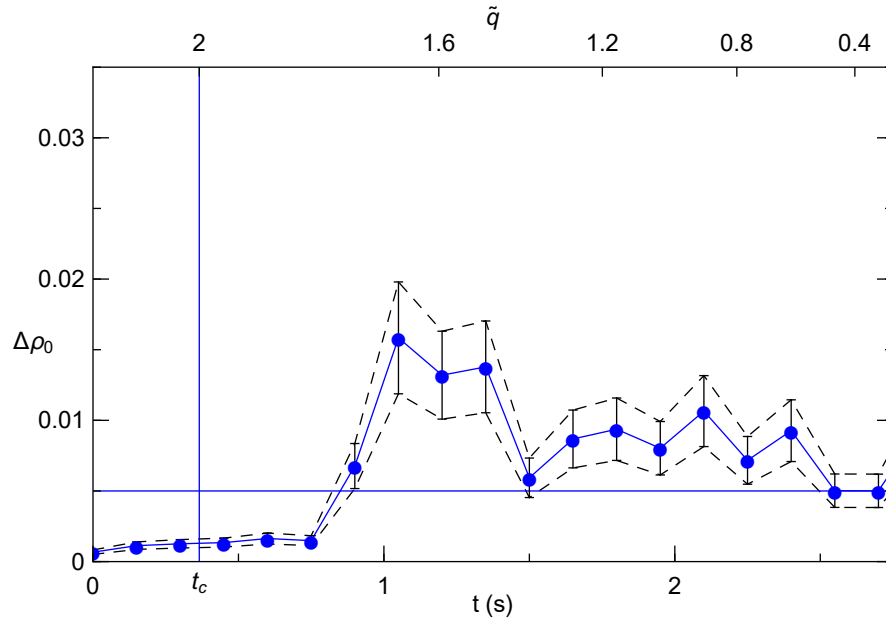
7.1.4.1 Data Analysis of Data Sets with Pollution

Despite the initial pollution and the appearing of unwanted atoms during evolution above the critical point, the data sets showing pollution can still be analyzed and compared to the clean sets. Values of \hat{t} and \hat{q} can still be extracted using two methods.

The first method relies on the fact that despite the slow linear decrease in ρ_0 before the critical point, the value of $\Delta\rho_0$ remains constant, as shown in the plots



(a) ρ_0 with pollution.



(b) $\Delta\rho_0$ with pollution.

Figure 7.12: **Measurements of ρ_0 and $\Delta\rho_0$ with pollution.** This data is taken during a 3 s ramp from 500 mG to 0 mG, with a critical magnetic field of 480 mG. (a) shows a linear decrease in ρ_0 before the critical point, followed by a sharper drop at the end of the freeze-out period. In (b), $\Delta\rho_0$ remains under its threshold until the end of the freeze-out period.

in Fig. 7.12. For the longest ramps, ρ_0 can slowly drop as low as $\rho_0 = 0.95$ before the more sudden drop caused by spin mixing after the freeze-out period. This rules out using the $\rho_0 = 0.99$ threshold to determine when the system unfreezes, since that would yield a negative value for \hat{t} and \hat{q} . However, $\Delta\rho_0$ remains under its threshold of $\Delta\rho_0 = 0.005$ until the end of the freeze-out period. The drop in ρ_0 caused by spin-mixing is accompanied by an increase in $\Delta\rho_0$, and it is only then that $\Delta\rho_0$ reaches its threshold. The $\Delta\rho_0$ measurements corresponding to the ρ_0 measurements in Fig. 7.12a are shown in Fig. 7.12b. Once the time t_{th} when $\Delta\rho_0$ crosses the threshold is known, the values of \hat{q} and \hat{t} can be calculated.

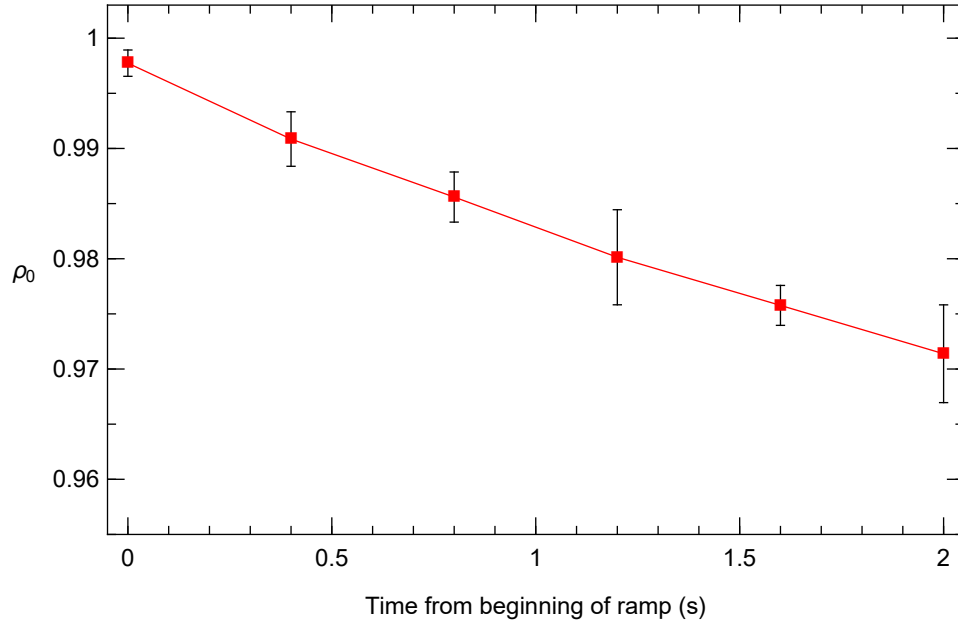


Figure 7.13: **Measurements of ρ_0 at constant high magnetic field showing pollution.** The magnetic field is kept at 2 G, which is higher than the critical magnetic field of 480 mG. Despite $\rho_0 = 1$ being the ground state, ρ_0 still decreases linearly during evolution. A linear fit yields $\rho_0(t) \propto -0.013 t$.

The second method consists of characterizing the rate of pollution and incorporating it into the data analysis. The generation of impurities was analyzed by letting the system evolve at constant fields over the critical point, as shown in Fig. 7.13. The rate at which ρ_0 decreases is practically constant, and a linear fit is performed. The

rate for Fig. 7.13 is $\rho_0(t) \propto -0.013 t$. The data is then compensated by adjusting the populations using the calculated rate, as plotted in Fig. 7.14.

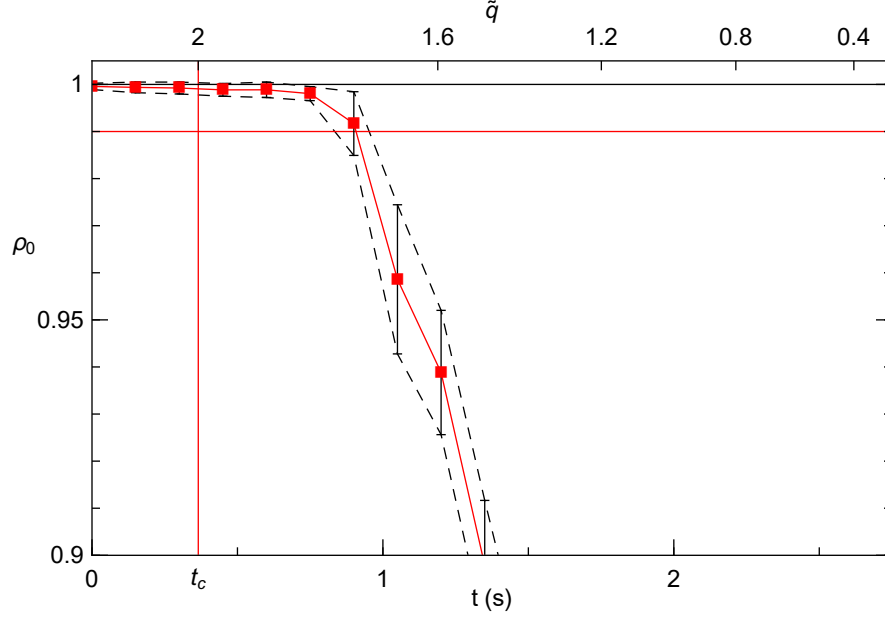


Figure 7.14: **Measurements of ρ_0 with pollution compensation.** The values of ρ_0 from Fig. 7.12a are adjusted to compensate for the linear decrease in ρ_0 due to pollution by using the data from Fig. 7.13.

7.1.4.2 Simulations with Pollution

In order to estimate the effect of pollution on our system, we use quantum simulations with $N = 4 \times 10^4$ atoms. The ramps start at 500 mG, given a critical magnetic field of 480 mG, similarly as in the experiment. However, instead of initializing the system in the $|0, N, 0\rangle$ Fock state, we set k pairs of atoms in the $m_F = \pm 1$ states, which results in an initial Fock state of $|k, N - 2k, k\rangle$. This is a particular state that is unlikely to exist in the laboratory. Indeed, one would expect a more complex superposition of Fock states, but the approach used is the most straightforward way to create a polluted initial state in the quantum simulation.

Simulations have been run with different numbers of impurities, and the results

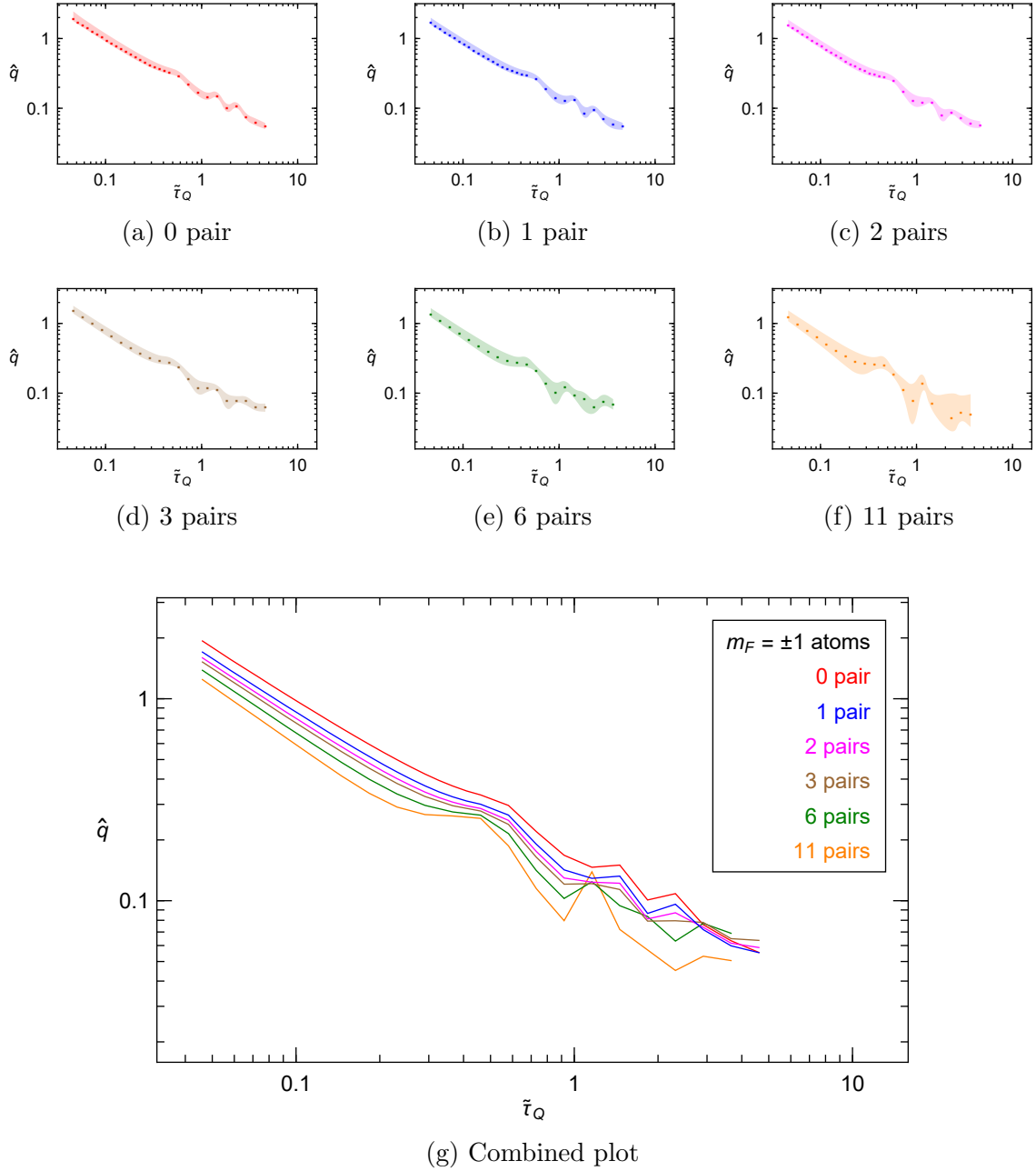


Figure 7.15: **Quantum simulations with pollution.** Quantum simulations are performed using an initial Fock state $|k, N - 2k, k\rangle$, where $N = 4 \times 10^4$ is the total number of atoms and k is the number of pairs of atoms in the $m_F = \pm 1$ states. The ramps start from 500 mG with a critical magnetic field $B_c = 480$ mG. The top red trace is the baseline with no pollution, and the numbers of pairs k shown are 1 (blue), 2 (magenta), 3 (brown), 6 (green), and 11 (orange) pairs. The ρ_0 threshold is 0.99.

are plotted in Fig. 7.15. Similarly to the decreasing number of atoms in the semi-classical simulations, the dynamics are accelerated when pollution is present. The scaling exponents from fits in the linear part are shown in Table 7.5.

Table 7.5: Effect of pollution on scaling exponents. This table summarizes the scaling exponents for \hat{q} when pollution is added to the initial state in the form of k pairs of atoms in the $m_F = \pm 1$ states. The fits are performed on the traces in Fig. 7.15 for $0.046 < \tilde{\tau}_Q < 0.231$, which corresponds to the linear region for all traces. The exponents are also displayed in Fig. 7.16.

Pairs of atoms in $m_F = \pm 1$	Scaling exponent for \hat{q}
0	-0.84(7)
1	-0.85(6)
2	-0.86(7)
3	-0.87(10)
6	-0.89(12)
11	-0.93(17)

It is not clear from looking at Fig. 7.15, but we see in Table 7.5 that the scaling exponents become more negative for larger numbers of impurities. For the simulation without pollution, the exponent is already more negative than the $-2/3$ value predicted by the KZM, which is not unexpected given the parameters used for the simulation. We saw earlier in the chapter that fits from simulations performed with ramps starting at a magnetic field closer to the critical point yield scaling exponents more negative than $-2/3$. We also argued that fitting the faster ramps also tends to give a more negative exponent than asymptotically long ramps.

Due to the time-consuming nature of running quantum simulations, a limited number of ramp times were tested, which explains the larger errors that for semi-classical simulations. Nevertheless, according to these quantum simulations with pollution in the initial state, the effect is stronger than what is observed, given that 22 pollution atoms out of a total of 4×10^4 can shift the scaling exponent from $-0.84(7)$ to $-0.93(17)$.

7.1.4.3 *Effect of Impurities on Scaling Exponents*

As suggested above by simulations, pollution in the form of pairs of ± 1 atoms in the initial state seems to have a noticeable effect on the scaling exponents. The trend shown is that increasing pollution makes the scaling exponent for \hat{q} more negative. However, as made clear in the bottom of Fig. 7.16, the fitting errors significantly increase with the number of pairs, and the error bars still overlap with the exponent given by the simulation without pollution. Out of the four data sets analyzed in this thesis, two showed signs of pollution: data sets #1 and #3. Using the first method described previously to compensate for pollution yields very similar scaling exponents extracted from ρ_0 and $\Delta\rho_0$. When comparing the scaling exponents from data sets #1 and #3 with those from data sets #2 and #4 (no pollution), the data sets with pollution show less negative exponents, even though the error bars from every data set still overlap. The scaling exponents extracted from simulations performed without impurities in similar conditions as the experiment are in stronger agreement with the results from the clean data sets. The data shows that additional impurities are created during the subsequent evolution, which is more complicated to implement numerically. We have also mentioned earlier that the initial Fock state is unlikely to happen in the lab. Attempting more complex initial states may give more insight in the role of pollution.

7.2 *Concluding Remarks*

The simulations in this chapter have proven useful to compare with our data and to go beyond the experimental constraints encountered in the lab, mainly a result of the limited lifetime of the condensate. Figure 7.16 presents a summary of the scaling exponents extracted from the data and the simulations studied in this chapter. We have shown the equivalence of quantum and semi-classical simulations, thus justifying the interchangeable use of the two methods. We initially studied the system in

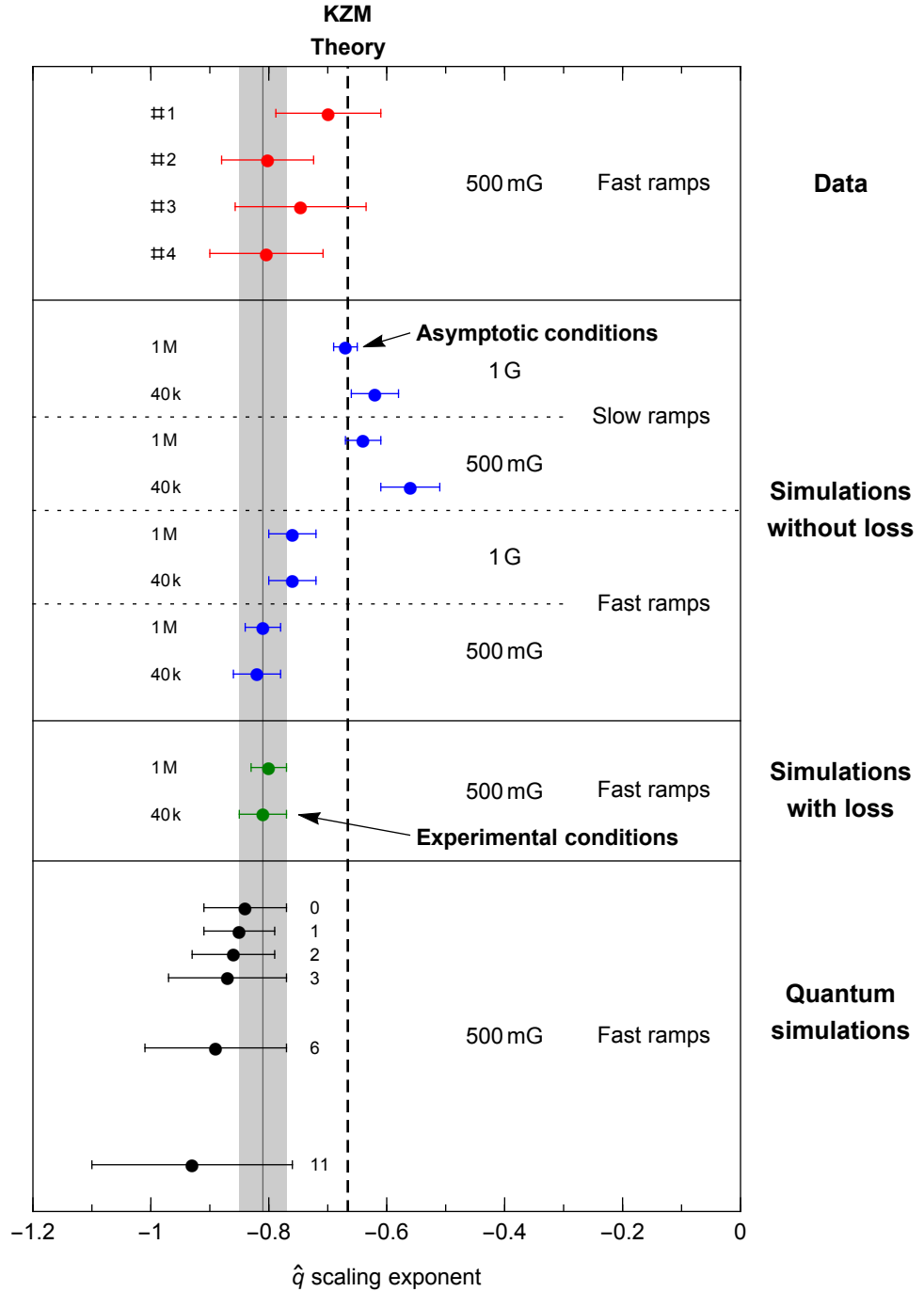


Figure 7.16: **Summary of scaling exponents.** The scaling exponents for \hat{q} from the experimental results and all the simulations are combined. The 1 M and 40 k labels indicate the number of atoms in the condensate (1×10^6 and 4×10^4 , respectively). For the simulations without loss, the exponents are grouped by ramp speeds and by initial magnetic field (1 G or 500 mG). The pollution in the form of number of pairs of atoms in the $m_F = \pm 1$ state is indicated in the quantum simulations. The gray line and shaded envelope indicate the scaling exponent and error from the semi-classical simulation performed in the same conditions as the experiment, and the vertical dashed line indicates the KZM theory value of $-2/3$.

asymptotic conditions, characterized by long ramps starting much higher than the critical point, with a large number of atoms and infinite condensate lifetime, and found that the scaling exponents converge to the KZM theory value. We also analyzed the consequences of atom loss and the effect of the initial number of atoms on the dynamics. When comparing the results from our data with simulations performed with experimental parameters, we determined that the scaling exponents determined experimentally matched well with simulations and were also slightly lower than the value predicted by the KZM.

CHAPTER VIII

CONCLUSION AND OUTLOOK

The focus of this thesis is the study of our system as it crosses a second-order quantum phase transition at a finite rate. In this context, we gave an overview of phase transitions, which range from simple first-order classical phase transitions to more complex continuous quantum phase transitions occurring at absolute zero. The history behind the inception of the Kibble-Zurek mechanism was presented. This theory was originally developed to predict the density of topological defects following the crossing of a continuous phase transition, and the scaling of their density with quench speed. Based on the premise that the energy gap between the ground state and the first excited state vanishes during a continuous phase transition, it also predicts a freeze-out time where the dynamics cease to be adiabatic in the vicinity of the critical point. The scaling of the time between the crossing of the critical point and the recovery of adiabatic evolution as the system is driven through the critical transition at a finite speed is the key measurement of this thesis. After having described our experimental apparatus, we presented the methods used to gather the data used in this study, as well as the data analysis including a loss model to determine the power law scaling exponent characterizing the dependence of the freeze-out time with the speed the system is driven through the critical point. A power law scaling was observed for the faster magnetic field ramps in the experiment, with a departure from the power law scaling for very slow ramps. The experimental results were discussed and compared with simulations, which suggest that the differences with the predictions from the KZM were likely due to atom loss and the resulting limitations in driving parameters. In fact, when simulations were performed in ideal conditions, with a large

number of atoms and asymptotically slow ramps starting at very high magnetic field, the critical scaling predicted from the KZM was recovered.

8.1 *Future Work*

As a closing to this thesis, we will now present an outlook in the form of some potential future projects to be performed by our group.

8.1.1 High Precision Measurements

As shown in Chapter 3, a measurement of the critical magnetic field B_c is equivalent to a measurement of the spinor dynamical rate c , given that $c = \frac{1}{2}q_z B_c^2$. Therefore, a precise measurement of B_c can lead to the precise determination of quantities relating to the spin dynamics of the condensate, such as the chemical potential or the peak density in the Thomas-Fermi approximation, as detailed in Chapter 6. The peak density can be expressed as $n_0 = \frac{7}{2} \frac{c}{c_2} \propto B_c^2$ [4]. The uncertainty Δn_0 in the determination of the peak density is thus related to the uncertainty ΔB_c in the measurement of the critical magnetic field by $\frac{\Delta n_0}{n_0} = \frac{2\Delta B_c}{B_c}$. For a measurement yielding $B_c = 0.480(2)$ G, the peak density can be determined with a relative uncertainty of $\frac{\Delta n_0}{n_0} = 0.8\%$.

Alternatively, if the total number of atoms and trap frequencies are well known, a precise measurement of B_c can result in a precise determination of the coupling strengths c_0 and c_2 , and eventually yield values for the scattering lengths a_0 and a_2 .

8.1.2 Spin Domains

As previously mentioned, the KZM was originally formulated in the context of the scaling of topological defects with quench speed during continuous phase transitions. In this thesis we instead focused our attention to the temporal evolution of the spin populations alone. Indeed, one of the main points in this thesis was to avoid the presence of defects in the form of spin domains. This was either performed by having a BEC small enough that the formation of domains would be energetically suppressed,

or at least by ensuring that the evolution after the critical point took place before the creation of domains if the BEC was large enough to allow them to form. However, now that the temporal scaling has been studied, one can consider moving on to the study of defect formation when the critical point is crossed at different rates. The measurement of the number of domains may also reveal a scaling law, establishing another connection with the KZM.

8.1.3 Energy Gap

A work in progress relies on the fact that the finite number of atoms in our BEC gives a non-zero value to the energy gap at the critical point. This energy gap is challenging to measure with the current number of atoms, but along with smaller BECs and specially tailored magnetic field ramps, the width of the energy gap might be measured. These conditions also open the door to an adiabatic crossing of the critical point.

8.1.4 Improving Spin-Nematic Squeezing

Another objective could be improving the measurement of the previously observed spin-nematic squeezing [33]. This work would primarily require enhancing our imaging capabilities in order to lower the detection limit, currently restricted by several sources of noise. Having the ability of reliably detecting small numbers of atoms would also open the door to a whole new category of experiments, including metrology techniques.

8.1.5 Measurement of Entanglement

Entangled states are distinctive quantum states that display nonlocal correlations, demonstrating the non-existence of any local hidden variable theory that is equivalent to quantum mechanics. The first observation of nonlocality and entanglement came in 1982, in optical systems [136]. However all the experimental realizations of

entanglement have been limited to microscopic systems (a few atoms or photons). It remains a challenge to prepare entangled states in many-body systems. Spinor BECs are known for their characteristic display of non-classical phenomena. The ground state of a ferromagnetic BEC at low magnetic field is a Dicke state with large value of total spin, which is known to have a strong many-particle entanglement. Preparing this state in our system could generate an entanglement of several thousands of atoms. This state can be prepared experimentally by adiabatically reducing the applied magnetic field to zero, or by using a reasonably long magnetic field ramp as the ones used in this thesis. These ramps been already implemented successfully, but the entanglement of the resulting state has not been established with certainty. Therefore, entanglement resulting from this technique can be detected by developing an entanglement witness that can be evaluated using easily measurable quantities [137]. This would not only lead to a deeper understanding of quantum effects in the macroscopic world, but also result in useful applications in quantum metrology.

APPENDIX A

FUNDAMENTAL CONSTANTS AND EXPERIMENTAL PARAMETERS

Table A.1: Fundamental constants (Source: 2014 CODATA) and useful ^{87}Rb properties [124].

Quantity	Symbol	Value
Fundamental Constants		
Speed of Light	c	$2.997\,924\,58 \times 10^8$ m/s (exact)
Permeability of Vacuum	μ_0	$4\pi \times 10^{-7}$ N/A ² (exact)
Permittivity of Vacuum	ϵ_0	$(\mu_0 c^2)^{-1}$
Planck Constant	h	$6.626\,070\,040(81) \times 10^{-34}$ J s
Elementary Charge	e	$1.602\,176\,620\,8(98) \times 10^{-19}$ C
Bohr Magneton	μ_B	$9.274\,009\,994(57) \times 10^{-24}$ J/T
Bohr Radius	a_0	$0.529\,177\,210\,67(12) \times 10^{-10}$ m
Boltzmann Constant	k_B	$1.380\,648\,52(79) \times 10^{-23}$ J/K
Basic Properties of ^{87}Rb		
Atomic Number	Z	37
Atomic Mass	m	$1.443\,160\,60(11) \times 10^{-25}$ kg
Natural Abundance		27.83(2)%
Nuclear Spin	I	3/2
Ground ($5^2\text{S}_{1/2}$) State Properties		
Fine Structure Landé g -factor	g_J	2.002 331 13(20)
Nuclear g -factor	g_I	−0.000 995 141 4(10)
Hyperfine Splitting	ν_{hf}	6.834 682 610 904 310(2) GHz
D_2 ($5^2\text{S}_{1/2} \rightarrow 5^2\text{P}_{3/2}$) Transition		
Wavelength (vacuum)	λ	780.241 209 686(13) nm
Lifetime	τ	26.2348(77) ns
Decay Rate	Γ	$2\pi \cdot 6.066\,6(18)$ MHz
$ F = 2, m_F = \pm 2\rangle \rightarrow F' = 3, m_F = \pm 3\rangle$		
Saturation Intensity	I_{sat}	1.669 33(35) mW/cm ²
Resonance Cross Section	σ_0	$2.906\,692\,937\,721(66) \times 10^{-9}$ cm ²
Scattering Lengths (s -wave)		
Scattering Length for Spin-0 Channel	$a_{F=0}$	101.8(2) a_0
Scattering Length for Spin-2 Channel	$a_{F=2}$	100.4(1) a_0

APPENDIX B

SINGLE FOCUS TRAP

The first three data sets used a cross trap geometry, which guarantees that the size of the condensate is smaller than the spin healing length, therefore preventing spin domains. However, the fourth data set was taken in a single focus trap. Unlike in the cross trap, a condensate in this cigar-shaped trap is no longer in the single mode approximation, and the formation of spin domains is energetically allowed.

The formation of spin domains (or the lack thereof) during a magnetic field ramp can be tested by observing the condensate in absorptive imaging. Absorptive images of the condensate are taken at regular intervals during the ramp and are shown in Fig. B.1. The same data is taken in fluorescence imaging and the values of ρ_0 are plotted in Fig. B.2. By comparing the images in Fig. B.1 with the data in Fig. B.2, it is clear that no domains are formed by the time t_{th} the system crosses the threshold. In fact, the $m_F = \pm 1$ clouds are barely visible in the absorptive imaging pictures at that time. After an evolution of 1 s, ρ_0 is less than 0.75, and there are still no visible domains in the $m_F = \pm 1$ clouds.

Given the lack of domains at times much later than t_{th} , we are confident that despite the large size of the condensate compared to the spin healing length, the determination of a scaling exponent is not impacted by spatial defects. The \hat{t} and \hat{q} plots for this data set (#4) are included in Appendix D, and the data shows a clear power law. The scaling exponents determined from the data set are tabulated in Tables 6.2 and 6.3.

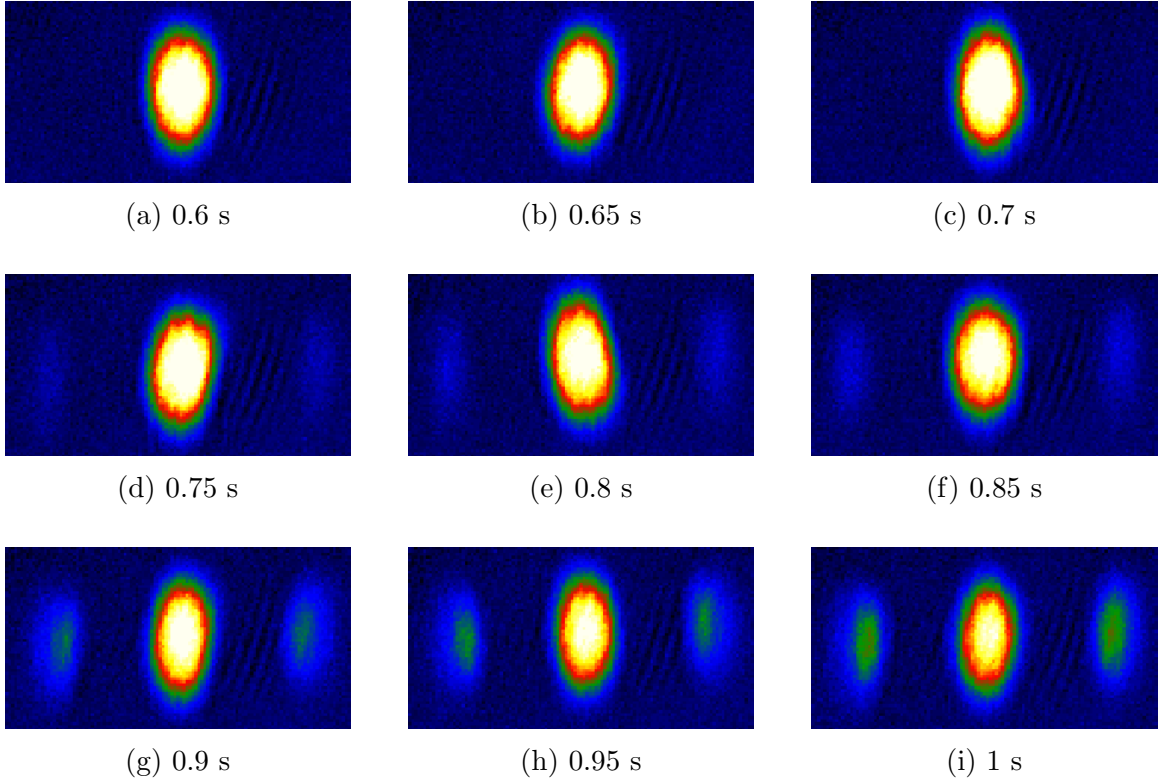


Figure B.1: **Monitoring domain formation in the single focus trap.** The condensate is observed in the single focus trap during a magnetic field ramp using absorptive imaging. The ramp brings the magnetic field down from 300 mG to 0 mG in 1.5 s, and the critical magnetic field is 260 mG. The measurements of ρ_0 for this ramp are shown in Fig. B.2. The threshold of $\rho_0 = 0.99$ is crossed between 0.65 s and 0.7 s.

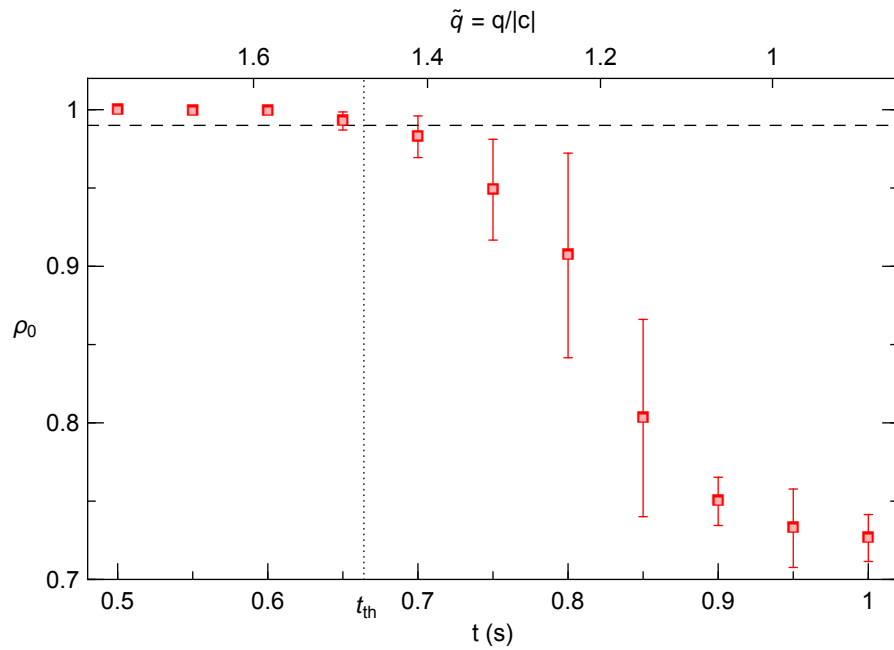


Figure B.2: **Measurements of ρ_0 during a magnetic field ramp in the single focus trap.** This plot shows the measurements of ρ_0 during a magnetic field ramp from 300 mG to 0 mG in 1.5 s. The horizontal dashed line shows the threshold of $\rho_0 = 0.99$, and the vertical dotted line indicates the time the threshold is crossed. This is the ramp used for the images shown in Fig. B.1.

APPENDIX C

EXPERIMENTAL ISSUES AND IMPROVEMENTS

In this appendix we address some of the issues faced while taking data for this thesis. The goal is not only to learn from these problems and improve the experiment, but also to estimate and if possible to quantify the impact on the results.

C.1 CO₂ Laser Modes

Here we will discuss the issues encountered with the mode of the CO₂ laser we use as the main dipole force trap. We assume that the dipole force trap has a perfect Gaussian mode, and in general it is a good approximation to calculate the trapping parameters, such as frequency. However, imaging the cross section of the CO₂ laser beam using a thermal camera shows that the mode is not always as clean as we expect, which sometimes results in double traps.

C.1.1 Laser Beam Cross-Section

Measurements are made with a Pyrocam Spirocon thermal camera. The mode of the CO₂ laser beam looks very much Gaussian until it reaches the AOM which is used to control the power sent to the chamber. A cross section of the CO₂ laser before the AOM can be seen in Fig. C.1.

The effect of the AOM on the beam can be characterized by looking at the cross section of the beam at different locations along the beam path. Our setup allows us to take a shortcut by taking advantage of the motorized translation stage. Recall that the experiment uses a 1:1 telescope on the way to the chamber that can be lightly tuned to change the waist of the beam inside inside the chamber. Instead of moving the thermal camera to multiple locations along the beam path, we can gradually

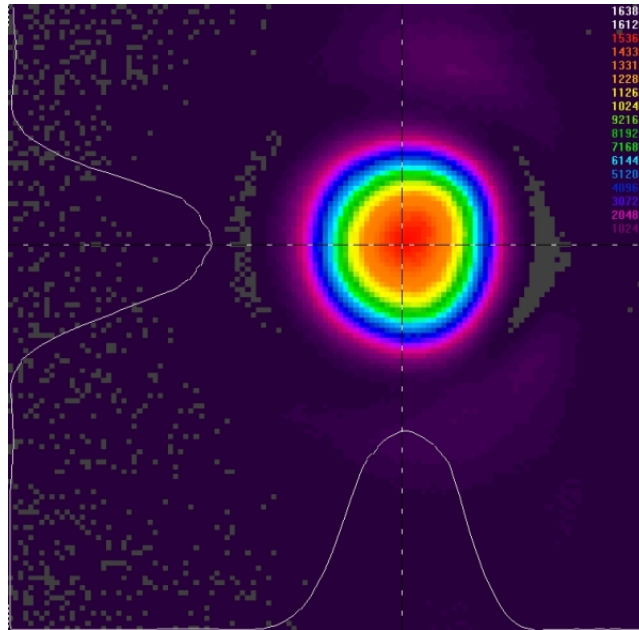


Figure C.1: **Cross section of the CO₂ laser before the AOM.** The mode is close to Gaussian, not only by looking at the color gradient, but also as indicated by the white traces showing the amplitude along the horizontal and vertical dashed lines.

translate one of the two lenses from the 1:1 telescope, which effectively displaces the focus through the plane of the camera. A sequence of cross sections of the beam are shown in Fig. C.2.

C.1.2 Double Trap

The previous section used cross sections of the CO₂ laser beam for its characterization, but another method can also be used to diagnose the mode of the optical trap. Once the temporal dark MOT sequence has ended, the collapsed MOT is overlapped with the optical trap. At that point, the trapping beams from the MOT are turned off, and the atoms can transfer to the dipole force trap. This takes place during ~ 300 ms, after which enough atoms have been collected in the optical trap and evaporation can begin. If the power of the CO₂ laser is turned off right before evaporation starts, the trapped atoms can expand and reveal information about the trap's geometry. This is the technique used to diagnose the shape of the trap for different positions of the

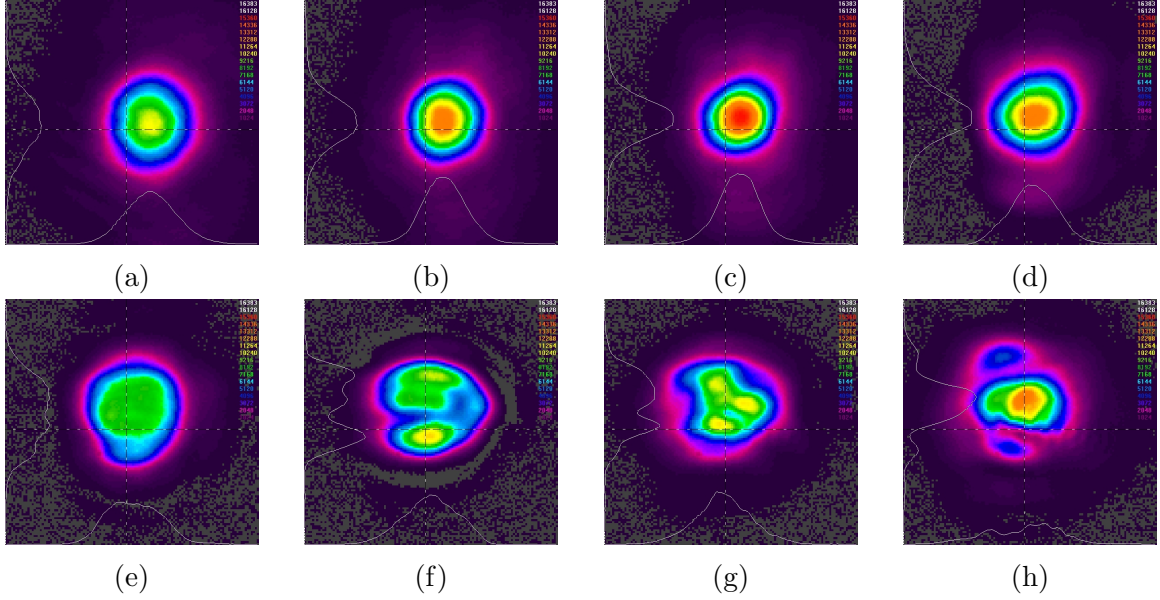


Figure C.2: **Cross sections of the CO₂ laser beam while changing the position of the lens mover.** Between each image, the first lens of the telescope is translated by 1 mm towards the chamber, which increases the divergence of the beam. The beam in image (a) is slightly convergent and focuses before the camera. The focus of the beam is located in the camera's plane in image (c). The position used for the loading part of the experiment when the atoms are transferred from the collapsed MOT to the optical trap corresponds to image (e). The lens mover is then translated 10 mm towards the direction of propagation, which considerably increases the width of the beam at the chamber.

motorized translation stage.

After the atoms are released from the dipole force trap, they are free to expand for 2 ms, and then probed for 0.1 ms with the MOT beams and imaged with the COHU camera. The time of flight (TOF) of 2 ms was chosen because a shorter TOF gives too small an image for the COHU's resolution, and waiting too long washes out the possible spatial features. A TOF of 2 ms saturates the camera's sensor, but the interest here is qualitative rather than quantitative. In fact, when counting the number of atoms transferred from the MOT to the optical trap, we let the atoms fall for 6 ms, which is enough time for the cloud to expand, thus bringing the intensity under the sensor's saturation threshold.

The COHU is located over the chamber, and the vertical axis on the images in

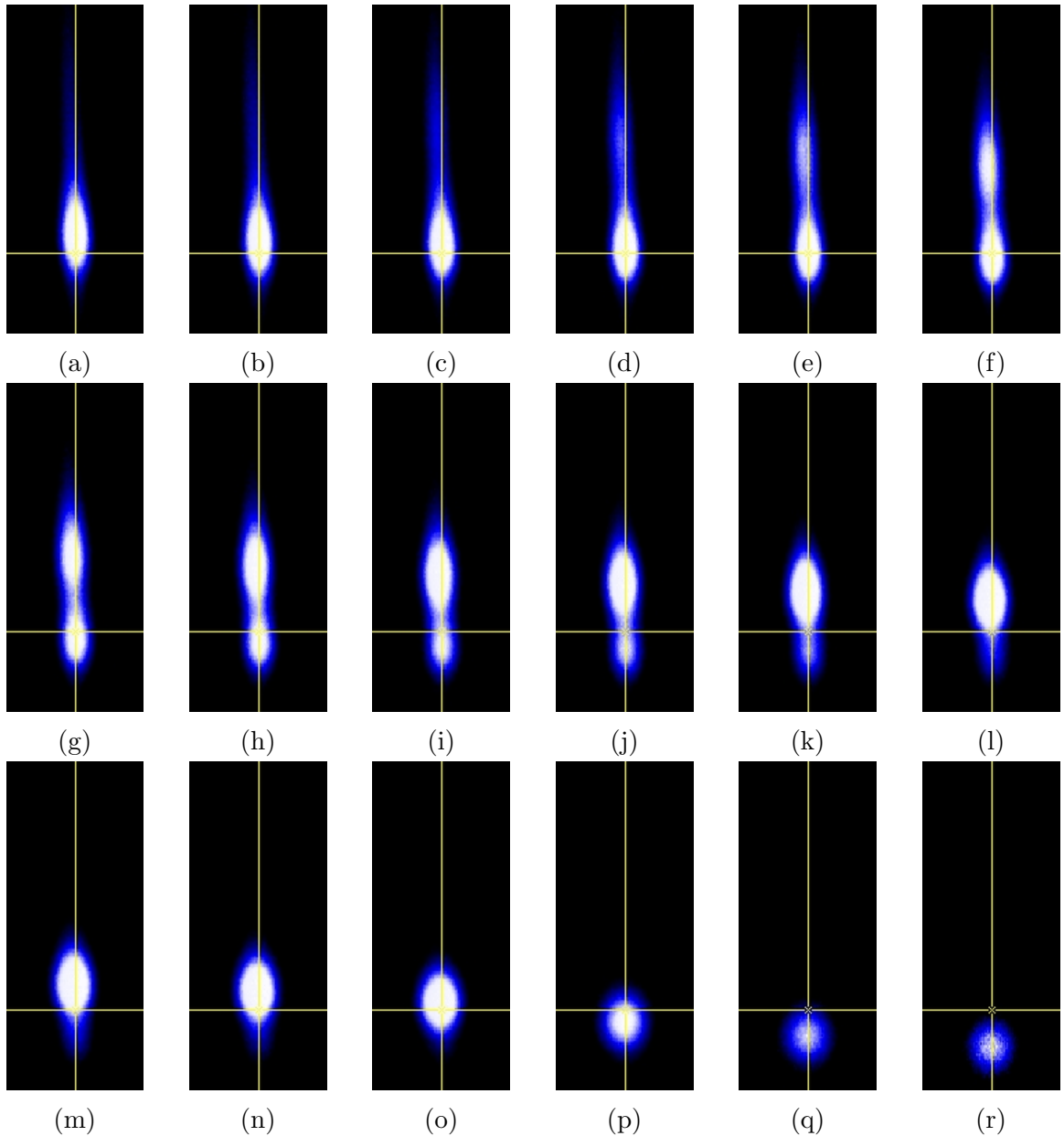


Figure C.3: **Double trap in the CO₂ laser dipole force trap.** This sequence of images from the COHU camera illustrates the case where the CO₂ laser optical trap actually consists of two traps. The first lens of the telescope is moved in the direction of propagation of the beam. When the problem was diagnosed, the location of the MOT had been optimized such that the collapsed MOT would be centered at the cross hairs, and the lens mover was in the position corresponding to image (f). In this case, the final number of atoms in the BEC was lower than usual, since the atoms transferred to the bottom trap in (f) would be lost as that trap disappears. The workaround is to change the location of the lens mover such that the collapsed MOT overlaps with what will become the final trap, such as in image (l).

Fig. C.3 correspond to the CO₂ laser beam's axis, with the top of the image being closer to the laser head. When translating the lens mover, one can clearly see the presence of two distinct traps, aligned along the axial direction of the laser. The first trap shrinks and disappears as the second appears above. If the transfer of atoms from the MOT to the optical trap takes place when the bottom trap is dominant, or even when there are two traps, the atoms in the bottom trap will likely be lost. The workaround is to setup the lens mover at a location where the overlap with the collapsed MOT is maximized with what will become the final trap for the BEC. In comparison, the ideal case with no double trap is shown in Fig. C.4.

C.2 Thermal Effects

Sometime during 2013 we noticed that one of the ZnSe lenses inside the vacuum chamber was glowing when the CO₂ laser was set at full power. It was only a small area of $\sim 1 \text{ mm}^2$. It turns out that after years of being surrounded by Rb vapor, the lenses became coated with a layer of Rb, or some compound created by the contact between Rb and ZnSe. As worrisome as this seemed at the time, the issue was not noticeable when looking at the images of BEC or the measured numbers of atoms. The power of the CO₂ laser measured after the chamber didn't show an abnormal loss in transmission, so the experiments continued. In the following months, the transmission through the chamber dropped little by little, but the atoms were still being trapped as usual, and the dynamics didn't show any change. It is only in the middle of 2014 that the effects of this glowing lens started to be felt. We noticed that the single focus trap would drift when the power of the CO₂ laser was kept at the low post-evaporation power. This issue is illustrated in Fig. C.5, and the displacement of the single focus trap is plotted in Fig. C.6.

This does not impact the dynamics when performing the experiment in the single focus trap. However, when the cross trap is used, the effect can be noticeable. The

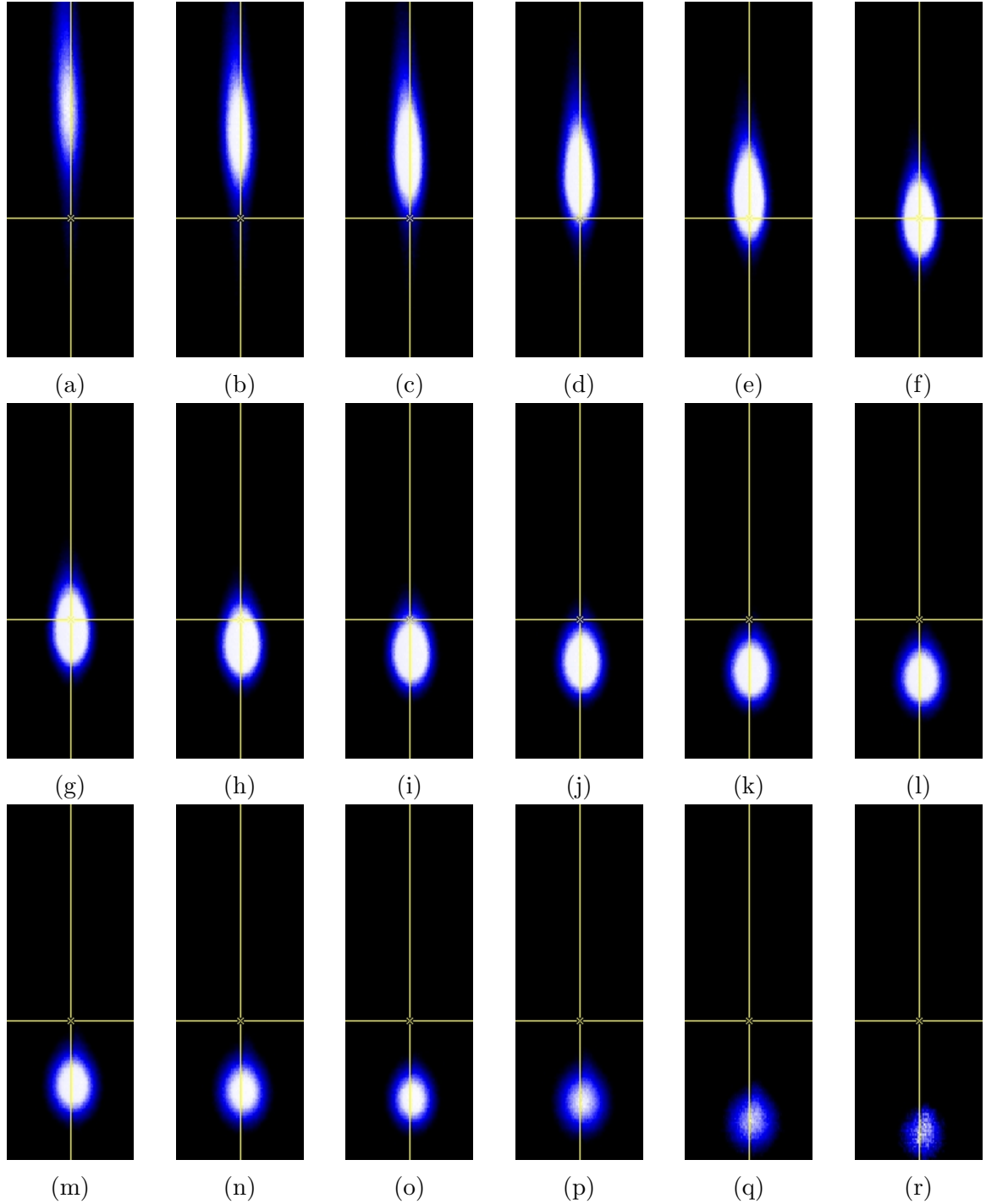


Figure C.4: **Single trap in the CO₂ laser dipole force trap.** This sequence of images from the COHU camera shows the geometry of the CO₂ laser dipole force trap as the second lens of the telescope is being translated along the beam's axis. Unlike in Fig. C.3, here we see the ideal case where a single trap is being compressed. The atoms are transferred from the MOT when the trap is in the position corresponding to image (f).

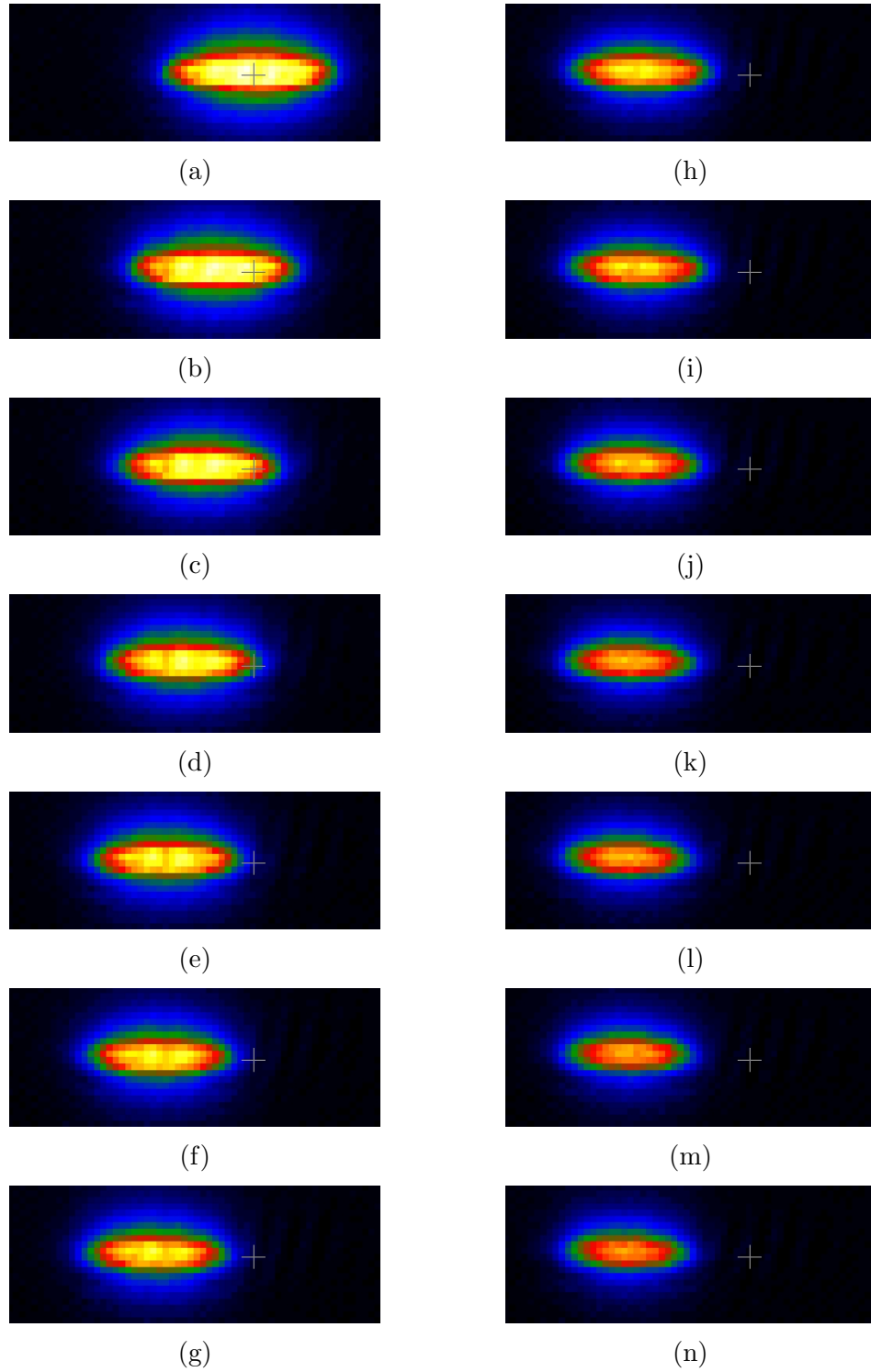


Figure C.5: **Drifting single focus trap.** This sequence of images shows the drift of the single focus trap along the trapping beam's direction of propagation. The images are taken 1 s apart. One pixel corresponds to $2.6 \mu\text{m}$, and the width of every image is $155 \mu\text{m}$.

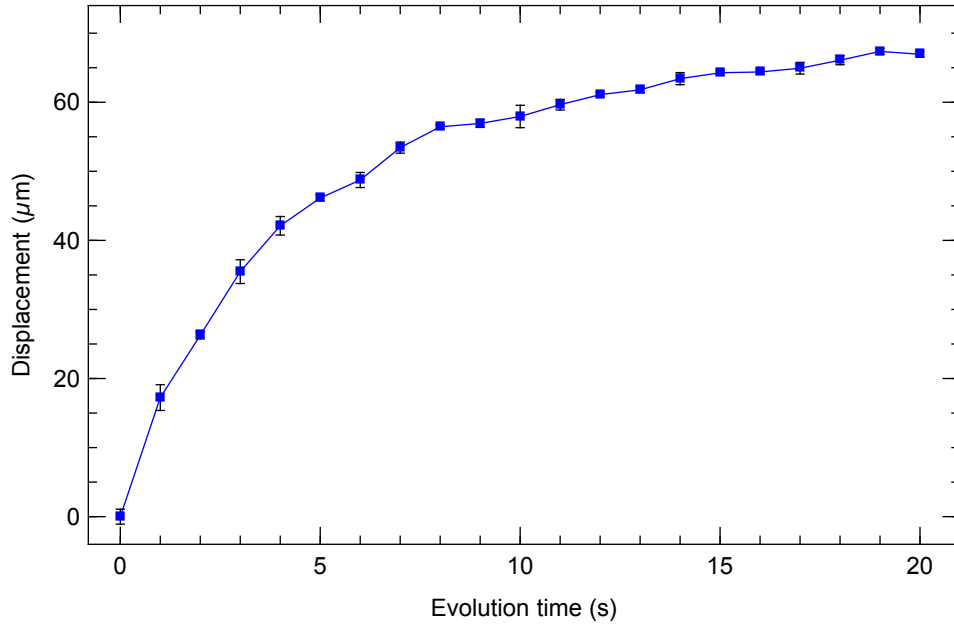


Figure C.6: **Single focus trap displacement.** The position of the focus of the CO₂ laser single focus trap is tracked along the propagation axis after various evolution times.

852 nm laser used for the cross trap has a waist of $\sim 20 \mu\text{m}$. Considering the images in Fig. C.5, the 852 nm laser would intersect the CO₂ laser beam at their respective foci, represented by the cross hairs. After a few seconds, the 852 nm laser meets the CO₂ laser trap far from its focus, and after 4 s of evolution, the 852 nm beam no longer intersects with the BEC.

This issue was diagnosed between the second and third of the four data sets studied in this thesis. The fourth only considered the dynamics in the single focus trap, so the data was not affected. However, the third data set was still taken using the cross trap. The fix for that data set was to wait 10 s with the CO₂ laser at low power before the start of the magnetic field ramps. Since the lifetimes in the cross trap prevent ramps longer than ~ 5 s, waiting an extra 10 s allowed the trap to undergo the faster part of the drift, and gave the opportunity to align the 852 nm laser with the single focus BEC still moving, but slow enough to allow several seconds of evolution in an

adequate cross trap.

C.3 IGBT

Another problem faced a few times has to do with the control system of the gradient coils. The experiment uses a single power supply to send current through the two pairs of large gradient coils, which are the MOT coils and the auxiliary gradient coils. Since the current used can be as high as ~ 500 A, a pair of robust switches must be used to orient the current to the pair of coils required at any given time. We rely on insulated-gate bipolar transistors (IGBTs), which can handle the required current. However, they show some vulnerabilities. Attempting to use the IGBT as a fast switch, in order to create a short magnetic field gradient pulse, for example, is lethal for the IGBT. An inductance spike due to the high inductance of the coils is the likely culprit for this scenario.

The other cause of failure is exposing an IGBT to a high current for a long time. This has happened in the past when keeping the purifying gradient on during long evaporation times (in the order of ten seconds). The consequence is an unusable IGBT, or burnt components on the gate driver circuit board that controls the IGBTs. To lessen the effect of inductance spikes, the system was improved by integrating a large snubber capacitor in the control circuit. Due to the repeated nature of these issues, the lab policy is now to constantly have spare IGBTs and control boards, or at least enough parts to recreate one. As a matter of fact, my first task when joining the lab was to solder one of the new driver circuit boards. In any case, a steady state experiment where none of these damaging conditions are met should not destroy any more IGBTs.

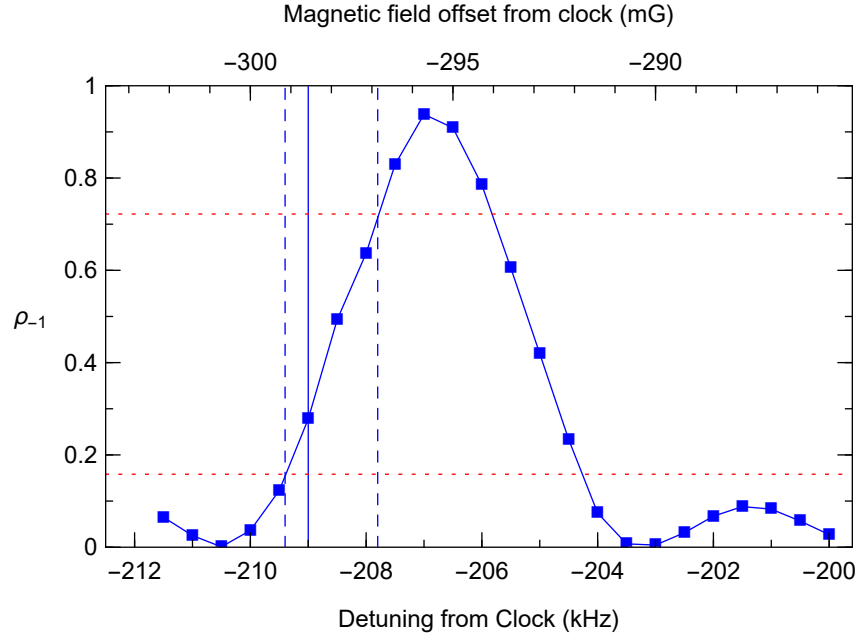
C.4 AC Stray Magnetic Field

The last issue presented in this appendix is the perturbation caused by a stray magnetic field oscillating at 60 Hz. Due to the large amount of electronic components

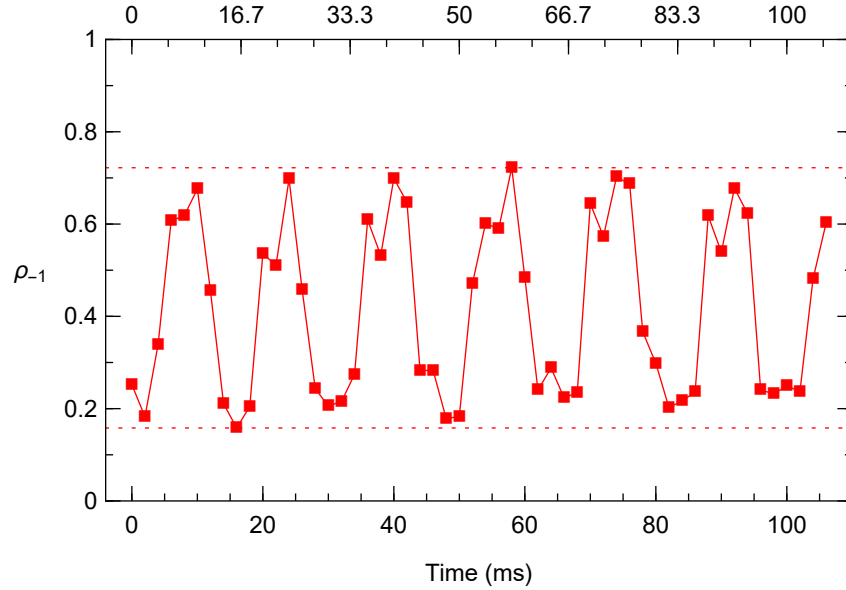
in the lab, the magnetic field has small fluctuations at 60 Hz and higher harmonics. The amplitude of these fluctuations have been measured by magnetometers in various locations in the lab, as well as at the location of BEC by measuring the linear Zeeman energy shift using microwave or RF transitions. The technique is the same whether microwaves or RF are used. The following explanation will be for microwaves, but the principle is the same for RF.

The method consists in using the $|F = 1, m_F = 0\rangle$ to $|F = 2, m_F = -1\rangle$ transition ($|1, 0\rangle$ to $|2, -1\rangle$ for short). The $|1, 0\rangle$ to $|2, +1\rangle$ transition can also be used. The interest is that these transitions are subject to Zeeman shifts due to an applied bias magnetic field. At the fields used for these diagnoses (~ 100 mG), the quadratic Zeeman shift can be neglected, and the effect can be attributed to the linear Zeeman shift alone. This gives a linear relationship between the bias magnetic field along the quantization axis and the frequency detuning Δ from the clock transition ($|1, 0\rangle$ to $|2, 0\rangle$), which is insensitive to the Zeeman shift. Once the detuning Δ is known, the power of the microwaves is adjusted such that the peak at the transition's frequency is broad enough to be ~ 10 kHz wide. Recall that the linear Zeeman energy shift is ~ 700 Hz/mG. This means that the frequency range of ~ 3.5 kHz between the minimum and the center of the peak in Fig. C.7a corresponds to a magnetic field range of ~ 5 mG.

By setting the detuning to an intermediate value on the side of the peak and measuring the spin populations as the system evolves in time, one can determine the range of the magnetic field fluctuations along the quantization axis. In the case of the data shown in Fig. C.7, the detuning was -209 kHz, as shown by the blue solid vertical line in Fig. C.7a. The evolution of the fractional population ρ_{-1} transferred to the $|2, -1\rangle$ state is plotted in Fig. C.7b. The graph shows a periodic pattern, with a clear period of 16.7 ms, as pointed out by the time scale on the upper axis. The minimum and maximum values reached by ρ_{-1} are indicated by the horizontal dotted lines. The



(a) Frequency spectrum on the $-\Delta$ microwave transition.



(b) Evolution of the fractional population transferred to the $m_F = -1$ state

Figure C.7: **Effect of the 60 Hz magnetic field fluctuations.** (a) Spectrum of the fractional population ρ_{-1} on the $-\Delta$ transition from $|1, 0\rangle$ to $|2, -1\rangle$. The vertical blue line indicates the detuning used for plot (b), which shows oscillations in ρ_{-1} despite a constant detuning. The dotted red lines in (b) indicate the maximum and minimum values in ρ_{-1} , and are reproduced in (a) to estimate the range of the magnetic field shift, shown by the vertical dashed lines.

same lines are reproduced in Fig. C.7a, and the corresponding detunings are shown by two vertical dashed lines. Finally, the range of the magnetic field spanned by the fluctuations can be estimated. For these measurements, the minimum and maximum field reached are -299.1 mG and -296.9 mG, which yields a range of 2.2 mG. This calculation gives the order of magnitude of the fluctuations of the magnetic field around the lab due to the 60 Hz (and higher harmonics) perturbation.

This is not a new problem, and the reason is still unclear. A guess is that it may stem from the organic growth of the experiment with new contributions to the electronic setup over the years, perhaps inducing a variety of ground loops and other nuisances. We mitigate the effect of this 60 Hz perturbation by syncing the beginning of every experimental cycle with the rising edge of the AC line, which is taken directly from an electrical outlet. The goal is to have the same magnetic field offset at any given evolution time during every experimental cycle.

C.5 Concluding Remarks

In this appendix we have presented some of the issues confronted while gathering data for this thesis, as well as some techniques to suppress them, and estimated the effect on the experiment. These issues included the imperfect modes of the CO₂ laser, causing a double trap in certain conditions. The drifting of the single focus trap caused by thermal effects was also discussed. Finally, the vulnerability of the IGBTs and the characterization of the AC stray magnetic field were addressed.

APPENDIX D

ADDITIONAL DATA

D.1 Measurements of ρ_0 for Every Magnetic Field Ramp

D.1.1 Data Set #1

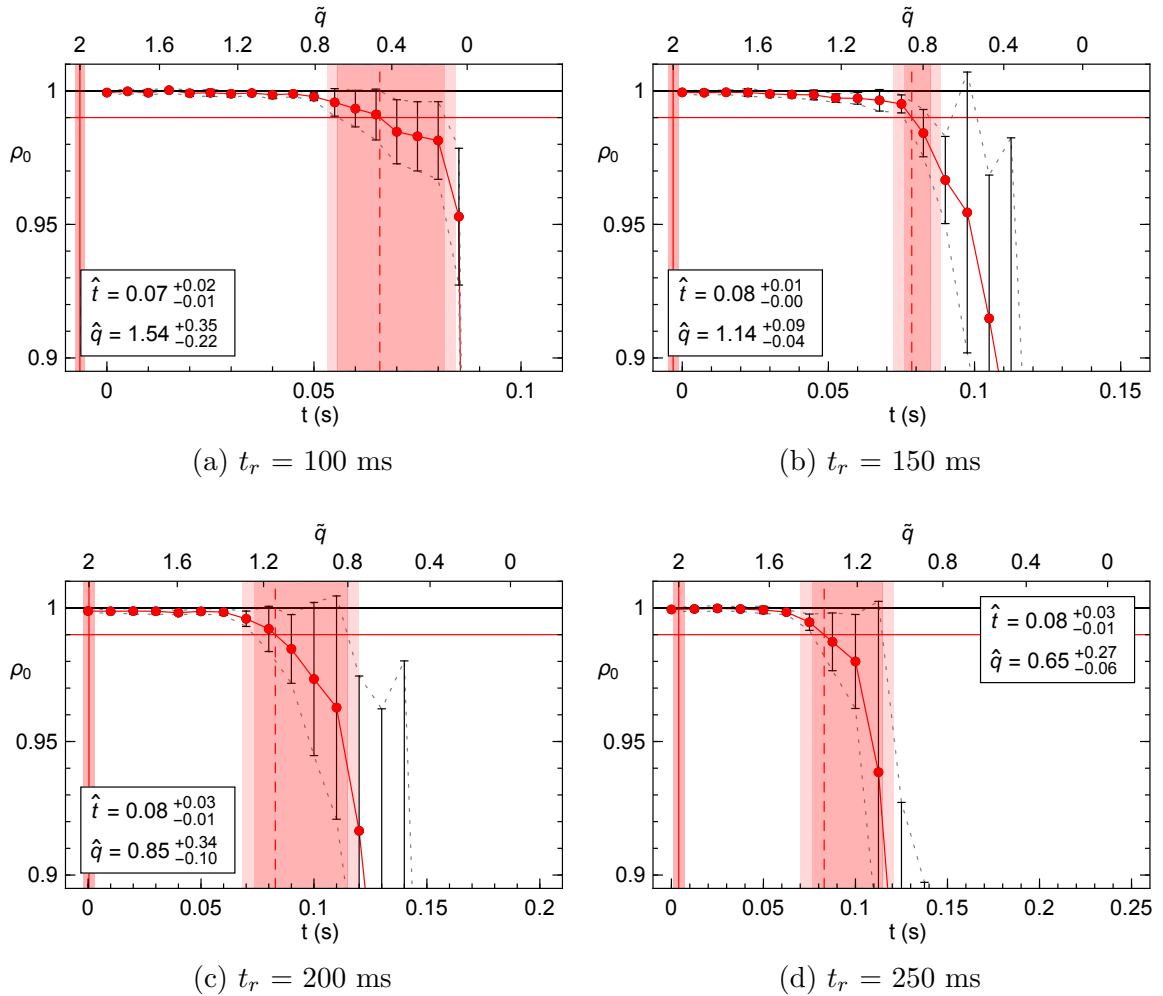


Figure D.1: **Measurements of ρ_0 during magnetic field ramps (data set #1).** The measurements of ρ_0 for all the ramp times from data set #1 are shown with the resulting values and errors of \hat{t} and \hat{q} . The ramps bring the magnetic field down from 500 mG to 0 mG in a time t_r .

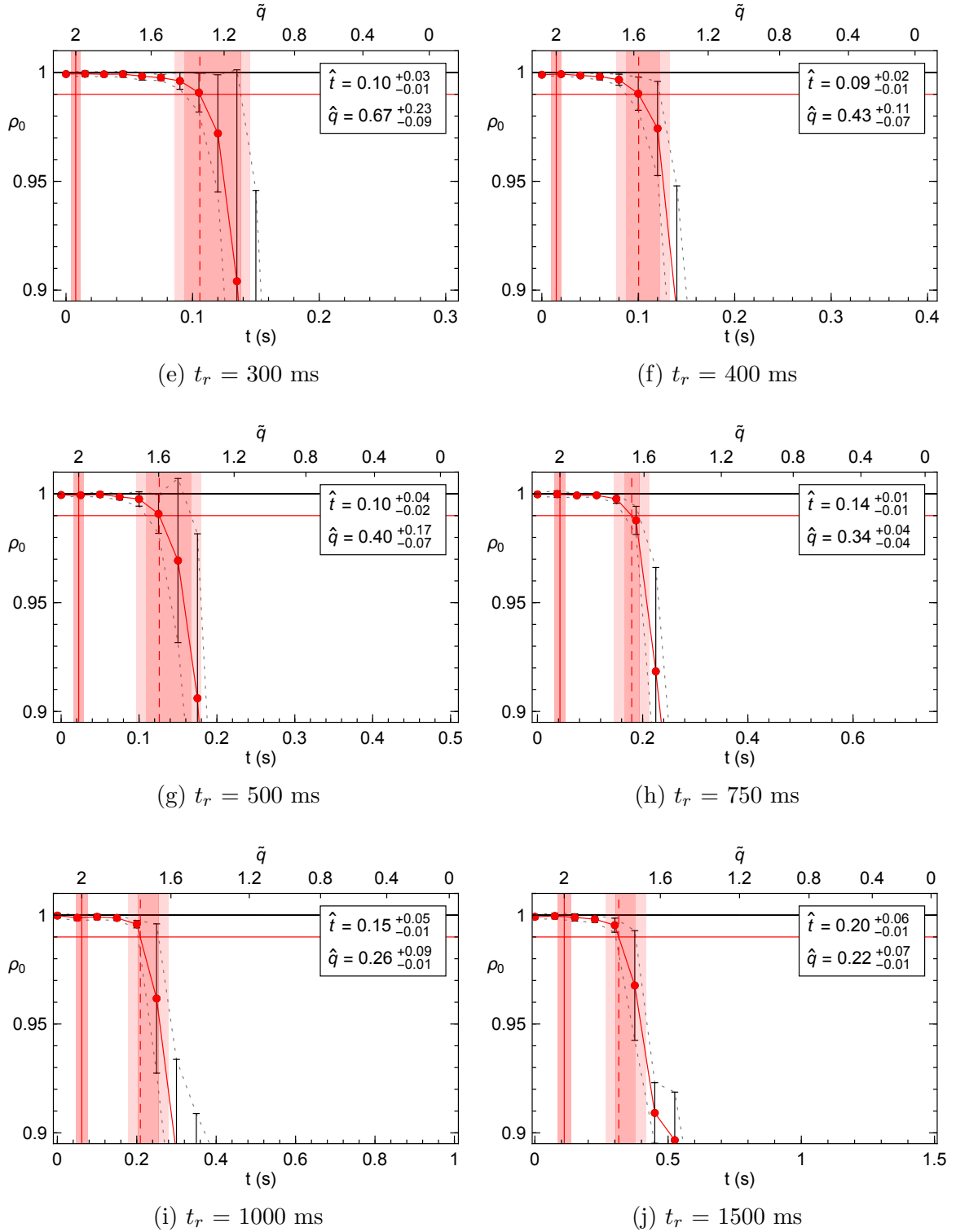


Figure D.1: Measurements of ρ_0 during magnetic field ramps (data set #1, continued).

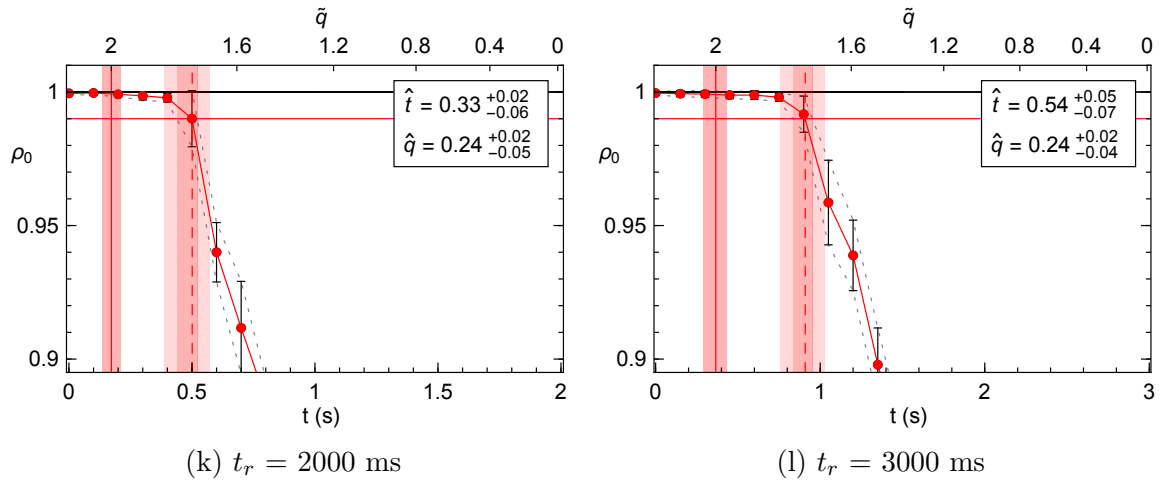


Figure D.1: Measurements of ρ_0 during magnetic field ramps (data set #1, continued).

D.1.2 Data Set #2

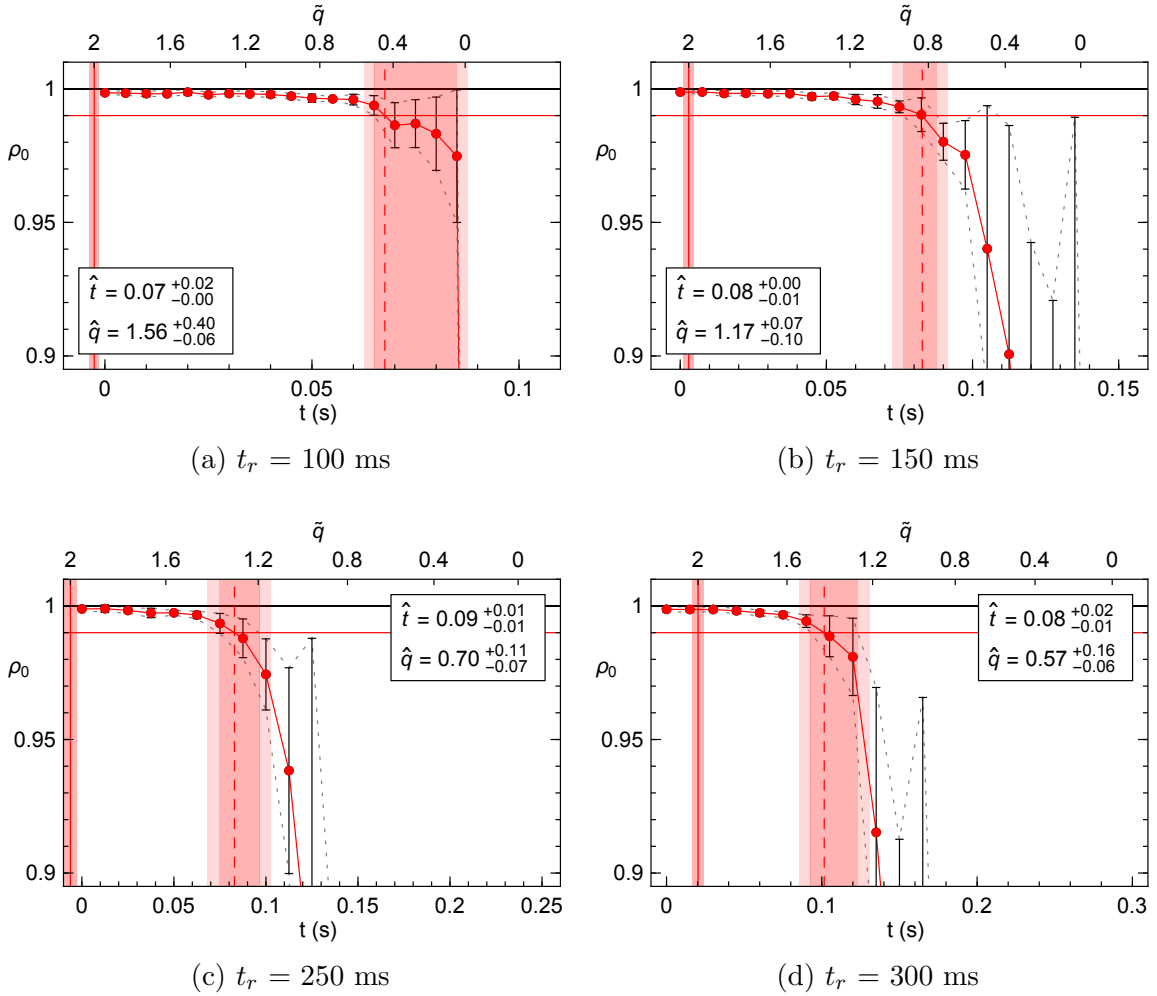


Figure D.2: **Measurements of ρ_0 during magnetic field ramps (data set #2).** The measurements of ρ_0 for all the ramp times from data set #2 are shown with the resulting values and errors of \hat{t} and \hat{q} . The ramps bring the magnetic field down from 500 mG to 0 mG in a time t_r .

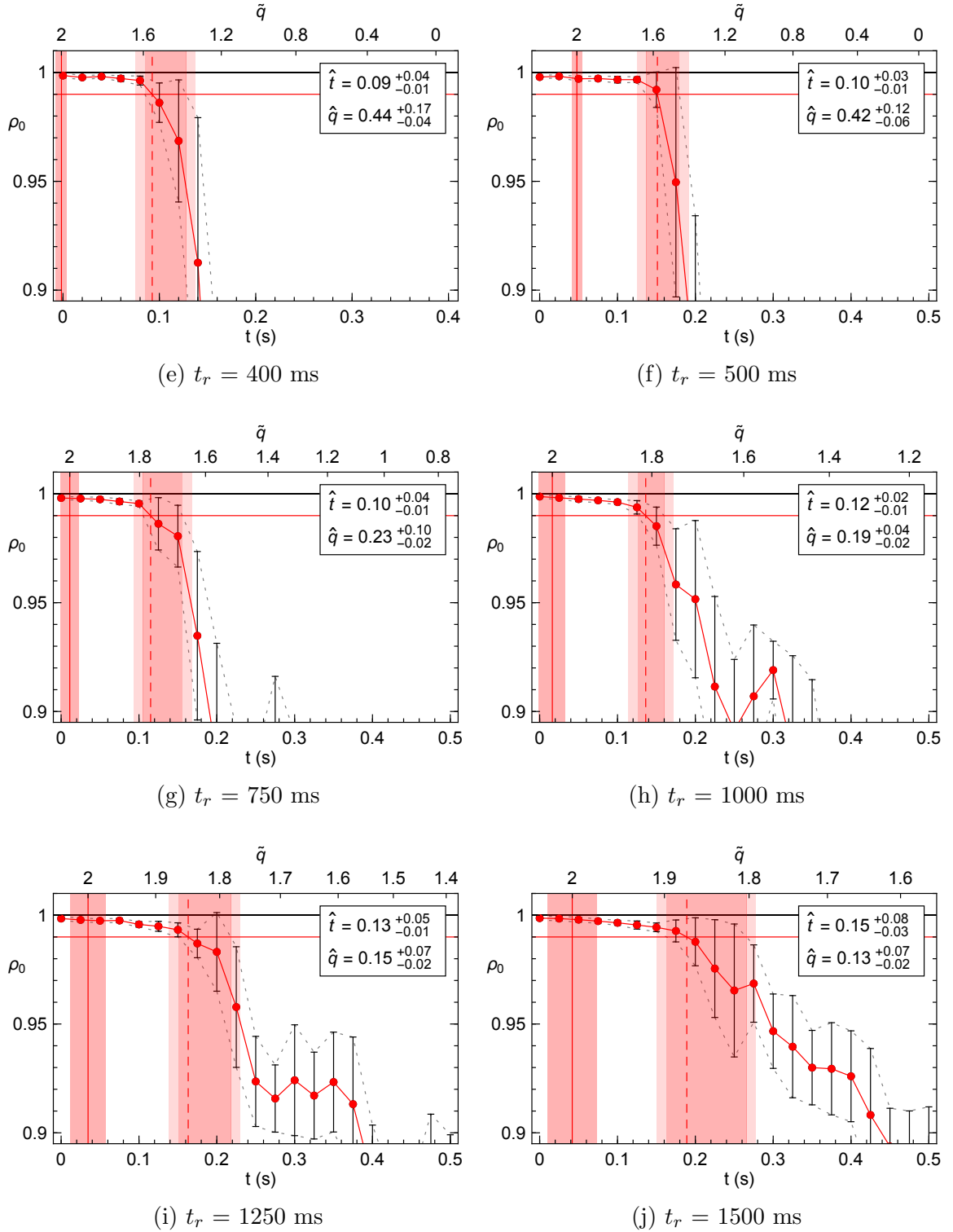


Figure D.2: Measurements of ρ_0 during magnetic field ramps (data set #2, continued).

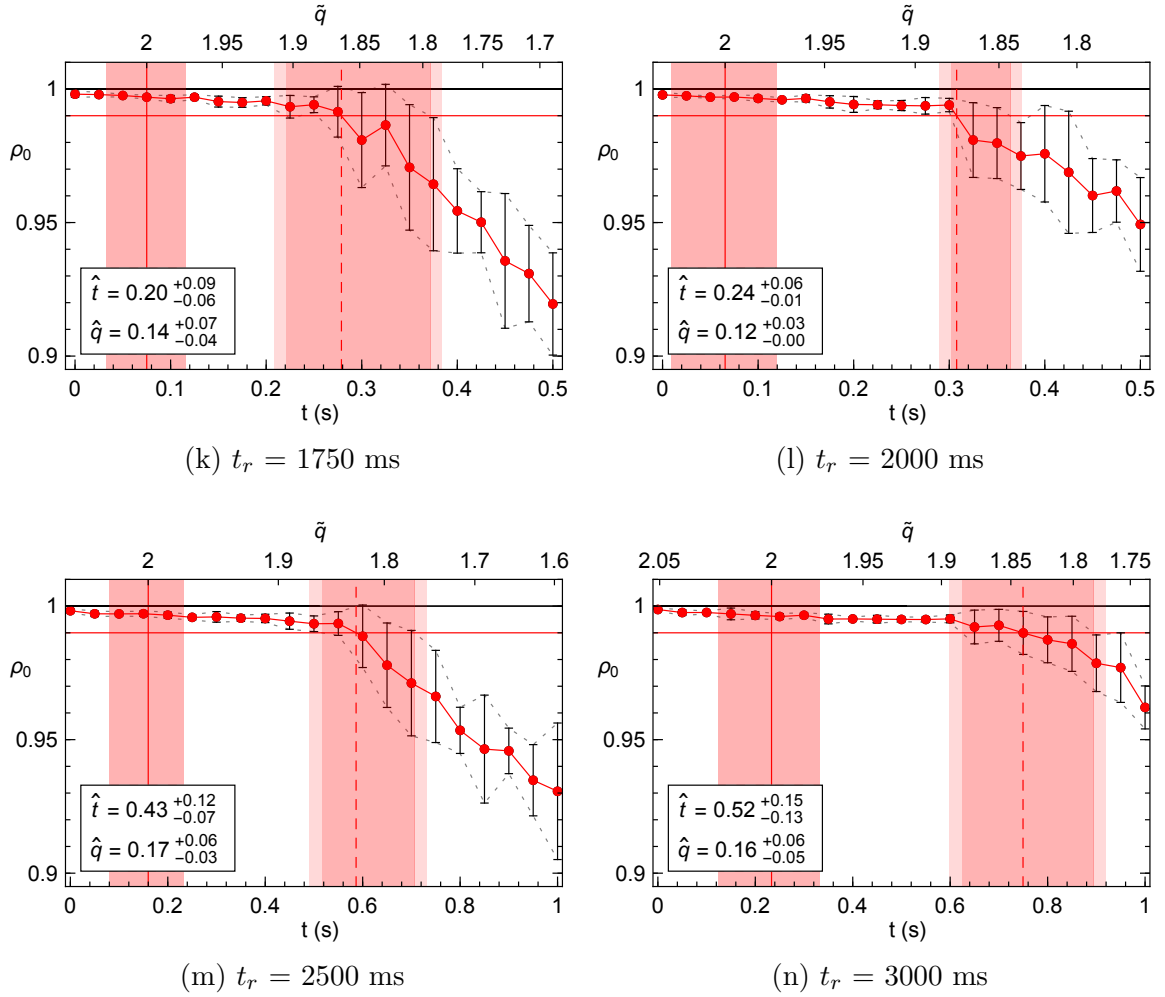


Figure D.2: Measurements of ρ_0 during magnetic field ramps (data set #2, continued).

D.1.3 Data Set #3

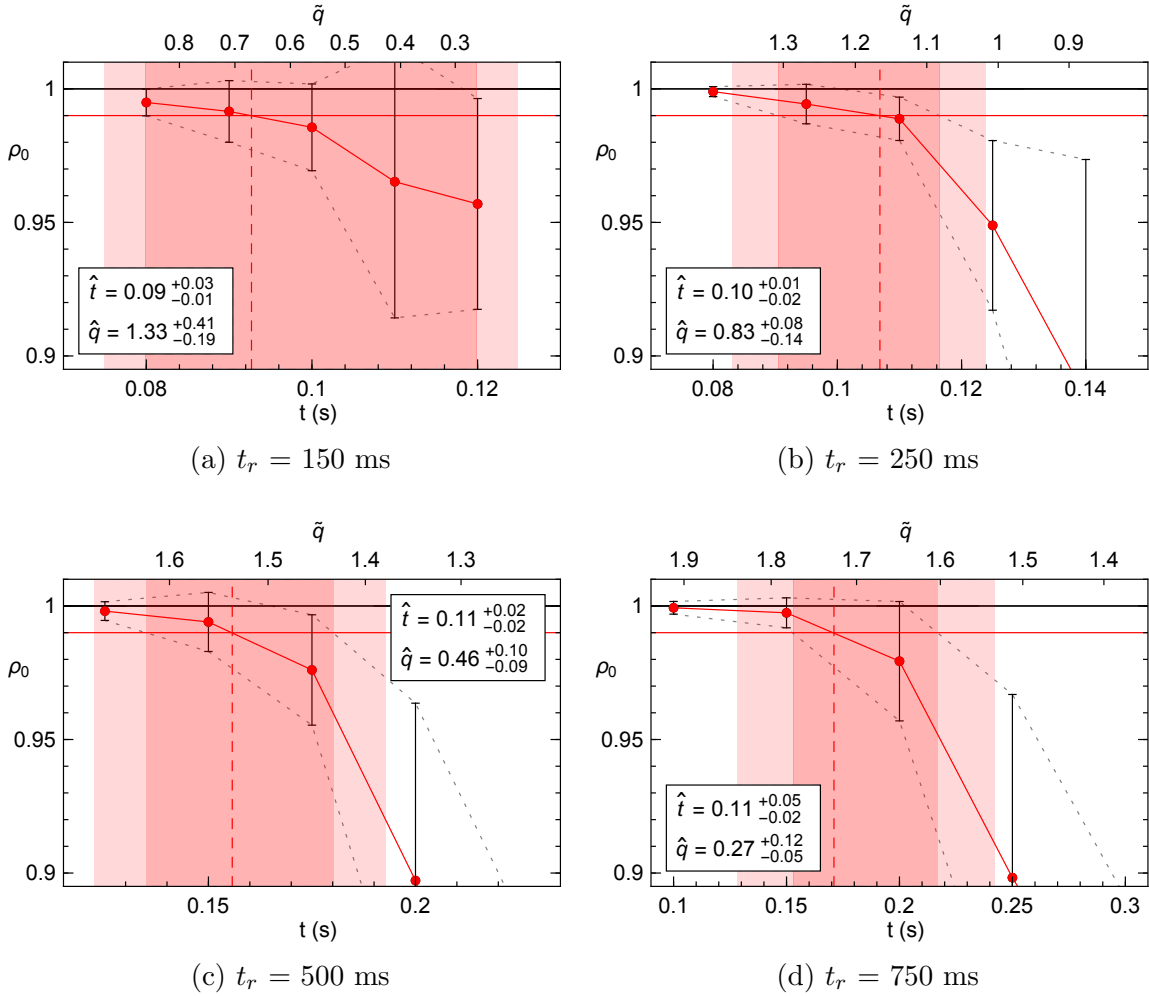


Figure D.3: **Measurements of ρ_0 during magnetic field ramps (data set #3).** The measurements of ρ_0 for all the ramp times from data set #3 are shown with the resulting values and errors of \hat{t} and \hat{q} . The ramps bring the magnetic field down from 500 mG to 0 mG in a time t_r .

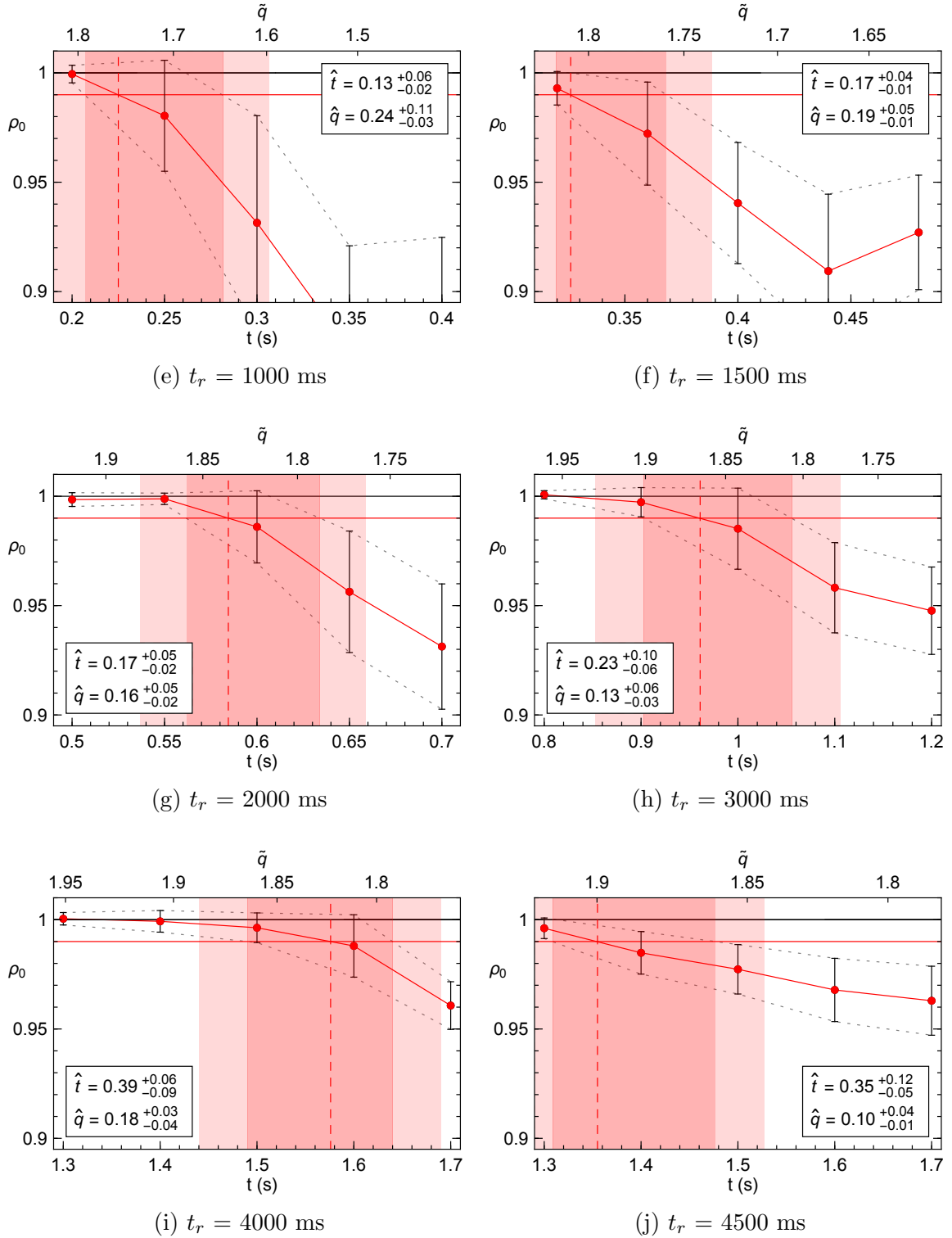
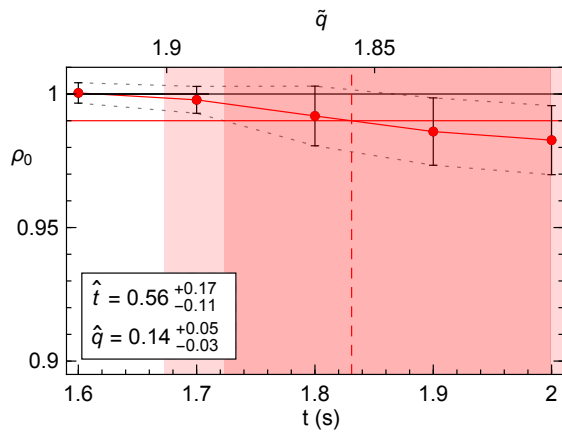


Figure D.3: Measurements of ρ_0 during magnetic field ramps (data set #3, continued).



(k) $t_r = 5000$ ms

Figure D.3: Measurements of ρ_0 during magnetic field ramps (data set #3, continued).

D.1.4 Data Set #4

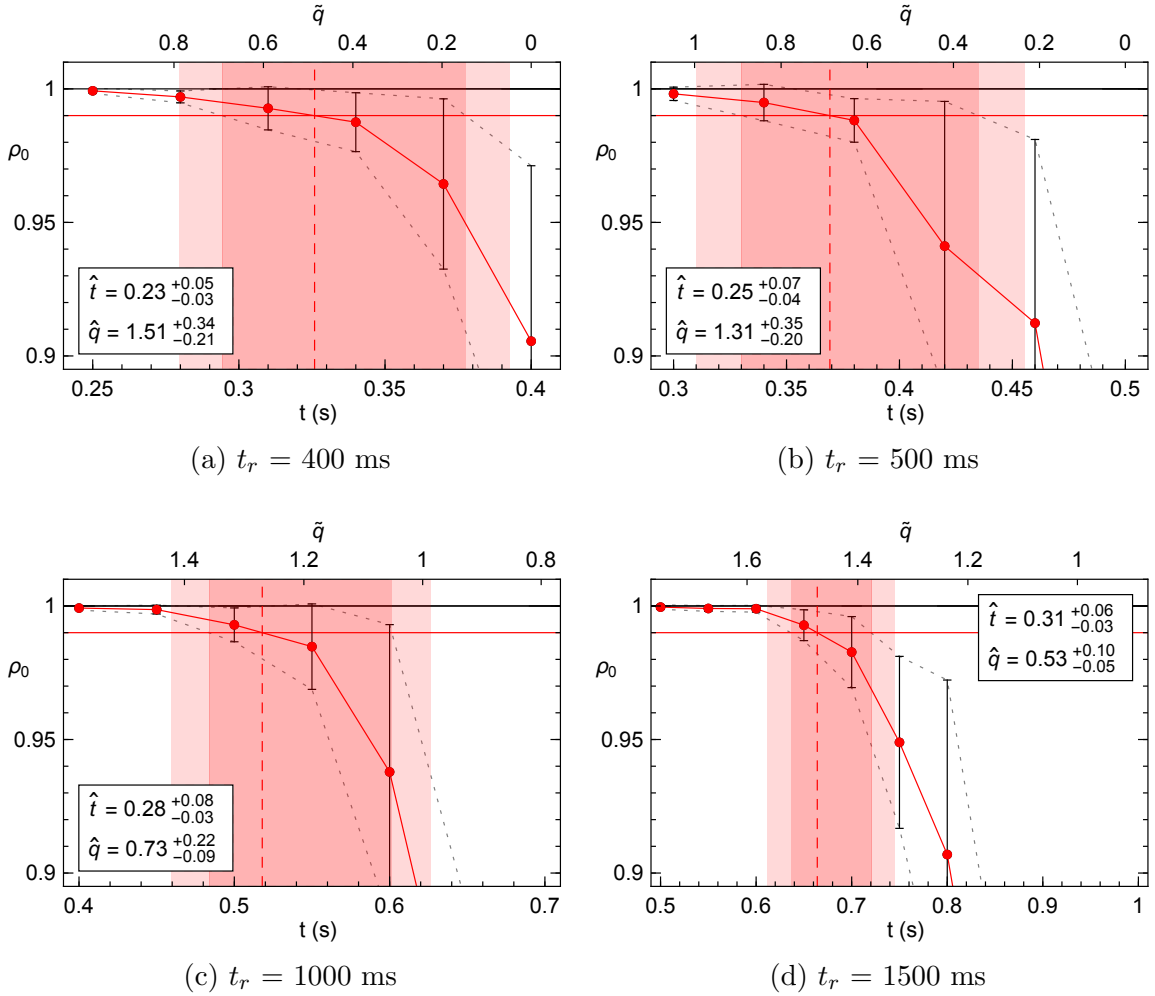


Figure D.4: **Measurements of ρ_0 during magnetic field ramps (data set #4).** The measurements of ρ_0 for all the ramp times from data set #4 are shown with the resulting values and errors of \hat{t} and \hat{q} . The ramps bring the magnetic field down from 500 mG to 0 mG in a time t_r .

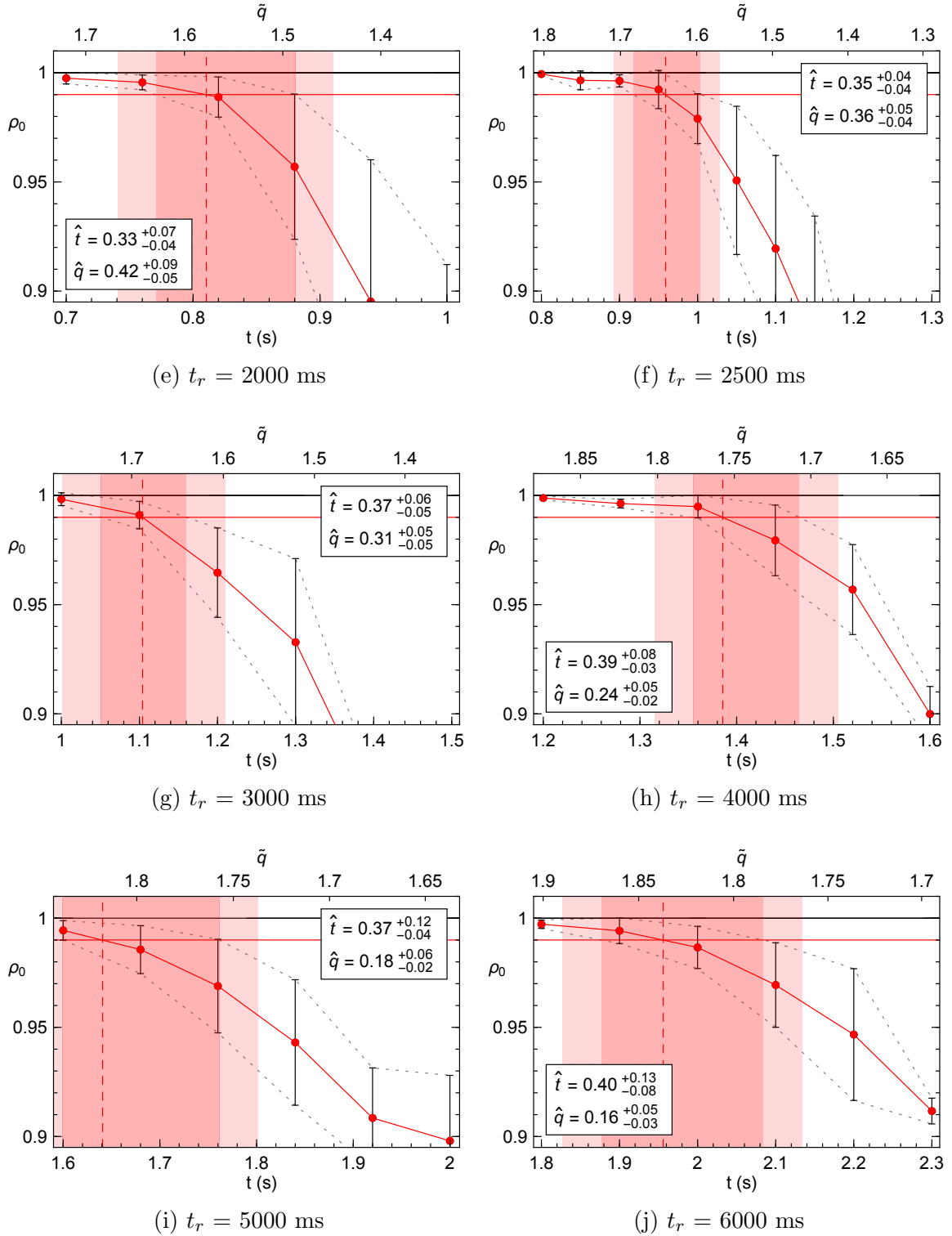
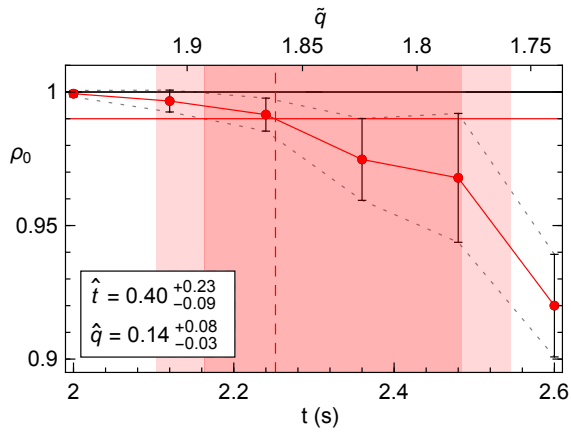
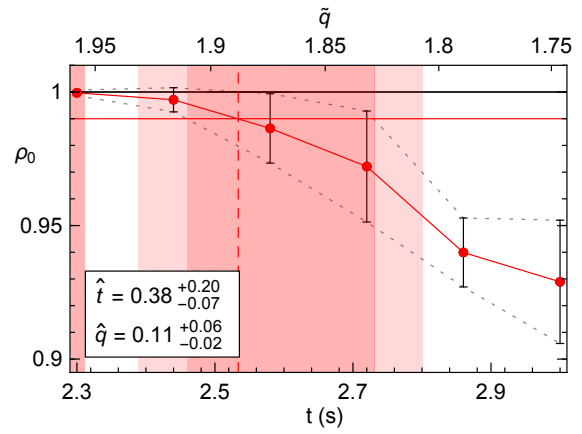


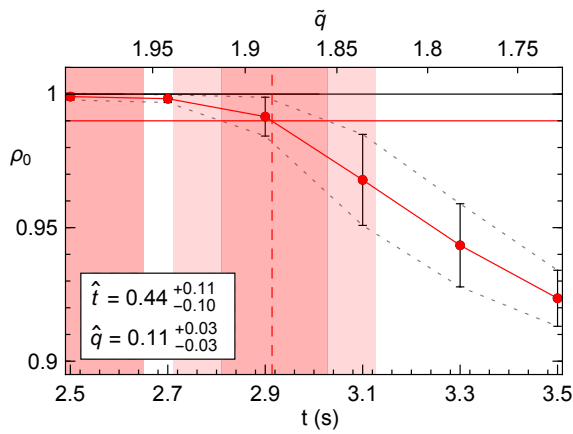
Figure D.4: Measurements of ρ_0 during magnetic field ramps (data set #4, continued).



(k) $t_r = 7000$ ms



(l) $t_r = 8000$ ms



(m) $t_r = 9000$ ms

Figure D.4: Measurements of ρ_0 during magnetic field ramps (data set #4, continued).

D.2 Plots of \hat{t} and \hat{q} for Every Data Set

In the following plots, \hat{q} and \hat{t} are plotted with respect to the characteristic magnetic field ramp time $\tilde{\tau}_Q$, given by the inverse of the rate of change of \tilde{q} at the critical point. The vertical error bars are found by combining the uncertainties in the determination of the time t_c when the system crosses the critical point and in the time t_{th} when the system crosses the ρ_0 (or $\Delta\rho_0$) threshold. The characteristic ramp times $\tilde{\tau}_Q$ integrate atom loss by including the changing value of c , whose initial value is calculated from the measurement of the magnetic field at the critical point. The error in the determination of the critical point therefore induces an uncertainty in $\tilde{\tau}_Q$ represented by the horizontal error bars. For every data point, a simulation is performed with the same experimental parameters (ramp time, number of atoms, and initial value of c) and their corresponding errors. For clarity, the simulations are plotted by interpolating between the output points as a gray dashed line, with a grey envelope displaying the error calculated using the same method as for the data. The insets show the data and simulations plotted in a log-log plot. Linear fits to the logarithm of the data and simulations give the scaling exponents. For the fits, the points represented by empty markers are not used, which restricts the fitting to the linear regions of the data, indicated by solid square markers. For each of the four data sets shown, the red plots show the values of \hat{q} and \hat{t} determined by measuring ρ_0 and using a threshold of $\rho_0 = 0.99$ to determine t_{th} . The blue plots use the standard deviation $\Delta\rho_0$ and a threshold of $\Delta\rho_0 = 0.01$.

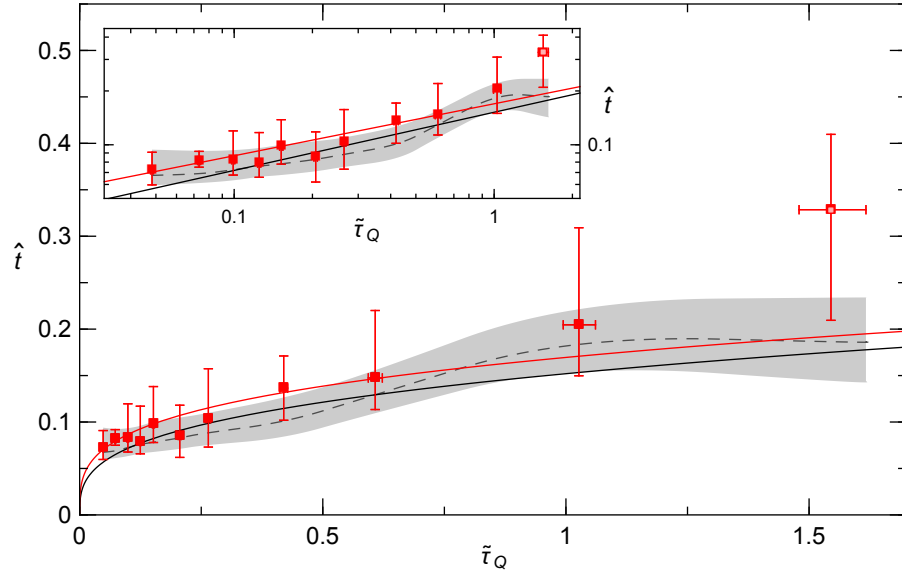


Figure D.5: **Data set #1**, \hat{t} , ρ_0 . Plot range: $0.048 < \tilde{\tau}_Q < 1.54$. Fit range: $0.048 < \tilde{\tau}_Q < 1.03$. Scaling exponents from fits: data: $0.28(7)$, simulations: $0.30(7)$.

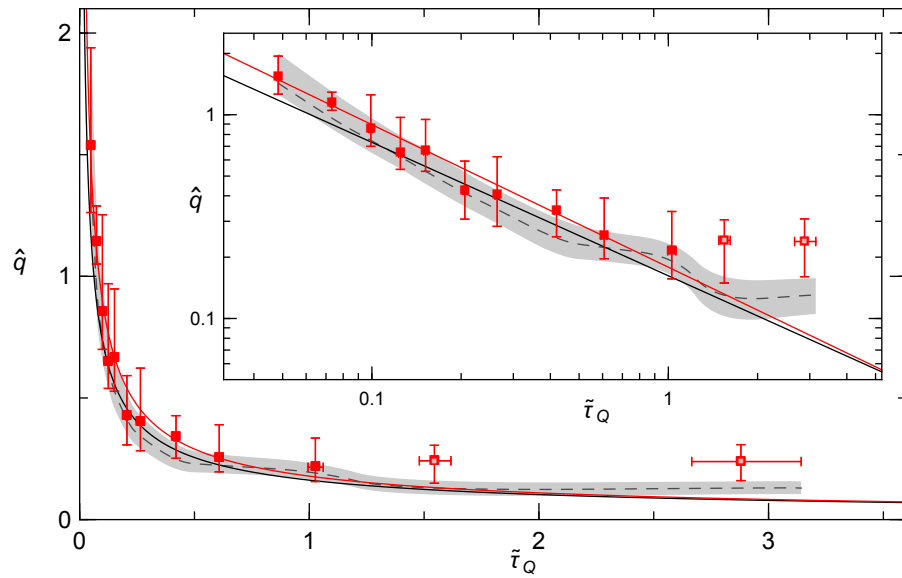


Figure D.6: **Data set #1**, \hat{q} , ρ_0 . Plot range: $0.048 < \tilde{\tau}_Q < 2.88$. Fit range: $0.048 < \tilde{\tau}_Q < 1.03$. Scaling exponents from fits: data: $-0.70(9)$, simulations: $-0.65(7)$.

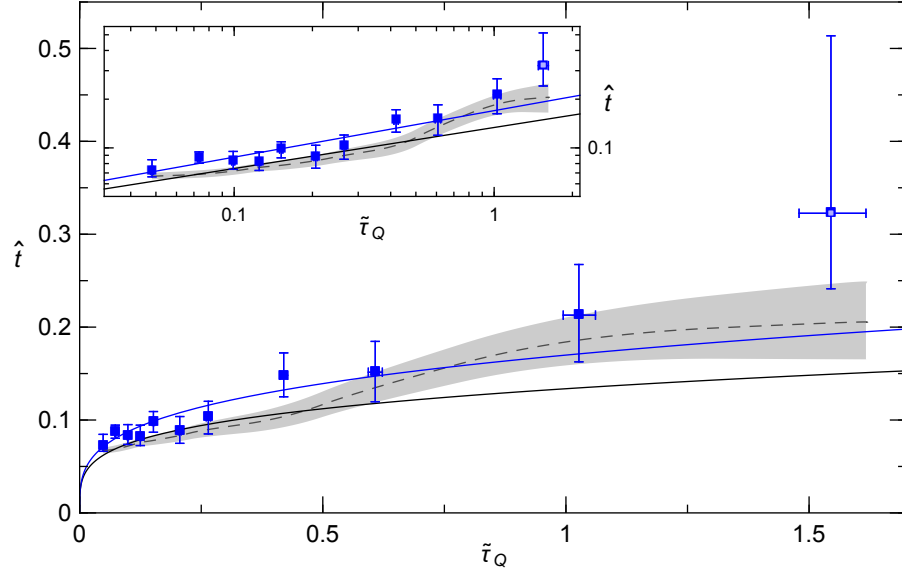


Figure D.7: **Data set #1**, \hat{t} , $\Delta\rho_0$. Plot range: $0.048 < \tilde{\tau}_Q < 1.54$. Fit range: $0.048 < \tilde{\tau}_Q < 1.03$. Scaling exponents from fits: data: $0.27(4)$, simulations: $0.24(3)$.

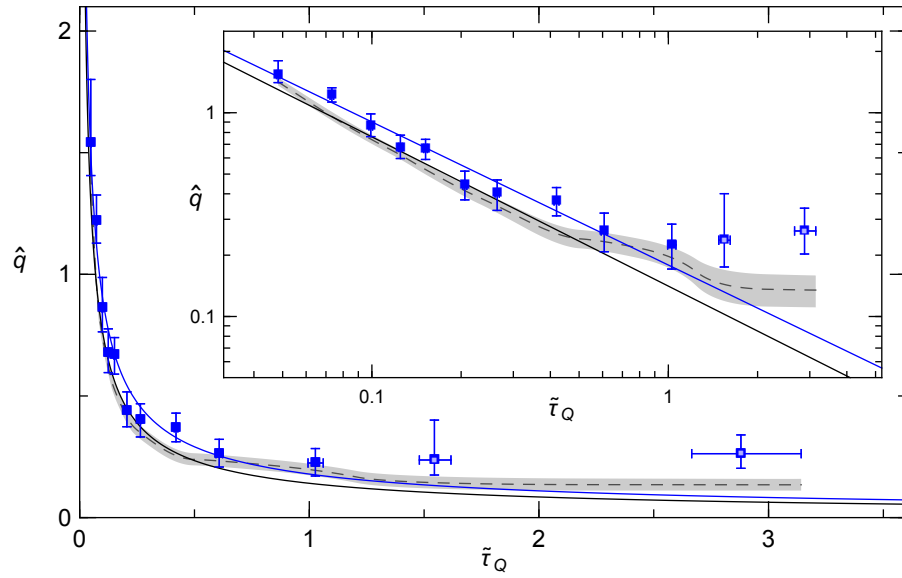


Figure D.8: **Data set #1**, \hat{q} , $\Delta\rho_0$. Plot range: $0.048 < \tilde{\tau}_Q < 2.88$. Fit range: $0.048 < \tilde{\tau}_Q < 1.03$. Scaling exponents from fits: data: $-0.70(6)$, simulations: $-0.65(3)$.

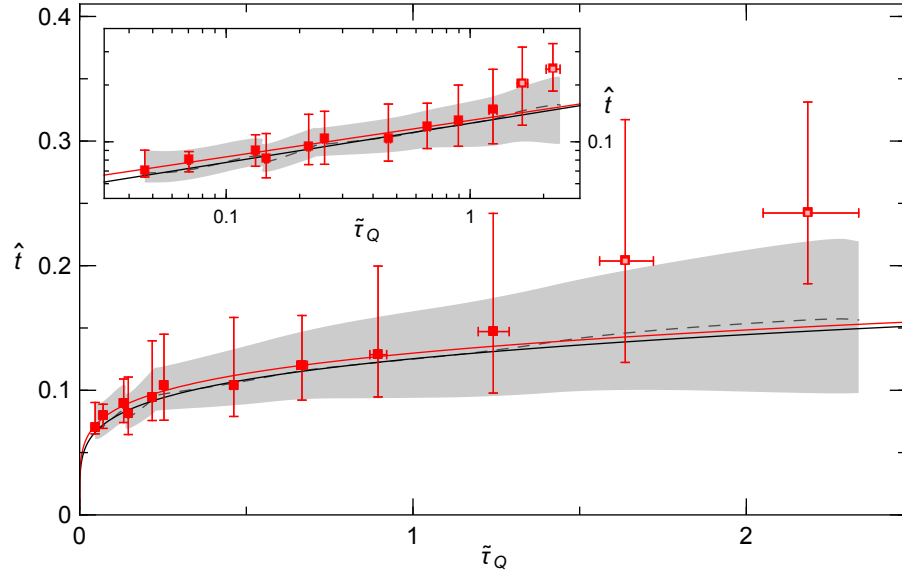


Figure D.9: **Data set #2**, \hat{t} , ρ_0 . Plot range: $0.046 < \tilde{\tau}_Q < 2.18$. Fit range: $0.048 < \tilde{\tau}_Q < 1.24$. Scaling exponents from fits: data: $0.18(7)$, simulations: $0.20(7)$.

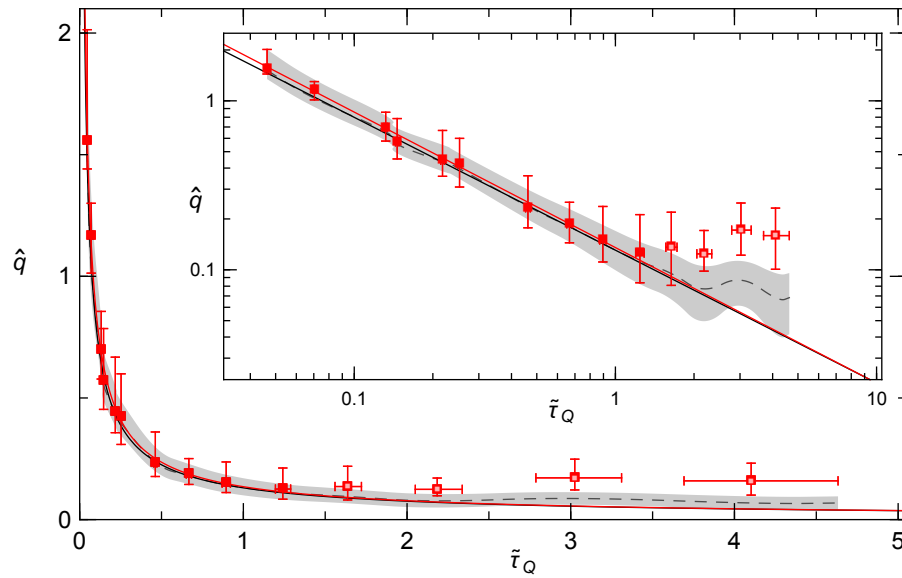


Figure D.10: **Data set #2**, \hat{q} , ρ_0 . Plot range: $0.046 < \tilde{\tau}_Q < 4.1$. Fit range: $0.048 < \tilde{\tau}_Q < 1.24$. Scaling exponents from fits: data: $-0.80(8)$, simulations: $-0.79(7)$.

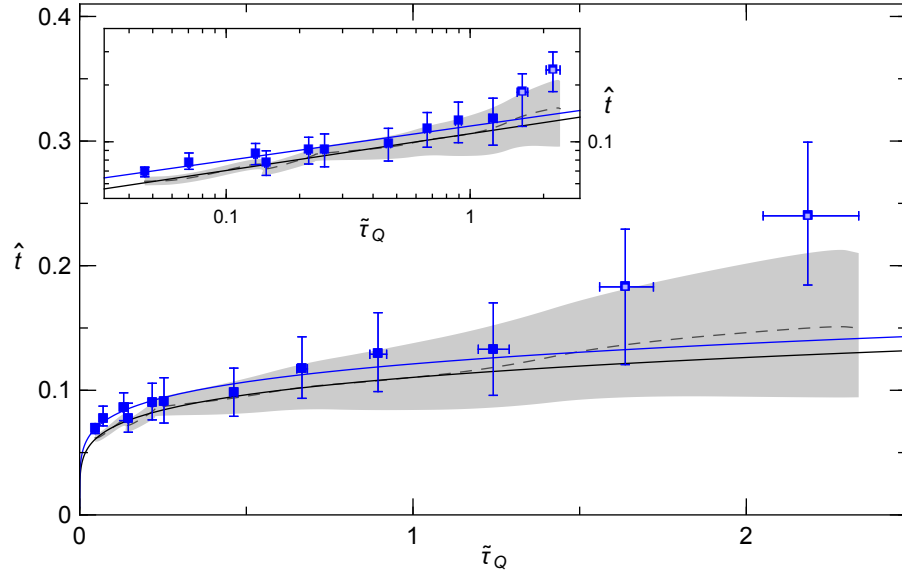


Figure D.11: **Data set #2**, \hat{t} , $\Delta\rho_0$. Plot range: $0.046 < \tilde{\tau}_Q < 2.18$. Fit range: $0.048 < \tilde{\tau}_Q < 1.24$. Scaling exponents from fits: data: $0.17(4)$, simulations: $0.19(4)$.

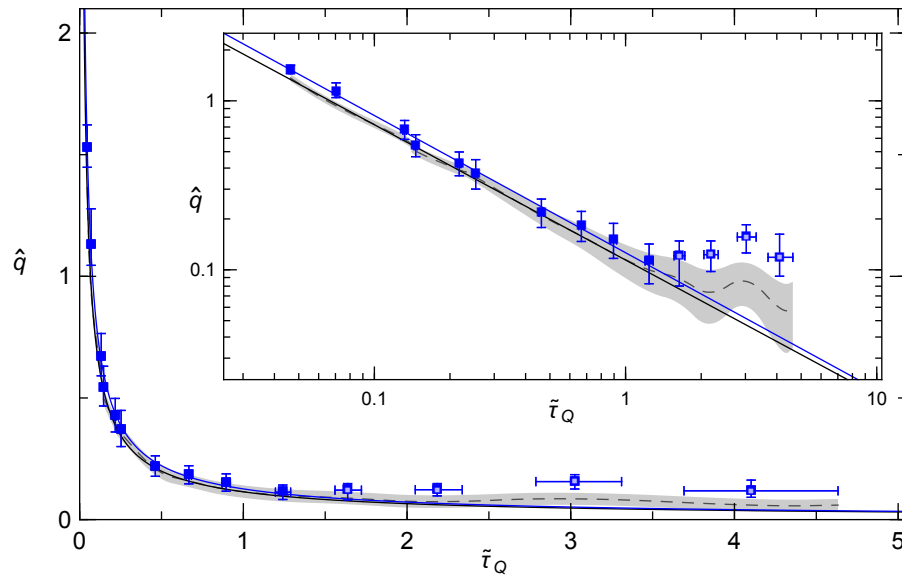


Figure D.12: **Data set #2**, \hat{q} , $\Delta\rho_0$. Plot range: $0.046 < \tilde{\tau}_Q < 4.1$. Fit range: $0.048 < \tilde{\tau}_Q < 1.24$. Scaling exponents from fits: data: $-0.81(4)$, simulations: $-0.80(3)$.

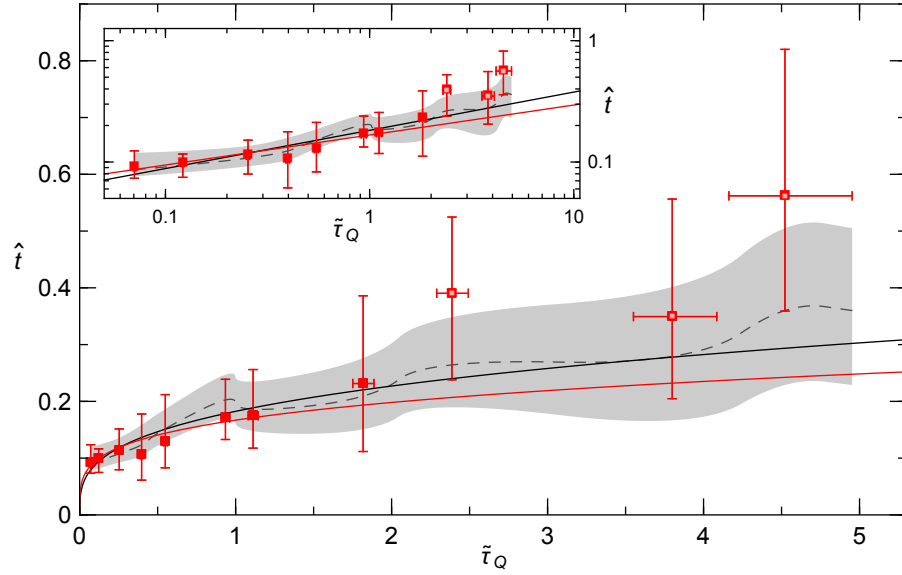


Figure D.13: **Data set #3**, \hat{t} , ρ_0 . Plot range: $0.07 < \tilde{\tau}_Q < 4.52$. Fit range: $0.07 < \tilde{\tau}_Q < 1.82$. Scaling exponents from fits: data: $0.20(9)$, simulations: $0.26(8)$.

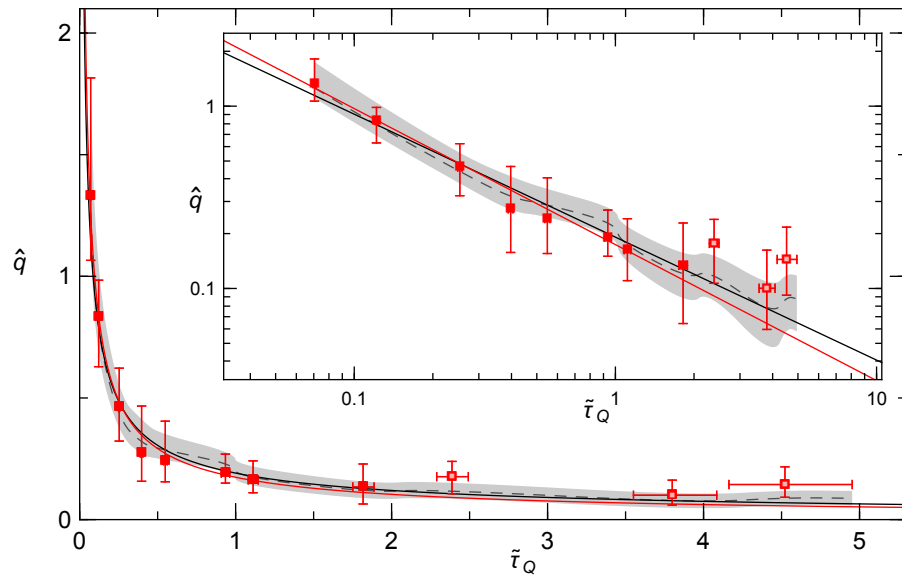


Figure D.14: **Data set #3**, \hat{q} , ρ_0 . Plot range: $0.07 < \tilde{\tau}_Q < 4.52$. Fit range: $0.07 < \tilde{\tau}_Q < 1.81$. Scaling exponents from fits: data: $-0.75(11)$, simulations: $-0.67(8)$.

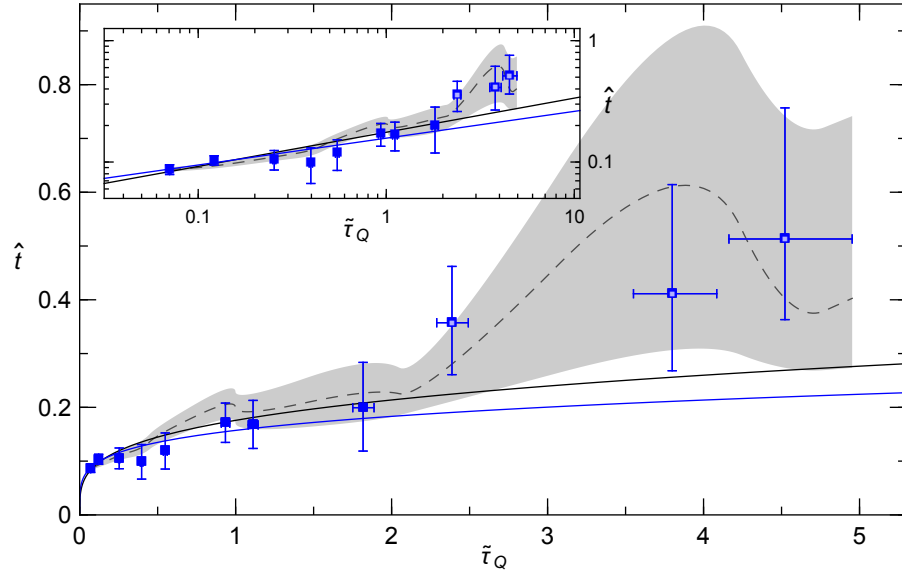


Figure D.15: **Data set #3**, \hat{t} , $\Delta\rho_0$. Plot range: $0.07 < \tilde{\tau}_Q < 4.52$. Fit range: $0.07 < \tilde{\tau}_Q < 1.82$. Scaling exponents from fits: data: $0.17(5)$, simulations: $0.25(4)$.

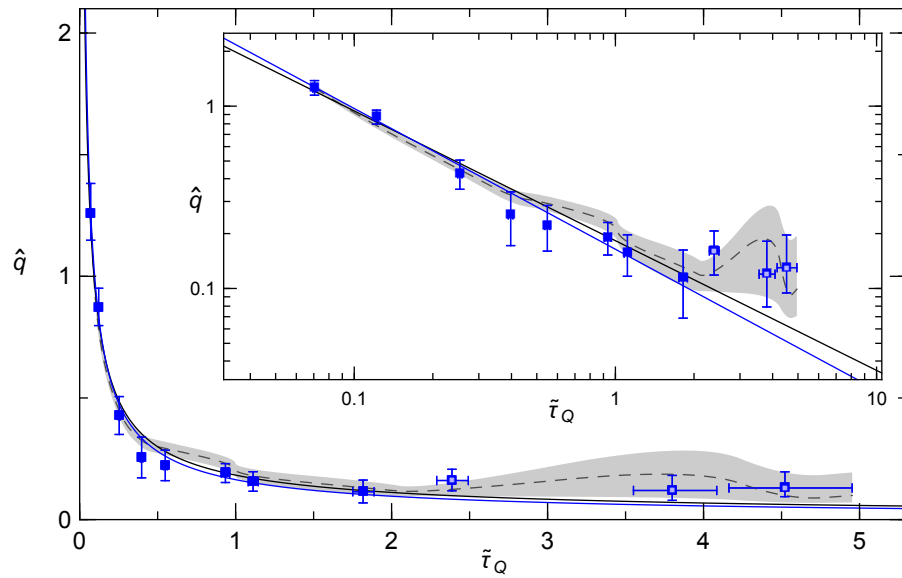


Figure D.16: **Data set #3**, \hat{q} , $\Delta\rho_0$. Plot range: $0.07 < \tilde{\tau}_Q < 4.52$. Fit range: $0.07 < \tilde{\tau}_Q < 1.81$. Scaling exponents from fits: data: $-0.77(6)$, simulations: $-0.70(3)$.

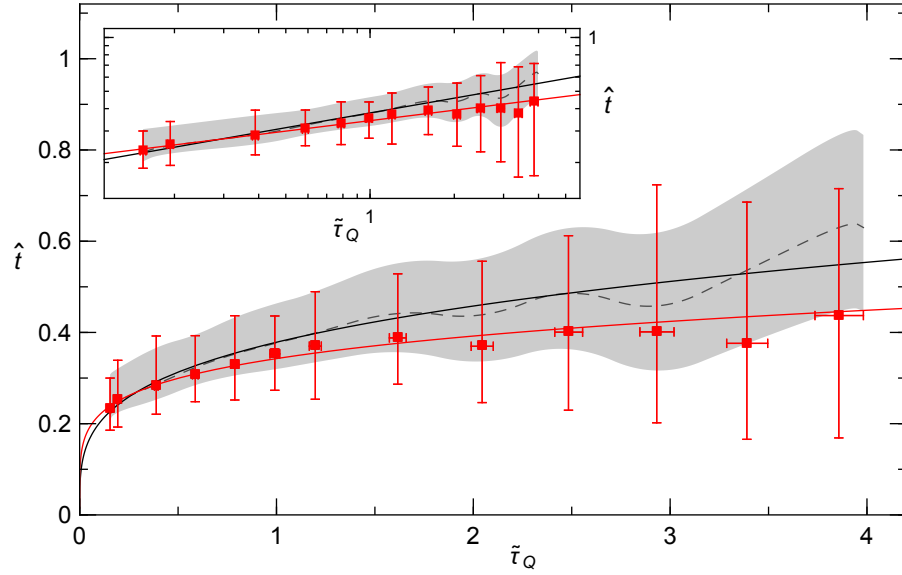


Figure D.17: **Data set #4**, \hat{t} , ρ_0 . Plot range: $0.15 < \tilde{\tau}_Q < 3.86$. Fit range: $0.15 < \tilde{\tau}_Q < 3.86$. Scaling exponents from fits: data: $0.17(8)$, simulations: $0.24(9)$.

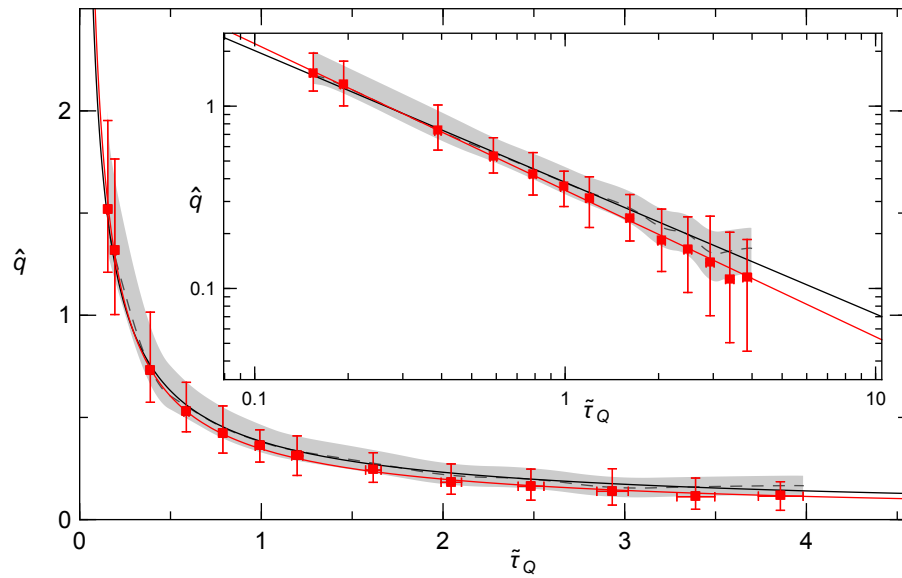


Figure D.18: **Data set #4**, \hat{q} , ρ_0 . Plot range: $0.15 < \tilde{\tau}_Q < 3.86$. Fit range: $0.15 < \tilde{\tau}_Q < 3.86$. Scaling exponents from fits: data: $-0.80(10)$, simulations: $-0.74(7)$.

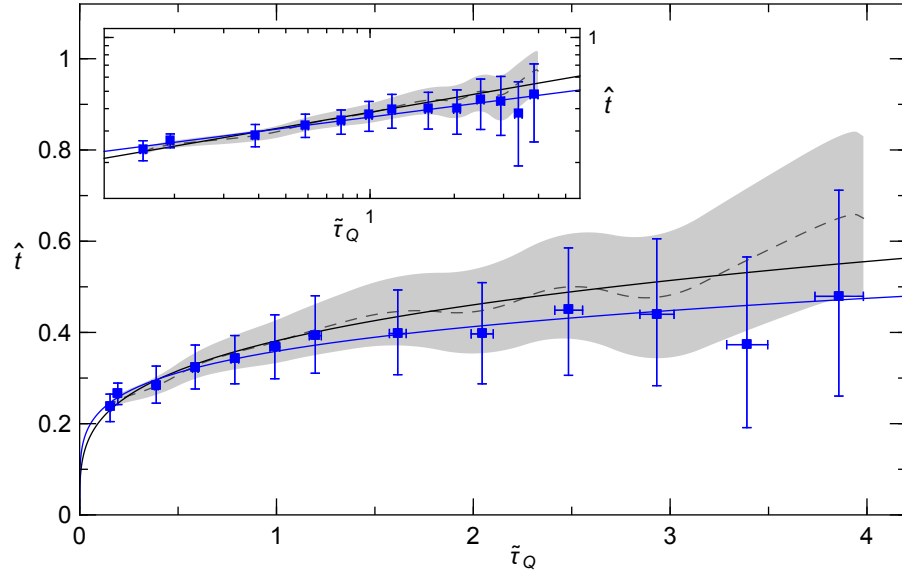


Figure D.19: **Data set #4**, \hat{t} , $\Delta\rho_0$. Plot range: $0.15 < \tilde{\tau}_Q < 3.86$. Fit range: $0.15 < \tilde{\tau}_Q < 3.86$. Scaling exponents from fits: data: $0.18(5)$, simulations: $0.25(4)$.

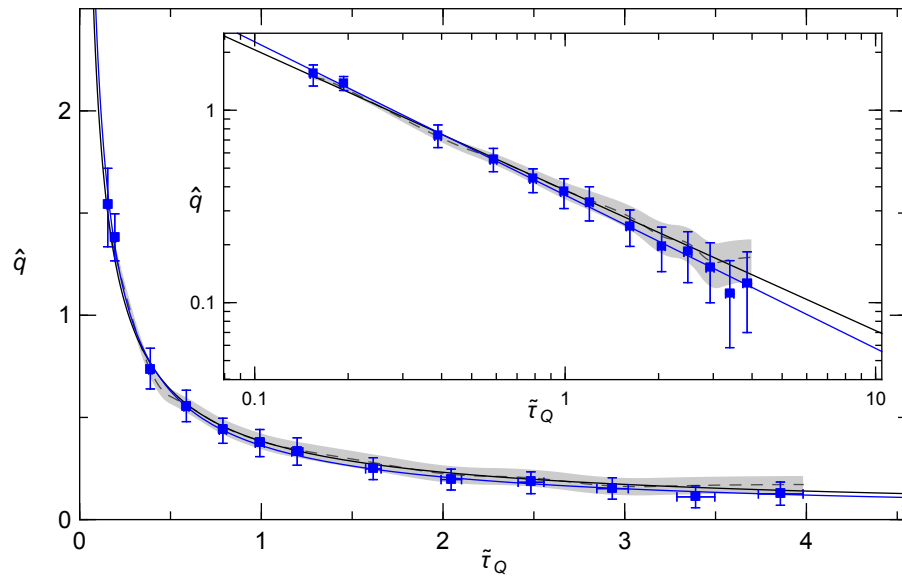


Figure D.20: **Data set #4**, \hat{q} , $\Delta\rho_0$. Plot range: $0.15 < \tilde{\tau}_Q < 3.86$. Fit range: $0.15 < \tilde{\tau}_Q < 3.86$. Scaling exponents from fits: data: $-0.80(5)$, simulations: $-0.73(7)$.

REFERENCES

- [1] T. Kibble, “Topology of cosmic domains and strings,” *J. Phys. A* **9**, 1387 (1976).
- [2] W. Zurek, “Cosmological experiments in superfluid helium?,” *Nature* **317**, 505 (1985).
- [3] S. Sachdev, *Quantum Phase Transitions* (Cambridge University Press, Cambridge, UK, 1999).
- [4] C. Pethick and H. Smith, *Bose-Einstein condensation in dilute gases* (Cambridge University Press, 2002).
- [5] W. C. Stwalley and L. H. Nosanow, “Possible ‘New’ Quantum Systems,” *Phys. Rev. Lett.* **36**, 910 (1976).
- [6] I. F. Silvera and J. T. M. Walraven, “Stabilization of Atomic Hydrogen at Low Temperature,” *Phys. Rev. Lett.* **44**, 164 (1980).
- [7] E. L. Raab, M. Prentiss, A. Cable, S. Chu, and D. E. Pritchard, “Trapping of Neutral Sodium Atoms with Radiation Pressure,” *Phys. Rev. Lett.* **59**, 2631 (1987).
- [8] C. Monroe, W. Swann, H. Robinson, and C. Wieman, “Very cold trapped atoms in a vapor cell,” *Phys. Rev. Lett.* **65**, 1571 (1990).
- [9] M. H. Anderson, J. R. Ensher, M. R. Matthews, C. E. Wieman, and E. A. Cornell, “Observation of Bose-Einstein Condensation in a Dilute Atomic Vapor,” *Science* **269**, pp. 198 (1995).
- [10] K. B. Davis, M. O. Mewes, M. R. Andrews, N. J. van Druten, D. S. Durfee, D. M. Kurn, and W. Ketterle, “Bose-Einstein Condensation in a Gas of Sodium Atoms,” *Phys. Rev. Lett.* **75**, 3969 (1995).
- [11] C. C. Bradley, C. A. Sackett, and R. G. Hulet, “Bose-Einstein Condensation of Lithium: Observation of Limited Condensate Number,” *Phys. Rev. Lett.* **78**, 985 (1997).
- [12] M. R. Andrews, C. G. Townsend, H.-J. Miesner, D. S. Durfee, D. M. Kurn, and W. Ketterle, “Observation of Interference between Two Bose Condensates,” *Science* **275**, pp. 637 (1997).
- [13] I. Bloch, T. W. Hänsch, and T. Esslinger, “Measurement of the spatial coherence of a trapped bose gas at the phase transition,” *Nature* **403**, 166 (2000).
- [14] M.-O. Mewes, M. R. Andrews, D. M. Kurn, D. S. Durfee, C. G. Townsend, and W. Ketterle, “Output Coupler for Bose-Einstein Condensed Atoms,” *Phys. Rev. Lett.* **78**, 582 (1997).

- [15] E. W. Hagley, L. Deng, M. Kozuma, J. Wen, K. Helmerson, S. L. Rolston, and W. D. Phillips, “A Well-Collimated Quasi-Continuous Atom Laser,” *Science* **283**, 1706 (1999).
- [16] I. Bloch, T. W. Hänsch, and T. Esslinger, “Atom Laser with a cw Output Coupler,” *Phys. Rev. Lett.* **82**, 3008 (1999).
- [17] B. P. Anderson and M. A. Kasevich, “Macroscopic Quantum Interference from Atomic Tunnel Arrays,” *Science* **282**, 1686 (1998).
- [18] M. Albiez, R. Gati, J. Fölling, S. Hunsmann, M. Cristiani, and M. K. Oberthaler, “Direct Observation of Tunneling and Nonlinear Self-Trapping in a Single Bosonic Josephson Junction,” *Phys. Rev. Lett.* **95**, 010402 (2005).
- [19] D. M. Stamper-Kurn, M. R. Andrews, A. P. Chikkatur, S. Inouye, H.-J. Miesner, J. Stenger, and W. Ketterle, “Optical Confinement of a Bose-Einstein Condensate,” *Phys. Rev. Lett.* **80**, 2027 (1998).
- [20] M. D. Barrett, J. A. Sauer, and M. S. Chapman, “All-Optical Formation of an Atomic Bose-Einstein Condensate,” *Phys. Rev. Lett.* **87**, 010404 (2001).
- [21] S. Inouye, M. R. Andrews, J. Stenger, H.-J. Miesner, D. M. Stamper-Kurn, and W. Ketterle, “Observation of Feshbach resonances in a Bose-Einstein condensate,” *Nature* **392**, 151 (1998).
- [22] H.-J. Miesner, D. M. Stamper-Kurn, J. Stenger, S. Inouye, A. P. Chikkatur, and W. Ketterle, “Observation of Metastable States in Spinor Bose-Einstein Condensates,” *Phys. Rev. Lett.* **82**, 2228 (1999).
- [23] D. M. Stamper-Kurn, H.-J. Miesner, A. P. Chikkatur, S. Inouye, J. Stenger, and W. Ketterle, “Quantum Tunneling across Spin Domains in a Bose-Einstein Condensate,” *Phys. Rev. Lett.* **83**, 661 (1999).
- [24] L. E. Sadler, J. M. Higbie, S. R. Leslie, M. Vengalattore, and D. M. Stamper-Kurn, “Spontaneous symmetry breaking in a quenched ferromagnetic spinor Bose-Einstein condensate,” *Nature* **443**, 312 (2006).
- [25] M. Vengalattore, S. R. Leslie, J. Guzman, and D. M. Stamper-Kurn, “Spontaneously Modulated Spin Textures in a Dipolar Spinor Bose-Einstein Condensate,” *Phys. Rev. Lett.* **100**, 170403 (2008).
- [26] L. S. Leslie, A. Hansen, K. C. Wright, B. M. Deutsch, and N. P. Bigelow, “Creation and Detection of Skyrmions in a Bose-Einstein Condensate,” *Phys. Rev. Lett.* **103**, 250401 (2009).
- [27] M.-S. Chang, Q. Qin, W. Zhang, and M. S. Chapman, “Coherent spinor dynamics in a spin-1 Bose condensate,” *Nature Physics* **1**, 111 (2005).

- [28] Y. Kawaguchi and M. Ueda, “Spinor Bose–Einstein Condensates,” *Physics Reports* **520**, 253 (2012).
- [29] D. M. Stamper-Kurn and M. Ueda, “Spinor Bose gases: Symmetries, magnetism, and quantum dynamics,” *Reviews of Modern Physics* **85**, 1191 (2013).
- [30] M.-S. Chang, C. D. Hamley, M. D. Barrett, J. A. Sauer, K. M. Fortier, W. Zhang, L. You, and M. S. Chapman, “Observation of Spinor Dynamics in Optically Trapped ^{87}Rb Bose-Einstein Condensates,” *Phys. Rev. Lett.* **92**, 140403 (2004).
- [31] E. M. Bookjans, C. D. Hamley, and M. S. Chapman, “Strong Quantum Spin Correlations Observed in Atomic Spin Mixing,” *Phys. Rev. Lett.* **107**, 210406 (2011).
- [32] E. M. Bookjans, *Relative Number Squeezing in a Spin-1 Bose-Einstein Condensate*, PhD thesis Georgia Institute of Technology 2010.
- [33] C. Hamley, C. Gerving, T. Hoang, E. Bookjans, and M. Chapman, “Spin-nematic squeezed vacuum in a quantum gas,” *Nature Phys.* **8**, 305 (2012).
- [34] H.-A. Bachor and T. C. Ralph, *A guide to experiments in quantum optics* (Wiley-VCH, 2004).
- [35] C. Gross, T. Zibold, E. Nicklas, J. Estève, and M. K. Oberthaler, “Nonlinear atom interferometer surpasses classical precision limit,” *Nature* **464**, 1165 (2010).
- [36] M. F. Riedel, P. Böhi, Y. Li, T. W. Hänsch, A. Sinatra, and P. Treutlein, “Atom-chip-based generation of entanglement for quantum metrology,” *Nature* **464**, 1170 (2010).
- [37] M. Koschorreck, M. Napolitano, B. Dubost, and M. W. Mitchell, “Sub-Projection-Noise Sensitivity in Broadband Atomic Magnetometry,” *Phys. Rev. Lett.* **104**, 093602 (2010).
- [38] W. Wasilewski, K. Jensen, H. Krauter, J. J. Renema, M. V. Balabas, and E. S. Polzik, “Quantum Noise Limited and Entanglement-Assisted Magnetometry,” *Phys. Rev. Lett.* **104**, 133601 (2010).
- [39] J. Appel, P. J. Windpassinger, D. Oblak, U. B. Hoff, N. Kjærgaard, and E. S. Polzik, “Mesoscopic atomic entanglement for precision measurements beyond the standard quantum limit,” *Proceedings of the National Academy of Sciences* **106**, 10960 (2009).
- [40] A. Louchet-Chauvet, J. Appel, J. J. Renema, D. Oblak, N. Kjaergaard, and E. S. Polzik, “Entanglement-assisted atomic clock beyond the projection noise limit,” *New Journal of Physics* **12**, 065032 (2010).

- [41] C. D. Hamley, *Spin-Nematic Squeezing in a Spin-1 Bose Einstein Condensate*, PhD thesis Georgia Institute of Technology 2012.
- [42] C. S. Gerving, *Dynamics of a spin-1 BEC in the regime of a quantum inverted pendulum*, PhD thesis Georgia Institute of Technology 2013.
- [43] C. S. Gerving, T. M. Hoang, B. J. Land, M. Anquez, C. D. Hamley, and M. S. Chapman, “Non-equilibrium dynamics of an unstable quantum pendulum explored in a spin-1 Bose-Einstein condensate,” *Nat. Commun.* (2012).
- [44] T. M. Hoang, C. S. Gerving, B. J. Land, M. Anquez, C. D. Hamley, and M. S. Chapman, “Dynamic Stabilization of a Quantum Many-Body Spin System,” *Phys. Rev. Lett.* **111**, 090403 (2013).
- [45] N. Goldenfeld, “Lectures on phase transitions and the renormalization group,” (1992).
- [46] R. Pathria and P. Beale, *Statistical Mechanics* (Elsevier Science, 1996).
- [47] S. Blundell and K. M. Blundell, *Concepts in Thermal Physics* (Oxford University Press, 2010).
- [48] J. M. Yeomans, *Statistical mechanics of phase transitions* (Oxford University Press, 1992).
- [49] D. Layzer, *Cosmogogenesis, The Development of Order in the Universe* (Oxford Univ. Press, 1991).
- [50] E. J. Chaisson and E. Chaisson, *Cosmic evolution: the rise of complexity in nature* (Harvard University Press, 2002).
- [51] G. Jotzu, M. Messer, R. Desbuquois, M. Lebrat, T. Uehlinger, D. Greif, and T. Esslinger, “Experimental realization of the topological Haldane model with ultracold fermions,” *Nature* **515**, 237 (2014).
- [52] L. Pryadko and S.-C. Zhang, “Fluctuation-Induced First Order Transition between the Quantum Hall Liquid and Insulator,” *Phys. Rev. Lett.* **73**, 3282 (1994).
- [53] A. Leviatan, “First-order quantum phase transition in a finite system,” *Phys. Rev. C* **74**, 051301 (2006).
- [54] M. Amin and V. Choi, “First-order quantum phase transition in adiabatic quantum computation,” *Phys. Rev. A* **80**, 062326 (2009).
- [55] P. Jakubczyk, W. Metzner, and H. Yamase, “Turning a First Order Quantum Phase Transition Continuous by Fluctuations: General Flow Equations and Application to d-Wave Pomeranchuk Instability,” *Phys. Rev. Lett.* **103**, 220602 (2009).

- [56] J. Dziarmaga, “Dynamics of a quantum phase transition: Exact solution of the quantum Ising model,” *Phys. Rev. Lett.* **95**, 245701 (2005).
- [57] M. Greiner, O. Mandel, T. Esslinger, T. W. Hänsch, and I. Bloch, “Quantum phase transition from a superfluid to a Mott insulator in a gas of ultracold atoms,” *Nature* **415**, 39 (2002).
- [58] W. S. Bakr, A. Peng, M. E. Tai, R. Ma, J. Simon, J. I. Gillen, S. Foelling, L. Pollet, and M. Greiner, “Probing the superfluid–to–mott insulator transition at the single-atom level,” *Science* **329**, 547 (2010).
- [59] D. Chen, M. White, C. Borries, and B. DeMarco, “Quantum Quench of an Atomic Mott Insulator,” *Phys. Rev. Lett.* **106**, 235304 (2011).
- [60] J. Dziarmaga, M. Tylutki, and W. H. Zurek, “Quench from Mott insulator to superfluid,” *Phys. Rev. B* **86**, 144521 (2012).
- [61] M. Vojta, “Quantum phase transitions,” *Reports on Progress in Physics* **66**, 2069 (2003).
- [62] B. Damski and W. H. Zurek, “Dynamics of a Quantum Phase Transition in a Ferromagnetic Bose-Einstein Condensate,” *Phys. Rev. Lett.* **99**, 130402 (2007).
- [63] B. Damski and W. H. Zurek, “How to fix a broken symmetry: quantum dynamics of symmetry restoration in a ferromagnetic Bose-Einstein condensate,” *New J. Phys.* **10**, 045023 (2008).
- [64] G. I. Mias, N. R. Cooper, and S. M. Girvin, “Quantum noise, scaling, and domain formation in a spinor Bose-Einstein condensate,” *Phys. Rev. A* **77**, 023616 (2008).
- [65] S. Sondhi, S. Girvin, J. Carini, and D. Shahar, “Continuous quantum phase transitions,” *Rev. of Mod. Phys.* **69**, 315 (1997).
- [66] T. W. Kibble, “Some implications of a cosmological phase transition,” *Phys. Rep.* **67**, 183 (1980).
- [67] W. Zurek, “Cosmic strings in laboratory superfluids and the topological remnants of other phase transitions,” *Acta. Phys. Pol. B* **24**, 1301 (1993).
- [68] W. H. Zurek, “Cosmological experiments in condensed matter systems,” *Phys. Rep.* **276**, 177 (1996).
- [69] P. Laguna and W. H. Zurek, “Density of kinks after a quench: When symmetry breaks, how big are the pieces?,” *Phys. Rev. Lett.* **78**, 2519 (1997).
- [70] P. Laguna and W. H. Zurek, “Critical dynamics of symmetry breaking: quenches, dissipation, and cosmology,” *Phys. Rev. D* **58**, 085021 (1998).

- [71] A. Yates and W. H. Zurek, “Vortex formation in two dimensions: When symmetry breaks, how big are the pieces?,” *Phys. Rev. Lett.* **80**, 5477 (1998).
- [72] J. Anglin and W. Zurek, “Vortices in the wake of rapid Bose-Einstein condensation,” *Phys. Rev. Lett.* **83**, 1707 (1999).
- [73] J. Dziarmaga, P. Laguna, and W. H. Zurek, “Symmetry breaking with a slant: topological defects after an inhomogeneous quench,” *Phys. Rev. Lett.* **82**, 4749 (1999).
- [74] N. D. Antunes, L. M. Bettencourt, and W. H. Zurek, “Vortex string formation in a 3D U(1) temperature quench,” *Phys. Rev. Lett.* **82**, 2824 (1999).
- [75] G. Stephens, E. Calzetta, B. Hu, and S. Ramsey, “Defect formation and critical dynamics in the early universe,” *Phys. Rev. D* **59**, 045009 (1999).
- [76] G. Stephens, L. M. Bettencourt, and W. Zurek, “Critical dynamics of gauge systems: spontaneous vortex formation in 2D superconductors,” *Phys. Rev. Lett.* **88**, 137004 (2002).
- [77] W. H. Zurek, U. Dorner, and P. Zoller, “Dynamics of a Quantum Phase Transition,” *Phys. Rev. Lett.* **95**, 105701 (2005).
- [78] A. Polkovnikov, “Universal adiabatic dynamics in the vicinity of a quantum critical point,” *Phys. Rev. B* **72**, 161201 (2005).
- [79] B. Damski and W. H. Zurek, “Adiabatic-impulse approximation for avoided level crossings: From phase-transition dynamics to Landau-Zener evolutions and back again,” *Phys. Rev. A* **73**, 063405 (2006).
- [80] R. Cherng and L. Levitov, “Entropy and correlation functions of a driven quantum spin chain,” *Phys. Rev. A* **73**, 043614 (2006).
- [81] A. Fubini, G. Falci, and A. Osterloh, “Robustness of adiabatic passage through a quantum phase transition,” *New J. Phys.* **9**, 134 (2007).
- [82] W. H. Zurek, “Causality in condensates: gray solitons as relics of BEC formation,” *Phys. Rev. Lett.* **102**, 105702 (2009).
- [83] J. Dziarmaga, “Dynamics of a quantum phase transition and relaxation to a steady state,” *Adv. Phys.* **59**, 1063 (2010).
- [84] I. Chuang, R. Durrer, N. Turok, and B. Yurke, “Cosmology in the Laboratory: Defect Dynamics in Liquid Crystals,” *Science* **251**, 1336 (1991).
- [85] M. J. Bowick, L. Chandar, E. A. Schiff, and A. M. Srivastava, “The Cosmological Kibble Mechanism in the Laboratory: String Formation in Liquid Crystals,” *Science* **263**, 943 (1994).

- [86] P. Hendry, N. Lawson, R. Lee, P. V. McClintock, and C. Williams, “Generation of defects in superfluid 4He as an analogue of the formation of cosmic strings,” *Nature* **368**, 315 (1994).
- [87] V. Ruutu, V. Eltsov, A. Gill, T. Kibble, M. Krusius, Y. G. Makhlin, B. Placais, G. Volovik, and W. Xu, “Vortex formation in neutron-irradiated superfluid 3He as an analogue of cosmological defect formation,” *Nature* **382**, 334 (1996).
- [88] C. Bäuerle, Y. M. Bunkov, S. Fisher, H. Godfrin, and G. Pickett, “Laboratory simulation of cosmic string formation in the early Universe using superfluid 3He ,” *Nature* **382**, 332 (1996).
- [89] S. Ducci, P. L. Ramazza, W. González-Viñas, and F. T. Arecchi, “Order Parameter Fragmentation after a Symmetry-Breaking Transition,” *Phys. Rev. Lett.* **83**, 5210 (1999).
- [90] A. Monaco, A. I. Chumakov, Y.-Z. Yue, G. Monaco, L. Comez, D. Fioretto, W. A. Crichton, and R. Rüffer, “Density of Vibrational States of a Hyperquenched Glass,” *Phys. Rev. Lett.* **96**, 205502 (2006).
- [91] R. Carmi, E. Polturak, and G. Koren, “Observation of Spontaneous Flux Generation in a Multi-Josephson-Junction Loop,” *Phys. Rev. Lett.* **84**, 4966 (2000).
- [92] A. Maniv, E. Polturak, and G. Koren, “Observation of Magnetic Flux Generated Spontaneously During a Rapid Quench of Superconducting Films,” *Phys. Rev. Lett.* **91**, 197001 (2003).
- [93] A. Del Campo, G. De Chiara, G. Morigi, M. Plenio, and A. Retzker, “Structural defects in ion chains by quenching the external potential: the inhomogeneous Kibble-Zurek mechanism,” *Phys. Rev. Lett.* **105**, 075701 (2010).
- [94] K. Pyka *et al.*, “Topological defect formation and spontaneous symmetry breaking in ion Coulomb crystals,” *Nat. Commun.* **4** (2013).
- [95] S. Ejtemaee and P. Haljan, “Spontaneous nucleation and dynamics of kink defects in zigzag arrays of trapped ions,” *Phys. Rev. A* **87**, 051401 (2013).
- [96] S. Ulm *et al.*, “Observation of the Kibble–Zurek scaling law for defect formation in ion crystals,” *Nat. Commun.* **4** (2013).
- [97] T. Donner, S. Ritter, T. Bourdel, A. Öttl, M. Köhl, and T. Esslinger, “Critical behavior of a trapped interacting Bose gas,” *Science* **315**, 1556 (2007).
- [98] X. Zhang, C.-L. Hung, S.-K. Tung, and C. Chin, “Observation of quantum criticality with ultracold atoms in optical lattices,” *Science* **335**, 1070 (2012).
- [99] N. Navon, A. L. Gaunt, R. P. Smith, and Z. Hadzibabic, “Critical dynamics of spontaneous symmetry breaking in a homogeneous Bose gas,” *Science* **347**, 167 (2015).

- [100] G. Lamporesi, S. Donadello, S. Serafini, F. Dalfovo, and G. Ferrari, “Spontaneous creation of Kibble-Zurek solitons in a Bose-Einstein condensate,” *Nature Phys.* **9**, 656 (2013).
- [101] D. R. Scherer, C. N. Weiler, T. W. Neely, and B. P. Anderson, “Vortex Formation by Merging of Multiple Trapped Bose-Einstein Condensates,” *Phys. Rev. Lett.* **98**, 110402 (2007).
- [102] C. N. Weiler, T. W. Neely, D. R. Scherer, A. S. Bradley, M. J. Davis, and B. P. Anderson, “Spontaneous vortices in the formation of Bose-Einstein condensates,” *Nature* **455**, 948 (2008).
- [103] L. Corman, L. Chomaz, T. Bienaimé, R. Desbuquois, C. Weitenberg, S. Nascimbene, J. Dalibard, and J. Beugnon, “Quench-induced supercurrents in an annular Bose gas,” *Phys. Rev. Lett.* **113**, 135302 (2014).
- [104] S. Braun, M. Friesdorf, S. S. Hodgman, M. Schreiber, J. P. Ronzheimer, A. Rivera, M. del Rey, I. Bloch, J. Eisert, and U. Schneider, “Emergence of coherence and the dynamics of quantum phase transitions,” *Proceedings of the National Academy of Sciences* **112**, 3641 (2015).
- [105] J.-M. Cui *et al.*, “Supporting Kibble-Zurek Mechanism in Quantum Ising Model through a Trapped Ion,” , arXiv:1505.05734 2015.
- [106] K. Murata, H. Saito, and M. Ueda, “Broken-axisymmetry phase of a spin-1 ferromagnetic Bose-Einstein condensate,” *Phys. Rev. A* **75**, 013607 (2007).
- [107] A. Lamacraft, “Quantum Quenches in a Spinor Condensate,” *Phys. Rev. Lett.* **98**, 160404 (2007).
- [108] H. Saito, Y. Kawaguchi, and M. Ueda, “Kibble-Zurek mechanism in a quenched ferromagnetic Bose-Einstein condensate,” *Phys. Rev. A* **76**, 043613 (2007).
- [109] H. Saito, Y. Kawaguchi, and M. Ueda, “Kibble-Zurek mechanism in a trapped ferromagnetic Bose-Einstein condensate,” *J. Phys. Condens. Matter* **25**, 404212 (2013).
- [110] B. Damski and W. H. Zurek, “Quantum phase transition in space in a ferromagnetic spin-1 Bose-Einstein condensate,” *New J. Phys.* **11**, 063014 (2009).
- [111] L. Carr, *Understanding Quantum Phase Transitions* (CRC press, 2010).
- [112] W. Hardy, M. Morrow, R. Jochemsen, and A. Berlinsky, “Magnetic resonance of atomic hydrogen at low temperatures,” *Physica B & C* **109**, 1964 (1982).
- [113] H. F. Hess, D. A. Bell, G. P. Kochanski, D. Kleppner, and T. J. Greytak, “Temperature and magnetic field dependence of three-body recombination in spin-polarized hydrogen,” *Phys. Rev. Lett.* **52**, 1520 (1984).

- [114] B. Johnson, J. Denker, N. Bigelow, L. Levy, J. Freed, and D. Lee, “Observation of nuclear spin waves in spin-polarized atomic hydrogen gas,” *Phys. Rev. Lett.* **52**, 1508 (1984).
- [115] C. C. Bradley, C. A. Sackett, and R. G. Hulet, “Bose-Einstein Condensation of Lithium: Observation of Limited Condensate Number,” *Phys. Rev. Lett.* **78**, 985 (1997).
- [116] T. Ohmi and K. Machida, “Bose-Einstein Condensation with Internal Degrees of Freedom in Alkali Atom Gases,” *J. Phys. Soc. Jpn* **67**, 1822 (1998).
- [117] T.-L. Ho, “Spinor Bose Condensates in Optical Traps,” *Phys. Rev. Lett.* **81**, 742 (1998).
- [118] C. K. Law, H. Pu, and N. P. Bigelow, “Quantum Spins Mixing in Spinor Bose-Einstein Condensates,” *Phys. Rev. Lett.* **81**, 5257 (1998).
- [119] T. M. Hoang, *Quantum control of a many-body system in a spin-1 Bose-Einstein condensate*, PhD thesis Georgia Institute of Technology 2013.
- [120] W. Zhang, D. L. Zhou, M.-S. Chang, M. S. Chapman, and L. You, “Coherent spin mixing dynamics in a spin-1 atomic condensate,” *Phys. Rev. A* **72**, 013602 (2005).
- [121] J. Goldstone, “Field theories with Superconductor solutions,” *Nuovo Cimento* **19**, 154 (1961).
- [122] M. D. Barrett, *A QUEST for BEC: an all optical alternative*, PhD thesis Georgia Institute of Technology 2002.
- [123] C. Klempt, T. van Zoest, T. Henninger, O. Topic, E. Rasel, W. Ertmer, and J. Arlt, “Ultraviolet light-induced atom desorption for large rubidium and potassium magneto-optical traps,” *Phys. Rev. A* **73**, 013410 (2006).
- [124] D. A. Steck, “Rubidium 87 D Line Data,” available online at <http://steck.us/alkalidata> 2001.
- [125] H. J. Metcalf and P. van der Straten, *Laser Cooling and Trapping* (Springer-Verlag, New York, 1999).
- [126] C. C. Bradley, J. Chen, and R. G. Hulet, “Instrumentation for the Stable Operation of Laser-Diodes,” *Rev. Sci. Inst.* **61**, 2097 (1990).
- [127] C. E. Wieman and L. Hollberg, “Using Diode-Lasers for Atomic Physics,” *Rev. Sci. Inst.* **62**, 1 (1991).
- [128] S. Friebel, R. Scheunemann, J. Walz, T. W. Hansch, and M. Weitz, “Laser cooling in a CO₂-laser optical lattice,” *Appl. Phys. B* **67**, 699 (1998).

- [129] R. Grimm, M. Weidemüller, and Y. B. Ovchinnikov, “Optical Dipole Traps for Neutral Atoms,” *Adv. Atom Mol. Opt. Phys.* **42**, 95 (1999).
- [130] T. Takekoshi, J. R. Yeh, and R. J. Knize, “Quasi-electrostatic trap for neutral atoms,” *Opt. Comm.* **114**, 421 (1995).
- [131] M.-S. Chang, *Coherent Spin Dynamics of a Spin-1 Bose-Einstein Condensate*, PhD thesis Georgia Institute of Technology 2006.
- [132] C. Finlay *et al.*, “International geomagnetic reference field: the eleventh generation,” *Geophysical Journal International* **183**, 1216 (2010).
- [133] J. R. Taylor, *An Introduction to Error Analysis*, Second ed. (University Science Books, 1997).
- [134] J. Nocedal and S. Wright, *Numerical optimization* (Springer Science & Business Media, 2006).
- [135] A. Del Campo and W. H. Zurek, “Universality of phase transition dynamics: Topological defects from symmetry breaking,” *Int. J. Mod. Phys. A* **29**, 1430018 (2014).
- [136] A. Aspect, P. Grangier, and G. Roger, “Experimental Realization of Einstein-Podolsky-Rosen-Bohm *Gedankenexperiment*: A New Violation of Bell’s Inequalities,” *Phys. Rev. Lett.* **49**, 91 (1982).
- [137] Z. Zhang and L.-M. Duan, “Generation of Massive Entanglement through an Adiabatic Quantum Phase Transition in a Spinor Condensate,” *Phys. Rev. Lett.* **111**, 180401 (2013).